INDENTATION-BASED MICROMECHANICAL INVESTIGATION OF B2 INTERMETALLICS AND BCC METALS



by

VINCENT GRÉGOIRE LOUIS GAGNEUR

A thesis submitted to the University of Birmingham for the degree of

DOCTOR OF PHILOSOPHY

School of metallurgy and materials

College of engineering and physical sciences

University of Birmingham

September 2024

UNIVERSITY OF
BIRMINGHAM

University of Birmingham Research Archive

e-theses repository

This unpublished thesis/dissertation is copyright of the author and/or third parties. The intellectual property rights of the author or third parties in respect of this work are as defined by The Copyright Designs and Patents Act 1988 or as modified by any successor legislation.

Any use made of information contained in this thesis/dissertation must be in accordance with that legislation and must be properly acknowledged. Further distribution or reproduction in any format is prohibited without the permission of the copyright holder.

Abstract

Whether it is for aerospace or nuclear applications, materials' high temperature performances are often a limiting characteristic for improving the efficiency of next generation equipment. Few classes of materials have the properties to withstand the high temperature and high mechanical stress of aerospace gas turbines, or the irradiation environment of nuclear power plants, which often comes at the expense of their room temperature properties, limiting their processability and applications.

One of the top class of materials for aerospace gas turbine application are nickel-based superalloys. Their success is in part due to their microstructure, consisting of a face-centred-cubic (fcc) γ nickel matrix, reinforced with ordered-fcc γ' Ni_3Al precipitates, offering astonishing high temperature performance in terms of yield strength, creep strength and melting point, whilst retaining a decent amount of room temperature ductility for processing. However, recent developments of nickel-based superalloys seem to reach a limit, and no major improvement of their high temperature performance have been seen over recent years, which opens the question of exploring other classes of materials to push mechanical properties even further.

Body-centred-cubic (bcc) metals usually display higher melting points than fcc metals, as well as being lower cost, and could potentially outcompete them for high temperature applications. Recently, a new class of alloys using bcc metals has been proposed, termed "bcc-superalloys", taking inspiration of nickel-based alloys in their microstructure template. These exploit a combination of a bcc disordered matrix, reinforced with ordered-bcc (B2) intermetallics. Many potential alloy systems display such phase equilibria that could realise the desired high temperature performance e.g. HEAs namely (Zr,Ti)(Ta,Nb,V)Alx type, beta titanium + TiFe, or Fe + NiAl. However, their application is currently limited by their lack of room temperature ductility.

Much has yet to be discovered as to bcc-superalloy mechanical behaviour, and the bcc crystal structure offers its share of unique behaviour, controversies, and challenges. Designing bcc+B2 alloys with increased room temperature ductility will necessarily involve a study of bcc, B2 and bcc+B2 mechanical properties, and in particularity their micromechanics, which dictate the larger scale deformation behaviour. A question then is to combine high-throughput alloy development, in response to modern economic and environmental challenges, and refined micromechanical alloy characterisation.

Micromechanical testing techniques, whether they be transmission electron microscopy (TEM), micro-tensile or micro-pillar compression, and/or single grain testing, are usually complex and challenging experimental procedures, which can be poorly adapted to the context of rapidly surveying a wide range of different alloy systems. Micromechanical characterisation is especially challenging when performed on bcc and B2 materials, as their multiple possible active slip planes, namely {100}, {110}, {112} and {123}, often have very similar geometry, leading to common issues of ambiguity in slip system identification. An alternative technique for slip activity characterisation is indentation-based slip trace analysis. The technique consists in indenting a polished sample using either a microhardness or a nano-indentation testing equipment, imaging the slip traces generated around the indents using scanning electron microscopy (SEM), and measuring the local crystal orientation using electron back-scattered microscopy (EBSD). From there, theoretical slip trace orientations at the surface can be calculated, and compared to the observed orientations, informing us on the likely active slip planes of the material. Since the experimental procedure is significantly less demanding than TEM or single crystal testing, the large increase in statistics obtainable could by-pass the limitations surrounding ambiguity in bcc slip behaviour, and be powerful in the context of novel alloy development where there is a need for quick property assessments. In this work, we will explore the possibility of using automated indentation-

based slip trace analysis to efficiently characterise the slip activity in bcc and B2 compounds, and assist the development of novel bcc+B2 alloys with improved room temperature ductility.

In Chapter 1, the prior literature is reviewed, setting the background motivation of aerospace, current & future materials, then discussing in detail bcc, B2, and bcc+B2 alloys and their micromechanics, as well as the specific challenges posed by the bcc lattice when it comes to slip activity characterisation.

In Chapter 2, the methodology for slip activity assessment developed throughout this thesis experimental chapters (3 to 5) is presented, giving recommendations for the associated experimental work and data analysis to replicate the experiments made throughout this thesis, or use the technique on different materials.

In Chapter 3, an automated slip trace analysis algorithm is presented, designed to fully exploit the potential of indentation-based slip trace analysis approaches. The methodology gives access to larger statistics than alternative TEM, micromechanical and/or single crystal testing approaches, with increased speed and repeatability over manually slip trace identification, in a highly simplified experimental procedure. It is first demonstrated in the simpler fcc Nickel system, and then used to characterise the slip activity of bcc Fe, B2 TiFe, B2 Ti_2AlMo, and B2 Ti_2AlNb. It is shown how unambiguous <111> {112} and/or {123} type slip is likely to be observed under many experimental constraints, and used to distinguish between key bcc and B2 slip activities, whilst the global statistics of plane orientations matched by the slip traces can be used to assess the likely dominant slip planes.

In Chapter 4, the new slip trace analysis technique is applied on a compositionally graded sample, B2 FeAl to B2 NiAl, with the aim to characterise the evolution of the slip activity as a function of composition. It is shown how, using the technique developed, we can accurately predict the B2 composition at which the transition in active slip system between <100> dominated B2 NiAl and <111> dominated B2 FeAl occurs. This approach can be used to rapidly study the impact of alloying additions on B2 slip behaviour in different ternary systems, and then to determine which B2 compositions are more likely to favour ductile behaviour within bcc+B2 systems. Also, the quasi-continuous information on slip activity as a function composition obtained offers a new kind of data to refine crystal plasticity models.

Finally, in Chapter 5, we dive deep into the statistics obtained via the technique. Through sample slip activity simulation, hypothesis testing, and confidence level assessment, it is shown how reliable conclusions on the samples' bulk slip activity can be made, whilst resorting to only minimal assumptions on the samples slip behaviours. We also show that the ambiguity in slip plane identification can be bypassed in almost any context, provided that sufficient data is gathered, which may now be acquired thanks to the automation and simplicity of the experimental procedure.

All experimental results obtained throughout these chapters, using our newly developed technique, give consistent results with literature, and the technique is currently being used to assist the development of bcc+B2 systems of particular interest, notably titanium-based bcc-superalloys. Ongoing work attempts to apply the technique to dual phase alloys, giving new insights as to bcc + B2 slip transfer mechanisms and the influence of B2 slip activity on the overall alloy slip activity.

Acknowledgements

I gratefully acknowledge PhD funding support from the University of Birmingham and Rolls-Royce plc, with a special thanks to Nigel Martin and Tim Moschini (Rolls-Royce) for their precious help and insights throughout this work.

A thanks to the Centre for Electron Microscopy (University of Birmingham), in particular Ludwig Schneider for their friendliness, support & assistance in this work.

I would like to thank warmly my supervisor, Alexander (Sandy) J. Knowles, for suffering through this project with me. Your support and knowledge were key to the success of this work, and your seemingly un-tarnishable enthusiasm was the only kick I needed to push through in times of doubts.

I would like to thank my friends in the Alloys for Extremes group, for enduring the hour-long presentations I inflicted upon them during our weekly group meetings. This work could not have been done without your helpful insights, support during experiments, and friendship. I would like to thank in particular Tom Blackburn, Kan Ma, and Matthew Lloyd who participated in the writing and reviewing of the Chapter 3 of this thesis, as well as gave precious help during experiments (notably the synchrotron XRD measurements).

Finally, I would like to thank my family and close entourage for their support throughout the duration of this project. I would not have been able to fully engage with it without the unbreakable trust I have in you always being there for me.

Authors contributions statement

All this thesis work was performed under the supervision of Alexander Knowles, who directed to the main areas of work investigated, as well as supported the writing and reviewing of every chapter throughout the duration of this project. He also provided the Ti_2AlNb and Ti_2AlMo samples analysed in Chapter 3.

Each chapter of this thesis was originally written as independent pieces of work in anticipation for their publication as journal articles, their abstract/introductions were slightly adjusted to fit better with the thesis format, and to reduce repetitions. Chapter 3's content and text were reviewed by UoB colleagues Dr Kan Ma and Dr Matthew Lloyd shortly before thesis submission, as well as Johann Magnussen at an earlier draft stage, who therefore all contributed to its writing. K Ma and M Lloyd gathered the Synchrotron XRD (SXRD) data presented in Chapter 3 with the help of other members of our group, K Ma also gave precious help with the SXRD analysis.

Johann Magnussen wrote an initial part of the code dedicated to calculating theoretical slip plane intersections with the sample surface for given grain Euler angles (during their master's thesis project 2019-20), which was translated from Python to MATLAB by Vincent Gagneur at the beginning of the RAST code development during this PhD thesis. Johann Magnussen also gave some valuable insights as for the validation of the code analysis parameters during the technique's development.

The bcc Fe sample (Chapter 3) was provided by Anastasia Vrettou (UoB). In Chapter 7, The TiFeAl samples were provided by Dr Rosie Mellor (Univ. Cambridge), whilst the TiFeNb and TiFeAlNb samples were made and characterised in part by respectively UoB undergraduate project students Abbie Jones and Alex McShane under the supervision of Vincent Gagneur (who also gave experimental assistance) and Alexander Knowles.

Other members of our group also gave precious help during some of the experimental work (sample preparation, heat treatments etc.), in particular Tom Blackburn. All members of the group participated in essential discussions/debates surrounding this work during group meetings throughout the whole duration of this project. The author gratefully acknowledges their support and contribution.

Apart from the aspects mentioned above, this thesis literature survey, sample preparation, characterisation, experimental, programming, and analytical work are the original work of the author, Vincent Gagneur.

Contents table

1 Literature review 1
1.1 Introduction 1
1.2 Background Motivation 2
1.2.1 Aerospace gas turbines requirements 2
1.2.2 Current Aerospace alloys 3
1.2.3 β/β’ bcc-superalloys 6
1.3 Bcc plasticity 12
1.3.1 Commonly reported slip behaviour 12
1.3.2 The Schmid’s law in bcc 13
1.3.3 Scale of observations and interpretation of wavy slip 14
1.4 B2 plasticity 15
1.4.1 <111> vs <100> slip direction 15
1.4.2 Dominant slip planes 15
1.4.3 Influence of composition and stoichiometry on slip 16
1.5 Bcc+B2 plasticity and design strategy 17
1.5.1 Consequence of slip transfer 17
1.5.2 Slip activity and slip transfer 19
1.5.3 bcc+B2 design strategy 22
1.6 Characterising slip behaviour in bcc and B2 22
1.6.1 TEM 22
1.6.2 Single crystal testing 24
1.6.3 Slip trace analysis in bcc and B2 25
1.6.4 Indentation-based slip trace analysis 26
1.7 Summary 28
2 Methodology 30
2.1 Sample preparation 30
2.1.1 Bulk samples 30
2.1.2 Diffusion gradient 30
2.1.3 Summary of samples studied in this thesis 31
2.2 Indentation slip traces 32
2.2.1 Analysis outside indents 32

2.2.2 Analysis inside indents 33
2.3 Imaging of slip traces 34
2.3.1 Analysis outside indents 34
2.3.2 Analysis inside indents 35
2.4 EBSD analysis 35
2.5 RAST Code analysis and parameters 35
2.5.1 Main parameters 36
2.5.2 Secondary parameters 40
2.5.3 Advanced statistical analysis (Chapter 5) 40
2.6 Data analysis 41
2.6.1 Bulk samples 41
2.6.2 Diffusion gradient 41
2.6.3 Advanced statistical analysis (Chapter 5) 41
2.7 Sources of biases in the statistics 42
2.7.1 Miscellaneous features 42
2.7.2 SEM imaging 43
2.7.3 Grain orientations 43
3 Automated indentation-based slip trace analysis for bcc and B2 plasticity 45
3.1 Abstract 45
3.2 Introduction 46
3.2.1 Slip characterisation in bcc and B2 alloys 46
3.2.2 Identifying key slip activities from indents 47
3.2.3 Automation challenges 48
3.3 Methodology 50
3.3.1 Automated slip trace analysis code development 50
3.3.2 Experimental work 59
3.4 Results and Discussion 61
3.4.1 Materials and indentation characteristics 61
3.4.2 Validation on fcc nickel & choice of analysis input parameters 63
3.4.3 Slip Trace Code Application to bcc and B2 samples 70
3.5 Summary 78
4 Evaluation of B2 intermetallic deformation behaviour using diffusion gradients and indentation-based slip trace analysis 79
4.1 Abstract 79

4.2 Introduction 80
4.2.1 Composition gradient exploration 81
4.2.2 Automated indentation-based slip trace analysis 82
4.2.3 Evidencing a slip direction transitions with indents 83
4.3 Methodology 84
4.4 Results and Discussion 87
4.4.1 Materials 87
4.4.2 Analysing slip traces inside indents 88
4.4.3 Slip trace analysis on a diffusion gradient 94
4.4.4 Validation of the experiment 98
4.5 Summary 104
5 Solving the problem of ambiguity in bcc slip plane identification using indents and statistics 105
5.1 Abstract 105
5.2 Introduction 106
5.2.1 Slip trace analysis and ambiguity in bcc 106
5.2.2 Hypothesis testing applied to indentation-based slip trace analysis 107
5.3 Methodology 112
5.3.1 Data characteristics, assumptions, and solutions 112
5.3.2 Step by step analysis process 122
5.4 Results 128
5.4.1 Demonstration - Analysis on TiFe 129
5.4.2 TiFe and meta-analysis 136
5.4.3 Comparison between samples of different slip activities 140
5.4.4 Exploring the limits of the technique 145
5.5 Summary 151
6 Conclusion 152
7 Future work 154
References 158
Appendix 1 167
Extra information on the algorithm 167
Appendix 2 168
Additional data on the B2 FeAl-NiAl diffusion gradient 168

1 Literature review

1.1 Introduction

Aerospace gas turbines are one of the most demanding high temperature mechanical components, as they undergo high level of stress and temperature during use. As a result, the materials used are pushed to their extreme in terms of strength, creep, and oxidation resistance. Currently, nickel-based superalloys are widely used for such applications. Those display a microstructure consisting in a face-centred cubic (fcc) matrix reinforced with ordered-fcc precipitates, which is thought to confer them high temperature strength and creep performance [1]. However, nickel-based superalloys are expensive materials, and twice as dense as typically used aerospace alloys. Also, no major improvement of their properties has been observed over the last decade, suggesting that these alloys are reaching their limits in terms of possible improvements.

This opens the question of switching alloy system, and a good candidate for the replacement of nickel-based superalloys are “bcc-superalloys”, which seek to exploit refractory bcc elements such as Mo and Nb, paired with a similar ordered/disordered microstructure to nickel superalloys. Typically, a promising class of alloys for aerospace gas turbine applications are titanium-based bcc-superalloys [2] [3], which consist of a bcc titanium matrix reinforced with ordered-bcc B2 TiFe precipitates. The cheaper and lower density of titanium combined with the high melting points of refractory elements could at term outcompete nickel-based superalloys. However, little is known about bcc superalloys mechanical properties and their lack of room temperature ductility hinders their development. If we seek to design bcc+B2 superalloys with improved room temperature ductility, an understanding of their micromechanics is required.

Dislocations motion governs the mechanical properties of metals, and are constrained by the geometries and diverse properties of their crystal lattices. More specifically, dislocation slip on a materials’ operating slip systems rules its larger scale deformation behaviour. The bcc crystal lattice has been known for over a century, and early researchers quickly noticed that it displays several “unusual” slip behaviour compared to the fcc and hexagonal close-packed (hcp) lattices, such as non-crystallographic slip [4] and non-Schmid effects [5]. As a result of the complexity of slip in the bcc lattice, the topic of bcc metals slip activities is controversial, with frequently contradicting reports from different researchers. This problematic extends to the ordered-bcc intermetallics, with the extra added complexity brought by the ordering of their crystal structure, which can favour different active slip directions, either <100> or <111>.

These controversies will be presented and discussed during this literature review. First, §1.2, we will focus on background motivations for the study of bcc metals and B2 intermetallics, through several examples of alloys used in aerospace and newly developed bcc+B2 alloy systems. Then, we will review previous reports on bcc plasticity §1.3, followed by a similar review of the ordered-bcc B2 intermetallics plasticity §1.4, with an emphasis on the slip activity. After that §1.5, we will investigate the role played by slip activity as to the mechanical properties of dual phase bcc+B2 superalloys. Finally, §1.6, an overview of the different

commonly used slip activity characterisation techniques will be given, highlighting their limitations when applied to bcc, as well as the potential for further development of indentation-based slip trace analysis.

1.2 Background Motivation

1.2.1 Aerospace gas turbines requirements[1]

Air transport is a key to the functioning of modern society, however, in the context of climate change, increasing passenger numbers, and increasing fuel cost, great internation research and development attention is focused on how to reduce fuel consumption, especially of the engine, for both environmental and economic reasons.

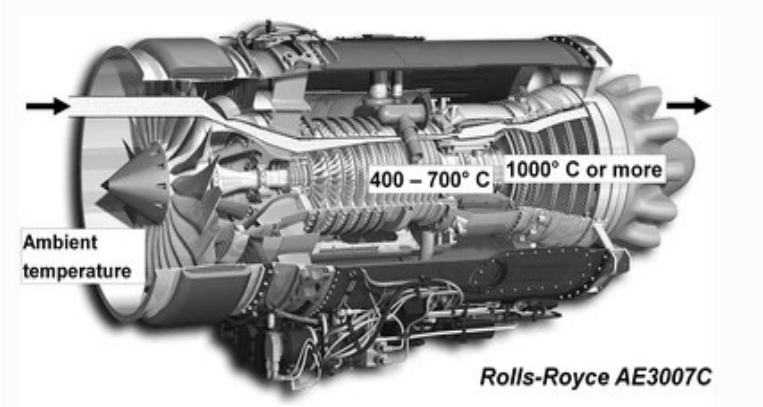


Figure 1: Cross-sectional view of Rolls-Royce AE3007C engine. The primary air flow path is highlighted, from [6].

There are two main approaches to decrease the fuel consumption of an aerospace jet engine:

1st: Decreasing the mass of the structure.

The lighter the structure is, the less energy is required to move it. In order to decrease the mass of the structure, we aim for materials with low density such as titanium and Nickel alloys (4 – 8 g/cm3) which are widely used in aerospace for their very good combination of mechanical properties and low densities. We can also aim to improve the mechanicals properties of the materials used (Yield strength and ductility, fatigue resistance…), which then allow us to build more mater-efficient engine parts.

2nd: Improving the engine efficiency.

The efficiency of an aerospace engine can be compared to a thermal engine efficiency, since the amounts of heat and work generated are directly linked to the amount of fuel consumed. The maximum Carnot efficiency achievable is given by the following relationship:

[1] Some of the content of this section was also published on https://more.bham.ac.uk/M4X/projects/jet-engines-turbine-blades-ti-superalloys/ (accessed 2024), our research group website, but originally appeared in my first year report: "Micromechanical Investigation of Novel Beta-Ti Superalloys for Aerospace Gas Turbines".

$$\eta_{cmax} = 1 - \frac{T_c dS_c}{-T_h dS_h} = 1 - \frac{T_c}{T_h}$$

Where T_c and T_h are respectively the temperatures of the cold and hot sources. This equation shows that in order to maximise the engine efficiency η_{cmax}, we need to increase T_c, the operating temperature of the engine.

The part of the engine undergoing the maximum amount of heat and stress are the gas turbines (Figure 1). It is this part of the engine that currently limits the operating temperature, as the materials used are pushed to their limit in terms of creep strength, melting point, and high temperature mechanical performance. In the next sections we will investigate what alloys are currently used, what are their main characteristics, and what substitutes could be investigated to enhance the properties of such engine parts.

1.2.2 Current Aerospace alloys

Advanced materials underpin the performance of modern jet engines. Titanium, Titanium aluminides and Nickel alloys are common in the aerospace industry for their good combination of low density, high mechanical strength, and creep performances. A review by Perez Prado [7] compares the properties of currently used high temperature alloys (listed in Table 1), which include α/β Ti 6-4 [8] [9] , ordered α TiAl and γ TiAl [10], and γ/γ' Nickel superalloys.

Table 1: Properties of titanium alloys, titanium aluminides, and Ni superalloys, from [7]

Property	Ti-based alloys	Ti_3Al-based α_2 alloys	TiAl-based γ alloys	superalloys
Density (g/cm^3)	4.5	4.1–4.7	3.7–3.9	8.3
RT modulus (GPa)	96–115	120–145	160–176	206
RT Yield strength (MPa)	380–1115	700–990	400–630	250–1310*
RT Tensile strength (MPa)	480–1200	800–1140	450–700	620–1620*
Highest temperature with high creep strength (°C)	600	750	1000	1090
Temperature of oxidation (°C)	600	650	900–1000	1090
Ductility (%) at RT	10–20	2–7	1–3	3–5
Ductility (%) at high T	High	10–20	10–90	10–20
Structure	hcp/bcc	DO19	$L1_0$	Fcc/$L1_2$

Also, it is important to keep in mind the order of magnitude of the raw materials price (from varied sources early 2021):

- Nickel ≈ 13000-17000 $ / metric ton
- Titanium ≈ 4250 $ / metric ton
- Aluminium ≈ 2000 $ / metric ton
- Iron ≈ 125 $ / metric ton

We will now review the main characteristics of these alloys in turn.

1.2.2.1 Ti based alloys

Two examples of Ti based alloys for high temperature aerospace applications are Titanium 6-4 (for Ti-6Al-4V at.%) [8] [9] and Titanium 6-2-4-2 (for Ti-6Al-2Sn-4Zr-2Mo at.%) [11] [12]. Their composition and microstructure vary depending on the manufacturer and application, and consist of a primary Hexagonal Close Packed (hcp) α phase (with various microstructures: lamellar/laths/equiaxed), surrounded by a secondary Body Centred Cubic (bcc) β phase. An example microstructure is given in Figure 2.

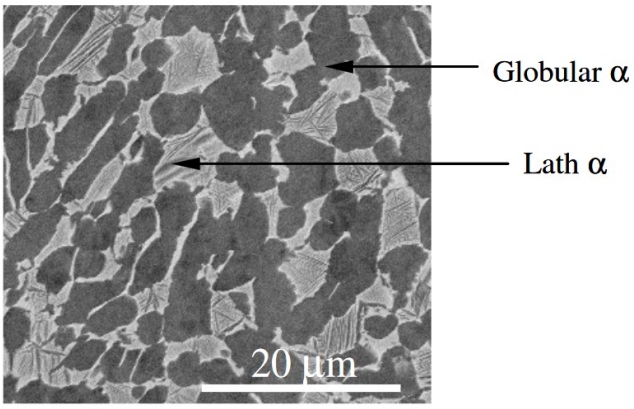


Figure 2: From [8], microstructure of a conventional Ti-6Al-4V.

These alloys display a very good combination strength and ductility, especially specific strength. However, they have limited resistance at high temperature (above 600°C [7]) compared to Ni superalloys which makes them less attractive for the higher temperature sections of gas turbines.

1.2.2.2 TiAl based alloys

Despite having a low melting point (T_m = 660,3°C) Aluminium is a very attractive element: it is light, cheap, easy to manufacture and helps increasing the oxidation resistance of Titanium and Nickel alloy systems. Titanium aluminides (Ti_3Al based and TiAl based alloys) [13] [14] [15] display the lowest densities amongst commercial aerospace alloys, and show very good creep performance at high temperature [10] [16]. Their composition and microstructures vary depending on the application (see F. Appel work on TiAl [10]). The alloy systems with the best high temperature aptitudes are nearly stoichiometric TiAl, displaying a γ face centred cubic (fcc) matrix combined with α_2 plates (ordered hcp), forming a lamellar microstructure as on Figure 3, a thin lamellar spacing being associated to good creep performance [16].

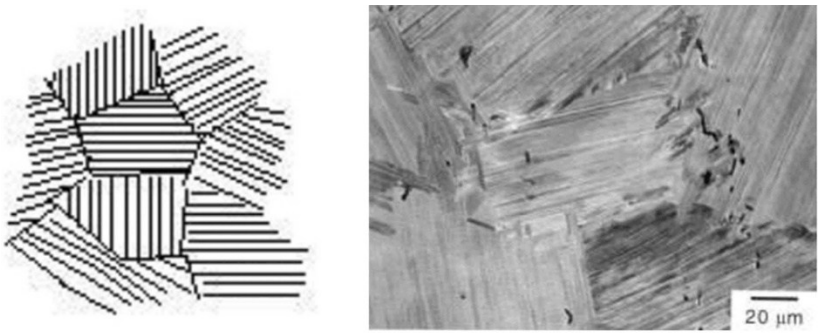


Figure 3: Reproduced from [14], example of a lamellar microstructure corresponding to a γ/α_2 Ti-Al based alloy (a) schematic from [17], (b) scanning electron microscope (SEM) micrograph from [13].

These alloys are limited in their applications by their poor room temperature ductility and strength in comparison to other Ti and Ni based alloys.

1.2.2.3 Nickel superalloys

Currently, Nickel alloys are widely used for gas turbine applications [1] [18] [19] [20] [21]. Their main representative are Ni-Cr-Al systems which display both high yield strength, good ductility, and high creep resistance at HT [1]. Such system consists in a microstructure of a γ fcc (face centred cubic) matrix reinforced with ordered NiAl γ' fcc precipitates, as represented in Figure 4.

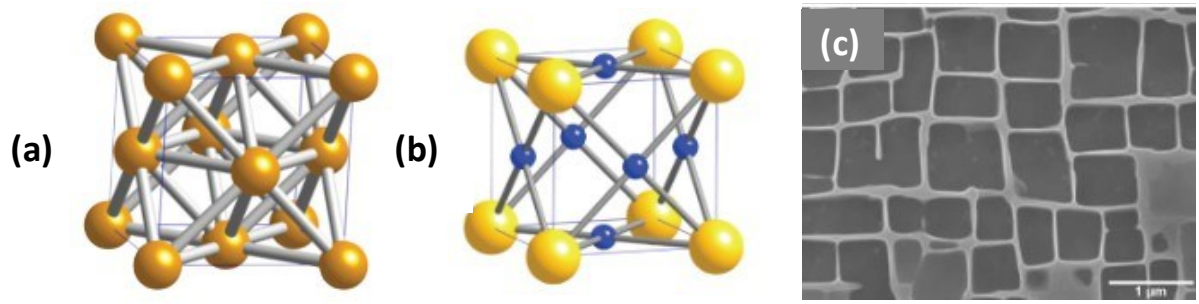


Figure 4: Crystal structure of (a) NiAl γ (fcc),(b) $NiAl_3$ γ' (ordered fcc) and (c) microstructure of a typical NiCrAl alloy, showing cubic darker contrast γ' precipitates within a γ matrix.

It was shown that the higher the volume fraction of the ordered precipitate, the better the high temperature yield strength of the alloy, as per Figure 5, from [1].

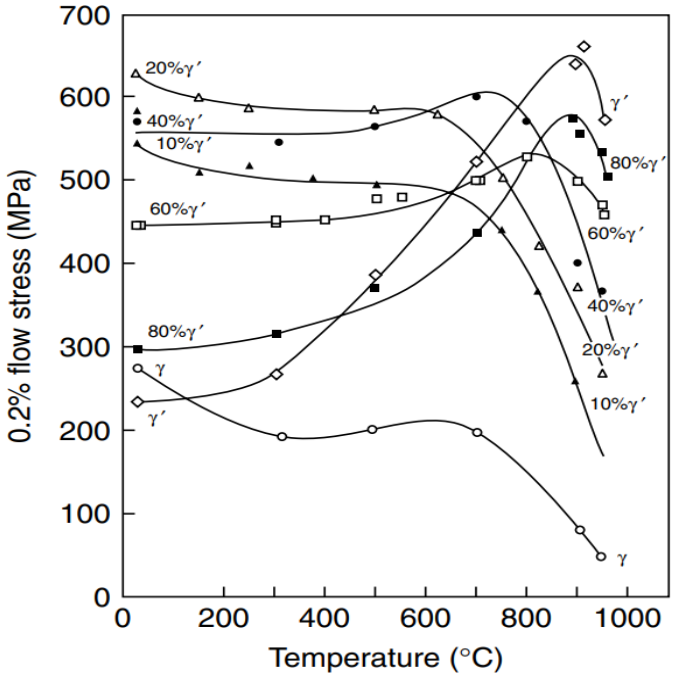


Figure 5: Variation of the yield stress with temperature for γ / γ' Ni-Cr-Al alloys with different γ' volume fractions [1]

The good high temperature performance of nickel superalloys is therefore associated to this particular microstructure: a high-volume fraction of highly coherent ordered precipitates. Despite showing an excellent combination of high temperature creep strength and tensile strength, nickel superalloys are twice as dense as commercial titanium alloys and have limited room temperature ductility. Nickel is also very expensive when compared to other potential base elements such as titanium and iron. Many elements with lower densities and/or higher melting points could be investigated as replacements for Nickel, which brings us to the beta phase alloy systems.

1.2.3 β/β' bcc-superalloys

1.2.3.1 Bcc superalloys and the β/β' system

We will define the concept of "bcc-superalloys" as alloys exploiting a body-centred-cubic (bcc) β matrix reinforced by ordered-bcc (B2 or $L2_1$) β' intermetallic phases [23] [24] [25] [22] [1], as illustrated on Figure 6. Miracle et al. recently created an additional definition of refractory high entropy superalloys (RSAs) [28], being a sub-set of refractory high entropy alloy (RHEAs) [29], which also show such a bcc + ordered-bcc microstructure template. This alloy structure was designed to mimic the γ/γ' structure of fcc nickel superalloys, but using bcc stabilising elements.

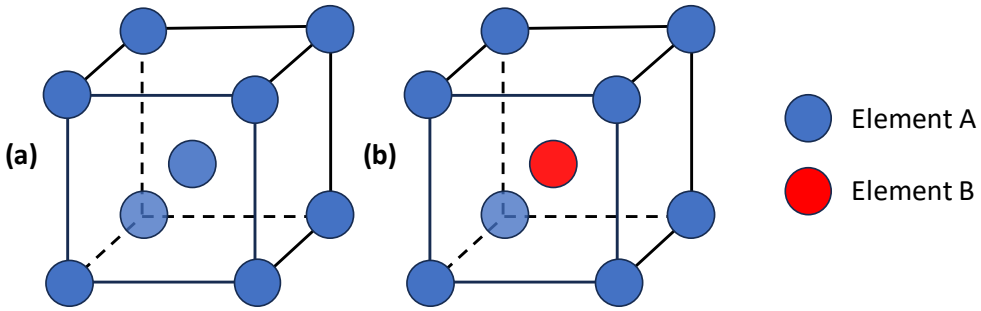


Figure 6: Cristal structure of (a) A2 β (bcc) and (b) β' (B2). Bcc elements can be e.g.: Ti, Fe, W, Al, Ni. B2 compounds can be e.g.: Ti-Fe, Ni-Al

Elements of columns 5,6 & 7 (e.g. Ti, Cr, Mo, Zr) typically favour the formation of bcc phases [1].

1.2.3.2 Attractiveness of bcc-based alloys

The creep performance of an alloy is linked to the next equation [1]:

$$\bar{\dot{\gamma}} = \frac{\dot{\gamma}\Omega^{2/3}}{D_{T_m}} \propto \exp\left\{-\frac{Q_v}{RT_m}\left(\frac{T_m}{T}-1\right)\right\}$$

Where $\bar{\dot{\gamma}}$ is the normalised creep sheer strain rate, Q_v is the diffusivity of the elements and T_m their melting point. This equation shows that the ratio T_m/T is of key importance, using higher melting points elements (also called refractory elements) can be a major lever to obtain better creep performance. Therefore, one way to design alloys working at higher temperature would be to replace currently used Nickel (Tm=1455°C) with higher melting point elements. Figure 7, from R. Jones [29], lists most metals melting points as a function of their density.

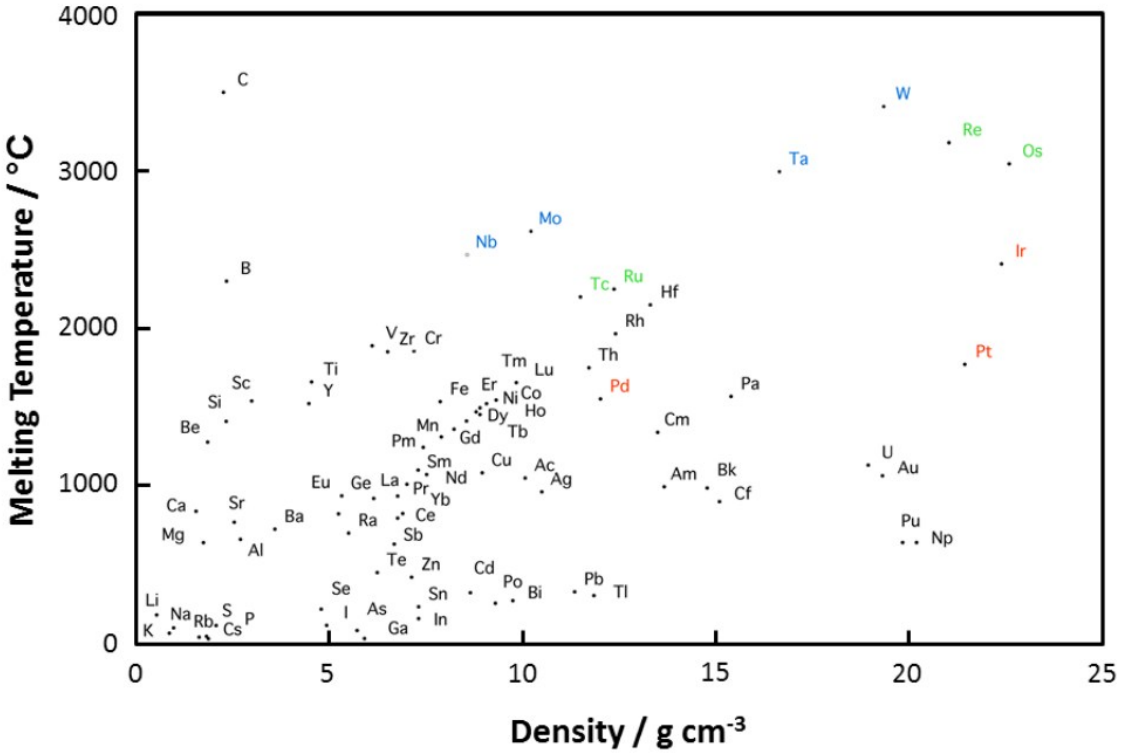


Figure 7: Graphic from R. Jones [29]. A plot of melting temperature against density of the elements. The refractory metals are colour coded according to their crystal structure: bcc in blue, hcp in green, fcc in red, and in black if several structures can be stabilised via specific heat treatments.

Elements such as Mo (T_m=2500°C) or Nb (T_m=2450°C) show very attractive combinations of low density and high melting point, they also stabilize β bcc crystal structures. Going for β based alloy systems could therefore allow us to make use of such refractory elements.

Most of the attempts to design new refractory β alloys aim to obtain an ordered/disorder phase system, similar to the one seen in γ/γ' Ni superalloys, but working in the β/β' system. We will now go through a few examples of such systems and their main characteristics.

1.2.3.3 Examples of bcc+B2 bcc superalloys

Here we will review the main characteristics explored in the literature of some working refractory β/β' like systems, to get an idea of the variety of systems, while comparing their microstructures and mechanical performances when data is present.

1.2.3.3.1 Mo-NiAl

With a nominal composition as Ni-45.5Al-9Mo (at.%) [30], this alloy system consists in a B2 NiAl matrix reinforced with A2 Mo fibers (rod like structures with square sections) [30] [31]. Those are obtained via directional solidification using a high temperature optical floating zone furnace. An example of the microstructure is shown Figure 8.

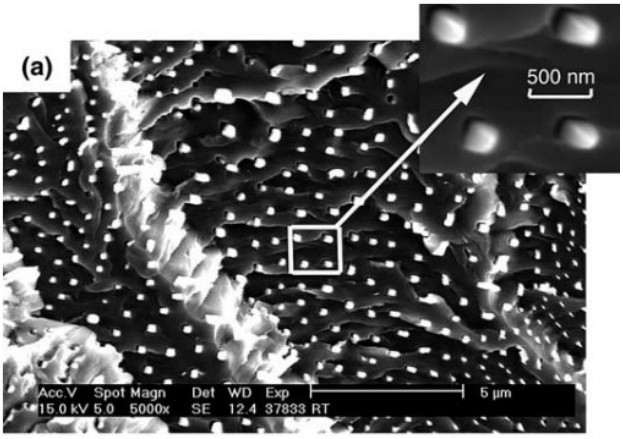


Figure 8: From [30], Scanning Electron microscopy (SEM) picture of a sample after tensile testing fracture, showing the Mo fibers (light contrast) within the NiAl matrix (dark contrast)

In [30] the lattice misfit between the phases was estimated to be ≈9%, the interface between the two phases is therefore probably incoherent. This alloy displayed a brittle to ductile transition at about 675°C, going from 4% elongation to fracture at RT to 28% at HT. Its yield strength was found to be 25-30% higher than that of NiAl single crystals.

1.2.3.3.2 Nb-PdHfAl

A few Nb based superalloys have been investigate in [32]. We will here discuss the system of 81.6Nb–6.3Al–2.8Hf–9.3Pd (at.%) which displayed the most interesting microstructure, shown on Figure 9. It consists in a Nb bcc matrix reinforced with $L2_1$ (a type of ordered bcc) Pd_2HfAl precipitates. The precipitates were obtained through aging of the as-cast alloy at 1000°C for 200 h.

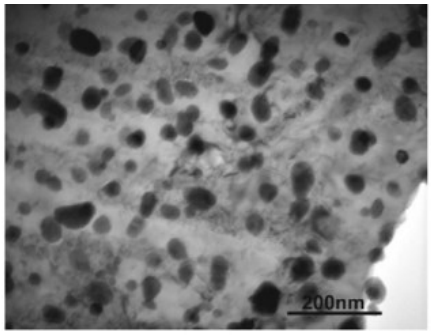


Figure 9: Bright field micrograph of 81.6Nb–6.3Al–2.8Hf–9.3Pd (at.%), showing $L2_1$-Pd2HfAl precipitates in a Nb matrix, from [32].

The precipitates were found to be fully coherent with the matrix. However, its mechanical properties were not investigated further.

1.2.3.3.3 Cr(Fe)-NiAl

A few systems exploiting B2 NiAl precipitates have been explored. Here we present recent work on chromium based superalloys [33] [34] [26] of composition Cr-5ni-5Al and Cr-5Ni-5Al-10Fe, of which key micrographs are represented in Figure 10.

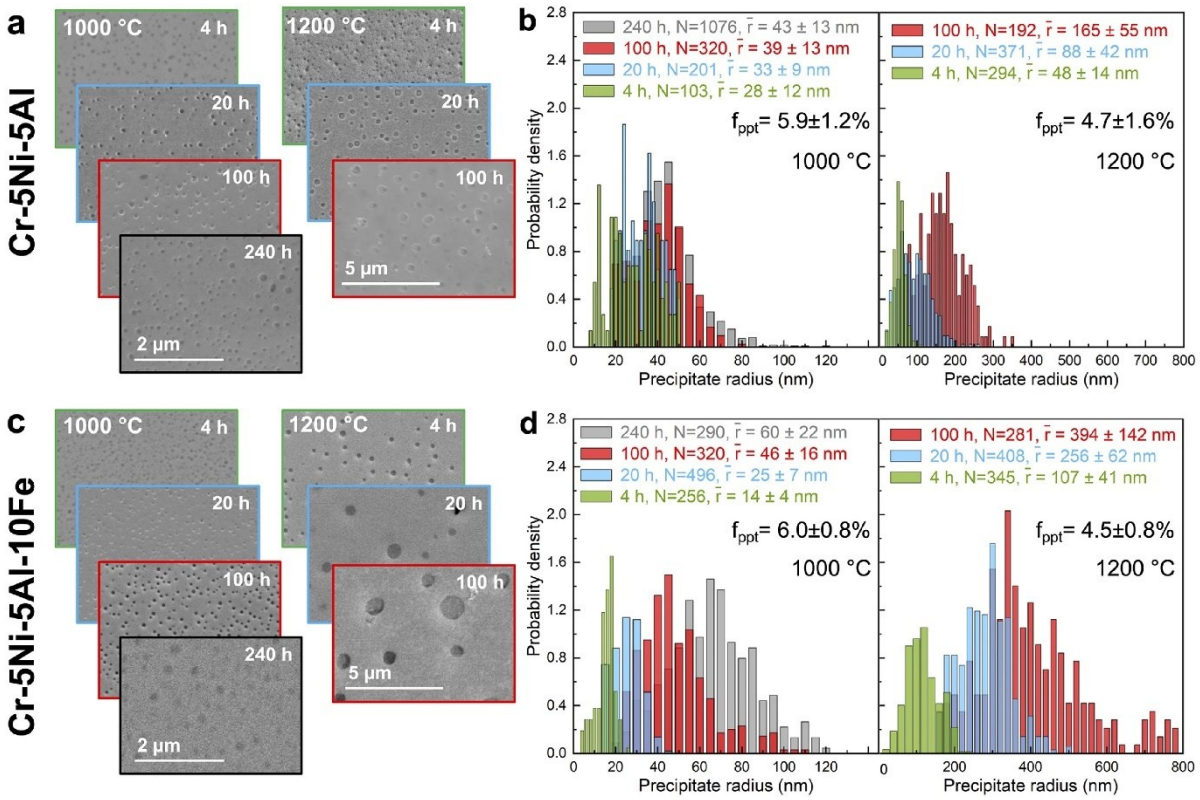


Figure 10: From [26], microstructure of (a) Cr-5Ni-5Al and (c) Cr-5Ni-5Al-10Fe aged at 1000 °C and 1200 °C for 4/20/100/240 h showing the coarsening of the precipitates with the corresponding precipitate size distribution in (b,d) respectively. f_{ppt} represents the area fraction of precipitate

These chromium alloys present a small area fraction (<6%) of highly coherent B2 precipitates (misfit ≈0.1%). A key finding was that they display a coarsening rate significantly lower than fcc and other bcc superalloys, suggesting good high temperature microstructural stability. Also, alloys with Fe additions were found to be strong with a compressive proof stress of ≈1300MPa at room temperature, and ≈360 MPa at 1000°C. This relatively high strength was attributed to Fe solid solution strengthening, and to diverse operating mechanisms for dislocation motion at the precipitate interface, which depends on the precipitate size.

1.2.3.3.4 Ti(Mo)-TiFe

One good candidate as base element for a β/β’ system is Beta titanium: titanium has both lower density, higher melting point (T_m=1668°C) than Ni and has been shown to display a wide range of β/β’ systems when mixed and aged conveniently with iron [2] [3] [35] [36], which also has higher melting temperature and lower density than Ni. Here we will present the Ti-Fe-Mo system explored in [3], with a composition of Ti–15Fe-22Mo (at.%). This system consists in a Ti-Mo rich matrix reinforced with B2 TiFe precipitates, as shown on Figure 11.

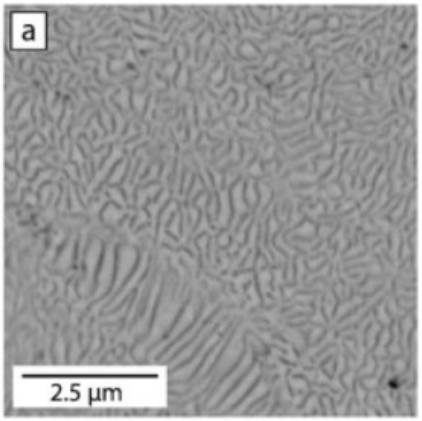


Figure 11: SEM backscattered electron (BSE) picture of the microstructure of the TI-Fe-Mo alloy explored in [3], showing lamellar B2 precipitates (black contrast) within an A2 matrix.

The alloy was tested using pillar micro-compression and displayed 1.9 GPa compressive proof stress, with 5% strain to failure. Its density was measured to be 6.68 g cm^{-3}. Its relative brittleness was associated with the presence of a small fraction of undesired omega phase. Also, micro compression testing performed in the same paper showed no slip propagation from the matrix to the precipitates, which is thought to be a source of embrittlement (see §1.5.1).

1.2.3.4 Comparison of mechanics in bcc-superalloys relative to fcc-superalloys

Many attempts at mimicking the nickel superalloys microstructure with bcc superalloys are available in the literature, with systems such as Mo-NiAl [30], Nb-PdHfAl [32], Cr(Fe)-NiAl [26] or Ti(Mo)-TiFe [3] [35] previously described. A trend in their behaviour is observable and was underlined in the literature (see in particular the work of Daniel Reed [1]):

- In comparison with fcc, the bcc crystal structure is less packed making slip more difficult, resulting in generally higher brittleness of bcc alloys
- Some systems attempting to mimic the γ/γ' system with a β/β' interface can show higher misfits than in the γ/γ' (ex: -6% misfit in the Ti-Fe-Mo system [3]), which is also a factor of increased brittleness as it results in more difficult dislocation motion between the phases.
- Bcc alloys are prone to brittle to ductile transition, meaning that they can have good ductility at high temperature, but their poor RT ductility limits their engineering applications.

There is generally very limited data concerning bcc-superalloys mechanical properties, in particular the question of ductility at room temperature is rarely evaluated, despite it being their main limitation. That is why, at a time where bcc-superalloys offer great interest for on-going high temperature alloy development, an analysis of the micromechanics and deformation behaviour of such alloys could help fill the lack of data, while bringing novel ductilisation strategies to this field of research.

In order to appraise their mechanical behaviour, an understanding of the deformation behaviour in both of their phases, namely the bcc phase, and the ordered B2 phase are

required. In the next sections 1.3 and 1.4, we will explore each of these phases' micromechanical behaviour, based on current literature. A note that we will not explore $L2_1$ specific behaviours (which can differ from B2's [37]) since most of current alloy development, including alloys investigated during this thesis, use B2 intermetallics. After that, in section 1.5, we will investigate how the differences in deformation behaviour between these two phases can affect the mechanical properties of dual-phase bcc+B2 alloys, and what alloy design strategies could be put in place to obtain the desired mechanical properties.

1.3 Bcc plasticity

Many high melting point elements stabilise a bcc crystal structure, and could present interest for a wide range of high temperature applications. The plasticity of metals is governed by the motion of dislocations. In bcc, dislocations move in the ½ <111> direction, on three main slip plane types, namely {110}, {112} and {123}. This seemingly straightforward statement can be, in practice, controversial. In this section we will go through the latest discussions on the topic, highlighting challenges and controversies specific to the bcc crystal lattice, and focussing mainly on room temperature (RT) behaviour.

1.3.1 Commonly reported slip behaviour

An extensive review from 2013 on slip in bcc has been made by C. R. Weinberger et al. [38], and surveys many previous reports of slip activity across several bcc alloys. Their general observation is that in bcc, at low temperatures (below RT), {110} planes are usually energetically favoured, whilst {112} and {123} planes get increasingly more activated as temperature increases. This, however, is a very generic statement. In practice, as is outlined in the review [38], different bcc materials were reported to display very different slip activities, even reports concerning the same alloy can be contradicting. For example, pure molybdenum was alternatively reported to slip predominantly on {110} [39] [40], and to slip on {110} and {123} [41], whilst tungsten was reported to slip predominantly on {110} [39], and later exclusively on {112} planes [38]. A common issue in these reports is that there is no real quantification of the prevalence of these slip planes, so when it is reported that "molybdenum slips on {110} and {123}", or "tungsten slips predominantly on {110}", it is difficult to assess what contribution each slip plane brings to the deformation of the alloy. Such statement can simply mean that both slip plane types were observed, in very specific crystal orientations, sometimes selected on purpose to favour the activation and observation of said slip planes.

A source of confusion in these reports concerns the interpretation of wavy slip traces, either as the closest matching plane orientation (e.g. {112}) or as multiple elementary {110} slip, which varies depending on the researchers (see discussion in §1.3.3). Another source of discrepancies comes from the mechanical testing techniques used, and the difficulty to unambiguously determine the slip plane associated to observed slip traces in bcc (those techniques and challenges will be discussed in §1.6). {123} planes in particular are rarely reported. Often, mainly to simplify simulations, modelers ignore {123} planes as an option when simulating plasticity [42] [43], limiting themselves to a competition between {110} planes and {112} planes. Similarly, a recent example of a meso-scale slip behaviour characterisation in tantalum [44], deformed at room temperature, quantifies {110} and {112}

slip activations, but discards the option of {123} slip as being, in bcc structural metals, “mainly a high temperature feature”.

A phenomenon is less likely to get reported if experimenters do not think said thing exists, which could be what is happening with {123} planes. Slip traces matching such orientations could be frequently “wrongly” attributed to waviness, i.e. considered composed of {110} & {112} slip [42], or explained by experimental uncertainties. Another factor concerning this lack of {123} slip reports is that many studies on bcc slip activity were performed at low temperatures (<RT) where high order planes are not expected to be frequently activated, which may bias our perception of their contribution to bcc metals plasticity in general.

Recently, a study of the deformation of ferrite (bcc Fe [45]) was performed via a series of micro-compressions. Considering the possibility of {110}, {112} and {123} type slip simultaneously, it was concluded that all three types of slip systems are active in ferrite at room temperature, and have very similar Critical Resolved Shear Stress (CRSS). This would mean that the main parameter for the choice of slip plane in this metal is geometry, and whether the stress components better favour one slip plane or the other. However, another investigation of ferrite, using micro-tensile experiments and also considering {123} slip, concluded on the absence of {123} type slip [46]. This, again, shows how controversial this topic is, and how delicate it would be to extrapolate conclusions from one experiment to bcc metals in general. From there, it is easy to imagine how including or eliminating the possibility of {123} type slip can affect crystal plasticity models (as suggested by [42]), on top of affecting experimentally reported slip behaviour.

1.3.2 The Schmid’s law in bcc

The Schmid’s law, usually taken as granted when studying fcc and hcp crystal structures, is not always obeyed in bcc [47] [48] [49]. One reason for that is the asymmetric nature of ½ <111> screw dislocations in bcc [47] [48]. The Schmid’s law, which postulates that the plane of atom with the highest Critical Resolved Shear Stress (CRSS) will be activated following deformation, no longer applies since the normal component of stress now also has a major impact on the choice of slip system. One consequence of that can be seen in the asymmetry of slip on {112} planes, which will show very different CRSS whether they are stressed in the twinning or anti-twinning direction, leading to tension/compression asymmetries in bcc [38].

These non-Schmid effects are predominantly observed at low temperatures (below RT). However, recent in situ TEM experiments [50] show non-Schmid effects occurring in tungsten at RT, which were further identified as impacting significantly the prediction of crystal plasticity in tungsten at RT [51]. Now, it is true that tungsten has by far the highest melting point of bcc elements, and what is true for tungsten at RT may happen at lower temperatures for other metals, but these observations highlight the necessity to avoid using the Schmid’s law to characterise slip activity, when possible, as using it may mislead our interpretations of slip behaviour in bcc.

1.3.3 Scale of observations and interpretation of wavy slip

The presence of cross-slip is usually associated to visible wavy slip in bcc, or "non-crystallographic slip" [5]. In general, a distinction is made between bcc alloys showing straight slip, usually more brittle, and alloys displaying wavy slip, usually more ductile. Indeed, a tendency to cross-slip gives more options for the material to accommodate to the strain, resulting on an increased ductility. It can also be a consequence, and therefore a sign, of a greater amount of active slip systems. The stacking fault energy (SFE) is also thought to affect the tendency for a material to cross slip, with higher SFE materials favouring cross slip [52].

This waviness of slip could be the main reason for how difficult and controversial slip system identification is in bcc. As presented on Figure 12 (a), extracted from [53], a wavy slip will often appear, when observed at the meso-scale, far from any crystallographic planes, hence why they are also called "non-crystallographic slip".

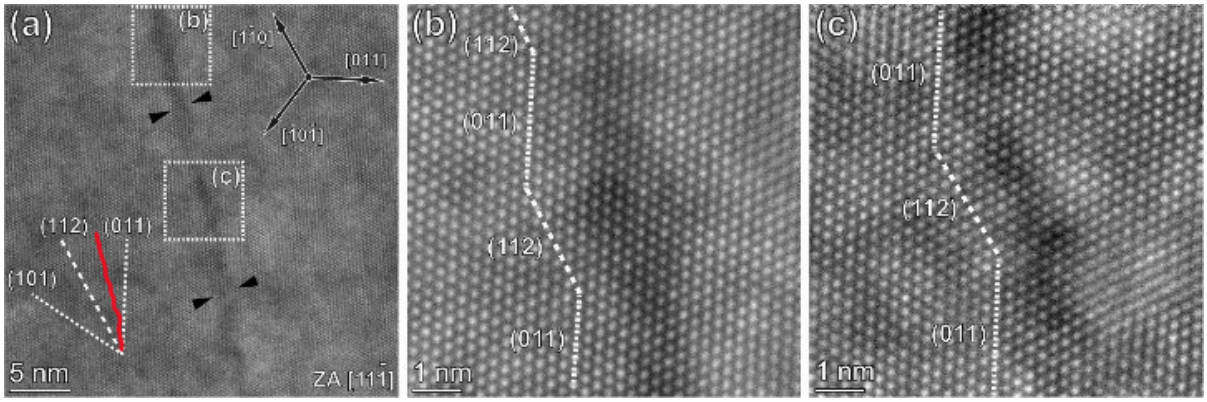


Figure 12: From [53], in an $Al_{0.5}NbTa_{0.8}Ti_{1.5}V_{0.2}Zr$ alloy, atomic scale HAADF-STEM imaging of a "non-crystallographic" or "wavy" slip, with [11$\bar{1}$] zone axis. (a) gives an overview of the slip observed, comparing its "meso-scale" orientation, in red, to {112} and {110} planes orientations. (b) & (c) show higher magnification pictures and propose a mechanism for the slip as elementary (011) & (112) slip.

In [53], it is argued that a non-crystallographic slip can be decomposed in smaller elementary slip, as illustrated by the Figure 12 (b) and (c). A similar interpretation is proposed by [4], using this time AFM imaging on compression deformed niobium single crystals. Such waviness complicates the identification of active slip systems, as a meso-scale observations could therefore be the result of smaller scale, intense cross slip between different active slip planes, difficult to identify precisely even when using the best available techniques (as we see on Figure 12, despite the atomic scale resolution, the decomposition in elementary slip can be subjective).

This phenomenon, pushed to the extreme, leads to observed slip on the Maximum Resolved Shear Stress Plane (MRSSP), which is often observed at higher temperature in bcc metals [38]: regardless of the crystal orientation relative to the stress, slip will follow the MRSSP and therefore is likely to have a non-crystallographic orientation.

These observations of wavy slip being composed of smaller scale elementary slip lead to an idea, which would be that actually, {112} and {123} type slip never activate, and that all if not

most slip in bcc can be explained as elementary small scale {110} slip regardless of temperature. One could then interpret the reports of {112} slip, and especially {123} slip, as being a misinterpretation of wavy slip traces observed at the meso-scale as matching closely corresponding plane orientations, in materials or experimental conditions favouring cross slip mechanisms (the former could be composed of elementary {110} slip, whilst the latter of elementary {110} and/or {112} slip). Whilst this debate is of interest, we can firstly stress that it contradicts the propositions of the two previously presented works [4] [53], where slip is proposed to be composed of {110} *and* {112} type slip. Secondly, room temperature in-situ TEM observations of {123} type slip in tungsten [50] and in β titanium [54], suggest that {123} slip does indeed exist as an elementary displacement path in bcc. The idea that wavy slip traces observed at low temperature (<RT) may be exclusively composed of {110} type slip remains plausible, but it is unlikely to be true at higher temperatures.

Due to waviness of slip, which is very frequently observed in bcc, the relative contribution of each plane type to the large-scale deformation of bcc metals is difficult to assess, and little quantitative information is available in literature on this topic, highlighting a need for a more quantitative assessment of slip behaviour in bcc. Challenges surrounding active slip plane characterisation, and quantification, will be discussed in more details in §1.5.

1.4 B2 plasticity

B2 compounds show a variety of properties, from hard to soft, and brittle to ductile. Here we will discuss the factors that control their mechanical properties, with a focus on slip systems.

1.4.1 <111> vs <100> slip direction

Ordered-bcc (intermetallic) B2 compounds share similar quirks with the bcc lattice, namely: non-Schmid effects, tensile compression asymmetries when <111>{112} slip is active, and the presence of wavy, or non-crystallographic slip [37] [55]. However, they also present their specific challenges. The presence of ordering in the B2 lattice affects its slip activity, as the motion of ½<111> type dislocations now also form anti-phase boundaries (APB). This leads to some B2 compounds favouring slip in the <100> direction, which, despite the longer Burgers vector, does not involve the formation of such APBs [37] [55] [56]. Therefore, the APB energy plays an important role in the choice of dominant slip system. However, there is an interplay of multiple material parameters that are thought to be responsible for the choice of slip direction, such as crystal anisotropy, width of splitting of dislocations, APB energy, and dislocation core structure [37] [56] [57]. Also, all these parameters can be influenced by temperature leading to significantly different B2 slip behaviours at lower or higher temperatures. The link between dominant slip direction and ductility is still controversial, and likely depends on multiple material parameters [37] [58].

1.4.2 Dominant slip planes

Due in part to the different possible active slip directions, very distinct slip systems may operate depending on the B2 compound. Generally speaking, at room temperature, B2 compounds show a great diversity of slip behaviour, often with restrained slip activities, for example: predominantly <111> {110} (e.g. FeAl [59] [60], CuZn [61]), <111> {112} (e.g. (Cu,Ni)-

Zn [61]), <100> {110} (e.g. TiFe [62]) or <100> {110} {100} (e.g. NiAl [63] [59] [64] [65]). Unlike bcc, where {112} slip is usually observed in conjunction with {110} and {123} type slip, some B2 compounds were demonstrated to slip predominantly on {112} planes [61]. {112} slip is proposed to be the most fundamental slip in B2 [37] (operating at very low temperatures), as opposed to {110} in bcc [38].

As described in [37], in <111> slipping B2 compounds, {110} planes are energetically favoured in terms of APB energy, with simulations suggesting <111> screw dislocation's core structure favour {112} slip. They propose that at low temperature (<RT), when the dislocation core structure has the most impact, {112} slip may be favoured, whilst a mix of {110} and {112} could be favoured at higher temperature as the APB becomes the main determining factor.

In <100> slipping samples, {100} type slip becomes an option, and only {100} and {110} planes allow deformation. In this situation, {100} slip is less frequently observed than {110} slip, which can be explained by its limited number of slip planes (three {100} planes vs six planes for {110}), and of course to different material parameters favouring {110} over {100}. As an example, in NiAl, which is considered strongly ordered, <100> slip is frequently observed, mainly on {110} planes, but also on {100} planes [63] [64] [65].

Similarly to bcc, it is unclear if {123} type slip was systematically taken in consideration as an option or not during these previous studies of B2 compounds micromechanics. The presence of non-crystallographic slip could very well be a sign of their existence (e.g. observed in [61]). A recent work on a multiphase Ti_2AlNb system [66] suggests that the B2 Ti_2AlNb matrix slips mainly on <111> {110} {112} slip systems, with some evidence of {123} type slip. They stress that {123} slip planes must have a significantly higher CRSS that the other slip systems, hence why it was less frequently observed in this alloy. However, these observations were made on very wavy slip traces at the meso-scale, and are therefore difficult to attribute unambiguously to {123} slip.

1.4.3 Influence of composition and stoichiometry on slip

Previous studies have demonstrated that the B2 slip activities can be modified by changes in composition, either stoichiometry, or with alloying additions [37] [61] [67]. Whilst stoichiometry deviations appeared to have only a minor impact on the slip activity of hard oriented NiAl crystals [67], ternary element additions were found to be decisive as to the operating slip systems. Two examples caught our attention, one on the FeAl-NiAl system [68], and another on the CuZn-NiZn system [61].

The first experiment aimed to study the transition of active slip direction at intermediate compositions between <111> dominated Fe-40Al at.% and <100> dominated Ni-40Al at.%. Through a series samples of intermediate compositions, compression deformed at room temperature and at 600°C, and characterised using Transmission Electron Microscopy (TEM), it was found that a transition in slip direction occurs around the composition 40Fe-20Ni-40Al at.%, which shifts towards higher Fe content at 600°C.

The second experiment studied the evolution of the slip activity of <111>{110} dominated CuZn with Nickel additions. Through a series of single crystal (mm scale) compressions at

diverse compositions, it was found that at a composition of Cu-14Ni-49Zn at.%, the slip activity of the alloy shifts from predominant {110} slip (binary CuZn) to predominant {112} slip (ternary composition). Also, the intermediate composition Cu-6Ni-48Zn at.% presents an intermediate slip activity likely to involve a mix of {110} and {112}.

The main idea proposed by Yamaguchi & Umakoshi [37] to interpret these changes in slip activity as a function of compositions is that, in response to increasing APB energy (which is linked to crystal ordering), the following transition in dominant slip system may happen:

<111> {112} → <111> {110} → <111> {112} → <100> {110}

The APB energy increases with temperature, which would explain why <100> type slip tend to be more frequently observed at higher temperatures [60] [69]. Of course, we have already discussed that more materials parameters affect the choice of slip system, but this simple idea, which considers only APB energy, supports well many experimental observations, including those presented in this section.

1.5 Bcc+B2 plasticity and design strategy

In dual-phase alloys, multiple material parameters influence interaction mechanisms between the phases, notably the lattice misfit and the precipitate size which can favour Orowan bowing, by-passing or precipitate cutting mechanism, but also the relative hardness of the matrix and the precipitates [70] [71]. In this section, we propose to focus on the importance of slip transfer, and the specific role of slip activity.

As we have seen, the topic of bcc and B2 slip activities is complex and not fully understood. It comes across that, at room temperature, bcc compounds usually slip on a variety of slip system including <111> {110}, {112}, {123}, with their relative contribution to the overall deformation still unclear and likely to vary depending on the metal. Meanwhile, B2 compounds usually show a limited variety of active slip systems, with possibly exclusively active <100>{110}, <111>{110} or <111>{112} slip systems. In the context of a dual phase bcc+B2 alloy, the B2 phase is therefore likely to be the limiting factor when it comes to the alloy slip activity, and risks participating in the embrittlement of the alloy.

In this section we will go through a few examples in literature exploring the question of slip transfer between phases. Examples on the bcc+B2 system are very rare, but we can also learn from other systems as the fundamental mechanical process may be similar.

1.5.1 Consequence of slip transfer

In the work of R. D. Jones et. al [29], the deformation behaviour of a fcc nickel-superalloy CMSX-4 (fcc matrix reinforced with Ni_3Al ordered fcc precipitates) is compared to a ferritic nickel bcc-superalloy (bcc matrix reinforced with $L2_1$ Ni_2AlTi precipitates). Using micro-compressions coupled with Digital Image Correlation (DIC), their work offers insights on the strain repartition within the microstructure of both alloys, which can be seen on Figure 13.

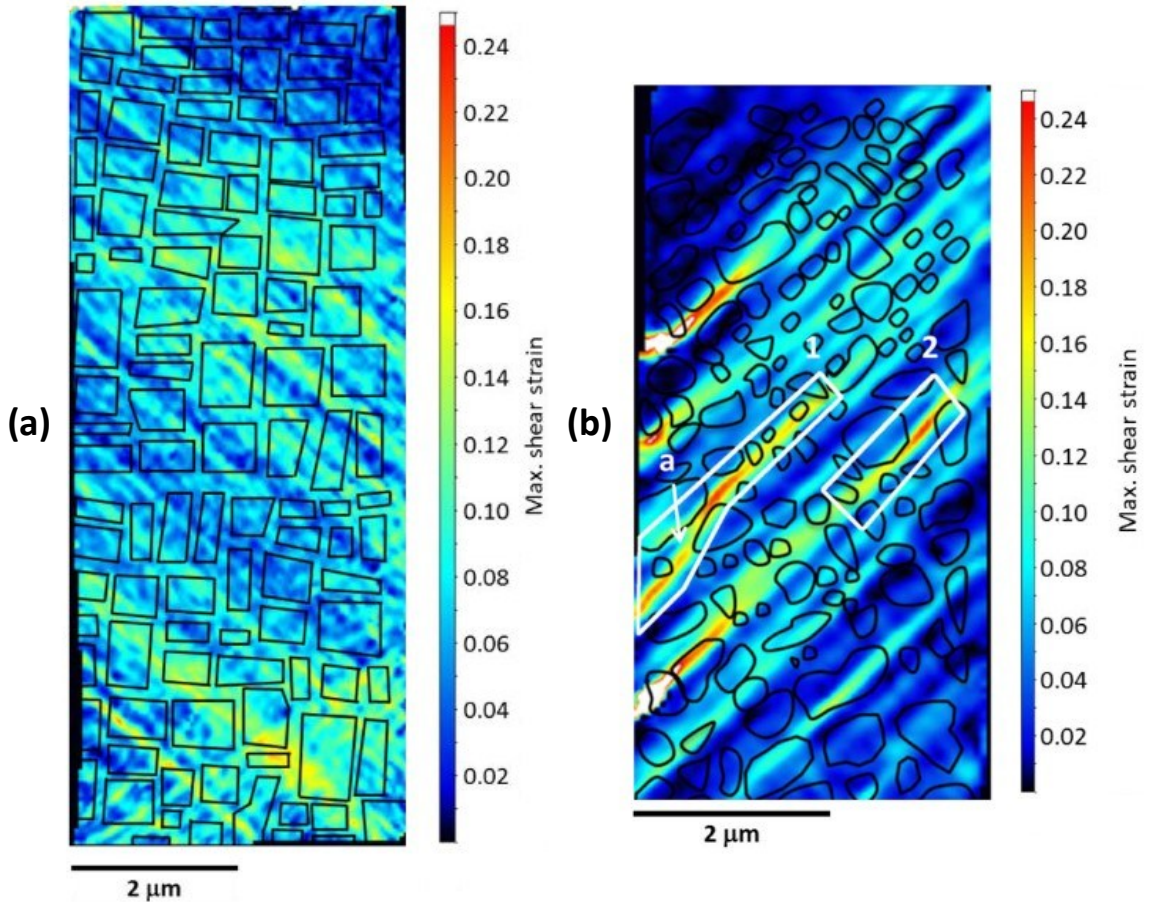


Figure 13: Adapted from [29], maximum shear strain mapping, deduced from digital image correlation (DIC), on compressed micropillars of (a) a fcc-superalloy CMSX-4, and (b) ferritic nickel bcc-superalloy Fe-Ni_2AlTi. The precipitates are outlined in black. On (b) the "a" arrow points at a bowing slip band, whilst the "1" and "2" arrows point at high local strains.

A key difference between the behaviour of the two alloys is that, in the bcc-superalloy (Figure 13 (b)), slip transfer is less frequent, with obvious bending of slip traces around the precipitates (arrow "a" on Figure 13). A consequence can be seen from the DIC determined shear strain map, as strain accumulates at the interface between the matrix and the precipitates, which is a likely explanation for the relatively higher brittleness of this alloy compared to the fcc alloy, as highly localised strain can favour crack nucleation. The strain distribution between the matrix and the precipitate was evaluated, revealing that the ratio between the average shear strain in the precipitates and in the matrix was of 1.02 in fcc-superalloy, and 0.9 in the bcc alloy (which can reach 0.8 locally, e.g. at arrows "1" and "2" on Figure 13). This is yet another demonstration of the lack of dislocation motion from the matrix to the precipitate, the strain concentrates in the matrix and tends to piles up at the interface with the precipitates. The absence of slip transfer in this bcc-superalloy was attributed to the 1.47-point higher lattice misfit than in the fcc-superalloy.

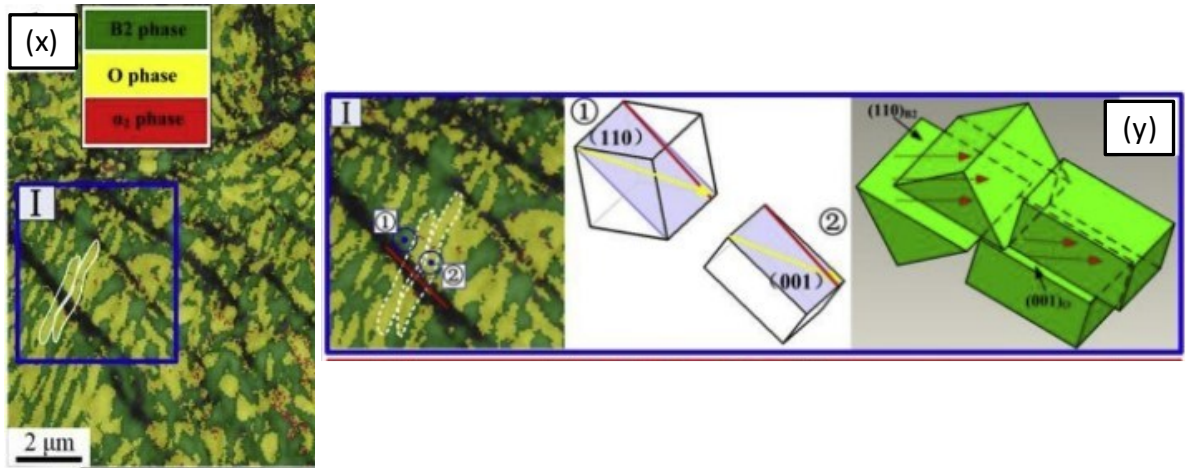
From this insightful work, we see that the presence or absence of slip transfer can have a dramatic impact on the deformation behaviour and strain localisation within a dual phase alloy.

1.5.2 Slip activity and slip transfer

The previous example from R. Jones et. al [29] shows what may happen if dislocations do not systematically cut through the intermetallic precipitates. One may then wonder what happens if the precipitates can get cut, but display a lower variety (or distinct) slip systems than the matrix. No such example on the bcc+B2 system was found in literature, but we can reason by analogy with other alloy systems, such as the γ/γ' & γ/α_2 microstructure of Ti-Al alloys [72], or the α/β situation which are more commonly studied [73] [74]. The α phase being hexagonal, very different slip systems than the bcc matrix may operate.

Let us take the example from the dual phase Ti_2AlNb alloy [66], where a B2 matrix thought to slip mainly on a mix of <111> {110} and {112} slip systems is reinforced with highly coherent O phase precipitates (a type of ordered α crystal structure), which are expected to slip on less numerous <110> {100} slip systems. The slip transfer mechanisms as a function of the incident slip system from the matrix was studied by the authors, and parts of their observations are represented on Figure 14. Note that twinning mechanisms also occurred and deformed the O precipitates under some geometrical constraints, but we will focus on the slip deformation mechanism.

(a) Slip transfer between B2 and O phase



(b) Slips blocked and bowing around the O phase

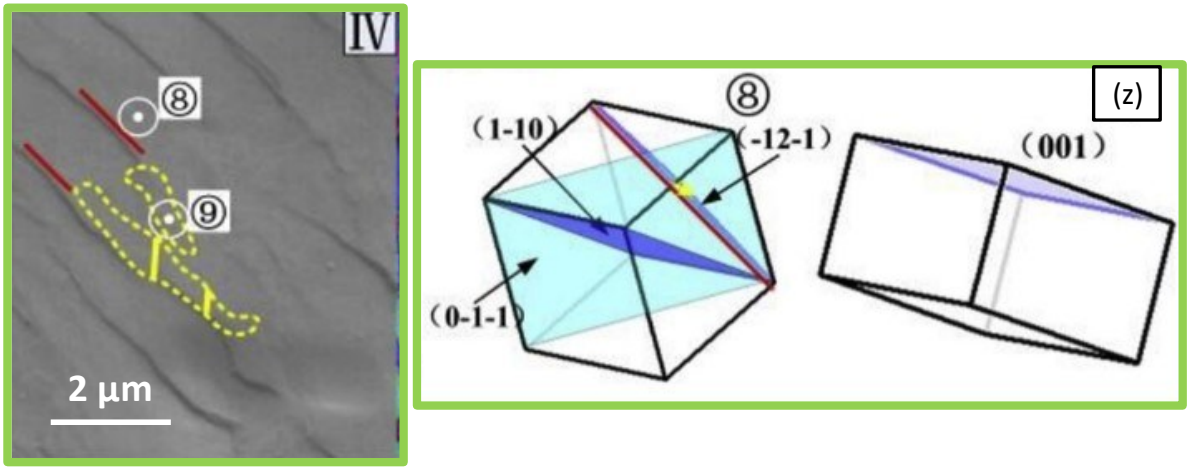


Figure 14: Adapted from [66], micromechanical interaction between B2 and O phase in Ti-22Al-25Nb at%. (a) slip transfer occurring, the colour code in (x) shows the phase distribution in the blue region "I". (b) Slip blocked by the O phase, or bending around the O phase. The crystal geometries of the B2 and O phases are represented accordingly with the numeration, and the O phase grains considered are outlined with white and yellow doted lines. Observed slip bands are represented with red lines.

It was concluded that the O phase blocks most incident slip, with 2 of the 24 active slip systems in the matrix able to transfer to the precipitates (12 slip systems can instead induce O phase twinning). As can be seen on Figure 14 (a), only a specific geometrical relationship between the slip systems allows for slip transfer, when both slip direction and slip plane are parallel. Slip traces of unfavourable geometries tend to bend around the precipitates, or are completely blocked by the precipitates (Figure 14 (b)), leading to the same kind of strain accumulation evoked in previous section §1.5. This example can be seen as a bit extreme, since the two-phase considered have very different geometries, and it seems that in this context only completely parallel slip systems in both phases my allow slip propagation.

We could also reason by analogy with the grain boundary interface to gain more insights on what may happen in a bcc+B2 alloy. When studying a grain boundary interface, where the

different grain orientations are likely to show misaligned operating slip systems (see next Figure 15), slip transmission is commonly observed, and the geometry of operating slip systems is thought to play an important role on this mechanism [75] [76]. A basic idea proposed in [75] and [76] is that the closer the incident and outgoing slip system are in orientations (both regarding slip direction and slip plane), the more likely slip transfer is.

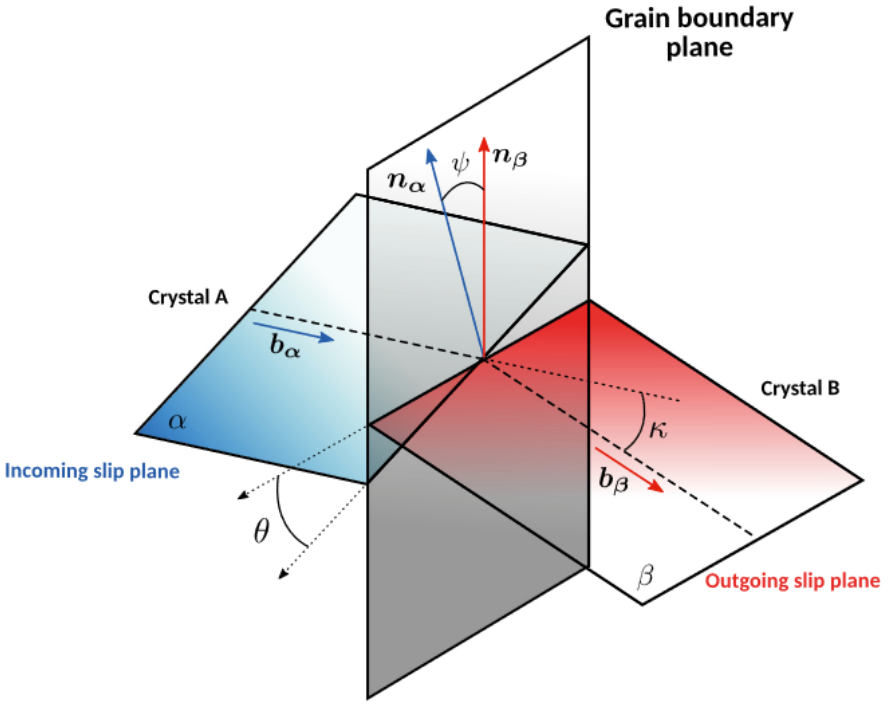


Figure 15: From [76], representation of the geometry of incoming and outgoing slip system at a grain boundary. "b_α" and "b_β" represents different burgers vector (slip direction), on distinct α and β slip planes. In their work, the angles θ, ψ and K are used as geometrical criteria to assess the likelihood of slip transfer at the grain boundary.

Therefore, if we conceptualize the bcc+B2 interface in a similar way to a grain boundary, we see that different active slip systems in the matrix or the precipitate will not necessarily block all slip propagation. For example, a <111> {123} slip from the bcc matrix could propagate to a <111> {112} slip in the B2 phase, as they can have very similar geometry, if for example cross-slip occurs. This kind of cross-slip commonly occurs in single phase bcc alloys, where cross-slip between {110}, {112} and {123} planes are frequently observed (see §1.3), a similar mechanism could therefore operate at the bcc/B2 interface. Meanwhile, a <111> {123} bcc slip will have difficulties transferring to a <100> {100} B2 slip system, which would involve a sharp change in both slip direction and slip plane. We see that different combinations of incoming/outgoing slip systems are susceptible to impact the likelihood of slip transfer at the bcc/B2 interface.

Taking all the previous discussion in consideration, we see that the slip activity in the B2 phase is likely to play an important role as to the slip transfer mechanism in a bcc+B2 alloy. Firstly, because it could completely block or force to bend incoming slip from the matrix, and secondly, because it could force incident slip to transfer on specific slip systems, restraining

the slip activity of the alloy. The B2 phase is likely to operate as a “dislocation filter”, allowing the propagation of some types of dislocation geometries, and blocking others.

1.5.3 bcc+B2 design strategy

Our objective is to ductilise bcc+B2 alloys at room temperature, whilst preserving their high temperature capabilities. As we have seen, some B2 slip activities can be very limited, and sometimes even favour <100> type slip which is distinct from the <111> type slip of the bcc matrix, offering limited options for slip transfer. A simple idea from there would be to target B2 room temperature slip activities involving the largest amount of active <111> type slip systems possible. We have seen examples of B2 compounds slipping mainly on <111> {112} or a mix of <111> {110} and {112}. These would be ideal as they display many common slip systems with the bcc matrix at room temperature, and may shift towards more restrained <100> type slip activities at higher temperatures (similarly to FeAl [68]), strengthening the alloy when ductility is less of an issue.

The implementation of such design strategy requires the slip activity to be characterised early in the alloy development process, so to build our alloys around this characteristic. This brings up the question of how to characterise efficiently slip activity in the very challenging system that is the bcc crystal lattice, which we will now discuss.

1.6 Characterising slip behaviour in bcc and B2

As discussed in the previous sections, the slip activity of bcc and B2 compounds can be controversial. The controversy comes in part from the techniques that are used to evaluate them, and the difficulties posed by the bcc lattice. In this section, we will go through the typical approaches used to characterise slip activity in materials, and how they apply to the context of bcc and B2 lattices. We will also discuss their limitations, and our proposition to fill the lack of quantitative data on bcc slip activity.

1.6.1 TEM

One of the most robust sources of data on slip activity has been from transmission electron microscopy (TEM) experiments that give direct insight into the dislocations and their geometry, including post-deformation dislocation characterisation [65] [53] and in-situ TEM deformation [77] [50] [78] [54]. On Figure 16 is an example from D. Caillard [50], showing the motion of a <111> dislocation moving on {123} planes at room temperature in tungsten, observed during in-situ tensile deformation of the sample.

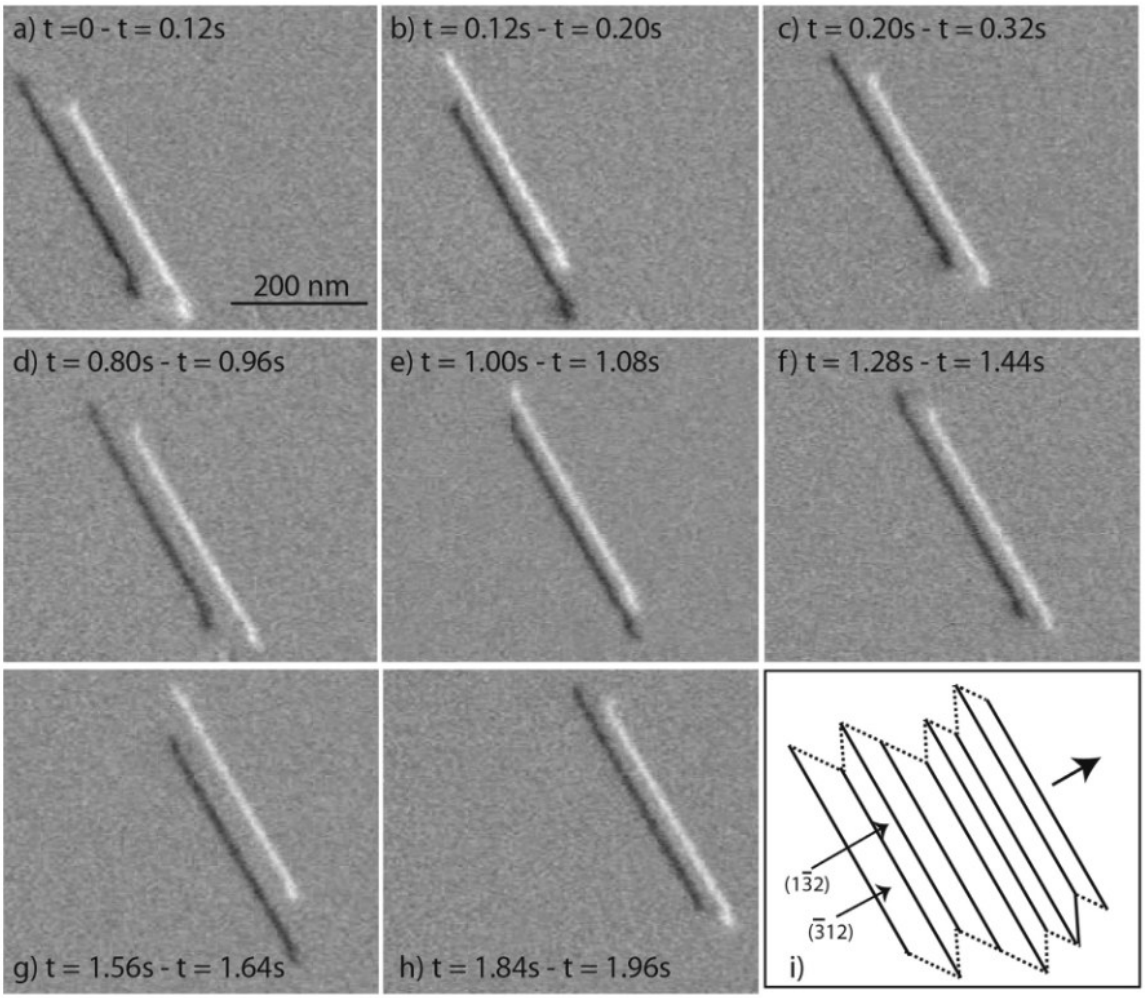


Figure 16: from [50], TEM observation of dislocation motion in Tungsten at room temperature during in situ tensile testing, all dislocation movements take place in less than a frame (<0.04)s and on {123} slip planes. The overall dislocation motion is represented on i). The straining axis is [110], the sample plane is (001), the burger's vector is ½ [111] and the diffraction vector is (100).

This experiment was particularly important during our survey of literature since it gives strong evidence to support the existence of {123} slip in bcc metals at room temperature, as a fundamental, elementary deformation path for dislocations. Such insights are fundamental to understand the micromechanics of metals. However, TEM experiments are complex, time-consuming and have limited statistics. They also require highly trained experimenters capable of performing dislocation analysis, and able to prepare and manipulate thin film samples. Also, for in-situ deformation, surface effects remain a question to extrapolate thin film slip behaviour to bulk sample slip behaviour. Finally, concerning post-deformation characterisation, unlike slip traces which are almost always observed on large samples, dislocations are not necessarily visible within the thin films extracted (dislocations annihilate at the surface to form the slip steps), or can in the contrary be very densely packed, which in both cases makes their observation and characterisation challenging.

1.6.2 Single crystal testing

Single crystal testing offers another informative source of data, including micro-compression [3] [45] [79] [80] [81] or micro-tensile tests [46] [82], where the 3D observation of slip usually helps identifying the active slip systems accurately. Beyond evaluating the critical resolved shear stress of the different slip systems, a particularly interesting data made from single crystal testing are the χ-ψ plots, of which multiple examples can be found in reviews [37] [38], and with reason since those are one of the main sources of "non-controversial" knowledge on the slip activity of bcc and B2 compounds. These consist of a series of uniaxial single crystal experiments (usually mm-scale), and compile on a single graphic the evolution between the angle on which slip occurs relative to the crystal orientation and the stress direction. Figure 17 shows examples of such plots, with the χ-ψ plots of B2 CuZn and B2 Cu(Ni)-Zn [61] stressed in compression, and bcc Fe [38] stressed in tension and compression, all at room temperature.

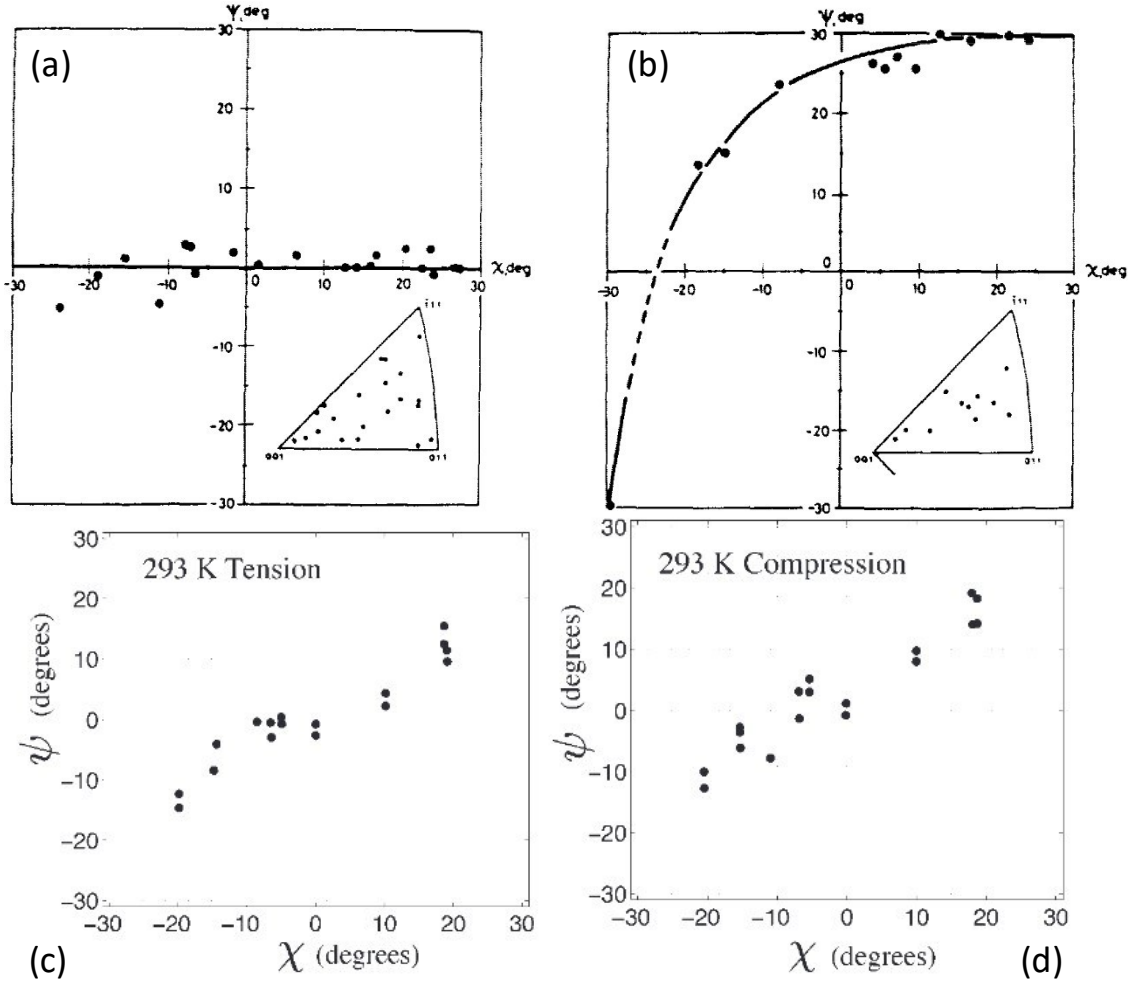


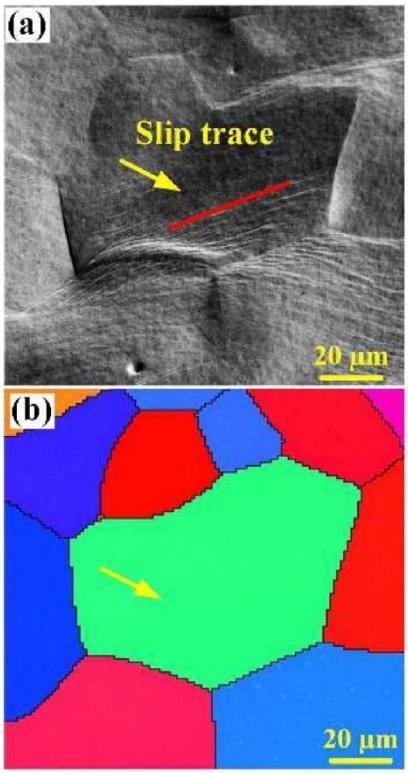
Figure 17: χ-ψ plots built from series of single crystal (mm-scale) deformed during uniaxial experiments. (a) and (b) from [61] show respectively the slip behaviour of <111>{110} slipping B2 CuZn and <111>{112} slipping Cu-14Ni-Zn (at.%), deformed in compression. (c) and (d) Show the slip activity of Fe-3Si (at%) single crystals, deformed respectively in tension and compression. The latter gives indication of slip on the MRSSP, whilst the former shows a slightly higher tendency for {110} slip.

The χ-ψ plots allow to easily identify tensile compression asymmetries in bcc, and provide strong evidence to identify some bcc and B2 materials bulk slip behaviour. On these graphics, χ represents the orientation difference between the MRSSP in the [111] zone axis, as given by the uniaxial stress component, and the normal of the $(\bar{1}01)$ plane of the crystal (χ is therefore crystal orientation dependant). ψ represents the angular difference between the experimentally measured slip plane, determined via slip trace analysis, and the $(\bar{1}01)$ reference plane. Consequently, if a χ versus ψ curve is horizontal at ψ = 0° (e.g. Figure 17 (a)), it means all slip were observed parallel to the $(\bar{1}01)$ plane, and therefore the sample likely slips exclusively on {110} planes. Meanwhile, ψ = 30° corresponds to the orientation of the $(\bar{2}11)$ plane, therefore a horizontal curve at this ψ (e.g. Figure 17 (b)) informs of slip exclusively on {112} planes. Finally, a curve where χ = ψ (e.g. Figure 17 (d)) is evidence of slip on the MRSSP (see discussion about non-crystallographic slip in §1.3.3). Tensile compression asymmetries are easily spotted by comparing Figure 17 (c) and (d), through the differences between the curves obtained from bcc Fe in tension or in compression. Also, we see in Figure 17 (b) that the slip activity of B2 Cu-(17)Ni-Zn (at.%) reacts very differently whether the $(\bar{2}11)$ plane is stressed in the twinning (χ > 0° in compression) or anti-twinning direction (χ < 0° in compression), which is characteristic of the asymmetry of slip on {112} planes.

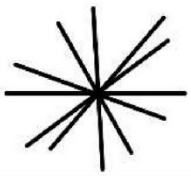
These conclusions are drawn from significantly larger statistics than typical TEM observations, and from larger samples. They are therefore likely to be more representative of the materials bulk deformation behaviours. However, the characterisation of intermediate sample responses, e.g. a mix of {110} and {112} slip, is difficult using this approach, and little insight is given as to the nature of slip on the MRSSP. They also require the preparation of large amounts of samples, and their deformation in consistent manners which can be both challenging and time consuming.

1.6.3 Slip trace analysis in bcc and B2

Conventional techniques used to characterise slip activities are challenging in bcc and B2 systems due to wavy slip and other anomalous behaviours described in §1.3, and their results are often difficult to extrapolate due to their limited statistics. When studying slip at a larger scale on polycrystalline samples, in an attempt to increase these statistics, the ambiguity in slip system identification becomes even more of a problem since we no longer have access to a "3D" information on the slip systems, and rely instead on the surface level observation of slip traces [44] [83] [84]. The following Figure 18 from [44] illustrates very well this approach, and its challenges in bcc.

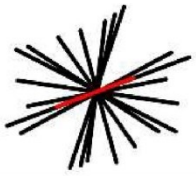


(c)



	Slip system	Schmid factor
1	(101)[-1-11]	0.2476
	(101)[-111]	0.3376
2	(10-1)[1-11]	0.2734
	(10-1)[111]	0.3118
3	(011)[-1-11]	0.1929
	(011)[1-11]	0.4991
4	(0-11)[-111]	0.2187
	(0-11)[111]	0.4733
5	(1-10)[-1-11]	0.0547
	(1-10)[111]	0.1615
6	(110)[1-11]	0.2257
	(110)[-111]	0.1189

(d)



	Slip system	Schmid factor
7	(2-11)[11-1]	0.1746
8	(-121)[11-1]	0.0798
9	(112)[11-1]	0.2543
10	(21-1)[1-11]	0.0276
11	(121)[1-11]	0.4185
12	**(-112)[1-11]**	**0.4460**
13	(12-1)[1-1-1]	0.0576
14	(1-12)[1-1-1]	0.3212
15	(211)[1-1-1]	0.1933
16	(2-1-1)[111]	0.0868
17	(1-21)[111]	0.3665
18	(11-2)[111]	0.4533

Figure 18: From [44], slip trace analysis methodology on polycrystalline tantalum deformed in tension at room temperature. (a) shows the slip trace analysed, (b) the local EBSD determined crystal orientation, (c) and (d) the calculated theoretical slip trace orientations for plane types {110} and {112} respectively. The Schmid factors from the table were used to determine the most likely slip system, i.e. "12". Note that the 24 {123} bcc slip systems were ignored during this analysis.

Indeed, as illustrated on Figure 18 (c) and (d), and on the following Figure 19, the distinct bcc slip plane types slip traces can have very similar geometry, especially {112} and {123} slip, making their unambiguous distinction particularly challenging when looking only at slip traces. Such analysis also gives little information on the active slip direction, which is of particular interest for B2 compounds. As illustrated on Figure 18, in the context of a uniaxial slip trace analysis experiments the ambiguity in slip plane identification can be partially lifted using the added information from the Schmid factor of the competing slip systems [44] [84] [85] [82], which comes with a risk as discussed in §1.3.2. When applied to bcc, large scale slip trace analysis approaches usually consist in combining additional techniques to the slip trace analysis, including AFM, DIC, ECCI or TEM to further identify the operating slip systems, in particular the slip direction [82] [84] [85] [86] [87] [88] [89]. These, however, add extra layers of complexity to the experimental procedure which may not be accessible to most researchers, especially since most of these combinatorial approaches are still in early-stage development.

1.6.4 Indentation-based slip trace analysis

The previously discussed techniques for dislocation/slip investigations of TEM, micromechanical testing, on single or polycrystal samples, although popular, have practical challenges. TEM and FIB sample preparation, single crystal fabrication, as well as performing

repeat uniaxial experiments are challenging, time intensive procedures that require skilled experimenters and expensive equipment. Meanwhile, the case of large-scale polycrystal investigations is complicated by the ambiguity in bcc slip plane identification, requiring the use of additional and often complex techniques. An alternative to these could be indentation-based slip trace analysis [90] [91] [92], which requires only a microhardness testing machine (or a nano-indenter) and a SEM equipped with an Electron Backscatter Diffraction (EBSD) detector to acquire a low resolution EBSD scan. This is particularly important in the field of novel alloy development, where there is a need for rapid property assessment. The Figure 19 describes the technique, as applied to a bcc or B2 sample.

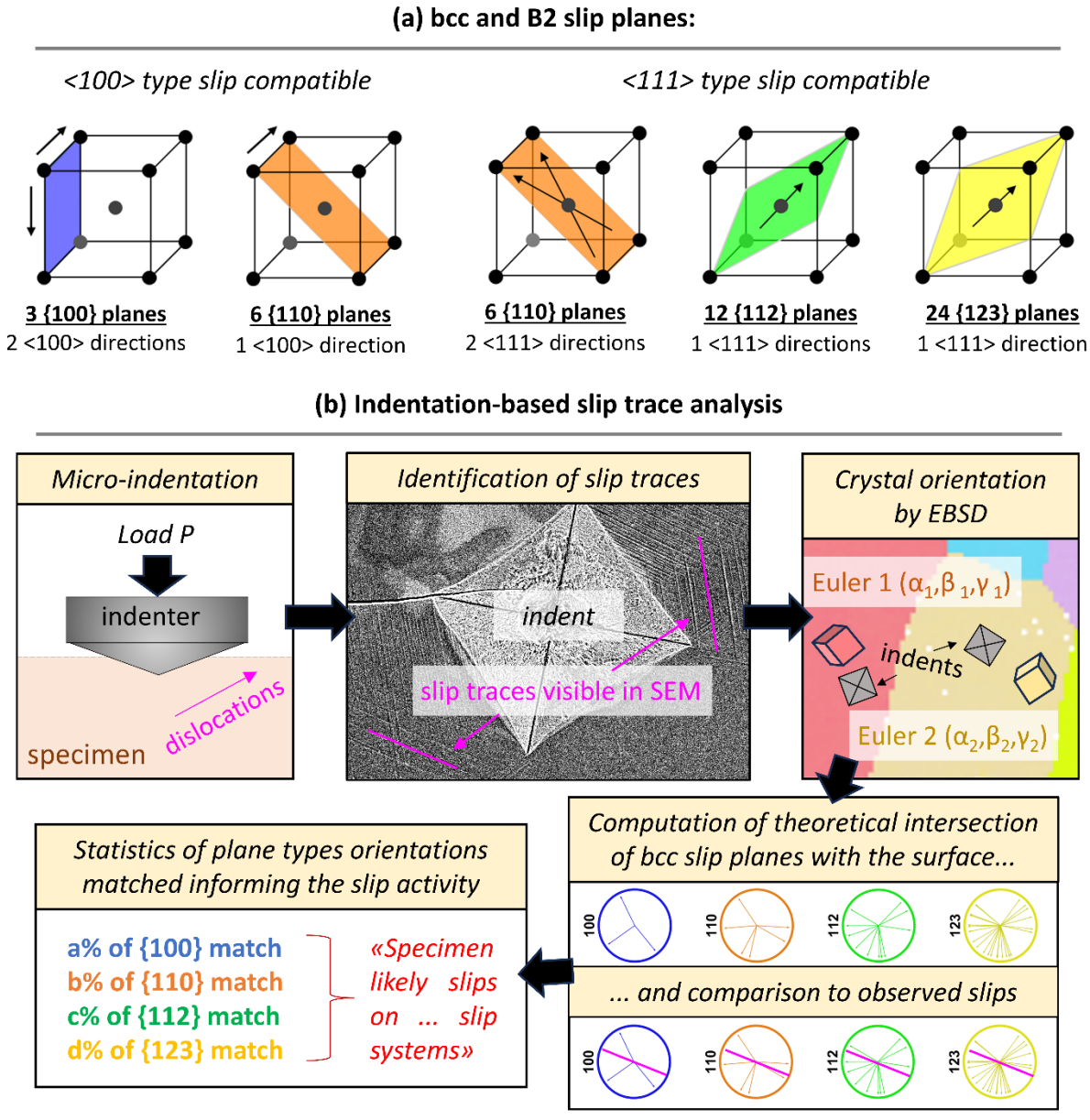


Figure 19: Overview of the indentation-based slip trace analysis methodology, applied to the context of a bcc or B2 sample. (a) bcc/B2 slip plane types geometries and corresponding slip systems compatible with <100> or <111> active slip directions. (b) Summary of the slip trace analysis process.

In this technique, a hardness (Vickers in Figure 19, but can be spherical) indent is performed on a polished and flat sample. The deformation generates dislocations in the material, and as the indenter pushes deeper in the material, these dislocations propagate to the surface following the active slip planes of the crystal, which is crystallography, bonding, and geometry dependant. This leaves slip traces at the surface of the sample near the indent, which can readily be observed using optical or electron microscopy. These slip traces can be visually identified, and their orientations compared to theoretical orientations for each possible material slip plane. These are calculated based on the local crystal orientation, determined via electron backscatter diffraction (EBSD), by finding the intersection of each slip plane with the surface for the specified crystal geometry. By identifying which theoretical orientations are close to the observed slip trace orientation (within a chosen angular range), we can deduce for each slip trace which slip planes are likely to have been activated. Repeating the indentations and quantifying the matched slip plane orientations across multiple indents, grains, and slip traces, gives us an indication of the preferred slip plane types of the sample, from which an attempt to deduce the slip activity of the samples can be made.

Examples of indentation-based slip trace analysis, as presented here in its most simplistic form, are uncommon in literature, especially in bcc. Indeed, performing indentation-based slip trace analysis has limitations, as the stress state is more complex than in uniaxial testing [88] [93], making correlation between slip trace orientation and Schmid factor difficult. As a result, when testing bcc, most slip plane observations made using this approach are ambiguous, giving limited information on the material, especially on the slip direction. There is to our knowledge no example in literature of a slip activity characterisation on bcc or B2 compounds which have been assessed exclusively from indentation-based slip trace analysis.

1.7 Summary

Building from this review of literature, we observe that much still needs to be understood about bcc and B2 micromechanical deformation behaviour, and that the few reliable techniques used to characterise them are usually highly complex, requiring expensive equipment, experienced users, and often lack in statistics. In the context of early-stage development of bcc+B2 compounds, the amount of potential candidate systems that need to be tested is very large, and there is a need to perform such micromechanical assessments as efficiently as possible.

The objective of this work is to develop a new methodology for rapid slip activity assessment during alloy development, using easily accessible equipment. This will be achieved by combining indentation-based slip trace analysis with an automated slip trace identification algorithm, which gives access to larger, more reliable statistics than manual approaches, and with greatly reduced experimentation time compared to alternative techniques. Specifically, we set a goal to apply this new methodology to bcc and B2 to support the early-stage bcc+B2 ‘bcc-superalloy’ development, to characterise B2 slip behaviour (e.g. <001> vs ½<111>), and identify whether this can help promote room temperature ductility within dual phase alloys.

The technique will first be presented in Chapter 3, demonstrated to work on fcc Ni, and used to clearly differentiate <111>{112} and/or {123} type slip activity from predominant {110} slip

activity in several bcc and B2 compounds. Then, in Chapter 4, the technique will be used on a diffusion gradient in the B2 FeAl-NiAl system, informing on the evolution of slip activity, and notably the change in active slip direction as a function of composition. Finally, in Chapter 5, an in-depth analysis of the statistics obtained via this approach will be performed, exploring the possibility of inferring “exact” bulk bcc/B2 sample slip activity from indentation-based slip trace analysis.

2 Methodology

This methodology section will outline the main practical steps to perform automated indentation-based slip trace analysis, as presented and used throughout this thesis, using the presently developed code 'Rapid Analysis of Slip Traces (RAST)' in the context of bulk samples, or across compositionally graded samples. The main sources of biases in the slip activity statistics measured are also discussed, which can affect in particular the advanced statistical analysis presented in Chapter 5.

This methodology Chapter was written to concentrate information spread out across the following chapters of work, focussing on the practical aspects of the technique. It has some overlap with the methodology sections focussed to the topics of Chapters 3 to 5 that give further detail and justifications as well as outline how the approach was developed, notably through experimental empirical observations described across these chapters that fed back into the overall RAST methodology.

2.1 Sample preparation

Two types of samples were prepared throughout this thesis, bulk (usually single phase) samples §2.1.1, and compositionally graded samples §2.1.2. Most samples were prepared via arc melting of commercially pure elements, followed by a heat treatment under protective argon atmosphere at a temperature stabilising the phase of interest. Here we outline the sample preparation that is required to allow slip trace analysis using our methodology, as well as how to prepare a compositionally graded sample. A summary of the specific materials produced and studied in this thesis is given §2.1.3.

2.1.1 Bulk samples

The slip trace analysis technique applied here relies on the Scanning Electron Microscopy (SEM) imaging of slip traces, combined with Electron Backscattered Detector (EBSD) imaging on deformed grains. Therefore, the samples analysed must be flat and polished before indentation to allow EBSD analysis, which should also be sufficient to allow slip trace imaging. In this thesis, the typical sample preparation follows these steps: grinding of the samples on sandpaper, from 400 grit size to 4000, followed by polishing with a 50 nm colloidal silica solution on a neoprene cloth for a duration of 1 hour. Note that most samples analysed in the thesis were hard and brittle which facilitates these polishing steps, but some ductile samples surface (e.g. fcc Nickel) can get scratched or etched if too much pressure is applied during grinding or too long of a polishing is performed. The sample size can be as small as a few mm square (depending on indentation load), although note that it is important to have access to a variety of grain orientations to increase the slip trace statistics.

2.1.2 Diffusion gradient

In Chapter 4 an analysis of a diffusion gradient between NiAl and FeAl gave access to a continuous composition range between Fe-35Al and Ni-40Al (at.%). To make such diffusion gradient, one should first prepare each end-member composition and heat-treat them independently to homogenise them in the phase region of interest. Each endmember should

then be cut, giving access to a flat surface, and ground from 400 to 2400 sandpaper grit size. Leaving some surface roughness can be useful to help favour contact between the samples during the diffusion heat-treatment. Also, the samples should be thoroughly cleaned so to avoid the presence of any contamination along the diffusion contact surface.

The ground surfaces should then be put in contact for the duration of the diffusion heat treatment. To do that, one can simply wrap both samples in molybdenum foil and tighten the samples in contact using e.g. a tungsten wire. In Chapter 4, a specially designed molybdenum capsule was used, and the samples were cut with precise dimensions using EDM to fit in the capsule. Then they were maintained in contact in this capsule by a screw which applied a pressure on the samples.

The diffusion heat treatment duration will vary depending on the temperature and the elements diffusing. The larger the diffusion zone, the more accurate the measurement of slip activity as a function of composition will be. In Chapter 4, a 100h diffusion heat-treatment was performed at 1000°C to maintain a stable B2 phase across the composition range, under protective argon atmosphere, which lead to ≈1mm scale diffusion region between the two endmembers compositions.

After diffusion heat treatment, the sample should be cut along the diffusion direction, and the sample grinding and polishing steps should be performed in a similar way to bulk samples (§2.1.1) to allow slip trace analysis.

2.1.3 Summary of samples studied in this thesis

Various metals and intermetallics samples were analysed throughout this thesis, Table 2 summarises corresponding targeted compositions, measured compositions using Scanning Electron Microscopy Energy Dispersive X-ray spectrometry (SEM/EDX), and heat treatments. The bcc Fe sample (polycrystalline ferritic steel) was analysed as received (the actual composition is given by the manufacturer). All samples were water quenched at the end of their respective heat treatments, to the exception of the fcc Nickel sample which was air cooled. The main crystal structure phase is also indicated, as well as miscellaneous phases when present (identified via SEM, EDX and/or EBSD analysis). Two B2 TiFe samples were prepared, one was analysed in Chapter 3 (S1) and the second in Chapter 5 (S2). The B2 crystal structures of TiFe (S1), Ti_2AlMo and Ti_2AlNb, were confirmed by Synchrotron XRD analysis (see Chapter 3), the other samples crystal structures are expected following their respective heat treatments (EBSD analysis can confirm whether the phase is fcc or bcc, but cannot distinguish bcc from B2). More details on each sample preparation/characterisation are given in their respective chapters.

Table 2: Summary table of the samples. Uncertainties associated to measured compositions in Chapter 3 are given by the Aztec EDX software, whilst Chapter 4-5's are deduced from three separate EDX area scans performed on the samples.

Sample	Target composition (%)	Measured composition (%)	Heat treatment	Phase	Other phases	Chapter
B2 TiFe (S1)	51 Ti 49 Fe	51.6±0.2 Ti 48.4±0.2 Fe	24H/1000°C	B2	- unknown Ti rich - hydrides	3
B2 Ti_2AlMo	50 Ti 25 Al 25 Mo	52.0±0.2 Ti 24.2±0.1 Al 23.7±0.1 Mo	100H/1200°C	B2	- unknown Ti rich	3
B2 Ti_2AlNb	50 Ti 25 Al 25 Nb	51.4±0.2 Ti 22.8±0.1 Al 25.7±0.1 Nb	100H/1200°C	B2	-	3
bcc Fe	≈100 Fe	≤0.28 C ≤0.045 P ≤0.043 S ≤0.35 Mn	-	bcc	-	3
fcc Ni	100 Ni	-	2H/700°C	fcc	-	3
B2 FeAl	60 Fe 40 Al	≈65 Fe ≈35 Al	24H/1200°C	B2	-	4
B2 NiAl	60 Ni 40 Al	≈60 Ni ≈40 Al	24H/1200°C	B2	-	4
B2 FeAl-NiAl (gradient)	-	-	100H/1000°C	B2	-	4
B2 Fe-15Ni-Al	45 Fe 15 Ni 40 Al	46.7±0.2 Fe 15.1±0.1 Ni 38.1±0.2 Al	24H/1000°C	B2	-	4
B2 Fe-17Ni-Al	43 Fe 17 Ni 40 Al	39.7±0.1 Fe 17.1±0.1 Ni 43.1±0.2 Al	24H/1000°C	B2	-	4
B2 TiFe (S2)	51 Ti 49 Fe	50.9±0.1 Ti 49.1±0.1 Fe	100H/1000°C	B2	- unknown Ti rich - hydrides	5

2.2 Indentation slip traces

Two types of slip trace analysis approaches were performed in this work, (1) on the outside of large indents (Chapter 3 and 4), or (2) on the inside wall of smaller indents (Chapter 4). Here we outline the main considerations and sources of bias in the slip statistics that can come with such indentations.

2.2.1 Analysis outside indents

In our work, Vickers microhardness indentation was used to deform the grains and generate slip traces. Note that nano-indentation and spherical indenter tips can also successfully generate slip traces visible with SEM imaging.

The impact of indentation load on the measured slip activity was not thoroughly investigated in our work, but quick assessments did not suggest any significant differences between the pattern of slip traces generated using larger or smaller loads. Therefore, the indentation load can be changed to adjust the size of indents relative to the grain size with likely only minor impacts on the measured slip activity. In this thesis, a ≈0.5 kg load was systematically used when analysing slip traces outside indents.

The technique can be used on any grain size sample, however, the analysis of multiple grains is required to reliably increase the statistics and minimize grain orientation related biases (see §2.7). This can be achieved either by performing several indents targeting different grains, or using larger loads to deform multiple grains simultaneously.

When using Vickers or Berkovich indenter tips, and indentation sizes larger than the grains, experimenters should lookout for possible biases, e.g. if grains imaged are systematically deformed at the corner of the indents, or parallel to their sides, as the differences in stress states around these indent shapes may favour the activation of different slip systems. To minimise these sorts of bias, rotating the indenter (or sample) between indentations will help randomise the stress condition in the grains analysed, gradually eliminating this bias as the amount of grains tested increases. Another way to avoid this bias would be to use spherical indenters as the stress state around the indent should be closer to isotropic. Finally, one could reduce such bias by using a combination of indentation loads and grain sizes so that the diameter of the latter is at least two or three times larger than the indents formed, so to see the "complete" slip trace pattern generated by the indentation. This, however, can make the experimental work longer as it requires one indentation per grain tested (and can be challenging for small grain size samples).

If performing multiple indents in the same grain, rotating a Vickers indent was found to only marginally affect the visible slip trace patterns. Hence, repeatedly indenting the same grain orientation is not an efficient way of increasing the slip trace statistics. It may, however, reduce the Vickers indenter shape stress state related bias, as different slip systems can have different contrast depending on the indent orientation relative to the grain (and therefore end up more or less represented in this grain's statistics).

2.2.2 Analysis inside indents

There are two main reasons why one may want to analyse slip traces inside indents rather than outside. Firstly, because some samples hardness (especially intermetallics) can be so high that no slip traces are visible via SEM imaging outside larger indents (which is a problem we encountered when analysing the B2 Ti_2AlFe compositions of high hardness presented in Chapter 7). In the context of a high hardness sample, slip traces were found to be more reliably visible on the inside of small indents. Secondly, it increases the resolution in composition of the slip activity measured on a compositionally graded sample, as the locally imaged slip traces can be more reliably correlated to the local material deformation (the slip traces are formed in the material in direct contact with the indenter tip, and likely travel through less material than if outside larger indents).

For the analysis inside indents, small indentation loads ≈0.02 kg should be used, as those typically highlight deformation inside the indents, especially when the samples are very hard. Small loads also help keeping the whole inside indent area in focus during SEM imaging, as the depth of the indentation is smaller.

Due to the more localised stress state, rotating the sample between small load Vickers/Berkovich indentations can help increase the variety of slip systems activated, even when indenting the same grain. It also changes the perceived orientation of the slip traces from a top view SEM imaging perspective, due to the inside slope of the indents. This will affect what theoretical slip plane orientations are found closely oriented with the observed slip traces, and therefore can give additional information on the possibly active slip systems.

2.3 Imaging of slip traces

After generating the slip traces via indentation, there is a need to image the slip traces. Scanning Electron Microscopy (SEM) was used in our work, alternatively one could use e.g. Atomic Force Microscopy (AFM) or optical microscopy. A wide range of SEM imaging conditions can be used to image slip traces for analysis using the developed code, one should target the greatest possible slip trace contrast, which may vary depending on the sample's hardness, microstructure, and slip activity. Secondary Electron (SE) and Backscattered Electron (BSE) imaging modes can be used to image the slip traces. The most important parameter to highlight slip trace contrast was found to be the use of a low acceleration voltage (typically 2 – 5 kV in this thesis) combined with a small working distance (WD ≈5 mm). Large pile-up slip traces (e.g if using large indentation loads on low hardness materials) can be imaged successfully using basic 20kV, 10mm WD SE imaging. All SEM images should be made using integration mode and small dwell times (e.g. 10 integers for 1µs dwell time), to avoid distorting of the pictures due to sample charging, and to cancel out part of the SEM imaging scan noise, which helps the automated line detection algorithm.

To detect the slip traces, the automated slip trace analysis code will analyse the pictures as ≈100*100px square segments at a time. We recommend using a combination of picture resolution and magnification so that on a given network of parallel slip traces, adjacent ≈100*100px square segments all contain a portion of a slip trace from this network (ideally one to two slip trace per segment). The magnification and resolution combination is not a "hard constraint" for the code, and various combinations allowed for suitable slip trace detection during our experiments. Also, these values should vary depending on the sample hardness and indentation loads (a higher sample hardness will lead to smaller indents, finer slip trace spacing, and therefore may need higher magnification and/or picture resolution).

2.3.1 Analysis outside indents

Typically, in our work, using an image resolution of 3072x2188px, ≈ x2000 magnification was used when imaging the entire slip trace pattern outside ≈0.5 kg indents on B2 intermetallics (one picture = whole area surrounding the indent, including the indent). If the grain size is smaller than the indents, one picture with higher magnification was made in each grain showing visible slip traces.

2.3.2 Analysis inside indents

When analysing slip traces inside small indents, imaging can be more challenging as the smaller slip steps require higher resolution imaging. In our work, using a TF Apreo 2S HiVac SEM, this imaging was usually made using BSE imaging, an acceleration voltage of 2kV, a working distance of 3.9 mm, and a small current of 25 pA, based on the instrumentalist's guide lines for high-resolution imaging. Using an image resolution of 3072x2188px, ≈ x20,000 magnification was typically used, focussing on the inside area of the indent (one image per indent).

2.4 EBSD analysis

Electron Backscatter Diffraction (EBSD) is performed on the samples to determine the crystal orientations of previously indented grains. The slip trace analysis requires an average grain orientation for each picture analysed. The EBSD mapping can be performed relatively coarsely, e.g. one could aim for >30 data points per grain analysed to avoid introducing un-necessary inaccuracy in this measurement. In our work, higher resolution EBSD mappings did not measure any major grain rotation/deformation around the indents (although note that higher sample ductility can be more prone to these kinds of deformation).

The inside part of the indents can sometime be indexed during EBSD mapping, it is important to exclude these areas from the grain reconstructions as they usually show very different crystal orientation when indexed due to the inclination of the sample surface inside the indents (and therefore could affect the average measurement of corresponding grains).

EBSD should be performed in the same microscope as the SEM imaging of the slip traces (EBSD at 70° tilt, SEM imaging at 0° tilt). If transferring samples between microscopes to perform one or the other, one should make sure that the orientation of the EBSD map matches the orientation in which the SEM pictures were taken, or keep track of this difference as accurately as possible (the code has a parameter to adjust the orientation of the pictures relative to the crystal orientations given). Note that small errors in sample tilt and small rotations between SEM imaging and EBSD mapping will increase the experimental error in slip trace orientations measured (and therefore may require the use a larger identification range IR, see §2.5.1.2).

2.5 RAST Code analysis and parameters

The code for Rapid Analysis of Slip Traces, named "RAST", was developed and applied to various bcc, B2 and fcc samples throughout this project to evaluate their slip behaviour. The development of the code architecture and functions is presented in Chapter 3 (§3.3), which we summarise here in the form of a practical user guide. This code is designed to automatically detect slip traces from pictures in a wide range of slip trace visibility contexts, and perform slip trace analysis based on local EBSD determined crystal orientations.

The RAST code provides a MATLAB based user interface to load images, mask unwanted features, and input crystal orientations from EBSD for the imaged grains. It then automatically segments each picture into ≈100×100px squares (detailed in §2.5.1.1), detects lines in each segment using a combination of contrast adjustment, edge detection, and Hough transform

functions, and scores each line based on a comparison of its orientation with those of lines in surrounding segments. Finally, each detected line is compared to code calculated theoretical slip plane orientations (based on the user entered crystal orientation) to identify matching plane types (detailed in §2.5.1.2). High-scoring lines, which likely align with slip traces, are selected for statistical analysis based on an experimenter-defined score threshold (ST, detailed in §2.5.1.3), the code also outputs figures for each analysed picture showing which lines are included in the statistics for various values of ST.

Note that RAST can be applied to mechanical testing techniques other than indentation, e.g. tensile tests. It performs best if imaged slip traces form networks of parallel slip traces, and local crystal orientations are approximatively constant within the imaged grain areas. Also, it can be adapted to crystal structures other than the bcc and fcc samples analysed in this thesis.

Masking unwanted features:

A part of the code offers the possibility to mask features on entered pictures, experimenters should manually mask areas that do not correspond to the grain orientation associated with the picture (e.g. other grains), or large linear features, e.g. scratches networks or large phases. When analysing slip traces outside large indents, the indents themselves should be masked as the high contrast of their edges can be considered by the code as "being slip traces". This typically does not happen when focussing the analysis on the inside of small indents, and both the inside and outside areas imaged can be included in the analysis without leading to errors in line detection.

Several analysis parameters dictate the slip trace analysis outcome, which must be selected by the user. We will now outline what motivates the choice of these parameter based on the current code design (on submission of the thesis). These choices are also discussed along the results of Chapter 3 and 4, and partly instructed by the analysis of fcc Nickel where the simple slip activity (4 possible {111} planes) gives reliable insights on the code parameters influence.

2.5.1 Main parameters

Three main parameters control the outcome of the analysis, which should be adapted depending on various experimental constraints. These include: the segmentation size (N), the identification range (IR), and the score threshold (ST). All these parameters are also described in Chapter 3 (§3.3). Here we outline the main motivations for the choice of these values, which should be picked in the order presented.

2.5.1.1 Segmentation size - N

The RAST code analyses the pictures as a matrix of small square segments of N*N px, N being defined as the segmentation size. Lines are detected by a Hough transform based algorithm in each of these segments. The size of the segments will impact the statistics in different ways.

The choice of segmentation size should be first and foremost motivated by the size and spacing of slip traces in the image slip trace networks relative to the picture resolution. Typically, having one to two parallel slip traces from the same network contained within two adjacent segments allows for good slip trace detection (it is better to have more slip traces in

adjacent segments than none). The value N should therefore be adapted depending on the picture resolution as well as the size of the features studied in the pictures.

Experimenters should avoid using N≤90px as smaller segmentation sizes can introduce large inaccuracies (which increase dramatically as N diminishes) in the slip trace orientation detection, due to the discontinuous nature of pixel segments. Consequently, the larger the segmentation size, the more accurate the slip trace orientation detection will be. This improvement in accuracy was found to be small for segmentation sizes between 100px to 140px, therefore there is no real benefits in going beyond these values for this purpose. If a low picture resolution forces the use of small segmentation sizes (N<90px), the added line orientation detection inaccuracy should be taken in consideration when choosing the identification range (IR, see §2.5.1.2).

Another motivation for the choice of N is that having more segments per picture can perform better when analysing wavy and/or curved slip traces, often present in bcc. Also, the segments are an essential part of the scoring procedure, and large amounts of segments per picture help strengthening its capabilities at differentiating lines detected along slip traces from lines detected on miscellaneous features.

In our work, on 3072x2188px resolution pictures, N=100px was used to analyse slip traces outside indents for all samples, giving satisfactory slip trace detection despite the variety in picture magnification and slip trace visibility. In Chapter 4 for the analysis of the diffusion gradient, an averaged analysis output from three analyses with N=100, 120 and 140px was used to reduce the bias of this choice on the outcome of the analysis, as the waviness of slip traces was found to evolve throughout the sample.

2.5.1.2 Identification range - IR

The identification range IR determines the maximum angular difference between a code detected line orientation in a segment and a theoretical slip trace orientation to consider the latter as “matching” the former. The value IR should be picked so to account for all experimental variabilities that can affect the detected slip trace orientation relative to its “real” theoretical orientation, which is calculated based on the EBSD determined local average crystal orientation by finding the intersection between the slip plane and the sample surface assumed perfectly flat. Here is a non-exhaustive list of experimental variabilities that risk affecting a detected slip trace orientation relative to its corresponding theoretically calculated one, and that should be considered when picking the value IR:

- EBSD crystal orientation measurement inaccuracies, typically considered to introduce ≈2° of error.
- Hough transform line orientation detection inaccuracies, which depend notably on the size of the segments (N).
- Un-evenness of the sample surface.
- Local crystal deformations due to indentation.
- Waviness of slip, which is a source of controversy in bcc.

- Errors in sample tilt and/or orientation between SEM imaging and EBSD mapping
- SEM Picture distortions due to sample charging
- For the analysis inside indent, the inclination of the surface indented which affects the top view orientation of the slip traces

One should seek to use the smallest IR possible whilst guaranteeing that most lines detected along slip traces are properly matching their originating slip plane theoretical orientation. However, many of the above variabilities are difficult to evaluate and control, especially the influence of waviness of slip on the perceived slip trace orientation. Thus, we recommend using larger values of IR when reasonable doubts on any of these factors subsist.

Increasing the IR will increase the confidence that lines detected along slip traces properly match the slip plane that formed the slip trace, which is essential to the statistical analysis and the interpretation of unambiguous slip traces (i.e. slip traces that do not match specific plane types). It will also increase the ambiguity in slip plane identification, as all slip traces will more likely match plane orientations unrelated to the deformation (e.g., a {110} slip will more likely be considered "closely oriented" to {112} theoretical orientation). Consequently, when using a larger IR, more data is needed to find statistically significant results, and to observe unambiguous slip traces. More insights on the influence of IR on the ambiguity is detailed in §3.4.2.2.3, and the influence of ambiguity and unambiguous observations on the statistical analysis is discussed throughout Chapter 5. Note that, in bcc, even an IR as high as 20° can allow the observation of unambiguous <111> type slip (i.e. slip trace that match exclusively {112} and/or {123} plane type orientations), if corresponding slip systems are active, given that a sufficiently large amount of uniquely oriented slip traces are analysed.

The best motivation for the choice of IR should be an empirical study of one's experimental setup, using a reference sample such as fcc Nickel, to evaluate these experimental variabilities, ours are presented in §3.4.2 and §4.4.2.

2.5.1.2.1 IR for outside indents analysis:

In our experiments, when analysing slip traces outside indents made on fcc Nickel (§3.4.2), it was determined that, for N≥90px, an IR of 5° guarantees close to 95% of correct slip plane attribution. However, it was decided to use an IR of 10° to guarantee closer to 100% of correct attribution, whilst increasing our confidence that wavy slip traces are properly associated to their originating slip planes, and strengthening the evidence brought by unambiguous <111> type slip trace orientations.

2.5.1.2.2 IR for inside indents analysis:

A similar survey was done in the context of the analysis inside microhardness indents in §4.4.2. From the analysis of fcc Nickel, it was determined, for N=100px, that an IR of 16° should be used to account for the increase in variability caused by the inclination of the surface, and maintain close to 100% of correct slip plane attribution (which should also be true for N≥100px).

2.5.1.3 Score threshold - ST

A scoring procedure attributes a score "S" to each detected line using the following neighbour comparison logic (further detailed in §3.3.1.4): for each detected line, the code compares its orientation to the orientation of lines detected in surrounding segments, one at a time, and adds $+1/n^2$ to its score per similarly oriented neighbouring line, with “n” a nearest neighbour comparison (n=1 for the directly adjacent segments, n=2 the second nearest segments, and so on). The greater number of lines of similar orientations that are detected in surrounding segments, and the closer they are (small “n”), the more the detected line's “score” will increase. Since slip traces usually form networks of parallel lines, lines detected that are aligned with slip traces are more likely to reach higher scores because of surrounding lines, in contrast to lines detected on isolated miscellaneous features or due to errors in the line detection (Hough transform related). The score threshold ST is a value selected by the experimenter after the automated analysis, it determines which line scores are included in the final statistics, such that all and only lines with a score $S \geq ST$ will be counted.

In principle, one should seek to use high values of ST to increase the confidence that all errors in slip trace detection are properly eliminated. However, error lines are usually quickly eliminated by the increase in ST, and going for too high of a ST will gradually delete lines detected along slip traces, which therefore risks reducing the variety of slip traces included in the statistics.

Another effect of an un-necessary increase in ST is that the scoring conditions (as currently defined in the code §3.3.1.4) will gradually bias the statistics in favour of straight slip traces over wavy slip traces. Indeed, lines detected in separate segments along wavy slip traces will likely display small differences in their orientations, unlike lines detected along straight slip traces which should have closer to identical orientations, making the former reach lower scores than the latter. This bias associated with the use of a large ST will affect the slip activity measured as (in bcc) {112} and {123} type slip traces are usually wavy, and therefore risk being under-represented compared to the usually straighter {100} and {110} slip traces. Such slip traces contributions to the deformation and the proper way to quantify them is a complex topic going beyond the scope of our investigations.

The best motivation for the choice of ST should be a manual inspection of the code generated figures at the end of the analysis, giving insights on which lines are eliminated or remain part of the statistics depending on the value of ST. Typically, one should make sure not to include in the statistics pictures containing visible errors in the slip trace detection (lines detected on other features than slip traces), which should be achieved by increasing ST until these unwanted lines are visibly eliminated, or in last resort by manually excluding the pictures concerned from the analysis. ST should not be increased further once all error lines are visibly eliminated.

In our work, ST=10 was selected for most analysis as it was typically the smallest ST giving satisfactory slip trace detection (close to all errors eliminated after quick visual inspection of the code generated figures). Note that the “ideal” value of ST also depends on the segmentation size and picture resolution. Alternatively, results can be presented for various

values of ST to gain insights on the influence of this value on the analysis output (e.g. see Appendix 2, Figure A2.2 and A.2.3), the variability introduced by the choice of ST being higher when smaller amounts of lines are considered for the statistics. We do not recommend using ST lower than 9, since ST is here to guarantee that errors in line detection are properly eliminated from the analysis. Hence, if an image does not show any lines detected for ST=9, due to poor resolution and/or slip trace contrast, we recommend eliminating it from the analysis rather than decreasing ST for the whole dataset.

2.5.2 Secondary parameters

Other code parameters, which remained unchanged throughout this thesis, can affect the slip trace analysis outcome. First, the amount of smoothing applied to the SEM pictures before the edge detection algorithm. This step can be very useful to eliminate SEM imaging related noise, as well as weak sample microstructure or texture contrast. By default, 10 whole image Weiner smoothing are reiterated on the pictures, which can be adjusted depending on the quality of the SEM pictures. Note that this type of smoothing is common practice in association with edge detection algorithm. Secondly, the scoring conditions can be adjusted. In particular, the condition for considering two neighbouring line orientations as being "similarly oriented" was ruled by the value $\Delta=3.6°$ throughout our work. The influence of Δ on the analysis output was not investigated thoroughly, but in principle higher values of Δ will help the detection of wavy slip traces (reducing the bias of the code in favor of straight slip traces), at the cost of a reduced distinction between lines detected along slip traces and errors.

2.5.3 Advanced statistical analysis (Chapter 5)

The more complex statistical analysis of Chapter 5 is made using separate functions from the previously presented code, and aims to better evaluate the confidence level of conclusions based upon the evidence gathered using RAST, moving from qualitative toward quantitative conclusions, including: p-value calculations and hypothesis testing. Its use is optional, and the sample slip activity assessments of Chapter 3 and 4 were made without it.

This advanced statistical analysis relies on a simulation, a "model", that is used to estimate the expected proportions of plane orientations matched by detected lines under different slip activity hypotheses. During this simulation, it is assumed than when a randomly selected grain gets deformed by an indentation, a random slip system will activate, selected amongst possible slip plane types in proportions corresponding to the "bulk sample slip activity" that we seek to infer, and lines detected along the resulting slip trace orientation will have some random angular error representative of experimental variabilities.

The parameters of this simulation should be adjusted to correspond as best as possible to the actual experimental conditions. For example, if it was empirically estimated, in a given experimental setup, that ≈100% of slip traces orientations detected are within 10° of their "true" theoretical orientations (as in our experiments), then the lines should be simulated with a normally distributed angular error so that, e.g., 99.7% of simulated line orientations are within 10° of their associated orientation (10° = 3 standard deviation of the random normally distributed angular error added to the selected theoretical slip trace orientation). These values should be adjusted if the experimental setup was determined to generate larger, or smaller

angular variabilities in the slip traces orientations detected, so to improve the truthfulness of the statistical analysis. Also, the IR used to match the simulated line orientations to the theoretical plane type orientations should be identical to the IR used when analyzing the experimental lines in the dataset considered.

2.6 Data analysis

Here are the main guidelines followed for the analysis of the data in this thesis in the context of a bulk sample §2.6.1, a compositionally graded sample §2.6.2, and when performing the advanced statistical analysis §2.6.3. Finally, the main sources of bias in the statistics that should be considered when drawing conclusions on the samples are listed in §2.7.

2.6.1 Bulk samples

Typical sample data analyses should be made comparatively, therefore, using similar code analysis parameters, imaging conditions as well as indentation methods in compared samples will limit sources of bias in their slip statistics.

The proportion of lines detected in each grain tested, matching each condition of interest (e.g. being closely {110} oriented, or unambiguously of <111> type) should be quantified from the data output by the code. Results should be given per grain, and represented as box plots to allow easy visualisation of the dataset variability. The average proportions of match between all grain tested, as well as the presence of unambiguous observations are key information giving insights on the samples slip activities. For example, observing an average 100% of {110} match in a sample can be indicative of a predominance of {110} type slip, whilst the measurement of unambiguous <111> type slip traces, even in small proportions, can be enough to prove the existence of {112} and/or {123} type slip in the samples.

2.6.2 Diffusion gradient

In the context of a diffusion gradient, each indent should be associated to a locally Energy-Dispersive X-ray spectroscopy (EDX) measured composition representative of the area were slip traces were imaged (See Chapter 4 methods). The proportion of lines matching the conditions of interest for each indent analysed can then be plotted as a function of the indent composition. Binning should be used when representing the data as the measurement per indent can have very high variability. E.g. in Chapter 4 a ± 1.25 Ni (at.%) binning was used, averaging the proportion of detected lines matching the conditions between all indents within the bin composition range.

2.6.3 Advanced statistical analysis (Chapter 5)

The conclusions made from the advanced statistical analysis presented in Chapter 5 are an integrant part of the chapter's result / discussion, and rely on several assumptions on the samples' statistical behaviours. The automated statistical analysis uses as inputs the list of grain orientations tested, and the average proportion of detected lines matching each condition of interest (matching a plane type orientation or an unambiguous <111> type orientation) between each grain tested. Two types of data are output by the statistical analysis:

- A Harmonic P-value (HMP) associated to each slip activity hypotheses tested, which transcribes how well supported by the data a hypothesis is.
- A hypothesis testing procedure, which formally rejects all hypotheses that have a HMP < 0.05 at a 95% confidence level.

A Bayesian analysis may consider the HMPs directly, with hypotheses better supported by the data (high HMPs) being "more likely to be true" than hypotheses less supported (lower HMPs). A frequentist analysis will only consider the formal hypothesis rejection, stating that rejected hypotheses can be considered false at the given confidence level, whilst any unrejected hypotheses can be true. We opted for both types of assessments to draw our conclusions in Chapter 5.

2.7 Sources of biases in the statistics

The measured sample slip activity can be biased by several sources, which are especially important to consider if performing the advanced statistical analysis presented in Chapter 5, and/or when looking for small statistical differences between samples (NB: conclusions drawn in Chapter 3 and 4 are largely unaffected by these biases). Since the thorough statistical analysis of Chapter 5 was performed towards the end of this project, long after the experimental work on the samples was performed, some of these biases (mostly Vickers indent shape and imaging condition related) can be present in the datasets analysed and may affect some of the conclusion on the bulk samples slip activities.

First, it is important to note that the stress applied by indentation is mostly compressive, hence the slip activity measured from indentations will be more closely related to the slip activity of the material in compression. Then, as we have discussed in the previous sections, the Vickers indenter pyramidal tip shape may promote the activation of different slip systems near its corners or parallel to its sides (as well as influence the tendency to cross-slip in those areas), whilst the use of a large N and the scoring conditions (and therefore choice ST) can favour the detection of straight slip traces over wavy slip traces. We will now list other sources of biases in the slip activity statistics, as well as ways to avoid them.

2.7.1 Miscellaneous features

The slip trace analysis can be complicated by the presence of specifically oriented microstructure (e.g. hydrides), sample texture, or if large networks of scratches are present on the sample, as lines detected along these types of features may mistakenly reach high scores. Microstructural features can have grain orientation relationships, e.g. hydrides could be systematically {110} oriented, which may affect the likelihood of corresponding slip systems to reach high scores. If such features cannot be avoided through sample preparation, one should inspect the figures output by the automated analysis, and include only pictures giving satisfactory slip trace detection for the statistical analysis. Another way to avoid such features can be to increase the indentation loads and reduce the magnification of the pictures, so that the scale of the slip traces is largely different to that of the miscellaneous features. For example, in Chapter 3, we were able to analyse B2 TiFe despite the presence of hydrides as

those were much smaller than the segmentation size and were not detected alongside slip traces.

2.7.2 SEM imaging

The imaging conditions and mode may affect the contrast of distinct slip systems. For example, the BSE imaging slip trace contrast can depend on the slip systems actual orientation relative to the grain orientation, whilst SE imaging contrast should mostly be affected by changes of topography. Both can be affected by the slip systems slip directions, and amount of pile up where the slip trace is formed.

Another source of bias can come from the use of different magnification sizes when imaging slip traces within the same grain. The statistics per grain, when analysing bulk samples, are calculated by summing all detected lines in a grain, this number of lines depending on the picture resolution and magnification relative to the slip traces dimensions. If distinct pictures made within a grain show distinctly oriented slip traces, their relative contributions to the grain's statistics can be affected by changes in magnification (at constant resolution). To avoid this, one should make sure to use the same imaging parameters within a grain. One should also avoid taking several pictures of similar slip trace networks within a grain (e.g. if resulting from different indents) so to avoid this problem of artificially over-representing them compared to other slip systems in those grains.

2.7.3 Grain orientations

As we have just seen, the grain orientation may affect the contrast of some slip systems depending on the grain orientation tested and the imaging conditions. More grain orientation related biases can exist and are outlined here.

Since the stress state applied by an indenter, even when rotated, is not "completely random", this also means that different grain orientations may favour different slip activities. Hence, a thorough statistical analysis should keep track of the grain orientations tested and check whether specific sample grain textures are biasing the orientations of grains tested (e.g. all grains tested could be systematically closely (100) oriented).

Another grain related bias comes from the possible ambiguity in the different plane types orientations due to their geometries. For example, some grain orientations can be very favourable to the observation of unambiguously {112} and/or {123} type slip traces, whilst others may make such observations impossible. In the absence of advanced statistical analysis (Chapter 5), and especially when comparing samples where small amounts of grains were analysed (Chapter 3 and 4), these geometrical biases can artificially change their relative "measured" slip activity. This bias can be quickly assed via the study of the code generated randomly oriented line statistics, which give an estimation of the probability of matching each plane orientation, assuming a random line orientation between 0 and 180° (more details in §3.3.1.8). Typically, one should start by comparing the random line statistics between the samples, check for significant differences in these statistics risking to bias the interpretation of the data, and only then compare their slip trace analysis outcome. Note that the more grain orientations are tested, the smaller these biases should become.

In the advanced statistical analysis of Chapter 5 a line orientation simulation is presented which considers these geometrical effects on a grain per grain, and plane type per plane type basis. Therefore, the slip activity assessments made from the advanced statistical analysis should be impervious to the changes in slip plane identification ambiguity caused by the crystal geometry, as they are an integrant part of the calculations (other grain orientation SEM imaging and stress state effects remain).

3 Automated indentation-based slip trace analysis for bcc and B2 plasticity

3.1 Abstract

B2 intermetallics are an important material class for high-temperature applications, as monolithic materials such as NiAl, or when used as a precipitate reinforcing phase within novel bcc-B2 'bcc-superalloys' such as Ti-TiFe or refractory high entropy superalloys. However, there is tremendous variability across B2 compounds in terms of strength and ductility, which is underpinned by their dominant slip systems. Here we have developed an automated indentation-based slip trace analysis method to accelerate the assessment, and better quantify the favoured slip systems in bcc and B2 samples, with a particular interest on distinguishing <111> vs <100> type slip character. The methodology consists in performing microhardness indentations, determining local crystal orientations using EBSD and imaging slip traces nearby the indents using SEM. Our code then automatically detects the orientation of the slip traces by segmenting the pictures, detecting lines locally using a Hough transform based algorithm, and scoring them for how likely they are to be aligned with slip traces. Combined with coarse EBSD data, the slip activity of the material is assessed based on how frequently each calculated theoretical slip plane type orientations were found closely oriented to the detected lines. The methodology was first validated on face-centred cubic nickel, and then applied to appraise four alloys, bcc Fe as control, compared to B2 TiFe, B2 Ti_2AlMo and B2 Ti_2AlNb. From a trivial experimental work, the analysis provides unambiguous evidence of ½<111> {112} and/or {123} type slip in bcc Fe and B2 Ti_2AlNb, and suggests slip predominantly on {110} for B2 TiFe and Ti_2AlMo. The automation unlocks indentation-based slip trace analysis as an accessible, high-throughput, cheap, and surface-level way of characterising the slip behaviour of alloys. The large increase in statistics compared to alternative slip characterisation techniques has the means to by-pass common issues surrounding ambiguity in slip plane identification in bcc and B2 compounds.

3.2 Introduction

3.2.1 Slip characterisation in bcc and B2 alloys

Dislocation motion and microscale slip are critically responsible for the bulk mechanical properties of engineering alloys, controlling both strength and ductility. The number and the type of available slip systems impact not only the ductility at the intragranular level, but also at the interface between grains or phases as it can oppose or favour slip transfer mechanisms. While the question of linking micromechanics to the bulk mechanical properties of materials is a subject of great complexities and debates, we here seek to study slip behaviour to aid in the design of novel body-centred-cubic (bcc) alloys, such as refractory high entropy superalloys and 'bcc-superalloys' which comprise ordered-bcc (L21/B2) strengthening phases in a disordered-bcc matrix [94] [26] [28], with improved room temperature ductility. These are subject to ongoing research for their promising high temperature performances, taking inspiration from the microstructure template of A1 Ni + $L1_2$ Ni_3Al in face-centred-cubic (fcc) superalloys and extending it to bcc.

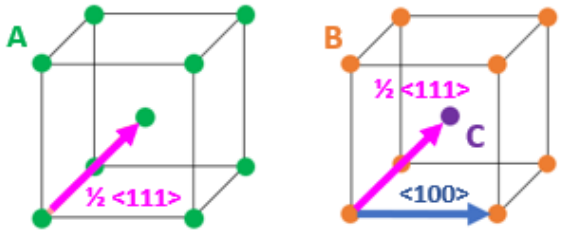


Figure 20: illustration of bcc and B2 crystal lattices (A, B, C representing any element) with arrows representing possible active burger vectors ½<111> or <100>.

Compared with fcc metals, the deformation mechanisms in bcc are significantly more complex. Notable characteristics inherent to the bcc lattice are its tensile-compression asymmetry and non-Schmid effects, both thought to be caused by the asymmetrical nature of the dominant ½<111> screw dislocations [38] . Whilst at room temperature bcc compounds usually slip on ½<111> {110}, {112} and {123} slip systems (subject to controversy [38]), B2 compounds show a great diversity of slip behaviour, often with restrained slip activities, for example: <111> {110} (e.g. FeAl [60], CuZn [61]), <111> {112} (e.g. Cu(Ni)-Zn [61]), <100> {110} (e.g. TiFe [62]) or <100> {110} {100} (e.g. NiAl [63] [64] [65]). Previous studies have demonstrated that the B2 slip activities can be modified by changes in composition, either stoichiometry or with alloying additions [37] [67], giving design opportunities within bcc+B2 alloy systems to control the B2 slip behaviour. However, this requires the slip activity to be characterised during alloy development to tune the mechanical response.

As discussed in Chapter 1 (§1.6), common approaches for slip activity characterisations, including experiments of TEM, single crystal, and micromechanical testing, have practical challenges. TEM and FIB sample preparation, single crystal fabrication, as well as performing repeat experiments are challenging, time intensive procedures which require skilled experimenters and expensive equipment. They also often lack representativity due to the limited statistics obtained via these techniques. Approaches aiming to assess larger scale

deformation slip behaviour include diverse slip trace analysis techniques (§1.6.3), which are especially complicated when performed on bcc, due to the very similar geometries of the different possible active bcc plane types (see Figure 19 (a) in §1.6.4).

An alternative to these could be indentation-based slip trace analysis (§1.6.4), which requires only a microhardness testing machine and a SEM equipped with an EBSD detector to acquire a low resolution EBSD scan. This is particularly important in the field of novel alloy development, where there is a need for rapid property assessment, and therefore, the possibility of using indentation-based slip trace analysis was investigated in this work.

3.2.2 Identifying key slip activities from indents

A basic indentation-based slip trace analysis, whilst giving slip planes, does not give information on the active slip directions, i.e. Burgers vector, without modelling, ECCI or DIC. As such, one could wonder what information can be gained from this analysis. Let us start by listing the typical room temperature slip activities that we are interested in identifying when studying bcc and B2:

- In a B2 compound, <100> type slip is commonly reported, and are restrained to the {110} and {100} plane types [64] [62].
- Typical slip activities for B2 compounds include either predominantly active <111> {110}, or <100> {110} slip systems [60] [62].
- Some B2 compounds are reported to slip mainly on <111> {112} slip systems [61].
- We can also expect mixed slip activities, such as <111> {110} {112} and <100> {110} {100} [66] [64].
- Finally, in bcc, we expect <111> type slip to occur on either {123}, {112} and {110} plane types. The occurrence and prevalence between the different slip planes is controversial, and has been reviewed in [38], which gives interesting insights.

An indentation-based slip trace analysis approach, due to the ambiguity in plane type identification, will be focussed on identifying “potentially active slip planes”, relying on mostly ambiguous observations, and will not give any direct information on the active slip direction. In this context, some slip traces can present particular interests for differentiating bcc and B2 slip activities:

- Slip traces matching only a {112} or a {123} plane orientation, or both, can only be the result of a <111> type slip.
- Slip traces matching only a {100} plane orientation can only be the result of a <100> type slip.
- Slip traces matching a {110} plane can be associated to <100> or/and <111> slip, but it is expected that some B2 compounds’ slip traces will match systematically (100% of the time) {110} planes. Therefore, the tendency for a sample to match {110} plane orientations is of particular interest.
- Similarly, the tendency to match {112} planes can be of interest for some B2 compounds.

Slip traces fitting the conditions listed above will be quantified during the analysis to help distinguish the main types of expected bcc and B2 slip activities. A key point to emphasise is that from simply looking at the active slip planes, evidence of either <111> or <100> can be obtained, however, <111> {110} and <100> {110} B2 slip activities cannot be differentiated if only {110} planes are active.

The deduction of the slip direction can only be done in specific, unambiguous situations, which further highlights the need for large statistics, to increases the likelihood of being in favourable geometrical conditions and observe such unambiguous slip traces. This becomes a problem since manually identifying large amounts of slip traces is a laborious and time-consuming process, prone to manual variability, mistakes, and experimenter bias, thus detracting from the inherent advantages of indentation-based slip trace analysis over alternative micromechanical-testing techniques. This helps explain why little experimenters have been using this experimental approach on bcc. These issues could be by-passed via automation of the line identification process, of which an approach will be discussed in the next sections.

3.2.3 Automation challenges

Recent parallel developments of slip trace analysis techniques have begun to incorporate automation. This has included a semi-automated approach where manually identified slip traces are automatically compared to calculated theoretical slip plane orientations [90], with a more recent example including whole image Hough transform based automated line detection [95] in the context of a tensile testing experiment.

The challenge of the slip trace identification automation is to make a code that can detect and analyse a variety of slip traces, with as little user input as possible. It should also be easily adaptable to a varying set of materials, to guarantee the comparability of the data, which means accounting for: different microstructures, textures, slip trace density, contrast, imaging conditions and sample cleanliness.

Hough transform based algorithms are widely used when it comes to line detection, notably for Kikuchi band recognition in EBSD software [96]. In short (see [95] which goes in more details), a Hough transform algorithm is able to find alignments of white pixels in binary pictures. When applied to a picture in which edge detection has been performed, it can detect the edges of straight objects (e.g. slip traces). The possibility of using a Hough transform algorithm for automatic slip trace detection was therefore investigated in this work. When we first apply such algorithm to pictures, from several samples and indents, it appears clear that the complexity and variety of pictures make any automation difficult:

- Any coarse variation of brightness/contrast, for example if the top of the picture is brighter than the bottom, affects the threshold-based edge detection algorithm and can completely obscure parts of the pictures from the analysis, which would easily be spotted by an experimenter. In [95], this thresholding was performed manually using Image J prior to the automated analysis.
- The presence of the indent in the pictures can generate mathematical errors due to its sides being detected and combined to real slip traces, giving out “fake” line orientations. The same problem applies to any surface contamination, secondary phases or scratches

which will inevitably be present as the number of indents and samples multiply. This analysis also struggles to detect curved or wavy slip traces, often present on bcc samples, or due to local crystal deformation caused by the indentation.

- The output, as in the number and what lines are detected, vary significantly depending on the Hough transform function variant used and its parameters (Amount of gap filled between detected aligned line segments, minimal length of the lines, maximum number of lines to detect etc.) which makes the method seemingly impossible to automate as the line detection settings would need to be optimised on a picture-to-picture basis.

A critical point here is that we have no way of separating the “real lines” detected on slip traces from any errors, which impairs the assessment of the analysis reliability.

In this paper, we propose an approach for this automation designed in particular to be easily transferable from sample to sample, enabling reliable statistical comparisons between them. We demonstrate that, without solving the ambiguity in slip plane identification, key B2 slip activities can be identified when analysing a variety of grain orientations, via the statistics of the plane types match frequency, and via the observation of unambiguous <111> {112} and/or {123} type slip which is likely (if such slip systems are active) under a wide range of experimental conditions. The automation increases the speed and repeatability of the technique, and allow us to better identify uncertainties and biases surrounding slip trace identification, which are significant improvements over manual slip trace identification and has the means to unlock the full potential of indentation-based slip trace analysis. First, the key aspects of the automation will be presented §3.3, after what the technique will be validated on fcc Ni §3.4.2, and finally used to appraise the slip activity of 4 samples §3.4.3, namely bcc Fe, B2 TiFe, B2 Ti_2AlNb, B2 Ti_2AlMo, identifying their respective and diverse slip activities, in agreement with previous work in literature.

3.3 Methodology

This methods section describes the technique of automated indentation-based slip trace analysis developed. Firstly in §3.3.1, will be described the algorithm used to automatically identify slip trace orientations from Scanning Electron Microscopy (SEM) pictures in various contexts of visibility and slip activity. Then in §0, the experimental work associated with the technique will be presented, as performed on the various bcc and B2 compounds that will be analysed in this work.

3.3.1 Automated slip trace analysis code development

Building from the prior art as to slip trace analysis (Chapter 1 §1.6.3-1.6.4), and in parallel to attempts at automating it [90] [95], key challenges for slip trace analysis technique are the reproducibility, speed and reliability. To resolve this, here we outline the development of a new automated code for indentation-based slip trace analysis. It will then be demonstrated to work on fcc Ni in §3.4.2, and applied to various bcc and B2 samples in §3.4.3.

3.3.1.1 Code overview

A MATLAB™ based code was developed to perform an automated slip trace analysis. Note that the MATLAB™ functions used are common algorithms and should be easily translatable in other programming libraries (e.g. Python). Some of the main MATLAB™ functions used are described in more details in appendix 1, and a preliminary version of the code will be uploaded in open access on GitHub.

The basic steps of the code will be detailed in turn in the next sections, which include: the manual input of pictures and Euler angles (§3.3.1.2), the image segmentation and line detection (§3.3.1.2), the scoring procedure (§3.3.1.4), the matching procedure (§3.3.1.5), and the counting procedure (§3.3.1.6). In addition to these steps, the code also generates figures and randomly oriented lines to assist the validation of the analysis output (see §3.3.1.8 and §3.3.1.9 respectively). The key elements of the automation are represented in Figure 21.

The main idea behind the code is to analyse the indent pictures not as a whole, but as a succession of small segments, where edges and lines are detected locally (Figure 21 (a)). This cancels the impact of variations in contrast between different areas of the pictures and unlocks a way to distinguish lines on slip traces from lines caused by errors in detection. With this segmentation, we find that lines detected on the same or similarly oriented slip traces tend to be packed together and have very similar orientations. On the other hand, lines detected on miscellaneous features or in empty areas tend to have more chaotic orientations and much fewer similarly oriented neighbours. This means that to discriminate lines detected along slip traces from errors, we can give a score to each line based on how many lines have similar orientations in neighbouring segments (Figure 21 (b)): the more there are, the more likely it is that this line is on a slip trace. The code then performs the comparison of every detected line against the theoretical slip plane orientations, calculated from the EBSD crystal orientation Euler angle inputted by the user (Figure 21 (c)). The statistics obtained on how often each slip plane type was matched by the slip trace line orientations, for a chosen line score (Figure 21 (d)), then give an estimation as to the favoured active slip planes in the

sample. In this way, the procedure also retains some quantitative information on the length of the slip traces, as a greater number of lines will be detected on longer slip traces. The next sections will go over each step of the analysis and describe their main components.

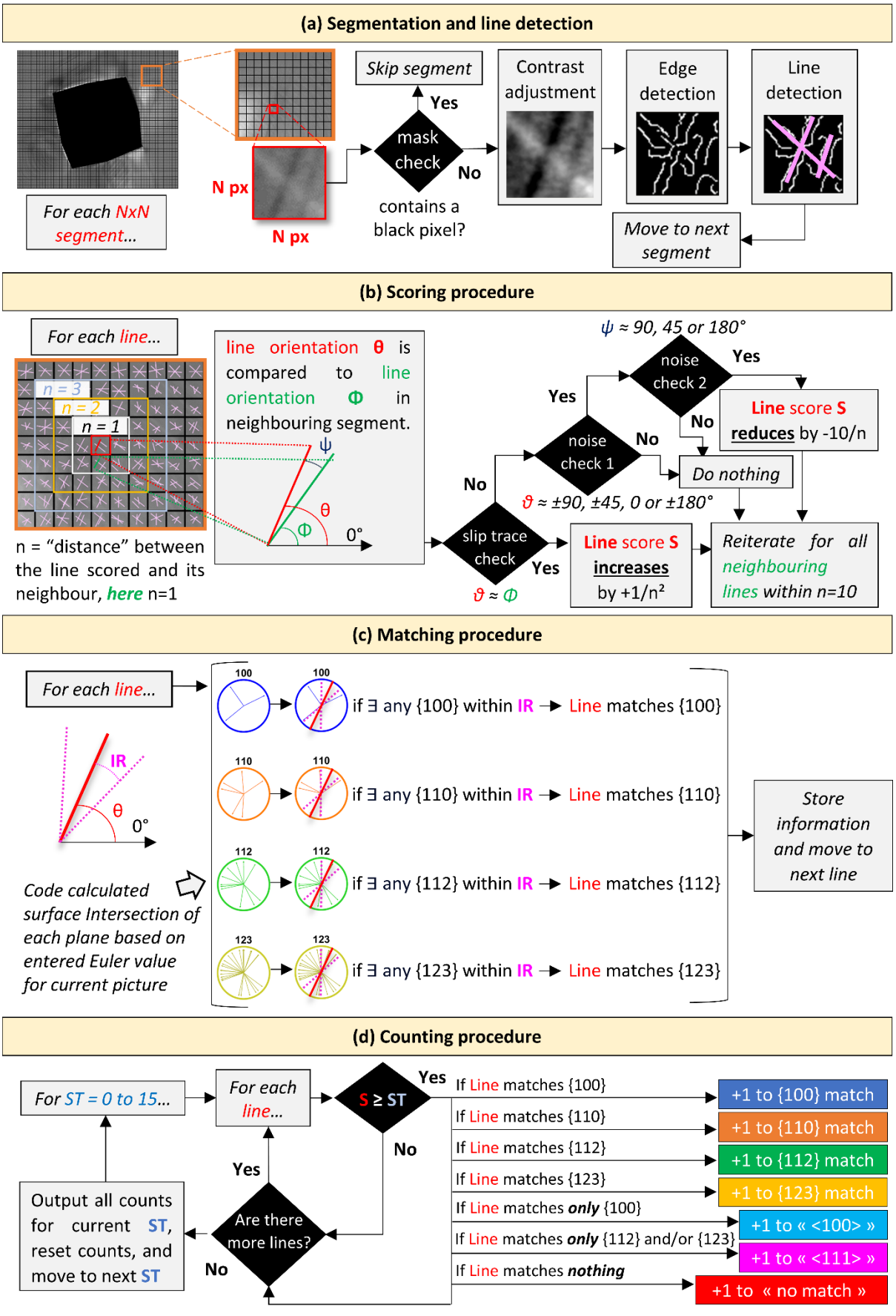


Figure 21: Key steps of the automation. Pictures, masks, and Euler angles are inputted manually. Analysis parameters N, S, IR and ST, and scoring conditions are described in §3.3.1.2 to §3.3.1.9.

3.3.1.2 SEM images loading, Euler angles input, and filtering.

Before going through the analysis, a part of the code is dedicated to manually loading the pictures, entering the EBSD determined average crystal orientation for each picture (Euler angle), and masking unwanted features. Note that these steps are quickly performed (≈20s per image) and could be further automated to enable the analysis of larger data sets.

The pictures are then automatically smoothed using a Wiener filter which is commonly associated to edge detection algorithms [97] [98]. This helps reducing the SEM scan noise of the pictures while preserving edges, therefore assisting the upcoming edge detection algorithm. This smoothing function is re-applied 10 times to the pictures, which tends to widen the more contrasted slip traces and blur miscellaneous texture related features. In most cases during our experiments, smoothing the pictures allowed for the detection of a wider variety of slip traces while increasing the signal/noise ratio, it only rarely obscured any slip trace network. One could critic the use of a filter on the data set, however, this filtering offers similar or reduced bias on the observed slip activity compared to a manual line identification: if a slip system does get blurred out by the filtering, it means it is poorly contrasted, and therefore would be more difficult to identify manually.

The regions masked on the pictures are set to a pixel value of 0 after smoothing which makes them easy to exclude from the rest of the analysis (see “mask check” condition in Figure 21 (a)).

3.3.1.3 Picture segmentation & line detection

The first step of the automated slip trace analysis consists in segmenting the pictures in small area segments to perform the line detection locally Figure 21 (a). **The images are analysed as a succession of small N*N px segments** (see §3.4.2.3 detailing the choice of N). Segments containing a pixel value of 0 (black pixel) should be limited to the masked parts of the image due to prior smoothing, and are automatically ignored for the remainder of the analysis.

A contrast adjustment is performed automatically on each segment. This step is useful mostly for debugging, highlighting contrast variations before the edge detection (an example is shown on Figure 23), but may be redundant with the edge detection function, which itself relies on contrast variations.

Edge detection is then performed on each segment using a Canny algorithm. The edges of objects, which includes slip traces, are identified by this function based on contrast variations in the respective segment. This function turns the segment into a binary image with white pixels at the edge of features.

Three lines are then detected in each segment using a Hough transform algorithm. Details on which functions were used and how they were set are available in Annex 1 A. In short, these functions were set to find the three longest alignments of white pixels in each segment, regardless of how discontinuous they might be. Having more than one line detected per segment sometimes allows the detection of intersecting slip traces. However, in most cases, some slip traces have higher contrast than others which stops them from both being detected within the same segment. Therefore, the main use of detecting more than one line is that the

edge detection usually finds two edges on a slip trace, one on each of its sides, which can then both be detected by the Hough transform, and helps increasing the quantity of lines detected on slip traces relative to the noise. Detecting "too many" distinct lines per segment will not change the reliability of the results, as lines that are not aligned with slip traces should be eliminated during the following scoring step. We limit ourselves to three lines per segment to reduce computation time, as it is very unlikely that more than 3 lines will be detected on a slip trace within the same segment.

3.3.1.4 Scoring procedure: slip trace signal vs noise distinction

In this part of the code, **a score S** is attributed to each line, which represents how likely it is to be aligned with a real slip trace (see Figure 21 (b)). After segmenting the picture and detecting lines locally, we now have what we can compare to a "matrix of line orientations". We will differentiate lines detected on slip traces, the "signal", from lines detected on miscellaneous features and SEM imaging related noise, the "noise".

Δ is the angular difference chosen to consider lines as being "closely oriented" to a compared orientation ("≈" symbol for *slip trace check* and *noise check* in Figure 21 (b)):

$$\theta \approx \theta' \Leftrightarrow (\theta' - \Delta) < \theta < (\theta' + \Delta)$$

In our work, this value was originally chosen to be Δ=3.6° based on an estimation of the line orientation detection accuracy of the Hough transform algorithm when applied to small <100px segments, but different Δ may be used: smaller Δ will tend to favour the detection of straight slip traces over the rest, while large Δ will help detecting wavier slip traces but at the cost of a weaker signal vs noise differentiation.

The scoring approach is based on a few assumptions about the characteristics of the lines detected. We will go through each assumption, and how the scoring procedure accounts for it.

For the signal, Lines detected on the same or similarly oriented slip traces tend to be packed together. This is translated by the "slip trace check" condition (see Figure 21 (b)), with a score S increase of $+1/n^2$ if the line scored and its neighbour have similar orientations (as per the value Δ). "n" is a comparison to nearest neighbors, where n = 1 is the directly adjacent segments, n = 1 second-nearest segments, and so on. The more neighbours and the closer such neighbours are to the line (small n), the more its score will increase.

The noise in line detection can come in two kinds. Firstly, lines can be detected on miscellaneous features e.g.: scratches, contamination, or sample texture. Such lines should be scarce, and tend to have different orientations from each other. Therefore, the "slip trace check" condition already accounts for this situation, as lines on such feature will tend to have a much smaller score increase than lines on slip traces. Note that many of these noise features can be avoided through thorough sample preparation, and are usually easily identifiable when checking the figures output by the code. Secondly, lines can be detected in segments from featureless areas. Such segments tend to be packed together, and in the absence of features, the lines detected in them can be biased in their orientations: they are likely to have

orientations of 0, ±180, ±90 or ±45° due to mathematical biases in the Hough transform algorithm, more likely to find long alignment of pixels in those directions (these artifacts are linked to the discontinuous nature of pixelized pictures). In addition to these lines, some lines can be detected on horizontal SEM scan noise (0, ±180°), due to the rastered nature of SEM image collection. The "slip trace check" condition alone will not eliminate such lines since they also tend to be similarly oriented with each other and close packed. We therefore need to add the two "noise check" conditions (Figure 21 (b)): first, "Noise check 1" checks if the line getting scored has a noise-like orientation, and second, "Noise check 2" checks if the *neighboring* line has a *different* noise-like orientation. If both conditions are met, the line is considered likely to be noise, and the score of the line is decreased by -10/n.

Notice that the lines in noise-like orientations are heavily disadvantaged, but not systematically eliminated. This is to allow that in high quality pictures, with high density of clearly visible slip traces, slip traces with such orientations may still be detected.

In summary with this scoring system, we can separate the noise from the signal. A high score S means a line is surrounded by a high number of lines of similar orientations, making it likely to be associated with a real slip trace. A low score can mean two things, either its score did not increase during scoring, i.e. it has an "uncommon" orientation, or it both increased and decreased, i.e. the line has a noise-like orientation and is surrounded with other noise-like oriented lines making it likely to be noise. Selecting only high scoring lines for the statistical analysis should now allow us to select signal over noise, i.e. lines detected on slip traces over lines detected due to errors or in featureless segments. As a side consequence of the current scoring conditions, straight slip traces are more likely to reach high scores than wavy or curvy slip traces, which may be adapted depending on the needs of the study.

Finally, it should be noted that the Δ=3.6°, +1/n² and the -10/n values were empirically determined through trial and error. They could be fine-tuned in the future e.g., by using machine learning. In the meantime, these simple empirically chosen conditions allowed for suitable slip trace detection across all samples we have tested so far (which therefore includes all the samples tested throughout this thesis).

3.3.1.5 Matching procedure: attributing slip planes to detected lines

Each detected line orientation is compared to the theoretical slip trace orientations of each bcc slip plane type, based on the Euler angle associated to the picture during the data input step (Figure 21 (c)). These theoretical orientations are calculated by the code, by finding the intersection between the respective slip planes rotated accordingly with the Euler value, and a theoretical perfectly flat horizontal sample surface.

IR is the *identification range*, defined as the maximum angular difference expected between the detected slip trace orientations and their originating slip plane theoretical slip trace orientation. The choice of this value depends on our estimation of experimental uncertainties, concerning notably the line orientation detection accuracy, the EBSD determined Euler angle uncertainty, and experimental variabilities such as waviness of slip, local crystal rotations, or unevenness of the sample surface (see §3.4.2.3 about choosing the value IR).

Each time a plane type presents one or multiple theoretical slip trace orientations less than "IR" degrees away from the observed line orientation, it is considered "a match", and is saved as such for this line. The plane type which offers the closest theoretical orientation to the line orientation is also identified for figure making. Note that matching more closely a plane type will not be used as information during the analysis: the data analysis will be performed under the assumption that any of (and only) the matching plane type orientations could be the originating plane type of the slip trace considered.

3.3.1.6 Counting procedure

The counting procedure, which outputs the data that we will analyse, is illustrated on Figure 21 (d), and takes in consideration notably the score S previously attributed to each line (see §3.3.1.4).

ST is the *score threshold*, defined as the minimum score a line needs to have to be counted in the statistics. For an increasing value of ST (limited to 15 since only a few lines reached a score superior to 15 in our data sets), is counted the number of detected lines which have been attributed a score S ≥ ST, that match the different plane types. Is also counted the number of lines matching exclusively {100}, and lines matching exclusively {112} and/or {123}, as those provide unambiguous evidence of respectively active <100> type and <111> type slip. If a line has not matched any plane orientations, the count of "no match" increases by 1 instead, such lines should only be observed if errors are present in the line detection and/or plane type attribution.

Detected lines can, and usually do, match more than one plane type (most slip traces are ambiguously oriented). In such case all plane types matched are counted as a match.

e.g.: a line matches both a {112} and a {110} plane orientation, the "count of {110} match" and the "count of {112} match" both increase by 1.

The choice of ST for the analysis will be discussed in detail in §3.4.2.3.

3.3.1.7 Figure making for line score S ≥ ST

After the counting is done, the lines are drawn automatically on the picture analysed at the position they were detected and coloured in the same colour as the slip plane type they match the most closely, or in the colour of the special conditions they fit (Colour coding as Figure 21 (c) and (d), which will be consistently used in this work), for each score threshold ST. The pole figures predicting the slip trace orientation corresponding to each plane type are drawn next to the figures for the Euler associated with the picture. These figures allow us to inspect the quality of the analysis, checking if the line detection and plane type attribution behaves as expected, if the pictures present obvious errors, and what ST performs better at eliminating the noise. Multiple examples of such figures will be presented in the results throughout this thesis.

3.3.1.8 Code generated randomly oriented lines for statistical testing

Random line orientations (uniformly distributed between 0 and 180°) are generated by the code, go through the same matching and counting procedures, use the same identification range IR and the same theoretical slip trace orientations as the detected lines for each picture and grain tested. These will be important to check the validity of the results in §3.4, as they give an estimation of the probability to match the different plane types or conditions due to chance alone.

A randomly oriented line either matches, or does not match a plane type, which is a binary yes/no outcome, making it a random binomial variable. We will call "matching a plane type" a success. In such context the expected value and the standard error of the binomial distribution describing our random experiment can be calculated, which will give respectively an estimation of the probability of success and the uncertainty on this estimation. To this end, according to binomial statistics, equation (1) can be used for calculating the expected value E, and (2) for calculating the standard error SE:

$$(1)\ E = n * p = \mu$$
$$(2)\ SE = \sqrt{np(1-p)}$$

In these equations, p is the probability of success (value between 0 and 1), in our case the probability for a randomly oriented line to match a chosen plane type given a specific set of grain orientation and IR, n is the number of tests, in our case the number of code generated lines which are compared to the theoretical slip trace orientations, and μ is the average amount of success expected if we were to repeat the same experiment (test n random line orientations) indefinitely. Dividing (1) and (2) by n to express these values as a proportion of lines, we obtain:

$$(3)\ E = p = \frac{\mu}{n}$$
$$(4)\ SE = \frac{1}{\sqrt{n}} * \sqrt{p(1-p)}$$

The probability p of matching can be estimated using (3), replacing μ by the amount of success obtained after comparing the randomly generated lines to the theoretical slip plane orientations. Let us now calculate how many lines n need to be generated and tested to guarantee that the standard error on this value p, as estimated by the randomly generated line population, is ≤ 1%. To do that, we solve (4) for SE = 0.01 and p = 0.5, since (4) will be maximal for p=0.5:

$$(5)\ n = \frac{0.5 * (1-0.5)}{0.01^2} = 2500$$

We obtain that 2500 randomly oriented lines need to be generated, which is a reasonable amount considering our code currently performs this action in less than ≈30s per grain tested.

In summary, by generating 2500 randomly oriented lines, and counting the number of times they match each plane types, an estimation of the probability of matching each plane type supposing a random line orientation by chance alone, in a set context of grain orientation and

IR, can be obtained. The same logic applies to other conditions such as being unambiguously <111>, matching exclusively {100}, etc. These estimated probabilities will be given as a percentage with a standard error ≤ 1%, which is maximal (=1%) if the event is estimated to have exactly 50% chance of happening.

3.3.1.9 Data saving

The output of the analysis consists in an Excel™ spreadsheet containing, for each picture, grain, and score threshold:

- what Euler values were entered
- how many lines were detected
- how many times each plane type was matched by the lines,
- how many times the lines fitted special conditions for unambiguous <100> or <111> type identification, or did not match anything
- how many randomly oriented lines were generated
- how many times the randomly oriented lines match the different plane types or fit the special conditions.

The data was designed to be treated using pivot charts in Excel, which is a powerful tool to easily spot grain or picture specific behaviour, as well as to identify and exclude errors from the data analysis.

3.3.2 Experimental work

Different bulk B2 alloys expected to exhibit a variety of slip activities were prepared by arc melting of commercially pure (>99%) elements (compositions in Table 3 and Table 5), these also present interest for ongoing development of titanium-based bcc+B2 alloys. The ingots underwent a homogenisation heat treatment at a temperature corresponding to stable single-phase B2, instructed by the best available phase diagrams [99] [100] [101]. A bcc Fe (low carbon ferritic steel DX54 [102]) sample was also prepared for comparison and an fcc Nickel sample for validation of the methodology. The latter was prepared from arc-melted commercially pure elements and annealed in the furnace to coarsen the grain structure and release residual stress induced by processing related deformation. The corresponding heat treatments are listed in Table 3. These were performed under a protective atmosphere by encapsulating the samples in quartz ampoules, with vacuum cycles and argon backfilling. The B2 samples were water quenched at the end of their respective heat treatments, whilst the nickel sample was air cooled.

Table 3: preparation conditions and target compositions.

Sample	B2 TiFe	B2 Ti_2AlMo	B2 Ti_2AlNb	Fcc Ni	Bcc Fe
Target composition (at%)	51/49	50/25/25	50/25/25	100	-
Homogenisation temperature (°C)	1000	1200	1200	700	-
Duration (hours)	24	100	100	2	-

All samples were mounted in Bakelite, prepared using grinding paper down to 4000 grit size and finished with a 50 nm colloidal silica polishing step on a neoprene cloth for a duration of 1 hour. Indentation was performed on a Mitutoyo HM-124 Hardness testing machine using a Berkovich tip, and a load of ~0.5 kg, held for 10 seconds, leading to indents ~60 µm wide, depending on the sample hardness. Each sample was indented 10 to 30 times depending on the quantity of identifiable grains. Such indents produced visible slip traces around the indents. The samples were manually rotated between each indentation, and different grains were targeted to help diversify the statistics for the slip trace analysis.

Scanning electron microscopy (SEM) operating at 20 kV combined with electron backscatter diffraction (EBSD) was performed on each sample in a TF Apreo 2S HiVac to determine the average crystal orientation in indented grains (at tilt = 70°). The mapping was usually coarse (10 µm step) to reduce the measurement time while keeping a reasonable amount of measurement points in each grain (>30 data points per grain). No twinning was observed, but some local crystal rotation, around a few indents, was marginally detected. The average crystal orientation of each indented grain was calculated based on the EBSD data, using the MATLAB MTEX toolbox, with attention ported to excluding the areas directly indented from the grain reconstruction (these are highly deformed and usually show a different grain orientation when indexed).

The samples were then imaged in the same microscope at tilt = 0°. A 3072x2188 px picture of each unique grain showing visible slip traces, close to the indents, is taken using imaging parameters offering the best slip trace contrast possible. Typical imaging settings used for each sample are listed in Table 4, which vary from sample to sample. Note that the magnification may vary within a sample to image smaller grains or slip trace networks, this however should not impact our interpretation of the data. Low acceleration voltage and small working distance usually help highlighting slip trace contrast, however, 20 kV ETD showed sufficient contrast for the softer Ti_2AlNb sample, backscattered electron imaging (BSE) can also be used. The pictures were taken in integration mode to get rid of as much SEM scan noise as possible and avoid sample charging. The areas imaged are manually associated with their corresponding average crystal orientation measured (a Euler angle), which were then used as input for the automated slip trace detection algorithm (§3.3.1.2). A 600s 20 kV energy-dispersive X-ray spectroscopy (EDX) area scan of a ≈400µm² area was performed on each sample to get their average bulk composition. Finally, each B2 sample was ground into powder, and analysed via Synchrotron X-ray diffraction (SXRD), which was carried on Beamline I11 at the Diamond Light Source, using a wide-angle position sensitive detector with an intrinsic 2θ step size of 4 millidegrees. A wavelength λ = 0.826596 Å, calibrated using a NIST Si 640c standard, was used.

Table 4: Imaging settings used for each sample.

Sample	detector	Magnification range	HV (kV)	Current (nA)	Dwell time (µs)	WD (mm)	Integration (scans)
Fe	ETD	x5000-x15000	5	3.2	0.5	7.5	10
TiFe	ETD	x2500-x5000	5	3.2	1	5	10
Ti_2AlMo	BSE	x1500-x2000	5	3.2	1	5	10
Ti_2AlNb	ETD	x1000-x1200	20	3.2	1	5	10
Ni	ETD	X650-x1200	10	3.2	1	5	10

3.4 Results and Discussion

In this section, the composition and microstructure of the studied alloys will firstly be presented, as well as general observations concerning their indentation-based slip trace analysis. Then the automated slip analysis is demonstrated in fcc Ni, and finally applied to the bcc Fe and B2 intermetallic to reveal their dislocation activities.

3.4.1 Materials and indentation characteristics

The B2 compounds average compositions measured from EDX area scans are available in Table 5, these compositions were considered close enough to the target compositions to meet the needs of the study, though it is noted that the stoichiometry of intermetallics can have important implications as to their properties [67]. Synchrotron XRD measurements confirming the B2 structure of TiFe, Ti_2AlMo and Ti_2AlNb are shown in Figure 22.

Table 5: Characteristics of the alloys. The B2 intermetallic compositions were EDX measured, uncertainties indicated here are given by the EDX software (Aztec). The bcc Fe composition is given by the manufacturer [102].

Sample	B2 TiFe	B2 Ti_2AlMo	B2 Ti_2AlNb	Bcc Fe	Fcc Ni
Expected RT slip type	<100>{110} [62]	-	<111>{110} & {112} [66]	½<111> [45]	<110> {111}
Target composition (at%)	51Ti-49Fe	50Ti-25Al-25Mo	50Ti-25Al-25Nb	100Fe	100Ni
Actual composition (at%)	51.6±0.2 Ti 48.4±0.2 Fe	52.0±0.2 Ti 24.2±0.1 Al 23.7±0.1 Mo	51.4±0.2 Ti 22.8±0.1 Al 25.7±0.1 Nb	≤0.28 C ≤0.045 P ≤0.043 S ≤0.35 Mn	-
Phase (XRD)	B2	B2	B2	-	-

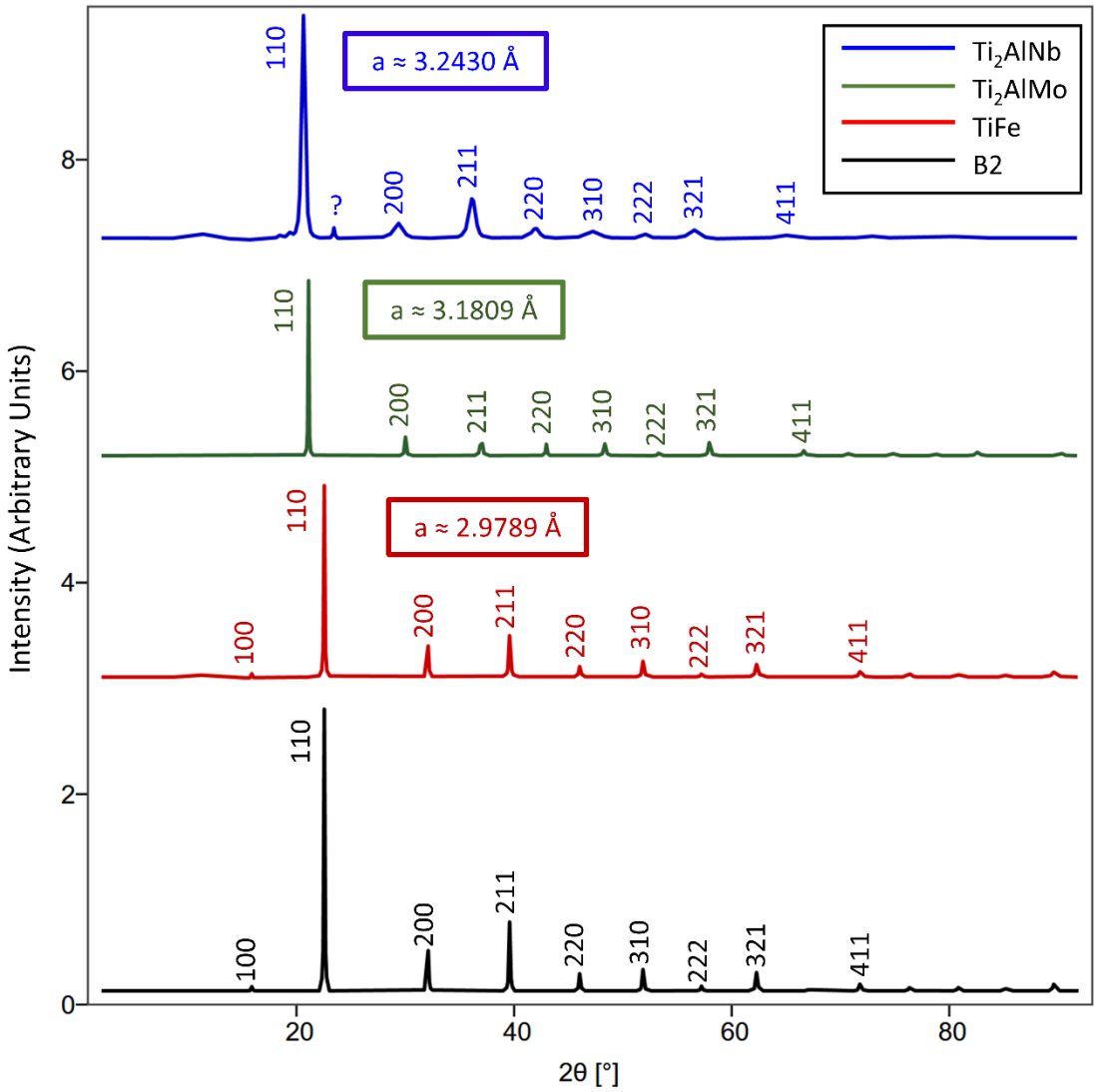


Figure 22: Synchrotron powder X-ray diffraction (SXRD) patterns of samples Ti_2AlNb, Ti_2AlMo and TiFe, analysed using CrystalDiffract™ version 7.0.2 (λ=0.82387 Å). The "B2" curve was obtained by fitting the B2 TiFe parameters from the ICSD data base to the TiFe experimental data. The lattice parameter α of each sample was obtained via automatic refinement of B2 TiFe parameters.

The grain size varies significantly between the samples, with for example Ti_2AlMo showing multiple ≈100 µm grains while Ti_2AlNb shows almost only a single grain over the whole ≈1 cm² sample surface. TiFe displays smaller grains, which are about 50µm in diameter, and Fe has even more refined grain structure 10-50 µm in diameter. No secondary phases were observed in Fe, Ni, and Ti_2AlNb. Cracking was observed near the Ti_2AlMo indents, however it is unclear whether these cracks appeared during indentation or later on sample manipulation.

Micro-indentations were performed on the samples with little regards for their proximity, focussing on targeting different grains. Some grains, notably in Ti_2AlMo and Ti_2AlNb, were indented several times in an attempt to diversify the statistics despite the small amount of available grain orientations. The proximity between indents is known to affect microhardness measurements, however it did not appear to affect significantly the resulting slip trace

patterns around them, and no major differences in the resulting statistics were later found for indents within the same grain. Rotating the indentation axis only marginally affected how contrasted some slip traces are from others, but did not fundamentally change the visible slip trace patterns; similar observations were also made in [3] and [91]. This means that only the change in grain orientation significantly affected the pattern of the slip traces and the resulting measured slip trace activity (which was confirmed through inspection of all the datasets). On a similar note, indenting close to, or on grain boundaries, which could affect a microhardness measurement, in our case helps diversify the slip activity statistics since multiple crystal orientations are stressed simultaneously.

A small number of ≈5µm wide titanium rich precipitates were observed in TiFe, and at the grain boundaries in Ti_2AlMo, as well as a Ti_2Fe phase in TiFe. There is debate as to whether Ti_2Fe is a stable phase within the Ti-Fe binary [103], it appears that trace amounts of oxygen >500 ppm can be sufficient to stabilise its formation. Such impurity may be present in the starting Ti sponge, or have occurred during the arc melting and encapsulation of the samples, for reference commercial Ti alloys typically contain 1500 ppm oxygen [103]. Those phases represent only a small area fraction of the sample surfaces and are much smaller than the indents, we can therefore consider that they will not affect most of the slip activity in the samples.

TiFe also displays darker contrast, similarly oriented precipitates, either very small or as large as the grains. These are thought to be hydrides formed during the sample preparation due to contact with water. TiFe is indeed also studied as a potential hydrogen storage material for its tendency to absorb hydrogen [104], see for comparisons well documented hydrides in Zirconium alloys [105]. The slip trace analysis was restrained to the monolithic B2 areas that were properly indexed as B2 TiFe and offered decent slip trace visibility.

Some pictures showed poor slip trace visibility, giving us doubts as to whether the code properly detected the slip traces, and were therefore ignored for the analysis. This concerned only a few pictures, either when very small grains were imaged in bcc Fe (low resolution/contrast of the slip traces), or in some contexts where large scratches networks were visible on the pictures, which can mistakenly be identified by the code as being slip traces. Note that these special cases are easily identified and eliminated from the analysis by looking at the code generated figures (e.g. see later figures in §3.4.2 and §3.4.3)). Also, most of these issues can be mitigated through thorough sample preparation (polishing and cleaning).

3.4.2 Validation on fcc nickel & choice of analysis input parameters

Before analysing the bcc and B2 samples of interest for slip behaviour, we must check that the code can perform an analysis on a simpler fcc system, namely nickel, where only 4 slip planes are activated, instead of the 45 different bcc slip planes.

To perform this validation, the code was adapted to predict the intersection of the four different fcc {111} slip planes with the sample surface based on the EBSD measured crystal orientation tested. The rest of the code remained unchanged, except this time the only case scenario we are interested in quantifying is whether the detected lines match one of the 4

predicted {111} plane orientations. A data set of 7 indent pictures, on 7 different grain orientation was tested. For comparison, a similar analysis was performed on the B2 TiFe sample (9 pictures in 9 different grains), looking this time at the frequency of {110} plane match as previous TEM reports in TiFe suggest <100> {110} slip systems to be predominantly activated at room temperature [62]. Both samples show very straight slip traces (see Ni on Figure 23, and TiFe on Figure 26).

We will use this data to study the influence of the main analysis parameters on the analysis output and get some insights on what parameter values to choose. These include:

- **the identification range, IR**: the maximum angular difference between a theoretical slip trace orientation calculated based on the EBSD data and the measured slip trace orientation to consider the theoretical slip plane type as a match (see §3.3.1.5).
- **the segmentation size N**: the picture is analysed as a succession of N*N pixels segments, with 3 lines detected in each segment (see §3.3.1.3).
- **the score threshold ST**: line orientations are tested through several conditions to attribute them a score S and distinguish those that are aligned with slip traces from those on random features, or detected due to errors (see §3.3.1.4). ST selects which line scores to include in the analysis, eliminating low scoring lines in the process (see §3.3.1.6).

As we are about to see, these three parameters affect the output of the slip trace analysis, and can influence each other. These give some flexibility in terms of parameters values we can use.

3.4.2.1 Score threshold & Segmentation size

We first study the effect of the change in score threshold for selecting which lines to include in the analysis, and how it interacts with the segmentation size N. Figure 23 (a) show a picture from fcc Ni at different stages of the automated slip trace detection process, and (b) an example of the lines detected and selected for ST = 0, ST = 6 and ST = 12 on this picture, using a segmentation size of 120*120 px, and a fixed IR of 10°.

Figure 23 (d) presents the output of the analysis for the whole data set, determined by calculating the proportion of detected lines matching {111} planes using an IR of 10° within each grain, and then calculating the average of this value between the grains, as a function of ST and N. By doing so, the same weight in the statistics is given to each grain tested, despite varying numbers of detected lines and unique slip trace orientations imaged. If the analysis works, it should be found that 100% of the slip traces, and therefore lines detected, match {111} plane orientations.

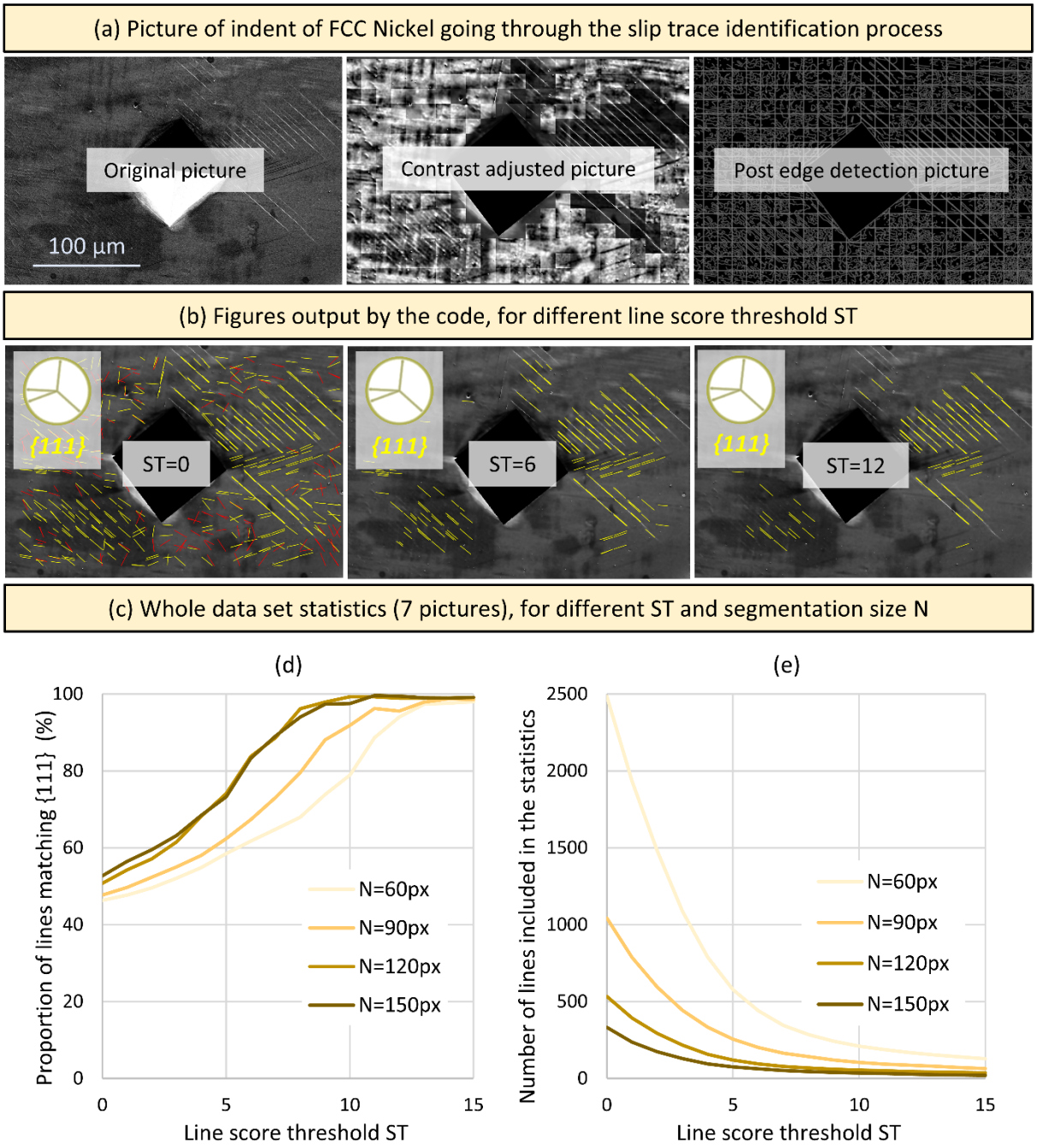


Figure 23: Showcasing the automated slip trace detection process on fcc Nickel. (a) Picture at different stage of the automation (b) Impact of the score threshold ST on what lines are selected for the analysis, lines matching {111} orientations are coloured in yellow, whilst lines that do not are in red. The theoretical {111} orientations for the grain orientation tested in this example are represented on these pictures. (c) Graphics including data from the 7 pictures analysed in the sample, the values presented are averaged between the pictures with (d) the proportion of lines matching {111} planes, for varying ST and N, and a fixed IR of 10°, and (e) the number of lines included in the statistics for varying ST and N.

3.4.2.1.1 Detecting slip traces and impact of ST:

Looking at Figure 23, the increase in score threshold ST, and therefore in the minimum score S of the lines included in the analysis, correlates with selecting lines aligned with slip traces for

all segmentation sizes. This can be seen from the pictures on Figure 23 (b), where the rogue line orientations present at low ST, which include lines not matching {111} planes (in red), disappear as ST increases, while the lines remaining at high ST are clearly aligned with the slip traces and systematically match {111} orientations. Also, looking this time at Figure 23 (d), and now considering all 7 pictures in the 7 grains tested, we see that the proportion of lines matching {111} plane orientations increases with ST, eventually reaching 100% for all segmentation sizes, suggesting that the signal/noise ratio is improved by increasing ST. The empirically chosen conditions for scoring are therefore demonstrated to give satisfactory results, showing that the code is able to automatically detect slip traces and separate them from errors in line detection, which was found to be true across all our samples. Note that, in the example of Figure 23 (b), this successful slip trace detection outcome was obtained despite the poor quality of the picture, which shows visible contamination and large scratches networks. The code is therefore expected to perform well at detecting slip traces in a large range of situations.

3.4.2.1.2 Other impacts of ST and N:

Figure 23 (e) represents the amount of lines considered for the analysis, as a function of N and ST, averaged between pictures. We see that increases in segmentation size N and score threshold ST both reduce the quantity of lines included in the analysis. This is expected since lines from noise get eliminated when ST increases, and the use of larger segmentation sizes results in less lines detected per picture. This change appears most significant for all segmentation sizes when ST increases from 0 to about 9, suggesting that this is the score range that most noise lines may reach, in agreement with Figure 23 (d). We also see that when a larger N is used, lines tend to reach lower scores, and less lines overall are detected and eliminated as ST increases (eventually reaching 0), and so care is needed as the scoring procedure risks losing discrimination power.

Increasing the line score threshold is overall beneficial, favouring signal over noise, up to the point where the number of lines detected becomes very low, as we risk reducing the variety of unique slip trace orientations detected. It should also be noted that the scoring procedure biases the detection in favour of long, straight slip traces, detected in large networks of multiple adjacent slip traces, over individual, shorter, or wavier slip traces. Therefore, the choice of score threshold is not universal and can be adapted depending on the imaging condition (amount of slip traces, visibility…) and if there are constraints on the segmentation size in our data sets.

Based on the data analysed here, we argue that we want to keep ST above 9 to guarantee sufficient noise filtering (although higher ST should be used for segmentation sizes <90px), whilst avoiding using large segmentation sizes if possible.

3.4.2.2 Segmentation size & identification range

The analysis (the code) was reapplied on the same data set for both the fcc Ni and the B2 TiFe samples, for varying segmentation size N and identification range IR. The score threshold was set to ST=12 (line score must be ≥12 for it to be counted in the statistics), visual inspection of the selected lines at this ST on the code generated figures suggested satisfactory slip trace

detection, although some marginal errors (noise lines) are still expected. The probability of matching each plane type due to chance alone, assuming a random line orientation, is calculated using 2500 code generated randomly oriented lines (see §3.3.1.8) for each grain orientations tested and IR used, it is then averaged between the grains to get an average probability for each IR. The results of this analysis are plotted in Figure 24.

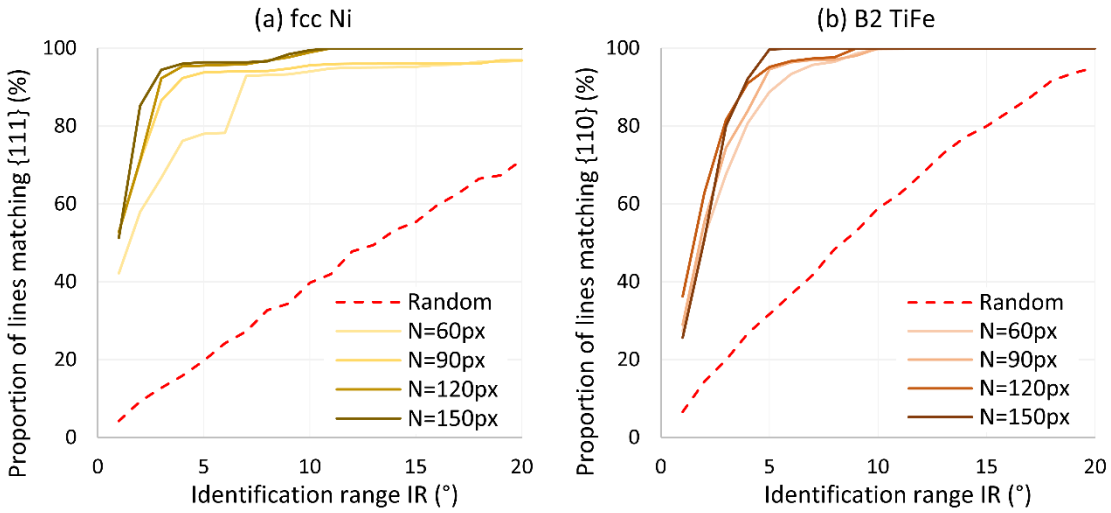


Figure 24: Proportion of detected lines matching {111} and {110} plane orientations in fcc Ni and B2 TiFe for different analysis parameters (segmentation size N and identification range IR). (a) Average proportion of detected lines in fcc Ni matching {111} per grain (b) Average proportion of detected lines in B2 TiFe matching {110} per grain. The "random" curve is obtained from comparing code generated random line orientations to the theoretical orientations of either {111} or {110} plane types in each grain tested.

3.4.2.2.1 Attributing the correct originating slip plane to a detected line

It can be seen on Figure 24 (a) that the code detected lines on the Ni dataset tend to match the expected {111} plane orientations more frequently than the randomly generated lines, reaching close to 100% of correct attribution as N and IR increase. A similar analysis can be done on Figure 24 (b), looking this time at the proportion of detected lines matching {110} planes in B2 TiFe, which reaches 100% as IR and N increase, more frequently than randomly oriented lines. These observations, that detected lines systematically match the expected slip planes in both samples, demonstrate that the code is a capable of attributing the correct slip plane to imaged slip traces, as long as correct analysis parameters IR and N are selected.

3.4.2.2.2 Influence of Segmentation size

It can be seen on Figure 24 (a) and (b) that using larger segmentation sizes increases the proportion of lines correctly attributed to their originating slip planes for most IR. This is expected since smaller segmentation sizes can induce imprecisions in the line drawing/line detection due to their inability to capture subtle changes in geometry as the amount of pixel reduces, which introduces discontinuities. Looking at this data, we see that N=90px presents significantly more misattributions than N=120px and above. We also observe that increase in segmentation size between N=120px and N=150px only marginally affected the outcome of

the analysis. In summary, the use of small segmentation sizes adds extra experimental uncertainty to the slip trace orientation measurement and a larger IR must be used to account for it, which can be detrimental to our conclusions as we are about to discuss.

3.4.2.2.3 Influence of Identification range IR:

In literature, typical manual slip trace analysis on bcc usually take 5° as identification range [17] [32], accounting mainly for experimental uncertainties surrounding EBSD determined crystal orientations, and we could arrive to a similar conclusion here. On Figure 24 (a), at 5° IR, more than 95% of detected lines detected in fcc Ni are properly attributed to {111} for N ≥ 90px. The same analysis can be made looking at the data from B2 TiFe on Figure 24 (b), with more than 95% {110} match for N ≥ 90px at 5° IR. However, as we are about to see, a larger IR may be used to increase our confidence that lines are properly associated to their corresponding slip plane types, without necessarily impeding the analysis.

Figure 25 represents more probabilities of matching as a function of the IR, calculated from randomly oriented lines and using the 9 grain orientations tested in the TiFe data set, for every bcc plane type and additional conditions, including: matching no plane ("no match"), matching only {100} planes ("<100>"), or matching only {112} and/or {123} planes ("<111>"). Note that these probabilities are independent from the sample actual slip activity and depend solely on the IR and the grain orientations considered. Each of these conditions are of interest for bcc and B2 slip trace analysis (as discussed in Chapter 1). The proportions of match can be interpreted as "probabilities of fitting a condition", assuming a random line orientation, and are given with a standard error of at worse 1% for P=50% (§3.3.1.8).

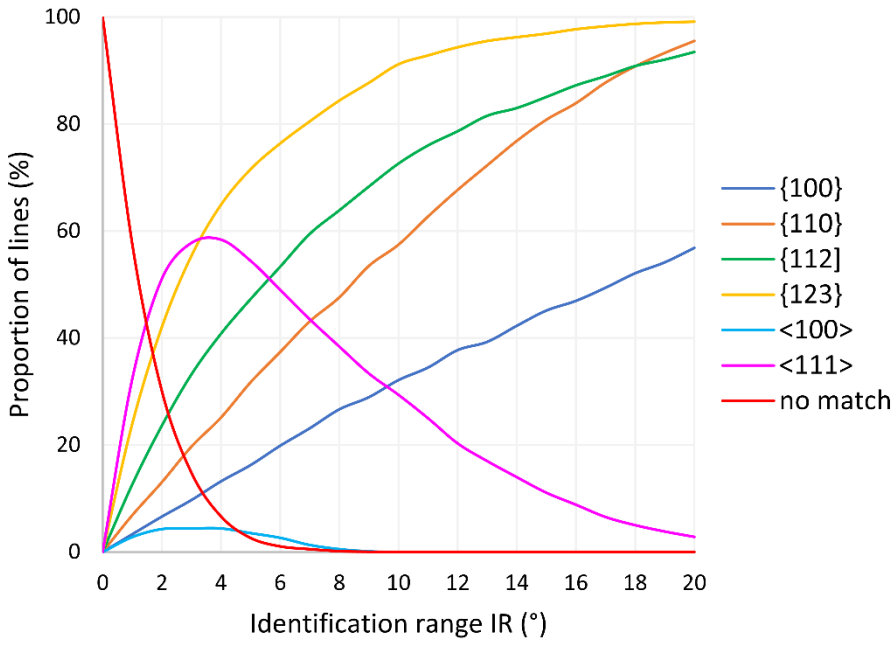


Figure 25: Additional data from randomly generated line orientations showing the average proportion of these lines, using the 9 grain orientations tested in B2 TiFe, that match each condition of interest for bcc and B2 slip trace analysis, including: matching each bcc plane type orientations, being unambiguously <100> (i.e. match only {100}) or <111> (i.e. match only {112} and/or {123}), and to match nothing.

As can be seen Figure 25, based on the grain orientations tested in TiFe, it is extremely unlikely (<5% chance) to observe unambiguous <100>{100} slip if they exist, even for IR lower than 5°. This means that it will be very difficult to find unambiguous evidence of the presence of <100> type slip in our samples in general. One reason for this is that we are considering the possibility of slip on <100> {100} and <111> {112} {123} slip systems simultaneously, and the large amount of the <111> exclusive plane type (36 distinct orientations) means that {100} type slip traces are likely to be ambiguous with their orientations. It could be argued that {123} planes should not be considered simultaneously with {100} since, to our knowledge, there has been no report of a B2 compound able to slip on both plane types simultaneously, and {123} planes are rarely even brought up when it comes to B2 slip activity. However, in this work, we prefer choosing the neutral option of considering both possibilities as {123} planes are often – maybe unfairly – put aside when studying the micromechanics of bcc alloys.

Let us now consider the choice of IR, specifically whether it should be kept as low as 5°. As the IR increases, the probability to randomly match any plane type, and therefore to be ambiguous, increases, meaning that observing a plane type match loses statistical power: observing a {110} match in a context where we have 20% chance of making this observation by accident represents more evidence in favour of the existence of such slip plane than if there was 90% chance of making this observation by accident. In the context of this work, we will not be performing in-depth statistical analysis and what we need more than statistical power is to be almost certain that the slip traces we detect match *at least* their originating slip plane type orientation, whilst allowing to not match other unrelated plane types. Indeed, it should be noted that we are looking at a limited data set, consisting of very straight slip traces, and it is unknown whether more experimental variability will be observed on different and larger data sets, e.g. what will happen when wavier slip traces will be present. Waviness of slip traces may introduce extra mismatch between theoretical and measured slip trace orientations that have not been observed on the two samples tested here, and therefore require the use of a larger IR.

In the context of differentiating B2 slip behaviours, we want to reduce the risk of observing lines unambiguously <111> by accident (e.g. due to an underestimation of experimental uncertainties) as those will be one of our main arguments to distinguish the different samples slip activity. This case scenario being equivalent to the probability of not matching {110} and {100} planes, the probability of observing such lines by accident decreases as IR increases, as can be seen on Figure 25 when looking at the "<111>" curve: observing such unambiguous <111> type lines, in the context of a larger IR, becomes even stronger evidence for the presence of <111> type slip, since those line orientations have to be even further from any {110} and {100} plane orientations.

In conclusion, although this sacrifices the (already meagre) chance of observing unambiguous <100> type slip, an IR >5° should be picked, to gain safety margin for experimental variability across different data sets, and strengthen the evidence brought by unambiguous <111> type slip traces. IR will be kept low enough to leave a (qualitatively) reasonably large probability of clearly identifying unambiguous <111> type slip, and to avoid situations where some plane types, in particular {110} and {112} planes, have a probability of being matched by accident

close to 100%. Note that in principle, as long as these probabilities are not exactly 100%, or 0%, it should be statistically possible to make unambiguous observations (e.g., see a slip that is clearly not a {110} plane). However, the quantity of grains which need to be analysed before such unambiguous observations are made may rise asymptotically as we get closer to 100% or 0% chance of matching.

3.4.2.3 Conclusion, choice of analysis parameter

From the data gathered and studied on fcc Ni and B2 TiFe, we see that a range of parameters can be used to reach correct slip trace detection and plane type attributions, each with pros and cons in their selection, but giving us flexibility for future analysis and additional experimental constraints. To summarize the main constraints relevant to the present work, and that will likely apply to most experimental situations, we have:

- The segmentation size, N, should be > 90px to avoid introducing unnecessary inaccuracy in line orientation detection, but it should be kept as low as possible to help the detection of wavy slip and increase the efficacity of the scoring procedure. Smaller segmentation sizes than 90 may still be used but only if combined with a larger IR.
- The score threshold, ST, should be ≥ 9, but not too large or we risk to unnecessarily erase useful data. Segmentation sizes smaller than 90 may require a larger ST to be used.
- The identification range, IR, should be at least 5° to guarantee close to 100% of correct plane type attribution (= the originating plane of the associated slip is within IR degrees), but it should also be kept low enough to leave a reasonably high probability of observing unambiguously <111> type slip, and leave some chance of not matching the different bcc plane types of interests (Probabilities<100%).

Based on these criteria, for our analysis of the BCC and B2 samples in this paper, we selected N=100px, IR=10° and S=10, as those should guarantee a good quality of slip trace detection and plane type identification in our samples and allowing to distinguish key bcc and B2 slip activities. In particular, the use of a “large” IR of 10° gives us some safety margin for possible unforeseen experimental variability, and increases our confidence that lines detected on slip traces properly match their originating plane types.

3.4.3 Slip Trace Code Application to bcc and B2 samples

To evaluate the deformation behaviour of bcc and B2 samples, the newly developed code was used to analyse pictures of indents and areas surrounding indents from B2 TiFe, Ti_2AlMo, Ti_2AlNb and bcc Fe, specifically to differentiate between their dominant operating slip systems. This section of the paper should be seen as a tutorial, giving an example scenario of how the code can be applied, and how to interpret the data gathered from the automated slip trace analysis.

A dataset of 8 to 17 pictures and associated Euler angles were collected and analysed for each sample, representative examples of the quality of the slip trace detection in each are shown on Figure 26. Pictures visually showing poor slip trace contrast or located in grain orientations poorly indexed during the EBSD mapping were ignored. Where several pictures were made within the same grain, the lines detected on each separate picture were summed to get the

total statistics for this grain. A score threshold ST=10, segmentation size N=100px, and identification range IR=10° were chosen for every sample, as these should guarantee that close to 100% of the lines counted for the analysis are aligned with slip traces and properly match their originating plane type (see §3.4.2.3). For ST=10, two of the imaged grains in bcc Fe had no lines reaching this score due mainly to the small grain size, and were therefore excluded from the analysis leaving 15 of the 17 imaged grains to be analysed. Only one grain orientation was tested for the Ti_2AlNb sample due to large grain size, however, 8 indents at different rotations were made in this sample, and many unique slip trace orientations were visible in the pictures (see Figure 26 (b)). Therefore, even though the data shows only for a single orientation, it is still expected to be indicative of the sample's slip behaviour.

The statistics obtained for all lines detected with a score $S \geq 10$, in terms of percentage of lines matching a given plane type, or fitting the unambiguous <111> condition by matching exclusively {112} and/or {123}, per sample and grains, are presented as box plots in Figure 27 (a). In addition to this analysis, 2500 randomly oriented lines were generated by the code (see §3.3.1.8) and compared to the same theoretical slip trace orientation for each sample and grain orientation tested. Figure 27 (b) shows the statistics obtained from these lines, giving an estimation of the probability to match each plane type or condition by chance alone in these grains, with an uncertainty ≤ 1%.

Note that the proportion of lines matching exclusively a single plane type have not been represented in the graphics, as they have close to 0% chance of being observed for most grain orientations (almost all slip traces are ambiguous), this includes {100} planes. However, we are likely to observe lines matching exclusively {112}, {123}, or both plane types, giving direct, unambiguous evidence of an active <111> slip direction in the samples concerned, those lines are noted "<111>". Also note that reducing experimental uncertainties (allowing for IR<10°), or making more assumptions (e.g. ignoring the possibility of {123} slip) in future experiments may allow the observation of more special "unambiguous" cases.

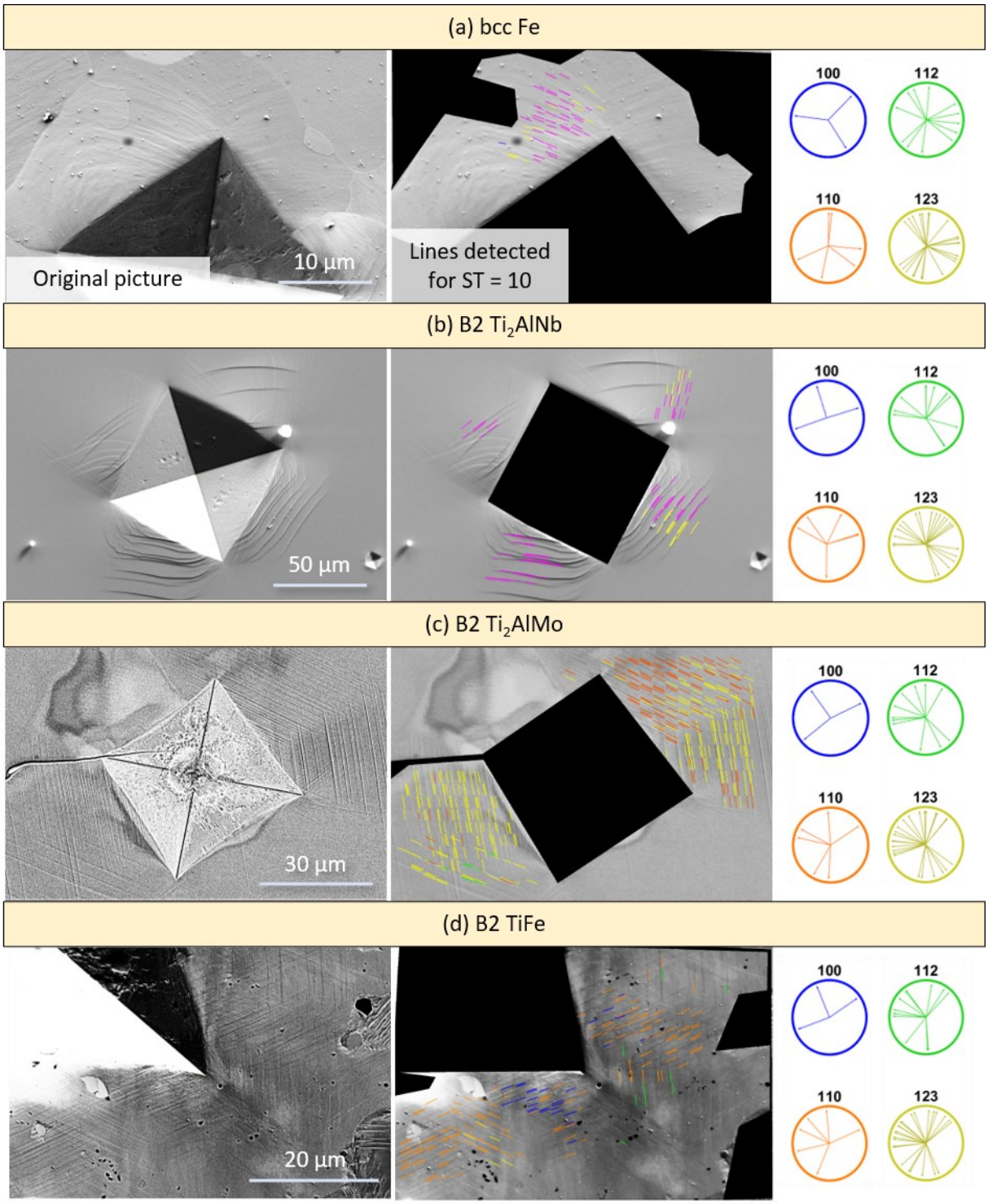


Figure 26: Code output, showing typical results for each sample. The lines represented have a score ≥ 10 (see §3.3.1.4) and are drawn at the position they were detected, in the colour of their closest matching theoretical plane type orientation, or in magenta if they are unambiguously <111> (= match {112} and/or {123} exclusively). The theoretical slip trace orientations, calculated from the average grain orientations measured where each picture was taken, are represented on the right side of the figures. The black areas on the pictures are areas manually masked before the analysis because they contained the indent and/or large miscellaneous features such as other grains (see §3.3.1.2).

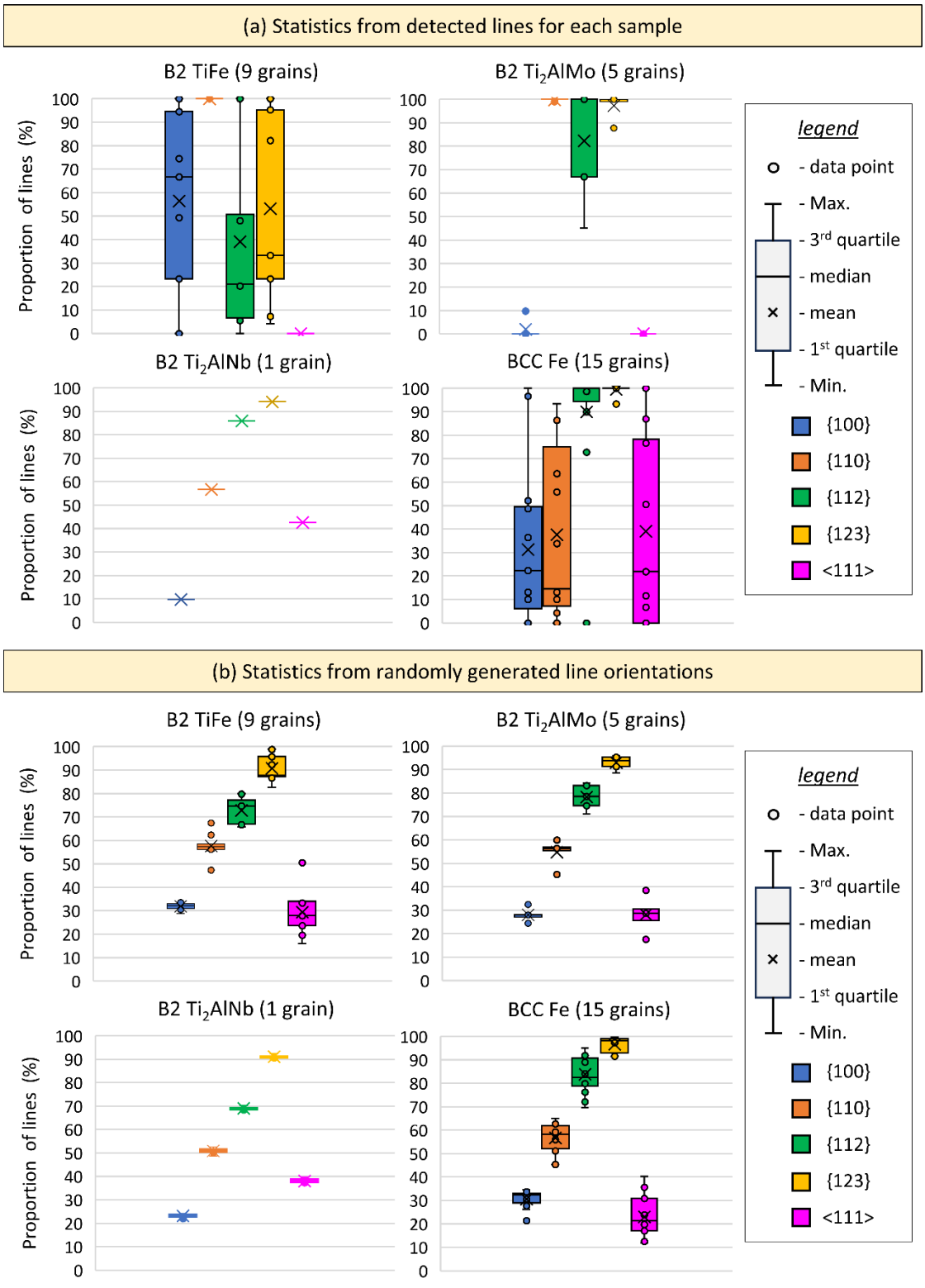


Figure 27: Outcome of the automated slip trace analysis on each sample. (a) Proportion of detected lines matching each condition, per grain (b) Proportion of code generated randomly oriented lines matching each condition, per grain. "<111>" refers to lines matching exclusively {112} and/or {123} plane orientations, whereas e.g. {110} refers to lines matching at least one {110} orientation. The "Max." and "Min." values are defined as the max. or min. data points ≥ or ≤ to 1.5*IQR+Q1 or 1.5*IQR+Q3 respectively, with Q1 the 1st quartile value, Q3 the 3rd quartile value, and IQR = Q3-Q1.

3.4.3.1 Qualitative observations

Before going deeper into the statistics, we can observe a first distinction between the samples from looking at the slip traces, as shown on Figure 26. Bcc Fe and Ti_2AlNb both display large numbers of curved and wavy slip traces, whilst TiFe and Ti_2AlMo show mostly straight slip traces. Wavy slip is often associated with cross slip and good sample ductility, which is more likely to happen if large numbers of independent slip systems are available for deformation. We also observe visible cracks around some Ti_2AlMo indents suggesting less ductile behaviour [106], although some curved slip traces are marginally observed in this sample. This qualitative distinction between ductile versus brittle was also observed when preparing the powders for diffraction measurements as the Ti_2AlMo and TiFe samples were easily crushed and milled into powder whilst Ti_2AlNb was significantly more ductile, which is testified by the larger SXRD peaks of the latter (§3.4.1 Figure 22) imputable to more lattice strain accumulated in the powder during preparation.

A sample slipping on <111> {112} and/or <111> {123} is expected to show greater ductility and more unique slip orientations due to the larger amount of available slip systems. These observations give a first argument to characterise the slip activity in our samples: bcc Fe and Ti_2AlNb show a larger amount of slip orientations, consistent with available slip systems of <111> {112} and/or {123) type, whilst TiFe and Ti_2AlMo show more restrained slip activity, consistent with the absence of high order slip planes.

3.4.3.2 Randomly generated lines & preliminary statistical considerations

Randomly oriented lines were generated and compared to the calculated theoretical slip plane orientations for each grain tested in each sample (2500 orientations per grain, see §3.3.1.8), they went through the same plane matching process as the lines detected on the samples, using the same IR=10°. The statistics obtained from these randomly generated lines have two uses. Firstly, if something in our experiments went wrong, e.g. if the crystal orientation entered are wrong or if large quantities of the lines counted are not aligned with slip traces or misattributed, it is expected that the sample statistics will end up similar to the randomly obtained statistics (this is typically what happens if we use a low score threshold ST and do not eliminate noise lines, see §3.4.2.1). Secondly, the statistics obtained give an approximation of how likely it is to match the different plane types, or to observe lines fitting special conditions (e.g. being unambiguously <111>) by chance alone in the grain orientations tested. This allows to check if some samples data sets are biased towards certain results due to the grain orientations tested.

The full statistics for the randomly generated lines, per sample and per grain orientations tested, are represented as box plots in Figure 27 (b). The box plot representation is very useful for qualitatively comparing data set, and represents the mean, median, first and third quartiles (ends of the box), and an estimation of the variability of the measurement across the data set (min. and max. values), it also highlights any outliers (data points outside the notches). These boxes were calculated using inclusive medians since all data sets have odd numbers of data points. Some outliers are observed, notably in bcc Fe, likely to be the result of the small size and high variability of the data: the measurement per grain oscillates between 100% of match

or 0% of match when very little unique slip orientations (e.g. 1 slip orientation) are measured in each grain, which happened frequently in bcc Fe due to the small size of the grains.

It can be seen of Figure 27 (b), as expected, that there is some variability in the proportion of slip planes or specific criteria matched by the randomly oriented lines between different grain orientations within a sample, which means that some grain orientations can be more favourable to the observation of certain matches than others. For example, in the TiFe data set, the probability of observing a line unambiguously <111>, supposing a random line orientation, varies from 20% to 50% chance depending on the grain orientation tested, with on average close to 30% chance across the data set. This highlights the need to consider these probabilities every time a new data set is tested as those can artificially affect the proportions of matches we observe.

These probabilities appear to be similar when comparing sample to sample (similar box plots), except for a slightly higher average probability of matching {123} planes for bcc Fe, which means that, due to the grain orientations tested (random chance), we are likely to observe more of these matches in this sample. Apart from that, the grain orientations tested are not biasing the statistics of the samples in favour of any specific, distinct slip activity, e.g. by favouring {110} matches: the data sets should be comparable.

One final point we need to make is that the statistics from randomly oriented lines, in terms of average proportion of lines matching the different plane types, is very similar to the statistics obtained from the analysis of the detected lines on B2 Ti_2AlNb and bcc Fe. Should we therefore conclude that these two samples measured slip activities are the result of errors in the technique, and sheer random chance? The answer is, statistically, we cannot know for sure.

When we expect a large variety of slip planes to be active in the samples, and add to those experimental variabilities (e.g. here wavy slip traces), the measured slip activity is expected to end up similar to the statistics from randomly oriented lines. Let us take for example bcc Fe. From literature [45] we expect {110}, {112} and {123} slip planes to have similar critical resolved shear stresses in this material, which means that under a random applied stress, we expect them to be activated proportionally with their respective amount of unique slip systems i.e. 12/48 {110}, 12/48 {112}, 24/48 {123}. In comparison, randomly oriented lines are expected to match the different plane types proportionally with their respective amount of distinct slip planes, i.e. 3/45 {100}, 6/45 {110}, 12/45 {112}, 24/45 {123}. If we express these as percentages we get:

(1) Expected bcc Fe slip activity: 0% {100}, 25% {110}, 25% {112}, 50% {123}

(2) Expected random error “slip activity”: 6.7% {100}, 13.3% {110}, 26.7% {112}, 53.3% {123}

As we can see, the expected proportions (1) and (2) are very similar, and if we add to that the ambiguity in plane type identification, the large variability of the data, and the little amount of unique grain orientations tested, we end up in a situation where it will be difficult to find statistically significant differences between a “random” behaviour, and the measured slip activity of bcc Fe. This reasoning can also apply to B2 Ti_2AlNb, if we assume that a mix of {110}

and {112} planes are active in this sample ([66] also suggest some active {123}). More data must be gathered, and a more complex statistical analysis must be performed to allow such distinctions, which goes beyond the scope of this work, and is the object of Chapter 5.

In the meantime, what we can say is that the statistics obtained on these two samples are the result of the analysis of lines detected on mostly straight slip traces (which can be validated visually, see Figure 26), performed in similar conditions, and using the same equipment as TiFe, Ti_2AlMo and fcc Ni (fcc Ni discussed in §3.4.2). These three samples present clear characteristics separating them away from a random slip orientation behaviour and therefore any errors in the analysis, with TiFe and Ti_2AlMo found to match {110} planes 100% of the type, and fcc Ni matching {111} planes 100% of the time. This means that apart from their similarities to randomly oriented line statistics, we have no reasons to think that the analysis did not work on bcc Fe and Ti_2AlNb.

3.4.3.3 Slip trace detection & statistics per sample

These preliminary statistical considerations showed that the comparison of the data sets between the samples should not involve significant grain orientation related biases. Figure 27 (a) shows how frequently each plane type was matched by the lines detected in each sample, per grain, and how frequently lines were unambiguously of the <111> slip direction type, meaning that they match exclusively {112}, {123} or both plane types.

Bcc Fe and B2 Ti_2AlNb show similar statistics (Figure 27 (a)), with on average close to 40% of the detected lines in each grain being unambiguously <111>. This means that we have substantial evidence of the presence of an active <111> slip direction in these samples. As for the active plane types, slip must be taking place on either {112} and/or {123} planes, but may also be taking place on {110} as all three plane types are frequently matched with the lines. These results are consistent with the expected slip activities of bcc Fe [45], and of Ti_2AlNb [66], as well as the apparent ductility of these samples (see §3.4.3.1).

Looking at the data from B2 TiFe and B2 Ti_2AlMo (Figure 27 (a)), it can be seen that 100% of the detected lines, in all grain orientations tested, match {110} plane orientations, which is clearly different to the statistics obtained in Fe bcc and Ti_2AlNb, suggesting fundamentally different slip behaviour. The present data suggests, indirectly, that TiFe and Ti_2AlMo slip exclusively on {110} planes. A more complex statistical analysis is required to measure how strong the evidence in favour of this hypothesis is, which will be the topic of a different work (Chapter 5). In the meantime, we can stress that roughly 18 unique slip trace orientations were analysed in TiFe, and 10 in Ti_2AlMo, of which all matched {110} plane type orientations, in a context where randomly oriented lines match these orientations only about 55% of the time. We know that slipping exclusively on {110} plane, whether it is <100> {110} or <111> {110}, is commonly reported for B2 slip activities, so we can reasonably say that the data presented supports this hypothesis for TiFe and Ti_2AlMo. This conclusion is also consistent with previous reports of <100> {110} slip in TiFe [62]. However, we cannot unambiguously determine the active slip direction <100> vs <111> in these samples.

On a similar note, we see that in bcc Fe (Figure 27 (a)), close to 100% of slip traces match {123} planes. However matching a {123} plane is very likely to happen by accident in this sample

(close to 95% chance), therefore, this observation alone should not be considered strong evidence in favour of a {123} slip activity in this sample, nor the relative frequency statistics {110} vs {112} vs {123}.

Many more comparisons can be made between the different plane types, and one may be interested in other plane types than the ones we have discussed. Let us take a last example to see the reasoning we can apply without extensive statistical analysis.

***Example**: differences in {100} plane match fractions between TiFe and Ti_2AlMo*

We notice on Figure 27 (a) that the proportion of lines matching {100} plane type orientations in B2 Ti_2AlMo is much smaller than in B2 TiFe, on average 2% and 58% respectively. This tempts us into thinking that there may be evidence of active {100} planes in B2 TiFe, as opposed to none in B2 Ti_2AlMo. Should we conclude, from this data, that the two samples have different slip activities? No, and that is typically where the notched boxes representation becomes useful. We see that many of the grain orientations tested in B2 TiFe show no {100} match, leading to overlapping notched boxes from the two samples: overlapping notched boxes can be interpreted as "a compatibility between data sets" as in it is plausible, from a statistical point of view, for both data sets to be obtained from the same sample behaviour. We can explain the difference between the two data sets by the small amount of data gathered and random statistical variability. An appropriate interpretation of this difference in {100} match fraction would be: "TiFe could be slipping a portion of the time on {100} planes, but no substantial evidence supporting the possibility of {100} slip was found in Ti_2AlMo. Both samples can have similar slip activities regarding {100} planes, including no {100} slip at all since no unambiguous {100} slip was observed, which is consistent with the idea that they slip close to 100% of the type on {110} planes".

From the few observations concerning the proportion of {110} plane match, and of unambiguously <111> type slip, we already have some interesting insights on the samples slip activities, and have gathered evidence supporting some key bcc and B2 slip activities for each, namely operating <111> {112} and/or {123} slip systems in bcc Fe and Ti_2AlNb, as opposed to slip exclusively on {110} planes for TiFe and Ti_2AlMo. This data was gathered from simple and quickly obtained experimental work involving: a few microhardness indents (checking multiple grain orientations are tested) ~10 min, good quality SEM images of the slip traces ~1h30 min, and a coarse EBSD mapping of each sample ~30 min, totalling 2 to 3 hours of experimental work. The previously time-consuming part of slip trace analysis, the slip trace identification and plane type matching, is now mostly automated and takes less than 15 min per sample, which unlocks indentation as a simple way to perform micromechanical testing on bcc and B2 compounds. However, the data gathered can be misleading and its analysis requires good knowledge of the influence of code related analysis parameters and underlaying statistical behaviour.

3.5 Summary

In this chapter, we presented a new approach for indentation-based slip trace analysis using an automated line detection algorithm. Different B2 and bcc compounds thought to exhibit a variety of slip activities were prepared, including B2 TiFe, B2 Ti_2AlMo, B2 Ti_2AlNb and bcc Fe, as well as an fcc Ni sample for validation. They were characterised using SEM and EDX analysis, then microhardness indented. EBSD was performed on each sample to determine the crystal orientation around the indents, and the slip traces in these areas imaged using SEM. Finally, the pictures were analysed using our newly developed code, determining the likely slip activities for each sample. The key findings of this study are the following:

- The methodology offers a high throughput slip trace analysis approach in hours rather than days/weeks, and with dramatically increased statistics compared to TEM or micropillars: <10 min for 10 indentations, <2h to perform a coarse EBSD mapping + image slip traces, <15 min for the code to run.
- The slip trace characterisation by the code correctly captures fcc Ni <110> {111} slip behaviour, which was used to determine the code key variable analysis parameters.
- The slip behaviour of bcc Fe, B2 TiFe, B2 Ti_2AlNb and B2 Ti_2AlMo were evaluated. Bcc Fe and B2 Ti_2AlNb showed substantial evidence of active <111> {112} and/or {123} slip systems, while B2 TiFe and B2 Ti_2AlMo showed data consistent with slip predominantly on {110} planes.
- The slip activity for bcc Fe, B2 TiFe, and B2 Ti_2AlNb are consistent with literature, while new insights have been gained as to the slip activity of Ti_2AlMo helping to explain its apparent brittleness.
- Further work includes the use of more complex statistical analysis to evaluate the contribution of competing active slip planes to the overall deformation behaviour and allow the identification of bulk bcc and B2 slip activities from indentation-based slip trace analysis (Chapter 5).

4 Evaluation of B2 intermetallic deformation behaviour using diffusion gradients and indentation-based slip trace analysis

4.1 Abstract

Differences in slip activity of ordered B2 intermetallic compounds are critically responsible for drastic changes in their mechanical properties, with <100> slip activity usually associated with high strength and poor ductility, while ½<111> slip activity usually allows for better ductility. This problem is especially important in the development of dual-phase bcc + B2 'bcc-superalloys', as it also affects slip transmission mechanisms between the phases, which if restricted can cause embrittlement. In this work, we investigate the effect of changes in compositions on the slip activity between <100> dominated NiAl and <111> dominated FeAl. A monolithic B2 composition gradient between 60Fe-40Al and 60Ni-40Al was prepared, and microhardness indents of small ≈0.02 kg load made across it. SEM imaged slip traces outside, and uniquely, inside the indents, were analysed using our recently developed automated slip trace detection algorithm. From this experiment, we show evidence of a transition in active slip direction from <111> to <100> at about 20-25Ni (at%), based notably on the unambiguous observation of <111>{112} and/or {123} slip in the 10-25Ni (at%) composition range. The data obtained is in very good agreement with previous observations from literature including TEM work on this composition range. The methodology proposed is much cheaper, time efficient, and easier to perform than conventional TEM or single crystal micro-testing. It also offers continuous, quantitative information on the transition regime, which unlocks a new kind of data for crystal plasticity models based on experimental slip behaviour for improved predictive behaviour.

4.2 Introduction

Bcc elements tend to display higher melting points than fcc metals. Recent attempts to exploit this property include the development of bcc+B2 'bcc-superalloys", which take inspiration from nickel superalloys γ + γ' structure by combining a disordered bcc matrix with ordered B2 intermetallics. When designing these new dual-phase systems, an understanding of the mechanical properties & behaviour of each component phase is required, in particular because different slip activities may occur between the two-phases.

Bcc alloys are generally considered to display <111> type slip, however, the character of their active slip plane is more controversial, but is commonly considered to be shared between {110}, {112}, and {123} plane types [38]. Ordered-bcc B2 compounds can display much more significant differences in their slip activity, with some compounds favouring <111> type slip while others favour <100>. Having <100> as active slip direction offers a very limited number of slip systems, due to <100> only being able to glide on {100} and/or {110} planes, which can limit ductility. When there are different active slip systems in the phases of a dual-phase alloys, dislocations are forced to change slip system at their interface, e.g. to propagate from <111> matrix to <100> precipitates. This mechanism may lead to situations where pile-up or by-passing mechanisms are preferred over precipitate cutting, leading to strain accumulation at the interface and possible embrittlement of the alloy [29] [107].

In the context of designing dual-phase bcc+B2 bcc-superalloys, the main factor limiting their advancement is often their lack off room temperature ductility. The design idea, from a slip direction point of view, would therefore be to have an intermetallic reinforcing phase also slipping in the <111> slip direction at RT, rather than <100>, favouring dislocation motion between the <111> slipping bcc matrix and the B2 precipitates via common active slip systems. Then if at high temperature <100> gets increasingly favoured in the intermetallic, which was reported to happen in FeAl [108], it could participate in impeding dislocation motion, improving high temperature strength and creep performance.

The ordering and bonding of a B2 compound plays a key role in the slip direction behaviour. Due to this ordering, a ½<111> dislocation creates an anti-phase boundary (APB), which raises the energy cost of this deformation path. This can lead to some compounds preferring <100> as an elementary displacement to avoid APB formation, despite the increased length of burger vector, and at the cost of restrained deformation options. Note than multiple material parameters are thought to control the active slip direction of B2 compounds [56].

This ordering energy is affected by the compound, stoichiometry, and the presence of alloying elements, which raises the question: what if could we could tailor, via alloying, the composition of B2 compounds to control their active slip direction? The impact of composition on slip activity of B2 compounds has been reported extensively in the review of I. Baker [55] and M. Yamagushi et. al [37]. As examples, in [61] were compared the slip activity of compounds in the B2 CuZn-NiZn composition range, and it was shown evidences of changes in slip activity as a function of the composition, from predominant slip on {110} at the binary CuZn composition, to predominant slip on {112} at the intermediate Cu-(14)Ni-(48)Zn (at%) composition. Another experiment studying the evolution of slip activity was a study by D. K.

Patrick et. al [108], in the B2 FeAl-NiAl system, surveyed through transmission electron microscopy (TEM). Evidence of an evolution of the slip activity was found at room temperature, with a transition from <111> to <100> type slip somewhere between 10 and 30 Ni at.%. This process of investigating a series of samples with TEM or single crystal testing are very challenging experiments: they require the preparation of multiple samples with the desired compositions, their mechanical deformation in consistent manners, and in the case of TEM, the difficult extraction of TEM foils followed by painstaking dislocation analysis. As an illustration of the difficulty it poses, in their TEM experiments [108], out of the 12 conditions they tested, 3 samples could not be analysed (due to breaking, or absence of visible dislocations), meaning that 25% of the data they tried to gather is missing. Also, despite the essential insights this experiment provided, the wide step between compositions of 10% Nickel content leaves a large composition range gap between 10 and 30% Ni where the transition of slip direction could be happening.

Bcc-superalloys based on many systems: Ti-TiFe [2], Fe-NiAl [29], Cr-NiAl [26], Ta-TiRu [27], Nb-PdAl [109], and refractory high entropy superalloys (RSAs, e.g. NbTaVTiZrAl [110] [53]) create a multitude of candidate B2 reinforcing phase compositions, with the understanding of slip system character of these still in its infancy. The object of our work is to present a new, more accessible, and high-throughput methodology for assessing this kind of composition dependant evolution of the slip activity, in hopes of using this data for on-going bcc + B2 alloy development. To this end, we will make use of the composition gradient approach [111], combined with our recently developed automated indentation-based slip trace analysis (see Chapter 3). The new methodology we propose offers a much higher composition resolution than previous TEM and single crystal testing-based experiments, giving access to a quasi-continuous information on the slip activity as a function of the composition.

4.2.1 Composition gradient exploration

Composition gradients can be obtained by heat treating samples of distinct compositions that are placed in contact, allowing diffusion of elements between them, which allows to access a continuous range of composition in a defined alloying system [111]. This approach can be used to appraise phase stability [112], strain hardening [113], solid solution strengthening [114], and various other material properties [115] as a function of the composition. Extending from this, an idea would be to investigate the evolution of slip activity across such gradients. To do that, we need to address two challenges:

- How do we deform the material locally, at specific compositions, across the compositionally graded sample so to make sure that the deformation observed can be associated to the measured composition?
- How do we detect, analyse, and quantify that deformation, and do so in a time and resource efficient manner?

To deform the material locally, a first idea would be to perform an array of micropillars across the composition range and nano-indent them, this would help guarantee a localized deformation observation. However, this involves a challenging experimental procedure, including a very long Focussed-Ion-Beam (FIB) micropillar preparation (although, Plasma Fib

could be used to do that more efficiently [116]), and repeated nano-indentations which are both delicate equipment to manoeuvre, requiring skilled experimenters, and are usually very expensive. An alternative, much simpler and accessible, would be to perform indention-based slip trace analysis across the gradient, using small micro-hardness indentation loads to achieve localized deformation, the possibility of which is investigated in this work.

4.2.2 Automated indentation-based slip trace analysis

In our recent work (Chapter 3) we have demonstrated that the slip direction of a B2 sample, in particular the presence of <100> {100} {110} or <111> {110} {112} {123} type slip can be evidenced by using automated indentation-based slip trace analysis. The technique developed can be used to determine the likely active slip planes in a sample from the analysis of SEM pictures of slip traces, in areas of known crystal orientation (EBSD determined), that surround microhardness-indents. It involves notably an automated slip trace detection algorithm, using Hough transform based line detection, and scoring of the detected lines based on how likely they are to be aligned with slip traces, and gives control on the signal to noise ratio by eliminating lines detected on miscellaneous features (e.g. phases, contamination, scratches, etc). The main interest of this approach is that it gives access to a more statistically quantitative information than TEM or micro-compressions, and the automated slip trace detection process is more repeatable (less prone to manual variability and experimenter bias) and is much faster than manual slip trace identification.

The measurement output by the code is a proportion of lines matching each plane type, or unambiguously matching a <111> type slip orientation, i.e. {112} and/or {123}, which can be given per picture, per grain, or per sample depending on which statistics we are interested in. A key point to emphasis is that slip trace orientations detected using this approach are very often ambiguous, in that they cannot necessarily be attributable to a single originating plane type (e.g. a given {110} slip may overlap with a {123} orientation, and many other combinations). However, the large statistics allow inference of key distinct slip activities, for example if a sample slips systematically on {110} planes we expect to find that 100% of the detected lines match {110} planes (which was true for B2 TiFe and Ti_2AlMo, see §3.4.3.3). It is also possible to frequently identify lines matching exclusively {112} and/or {123} planes when such slip planes are active, which gives unambiguous evidence of active <111> type slip in the sample as only this slip direction allows for slip on these planes.

In this paper, we will apply this technique to a B2 FeAl-NiAl composition gradient in order to study the evolution of slip activity across its composition range, and in particular compare our experimental results to the TEM work of D. K. Patrick et. al [108] on the same system. Another interest of studying this system is that B2 NiAl and B2 FeAl are common intermetallics which present interest for on-going development of bcc+B2 RSAs and bcc-superalloys (e.g. [31] [26]). A particularity of this experiment is that we will be performing the slip trace analysis *inside* the indents, rather than on slip traces *outside* the indents which is very unusual as far as indentation-based slip trace analysis is concerned. This choice will be discussed, and the validity of the experiment demonstrated in section §4.4.2.

4.2.3 Evidencing a slip direction transitions with indents

A key limitation of indentation-based slip trace analysis is that we do not know the slip direction from looking at the slip traces (although, this could be by-passed using DIC [89]).We can, however, deduce the slip direction from the slip planes observed in specific unambiguous contexts. Let us see how this logic applies to the context of a B2 FeAl-NiAl diffusion gradient.

In our previous work (Chapter 3), we were able to gather strong evidence supporting that B2 TiFe slips exclusively on {110} planes, whilst bcc Fe showed unambiguous evidence of active <111>{112} and/or {123} slip systems. We noted that the technique has limitations: Firstly, {112} and {123} planes are difficult to tell apart due to the similarities in their geometries and the experimental uncertainties, which make them likely to be ambiguous with each other. Secondly, it is difficult to give unambiguous evidence of <100> type slip, as we cannot tell apart <100>{110} from <111>{110} slip behaviour, as they both lead to the measurement of active {110} slip planes.

This leads to a problem, what if in the composition gradient, the transition in slip system involves only <100>{110} to <111>{110}? In such scenario, we will not measure any change, and measure the same active {110} planes across the whole composition range. Thankfully, it is argued in [55], [61] and [37] that a transition in slip direction in a B2 system as a function of APB should involve the following transition in slip systems:

Low APB - <111>{110} → <111>{112} → <100> {110} - *high APB*

As suggested by M. Yamaguchi and Y. Umakoshi [37], the APB of <111>{112} should be temporarily lower than the APB of <111>{110} close to the transition in active slip direction, leading to a likely predominance of <111>{112} type slip, which was found to be true in the B2 CuZn-NiZn system [61]. Therefore, at room temperature, we expect the transition in slip direction from <100> to <111> as a function of composition to be accompanied with a transition in active slip plane, from predominantly {110} to predominantly {112}, to predominantly {110} as the APB decreases. This scenario is typically what we would expect to see in the B2 FeAl-NiAl system, as <111> slipping B2 FeAl is considered low APB, whilst <100> slipping B2 NiAl is considered high APB [69]. This means we should be able to observe such transition in slip direction using indentation-based slip trace analysis, by evidencing the presence of unambiguous {112} and/or {123} type slip in the transition regime. We will now proceed to discuss the experimental procedure followed to perform this experiment.

4.3 Methodology

A compositionally graded sample was prepared between <111> dominant B2 FeAl and <100> dominant B2 NiAl. First, monolithic samples of the endmember compositions were arc melted from commercially pure elements, with the target compositions respectively 60Fe-40Al and 60Ni-40Al (at%), aiming for the same off-stochiometric aluminium contents as [108] to replicate their experimental conditions & enable direct comparison to their detailed TEM work. The two endmember samples were separately homogenised by glass encapsulation under argon atmosphere and heat treated 24h at 1200°C, followed by a water quench.

After the endmember compositions were prepared, the compositionally gradient was prepared as follows: Electrical Discharge Machining (EDM) was used to cut them in disk shapes ≈1cm diameter, then each sample was ground down from 400 to 2400 grit size sand paper, and finally they were put in contact along the grinded surface using a molybdenum capsule with a small load applied with a screw to ensure good contact between the samples during heat treatment.

The diffusion couple was then encapsulated under argon atmosphere and heat treated 100h at 1200°C, following a water quench. After the heat treatment, the two endmembers were found to be successfully bonded together along the contact surface. The diffusion couple was then cut along the diffusion direction, mounted in bakelite, grounded down from 400 to 4000 grit, and finally polished using 50 nm OPS colloidal diamond particle solution for 60 min.

Scanning electron microscopy (SEM) Elemental Dispersive X-ray (EDX/EDS) mapping of the sample was performed to identify the diffusion zone, inside an Apreo HiVac SEM (line scan with 50 measurements of 5s acquisition time each, at 20kV). The sample was then indented with a Mitutoyo HM-124 Hardness testing machine using a Berkovich tip, with the smallest load available (≈0.02 kg) throughout the diffusion zone, which resulted in slip traces outside, but most importantly inside the indents, visible using high resolution low voltage SEM. The process of indentation and slip trace analysis was iterative and the sample was characterised in successive indentation batches performed on separate days. The experimental procedure consisted in the following steps:

- perform a series of 20-40 indents in regions of interest across the gradient, with a particular attention to targeting different grains. The sample is rotated between each indentation to increase the variety of stress conditions (Figure 28 (a)).
- analyse each indent, imaging them using high resolution low voltage SEM, measuring the composition at each indent with three 30s EDX point scans as per Figure 28 (b), and performing a coarse EBSD mapping of the grains indented to get their crystal orientation in relation to the imaged slip traces.
- perform automated slip trace analysis (as per Chapter 3) on the data gathered, identifying whether some compositions ranges are under-represented in the statistics, or if some areas show signs of evolutions in slip activity, identifying whether to make further indents near those regions.
- repeat the indentation process and analysis targeting the regions identified until sufficient data is gathered.

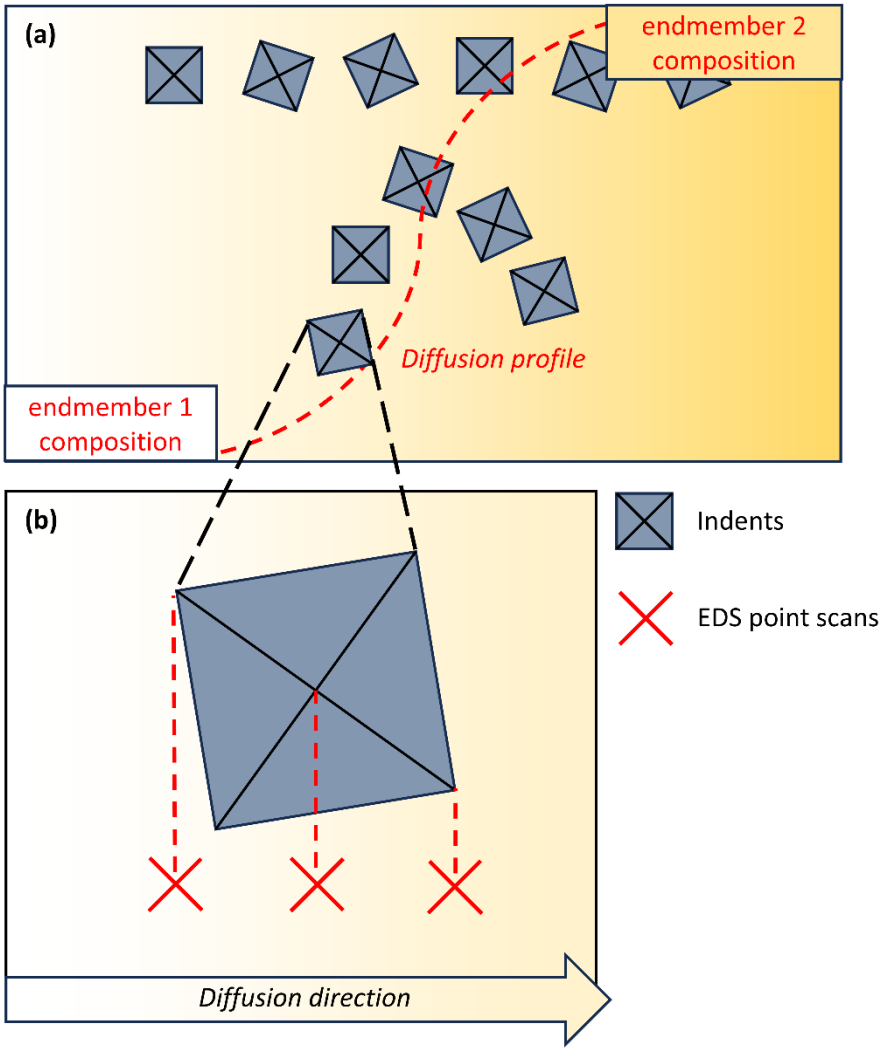


Figure 28: Indentation methodology. (a) typical positioning of the indents relative to the diffusion profile, more indents are made near sharp changes in composition. (b) typical position of the EDX point scans to determine each indent composition.

In total 101 indents were analysed, made in 4 batches. The outcome of the analysis from separate batches, performed on separate days, were consistent with each other, suggesting comparable experimental conditions and repeatability of the experiment. Each batch represents an experimental work of about 4h including indentation (<45 min), a coarse EBSD mapping (<15 min), high-resolution SEM imaging of the inside of the indents (<2.5h), and EDS measurement of the indents (<30min). The analysis of the slip traces is mostly automated and takes <30min per batch. The imaging parameters used are listed in the table 2, and may vary slightly between the batches, low acceleration voltage is the most important parameter when imaging slip traces to improve resolution and contrast, whether it is outside or inside the indents.

The first batches typically had poorer imaging quality, which was improved over the duration of the experiment through trial and error. Each analysed picture was inspected to check that the code properly detected visually identifiable slip traces. As a result, 2 indents in the Ni rich part of the gradient were ignored during the data analysis due to poor slip trace contrast and

obvious errors in the line detection (the slip trace contrast was overall lower in the Ni rich part of the sample).

In addition to the B2 NiAl-FeAl sample, previously studied (in Chapter 3) fcc Nickel sample known to slip exclusively on {111}, and B2 Ti_2AlMo thought to slip exclusively on {110}, were indented using low load (≈0.02 kg), and visually identifiable slip traces inside the indents imaged in similar conditions to the gradient. The objective of these samples was to demonstrate the possibility of using slip traces inside the indents for the slip trace analysis, by comparison to the prior data outside of the indents. The samples were rotated between each indentation and different grains were targeted.

Finally, two bulk B2 Fe-Ni-Al samples of target composition Fe-(15)Ni-(40)Al and Fe-(17)Ni-(40)Al (at%) were prepared, instructed by the gradient work, to confirm the outcome of the slip trace analysis on the B2 FeAl-NiAl gradient. The samples were arc melted, heat treated at 1000°C for 24h, mounted, grinded and polished in similar conditions to the gradient sample. Indentation slip trace analysis was performed in similar manner to our previous work (Chapter 3) using a load of 0.5 kg, and analysing the slip traces outside the indents (using code parameters IR=10°,N=100px and ST=10). Fe-(17)Ni-(40)Al was also indented using small load ≈0.02 kg, and the slip trace analysis was performed inside the indents to compare its statistics directly to the ones obtained in the diffusion gradient.

All these samples were imaged in the same Apreo HiVac SEM, but since the visibility of the slip traces varies between the samples, and sometimes within a sample, different imaging conditions may have been used, which are listed in the following Table 6 (a picture resolution of 3072x2188 px was consistently used).

Table 6: imaging conditions used across samples in this work, "outside" and "inside" referring to the kind of slip trace analysis performed

Sample	Mode	detector	WD (mm)	Current	Magnification	HV (kV)	Dwell time (µs)	Line scans
FeAl-NiAl (inside)	Immersion	BSE	3.9	25 pA	x20000-x25000	2	5	10
Fe-15Ni-Al (outside)	Standard	ETD	3.9	0.8 nA	x2000-x2500	2	1	10
Fe-17Ni-Al (outside)	Standard	ETD	4	0.8 nA	x15000-x35000	2	1	10
Fe-17Ni-Al (inside)	Immersion	BSE	3.9	25 pA	x50000-x65000	2	3	8
Fcc Nickel (outside)	Standard	ETD	5	3.2 nA	x650-x1200	10	1	10
Fcc Nickel (inside)	Standard	ETD	5	0.10 nA	x8000-x15000	2	1	10
B2 Ti_2AlMo (outside)	Standard	BSE	5	3.2 nA	x1500-x2000	5	1	10
B2 Ti_2AlMo (inside)	Immersion	BSE	3.9	0.1 nA	x20000-x35000	2	1	10

4.4 Results and Discussion

4.4.1 Materials

A B2 FeAl to B2 NiAl compositionally grade sample was prepared to study the transition from <111> to <100> type slip. The sample's composition was measured by SEM EDX (Aztec software) across the diffusion zone, shown in Figure 29.

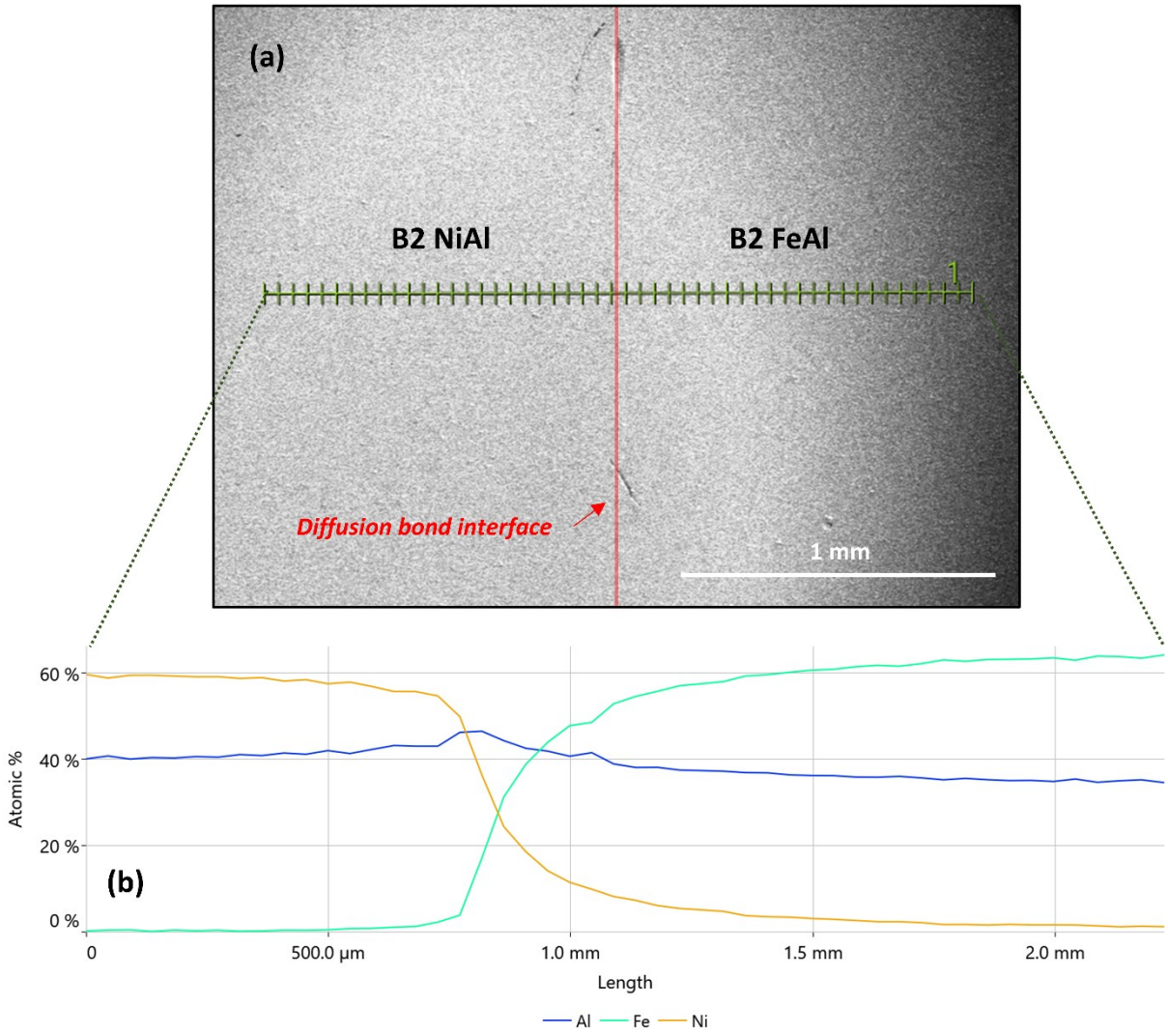


Figure 29: EDX measured composition across the B2 NiAl-FeAl diffusion couple. (a) SEM picture of the sample and localisation of the point scans and (b) atomic % composition for each element.

The diffusion zone spans over about ≈2mm, with some regions showing sharper changes in compositions than others, which is typical of compositionally graded samples due to differences in diffusion rates for different species, and changes in diffusivity with composition. The composition of the B2 FeAl rich side of the sample is slightly lower in Al content than targeted (≈35 at.%), and a small portion of the gradient displays higher (close to 45%) Al content. Despite these small variations in Al content, we consider the sample to be close enough to the target to meet the needs of the study, and no variation of the slip activity

correlating with Al content variation was found (nor with the diffusion rate). The sample was found to be single-phase across the whole composition range.

The bulk B2 Ni-Fe-Al validation samples compositions were measured using 3 EDX 20kV 60s map scans of ≈500µm, finding a composition of respectively (15.1±0.1)Ni-(38.1±0.2)Al-(46.7±0.2)Fe and (17.1±0.1)Ni-(43.1±0.2)Al-(39.7±0.05)Fe (at.%), which are very close to the targeted compositions, although we note that the differences in Al content are susceptible to affect slightly their slip activities when compared with corresponding Ni content compositions in the gradient. We will now proceed to the result of the slip trace analysis of the different samples, starting off by discussing the choice of analysing slip traces inside microhardness indents.

4.4.2 Analysing slip traces inside indents

In our early attempts at using indentation-based slip trace analysis on these diffusion gradients, we encountered a major problem: on some samples, no matter what load we would use, no slip traces would be visible surrounding the indents, probably due to the particularly high hardness of some intermetallics. This was obviously a blocking problem since we rely on observing such slip traces for our analysis. However, we then noticed that when using very small indentation loads (≈0.02 kg), many "slip-like" deformations, i.e. lines, were visible on the inside walls of the indents. We therefore decided to try to analyse these features, using the same procedure as when doing slip trace analysis outside the indents, but accepting a larger angular difference between the theoretically calculated slip trace orientations and the observed ones. On top of offering slip trace visibility in contexts where slip traces outside indents are very difficult to see, a major advantage of such analysis is the added precision on the composition that can be associated with the deformation: whilst a slip trace outside an indent can be the result of dislocation motion across a range of compositions, the slip traces inside the indents are more likely to be the result of deformation for the local composition.

4.4.2.1 Demonstration on fcc Nickel and Ti_2AlMo

To validate that indentation-based slip trace analysis can be performed inside the indents, the approach was demonstrated on fcc Ni and B2 Ti_2AlMo test samples. Crucially, the experimental uncertainty regarding the slip trace orientation identification was established based on this analysis. To this end, we performed an analysis in similar conditions to those for the gradient samples, on the inside of small indents made in the following samples:

- Fcc Nickel, which we used as a reference and demonstration in Chapter 3, as only 4 {111} slip planes are expected to be active in this sample.
- B2 Ti_2AlMo, because based on our previous work (Chapter 3) we suspect it to slip exclusively on {110} planes (only 6 possible planes), but also because the visibility of the slip traces in this sample is of excellent quality.

These two samples were indented in multiple grains using a low load (≈0.02kN) which resulted in straight slip traces mostly inside the indent. The slip trace analysis was performed using our previously developed automated slip trace detection algorithm, but focussing on the inside of the indents (the outsides were manually masked). The analysis was repeated on the same data

sets using varying identification range IR, which is the maximum angular difference between a theoretical slip trace orientation calculated based on the EBSD measured local crystal orientation, compared to the detected line orientation, to consider the plane type orientation as a match (see Chapter 3 §3.3.1.5 for details). These results from inside the small indents are compared to the analysis of slip traces outside large indents, using previously collected data sets on this samples from Chapter 3. A line score threshold (ST) of 10 and a segmentation size (N) of 100px is used, inspection of the code generated figures suggested good slip trace identification at this score (good signal/noise ratio), although some minor errors in line detection are always expected. These results are represented on Figure 30, where the "outside" data is obtained by averaging the proportion of match between all grains tested (6 grains for Ni, 5 grains for Ti_2AlMo) from Chapter 3, and the "inside" data is obtained from averaging between all small indents analysed in the present work (16 indents for fcc Ni, 11 indents for Ti_2AlMo).

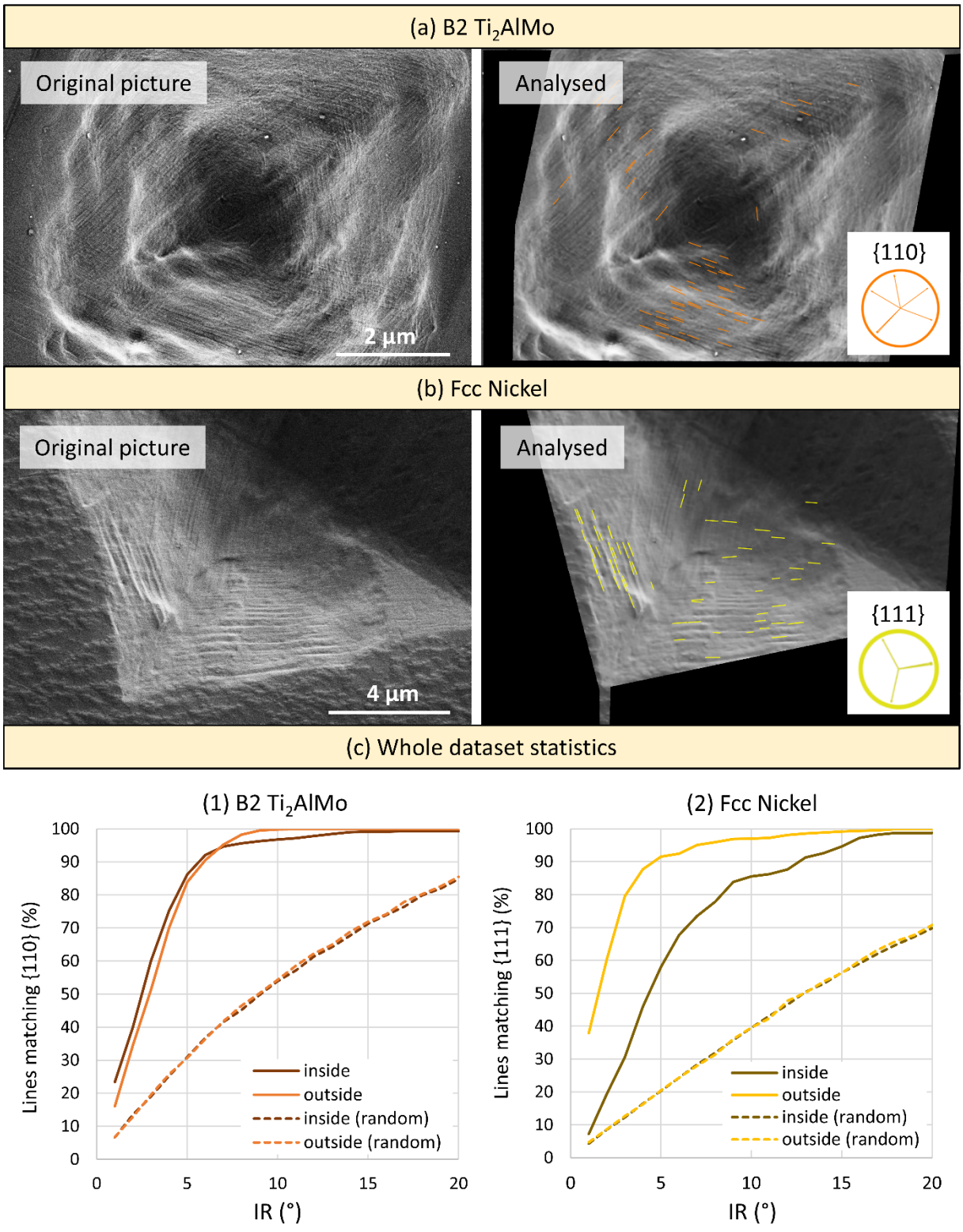


Figure 30: Analysis of slip traces inside vs outside the indents, in fcc Ni and B2 Ti_2AlMo. (a) and (b) show representative examples of pictures analysed inside small indents, with the corresponding theoretical slip trace orientations in local grain. In (c), (1) and (2) show the proportion of lines correctly attributed to the expected active plane type across the whole datasets. Results are plotted as a function of the identification range IR, i.e. the maximum angular error tolerance to consider orientations as matching. The "random" curves are

obtained from simulating randomly oriented lines (as per §3.3.1.8) and comparing them to the same theoretical slip plane orientations as the detected lines.

Let us start by looking at Figure 30 (c), where the "outside" curves show the results obtained from analysing slip traces outside large indents in each sample (from Chapter 3), for different IR. We see that at IR = 5° close to 90% of detected lines in both samples are properly attributed to the expected slip plane type, and close to 100% at IR = 10°. This means that experimental variabilities using N=100px are likely at worse close to 10°, in terms of maximal angular difference between the theoretical slip trace orientations calculated from the measured crystal orientation and the actual detected line orientations on these slip traces. Looking this time at the "inside" curves, obtained from the analysis of slip traces inside small microhardness indents, we see that at 10° of IR lines no longer match systematically the correct plane types. The two sample behave slightly differently, with Ti_2AlMo matching the correct plane type more frequently than fcc nickel, which is likely due to higher probability of randomly matching {110} in the former than that of matching {111} in the latter (random curves). The common observation from both samples' behaviour is that at about 16° IR we obtain close to 100% of correct slip trace attribution. This proportion needs to be put in perspective with the probability for a line to match the correct plane by chance alone (random curves), estimated at this IR to be about 70% for Ti_2AlMo and 60% for fcc Ni, which in both cases is significantly lower than the measured proportion of matches.

This result suggests that performing the slip trace analysis on slip traces inside microhardness indents increases the maximal angular error between the measured slip trace orientations and the theoretical calculated slip plane orientations from ≈10° to ≈16°, as is expected since the slope of the inside of the indent should affect the perceived intersection of the slip planes and the sample surface. 16° is therefore our best estimation of the optimal IR which should be used in this context.

An interesting aspect to note is that, unlike when doing the slip analysis outside the indents, rotating the samples between indentations now systematically influences the observed slip trace orientations, due to the change in surface inclination. We could also argue that different orientations of the indenter are more likely to promote the activation of different slip systems in this context than when doing the slip trace analysis outside larger indents, due to the more localised load state. Therefore, when performing the slip trace analysis inside small microhardness indents, performing several indents in the same grain, and rotating the sample between indentations substantially helps to increase the statistics of slip traces observed as opposed to when doing slip trace analysis outside the indents where this has little influence on the statistics, and we rely more on different grain orientations.

4.4.2.2 Increased experimental uncertainties and consequences

In theory, we can perform our slip trace analysis inside the indents using the same methodology as if we were performing it outside the indents, as long as we increase the IR to 16° to guarantee close to 100% of correct slip plane attribution. Now the question is, using an IR of 16°, will we be able to differentiate between plane types, or is the ambiguity in plane type identification going to be problematic? For that, let us look at Figure 31 reproduced from

Chapter 3, where the probability of matching each bcc plane type and other specific conditions were estimated from randomly oriented lines as a function of IR, using the 9 grain orientations tested in B2 TiFe.

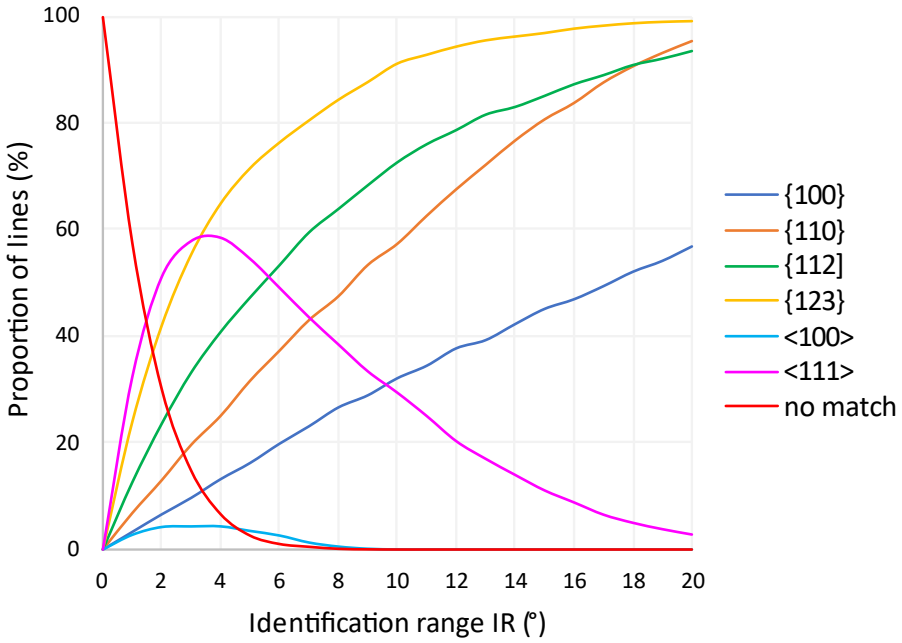


Figure 31: Reproduced from Chapter 3, data from randomly generated line orientations showing the average proportion of these lines, using the 9 grain orientations tested in B2 TiFe, that match each condition of interest for bcc and B2 slip trace analysis, including: matching each bcc plane type orientations, being unambiguously <100> (i.e. match only {100}) or <111> (i.e. match only {112} and/or {123}), and to match nothing.

As can be seen on Figure 31, at 16° IR the probability to match each plane type is, on average in each grain tested, much higher than at 10° IR. For example, using this IR, {123} planes should be matched close to 99% of the time meaning that close to all the slip traces will be ambiguous with a {123} plane, regardless of their orientation and originating plane type. However, the probability to match {100} planes is still very low, close to 50%, and the probability of matching {110} and {112} planes are close to 85%, meaning that we should still be able to differentiate between a sample that slips on such plane types 100% of the time, and a sample that does not. More importantly, we see that the proportion of unambiguous <111> match at 16° is of about 10% on average. This means, and this is crucial for our experiment, that at IR = 16° we should be able to observe unambiguous <111> type slip if {112} and/or {123} slip planes are active in the samples.

These “extreme” probabilities, either close to 100% or 0%, mean that we need to be cautious during the analysis, as more data is needed to make sure that we do not “miss” important information, e.g. unambiguous <111> type slip if such slip exists. Also, from our previous work (Chapter 3) we know that the probability of matching each condition can vary significantly between grain orientations tested, this means it is likely that in some grain orientations, the observation of unambiguous <111> type slip is simply impossible, whereas another grain orientation may be significantly more favourable to their observation. This highlights the

importance to put the experimental results in perspective with which grains were tested, and what probabilities of matching were estimated in these grains.

Another point to make is that we could increase the IR beyond 16°, to get a safety margin for extra experimental variability (similarly to what we did in Chapter 3 when choosing 10°), and still get a chance to observe differences in slip activity. However, this may dramatically increase the number of indents and grain orientations we need to test if we want to observe significant (i.e. unambiguous) results, which motivates us in keeping the IR as low as is reasonable, at 16°.

4.4.2.3 Picking analysis parameters, and code related line detection biases

In Chapter 3, we identified 100px segmentation size, a score threshold of 10 and 10° of IR as optimal performing analysis parameters, with minor variations in measurements when changing these values. We have just established that for an analysis inside of indent, we should now use an IR of 16°, but what about the other code related parameters?

The segmentation size and score threshold have an influence on what type of slip traces will be best detected. Typically, smaller segmentation sizes add experimental uncertainties on the line orientation detected, due to the increased discontinuity of the pixel segment, but may perform better when detecting wavy slip traces. In a similar manner, the scoring procedure tends to favour the detection of straight slip traces over wavy slip traces, meaning that high score threshold will select proportionally more straight slip traces than wavy slip traces. These two parameters also interact with each other, as larger segmentations sizes will lead to smaller score increases of the lines.

While in our previous work it made sense to select a unique set of parameters for the analysis, since the visibility of the slip traces was rather similar across and within the samples, is it still the case in the composition gradient? In this gradient, the hardness and deformation behaviour evolve throughout the sample due to changes in composition, which affects the visibility of the slip traces, which is typically poorer in the Ni rich part of the sample. Also, the imaging of the 99 indents was performed across a longer experimentation time, in several SEM sessions, meaning that the quality of imaging for the first indents is poorer than the latest (quality of the focus, contrast changes, etc.). Finally, the behaviour of the slip traces evolves throughout the gradient, not only in terms contrast, but also in terms of waviness (§4.4.4.1). All these aspects taken in consideration, we end up in a situation where whilst a certain set of segmentation size and score threshold may be optimal for slip trace detection in some of the indents imaged, other parameters could guarantee a higher quality analysis on other sets of indents.

For this reason, we believe a more truthful representation of the slip trace analysis would be to simultaneously show analysis outcomes using different parameters, this will guarantee that we are not cherry picking the most convenient analysis output to fit our narrative. To this end, we will show in §4.4.3.1 (Figure 34) and in appendix 2 (Figures A2.2 and A2.3), the analysis output of the analysis of the gradient for an IR of 16°, with varying segmentation sizes of 100, 120 and 140px, and a score threshold varying from 9 to 12. Note that all these values were identified in Chapter 3 as guaranteeing good slip trace analysis outcome, they are all

individually valid, but there is variability in their output: they “see and quantify” slip activity slightly differently, in the same way that different experimenters can have different criteria for manually drawing and counting slip traces.

4.4.3 Slip trace analysis on a diffusion gradient

4.4.3.1 Measurement across the FeAl-NiAl diffusion gradient

A compositionally graded B2 FeAl-NiAl sample was prepared, and indented across compositions ranging from (0)Ni-(65)Fe-(35)Al to (60)Ni-(0)Fe-(40)Al (at.%). Our automated slip trace analysis methodology was applied to a set of 99 small microhardness indents, which were imaged to emphasis the slip traces visible inside the indents (some slip traces outside the indents were also marginally detected) and EDS measured to get the average composition for the indent area. The average Ni (at%) composition will be used when plotting the data, and the uncertainty on this measurement is given in annexe 2 Figure A2.1, which varies depending on how sharply the composition evolves near the indents, but remains mostly between ±0.5 to ±2 Ni at.% (standard error), and should only marginally affect the interpretation of the data. The key experimental results for interpreting the data are represented on Figure 32, using as analysis parameters: an identification range IR=16°, a line score threshold ST=10, and the results averaged between an analysis made with a segmentation size N=100px, N=120px and N=140px (see previous §4.4.2.3 and Chapter 3 for details). Additional analysis outputs are available in appendix 2 (Figures A2.2 and A2.3), using different code analysis parameter, giving an idea of the variability of the analysis outcome for varying segmentation size and line score threshold, we note that all analysis parameter combinations lead to similar measurements.

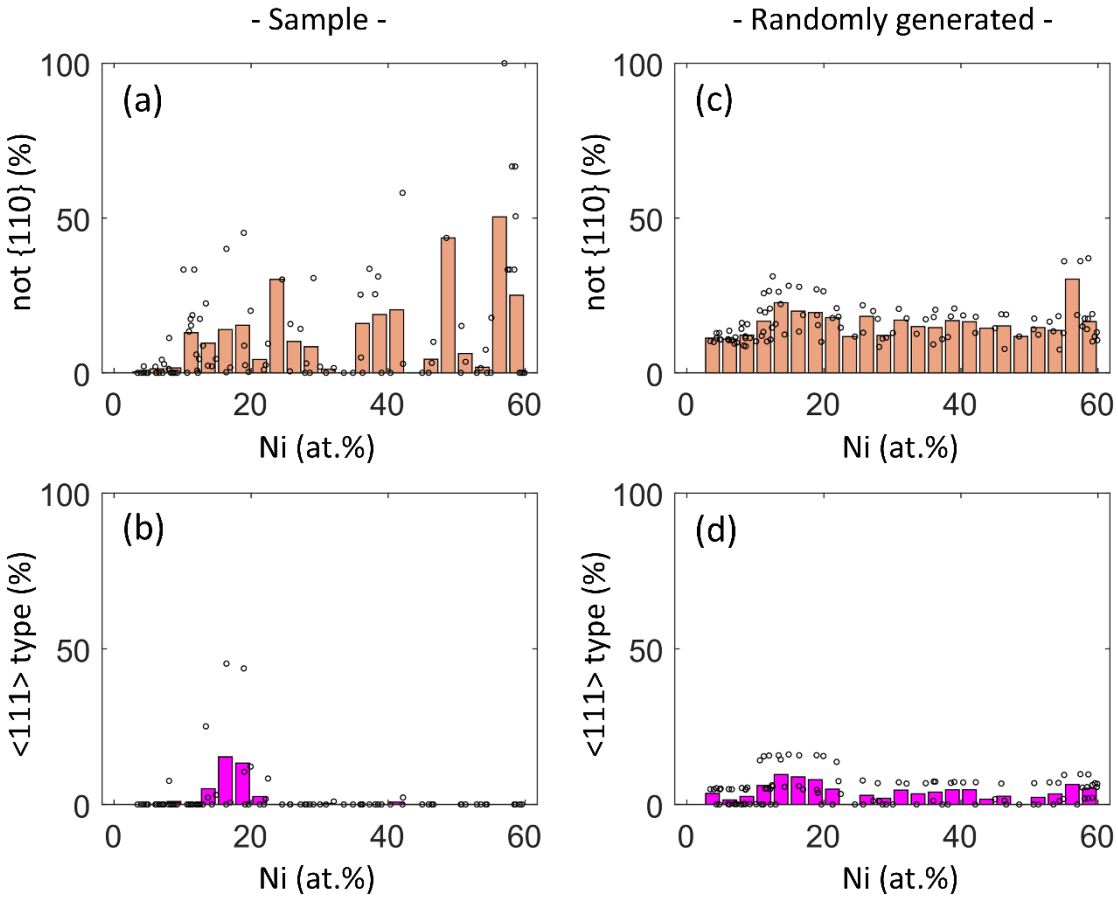


Figure 32: Results of the analysis for each indent (dot), as a function of the average indent composition. (a) and (b) represent the proportion of lines detected in the indent which fit the condition, either (a) that do not match a {110} orientation or (b) that match exclusively a {112} and/or {123} orientation. (c) and (d) show the proportion of randomly generated lines fitting each condition. Indents that show no lines reaching a score of 10 are ignored from the analysis. The bins show the average y-value of all data points (dots) within ±1.25% Ni, which is of the same order of magnitude as the standard error on the compositions (see appendix 2).

We will first go through some preliminary statistical considerations (Figure 32 (c) & (d)), and then interpret the outcome of the slip trace analysis (Figure 32 (a) (b)). Once we are done with this analysis, we will further confirm our interpretation using validation samples and previous work in literature (§4.4.4).

4.4.3.2 Preliminary statistical considerations

Let us first evaluate the likelihood for lines to randomly match each condition in the analysed grain orientations. As per Chapter 3, for each indent analysed, 2500 randomly oriented lines were generated and compared to the corresponding theoretical slip plane orientations of their respective grain. The resulting proportion of lines that match unambiguous <111> orientations (exclusively {112} and/or {123}), and proportion of lines that **do not** match {110} orientations, gives an estimation of the probability of observing such lines by chance alone, which are represented on Figure 32 (c) and (d). This value is given for each indent (indents in the same grain show similar probabilities) as a function of the average Nickel at.% composition of the

indent considered. These probabilities of matching are given with a standard error ≤1%, maximal (=1%) if the event has 50% chance of happening, and lower if this probability is close to 0 or 100%.

The grain structure of the sample evolves along the diffusion area, with larger grains on the FeAl side than on the NiAl side. As a result, the number of grain orientations tested along the gradient may vary, affecting the diversity of slip traces observed and local biases in plane type match proportions. On Figure 32 (c) & (d), we see the probability of randomly matching for each indent tested, calculated from the corresponding indent grain orientation. We can qualitatively estimate the number of grains tested throughout the gradient from these (the same grain tested will show approximatively identical probability of matching), which is of about 2 distinct grain orientations per composition, with some areas as between 10-13 Ni at% likely to have one more unique grain orientations tested, making it 2 to 3 unique grain orientations tested at these. As we have argued in §4.4.2, the number of grains tested is not the only source of variety in the statistics, since the perceived orientation of slip traces inside small indents is affected by the orientation of the indent itself (the pyramid shape slope inclination), and the variation in indent orientation may favour the activation of different slip systems, even if the indents are made within the same grain.

Figure 32 (c) represents the probability to match **no** {110} planes due to chance alone (assuming a random line orientation). We see that this probability is rather evenly distributed across the whole composition range, although we note that it is slightly lower in the Fe rich part of the sample, and slightly higher in the 10-20Ni (at.%) composition range. This probability is mostly within 10 to 20%, and never quite reaches 0%, meaning that all grains should allow the observation of lines that do not match {110}, i.e. it is possible to identify slip traces as being clearly not the result of {110} slip planes, throughout this sample.

Figure 32 (d) represents the probability for a line to be considered unambiguously <111> due to chance alone (assuming random line orientation), i.e. to match exclusively {112} and/or {123} plane orientations. Although this probability appears rather even across the composition range, mostly between 0 to 10%, we see that some grain orientations tested within the composition range 10-20 Ni (at.%) have an increased likelihood of showing unambiguous <111> type slip traces compared to the rest of the composition gradient. This means in such grains that errors in line detection, if they exist, are more likely to fit this condition due to chance alone. Also, the proportion of observed <111> type slip, if {112} and/or {123} slip are active, may appear comparatively higher here than in the rest of the sample. We see that in many grains throughout the composition range this probability is estimated to be close to 0%, meaning that it is almost impossible to observe unambiguous <111> type line orientations in those grains, even if <111> type slip is active.

In summary, before interpreting the slip activity measured, we need to remember that:

- A few grain orientations tested at 10-20Ni (at.%) have a slight bias in favour of observing unambiguous <111> type slip compared to the rest of the sample.
- The probability to match {110} planes is on average slightly higher in the 0-10%Ni (at.%) range.

- The representativity, in terms of unique grain orientations tested, and therefore unique slip trace orientation observed, is lower at the two ends of the gradient, meaning we are more likely to "miss" unambiguous observations in those areas.

4.4.3.3 Measured {110} match and unambiguous <111> match

Two plots are represented on Figure 32 (a) and (b), as they both give key insights on the slip activity across our gradient. First, for each indent, the proportion of lines that do not match {110} planes, i.e. lines that are clearly not aligned with {110} planes, and secondly the proportion of lines unambiguously <111> types, i.e. lines that are aligned only with {112} and/or {123} planes, as a function of the average indent Nickel content (at.%).

First let us look at the proportion of lines that do not match {110} orientation, Figure 32 (a). We see that on the FeAl rich side of the sample 0-10%Ni, close to 0% of these lines are observed, and therefore most indents tested in this part of the sample show slip traces matching {110}. This would be consistent with the idea that in this composition range, only {110} planes are active, or are at least predominant, in a similar way to our previously analysed monolithic B2 TiFe and B2 Ti_2AlMo (Chapter 3). This observation should be put into perspective with the rest of the gradient (10% Ni and above), where slip traces that are clearly not {110} planes are repeatedly detected, meaning that we have substantial evidence of the existence of active slip plane types other than {110} across the composition range 10 to 60% Ni.

On Figure 32 (b), this time looking at the proportion of lines unambiguously <111>, we see that a specific composition range of the sample stands out, between 10-25% Ni at%. In this region of the gradient, the indents analysed repeatedly show lines that are unambiguously <111>, supporting the existence of <111>{112} and/or <111>{123} type slip. However, across the composition range 25-60% Ni no evidence of such slip activity was observed. From these observations, we can propose three distinct slip activities across the composition gradient Fe35Al-Ni40Al:

- Between 0-10% Ni, close to all lines detected match {110} orientations, implying that slip on {110} planes is predominant.
- Between 10-25% Ni, the multiple observations of unambiguous <111>{112} and/or <111>{123} lines are consistent with the existence of <111>{112} and/or {123} slip, the bell curve shape of the data (Figure 32 (b)) suggesting that only a small composition range favours this type of slip.
- Between 25-60% Ni, we have evidence of the presence of slip traces that are not {110} planes, but no evidence of unambiguous slip on {112} and/or {123}. Since all lines detected match at least one plane type, this means that all slip traces in this part of the sample match either {100} or {110} slip planes. This can be interpreted as an indication of the existence of <100> {100} type slip. However, we do not have unambiguous proof of the existence of {100} type slip, because most lines matching {100} also match {123} orientations (being ambiguous between the two). What we can say is that the data gathered *supports* the hypothesis of a mix of active {100} and {110} slip planes, suggestive of <100> slip.

- The data supporting the idea of active <100> slip direction in the Nickel rich part of the sample, followed by the unambiguous activity of <111> slip directions at the intermediate 10-25% Ni range, we therefore propose that it can be inferred the presence of <111> type slip on the Fe rich part of the sample, based on the overall evolution of slip activity across the gradient.

In summary, based solely on our interpretation of the data gathered during the experiment, and what is known of common B2 compounds slip activities, we propose the following transition in dominant active slip systems as the nickel content increases:

Fe rich <111> {110} → <111> {112} and/or {123} → <100> {110} & {100} *Ni rich*

A transition in slip direction from <100> to <111> appears to take place (or initiate) at about 20-25Ni at%. However, not all these proposed slip activities have the same amount of data and level of evidence to support them. Putting a quantified uncertainty of each of these conclusions requires an in-depth statistical analysis, which is a complex task and is the topic of our onward work (see Chapter 4). In the meantime, all the statements above can be made qualitatively, whilst keeping in mind the small bias favouring <111> type slip observation in the 10-20 Ni at.% range due to the grain orientation tested, and that the data gathered in the 0-10 Ni at.% range has limited statistics. We will qualitatively say that the data gathered strongly supports the existence of <111> {112} and/or {123} type slip in the 10-25 Ni at.% range, moderately supports the presence of <100> {100} {110} type slip in the Ni rich part of the sample, whilst the predominant <111> {110} slip activity for Fe rich compositions is deduced comparatively from the overall evolution of slip activity across the gradient

4.4.4 Validation of the experiment

Data was gathered using our automated slip trace analysis applied to the inside of small microhardness indents, across the B2 FeAl-NiAl composition range, which supports the evolution of slip activity just discussed. We understand that this experimental approach is rather unusual, and is therefore prone to unforeseen experimental variabilities and/or errors. We therefore undertook additional verifications to see whether our interpretation of the data holds, namely a visual survey of the slip traces in the gradient §4.4.4.1, the analysis of the slip activity of bulk B2 NiAlFe samples of compositions predicted to be near the transition regime §4.4.4.2, and, of course, the comparison to previous TEM work made on this system from literature §4.4.4.3.

4.4.4.1 Visual assessment

A first qualitative assessment is to simply look at the slip traces, to see if we can observe an evolution in the slip behaviour. Figure 33 shows representative examples of indents in the 3 main composition regions identified, namely 0-10 (a), 10-25 (b), and 25-60 (c) Ni at.%. The lines detected for a segmentation size of 100px, a score threshold of 10, and an identification range of 16° are shown on the SEM micrographs.

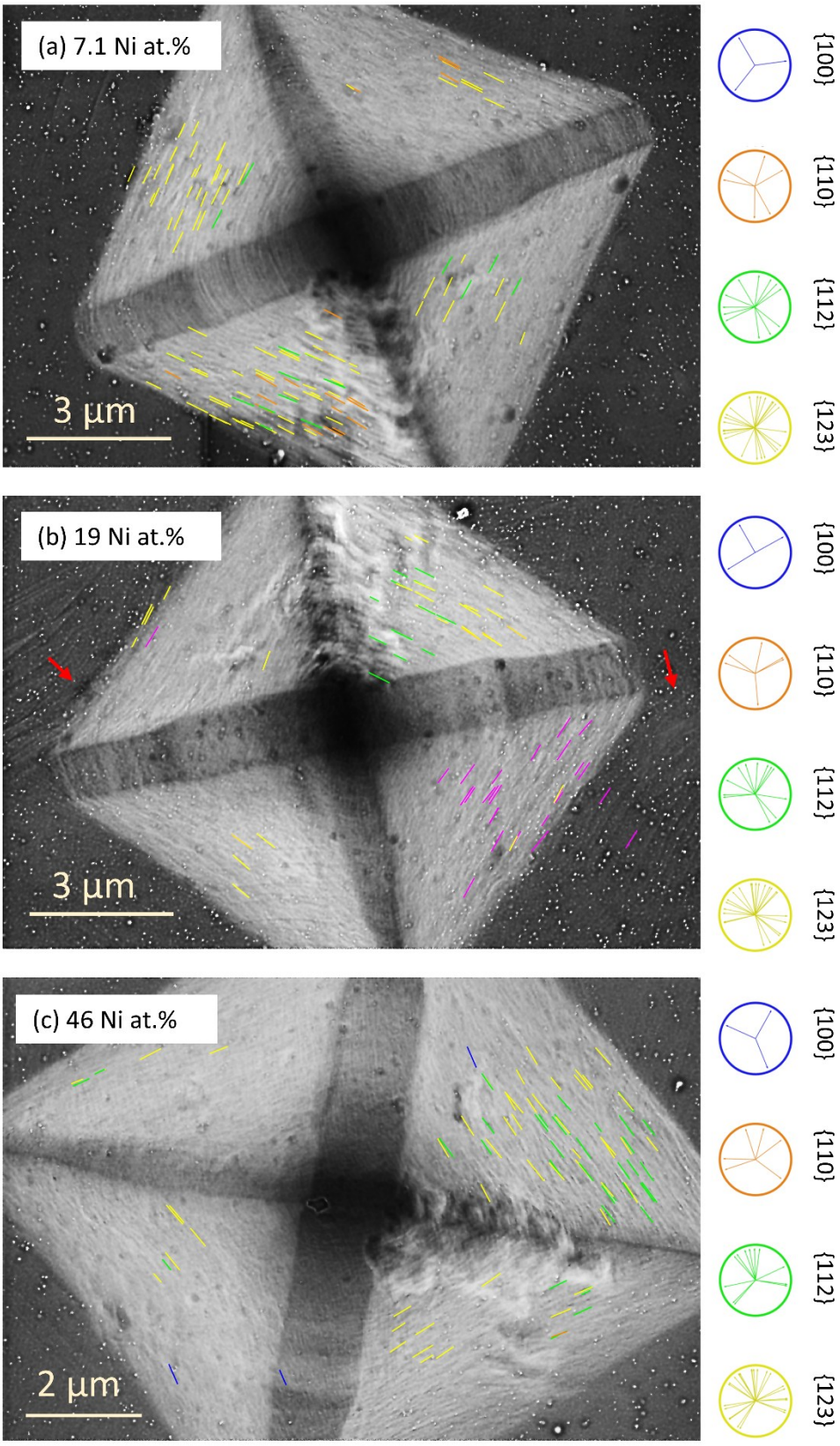


Figure 33: Examples of indents of different compositions in the 3 regions of interest. Lines automatically detected on these figures are represented in the colour of their closest matching plane type (corresponding theoretical orientations for the grain are shown on the right-hand side), or in magenta if they match exclusively {112} and/or {123} (i.e. <111> type). In (b) red arrows point at visibly curved slip trace networks outside the indent.

As seen on Figure 33 (a) and (c), slip traces observed within and near the indents close to the end compositions tend to be straight and well defined, as opposed to slip traces observed in the 10-25 Ni at.% range, as shown in Figure 33 (b), which show much more signs of waviness, with some almost circular slip traces outside the indents (identified with red arrows on the figure). Waviness of slip is often associated with ductility, and importantly, with a tendency to cross-slip [4] [53]. Or, cross-slip may be facilitated by the presence of a greater amount of available slip systems, in particular {112} planes. Therefore, the increased waviness of slip traces in the 10-25% compositions range supports the transition in slip system to <111> {112} and/or {123} as proposed from the slip trace analysis §4.4.3.3. Another interesting observation is that unambiguous <111> slip traces are observed outside the indent, on a straight slip trace, on the indent at 19 Ni (at.%) (Figure 33 (b)), which cannot be due to waviness, nor to the slope of the inside of the indent. They are unambiguous and extremely likely the result of a <111> type slip, as no possible {100} nor {110} plane match this orientation within 16°.

4.4.4.2 Bulk B2 NiAlFe samples

In order to validate that the slip activity measured inside the gradient is predictive of corresponding bulk samples slip activity, two samples of composition Fe-(15)Ni-(38)Al and Fe-(17)Ni-(43)Al (at%) were prepared and investigated via automated indentation-based slip trace analysis. The slip trace analysis of the gradient (§4.4.3.3) predicts that these B2 compositions should display intermediate slip activities, with notably the existence of <111> {112} and/or {123} type slip, possibly dominant as suggested by studies on the B2 CuZn-CuNi system [61]. A note that the Al content in these samples is slightly different than those of the gradient at these Ni compositions, and therefore may marginally affect their slip activity compared to the gradient.

The bulk samples were analysed first in the same conditions as samples in Chapter 3, outside large indents, using IR=10°, ST=10 and N=100px. The second sample (17Ni) was also analysed in a similar condition as the gradient sample, by performing the analysis on the inside of small indents using IR=16°, ST=10, and showing the statistics per indent averaged between three analysis performed at N=100, 120 and 140px (similar to the data previously shown Figure 32). Each sample analysis outcomes are represented on Figure 34, including example of indents showing slip traces on Figure 34 (a) and (b), and box plots of the statistics obtained in the different grains or indents analysed in Figure 34 (c).

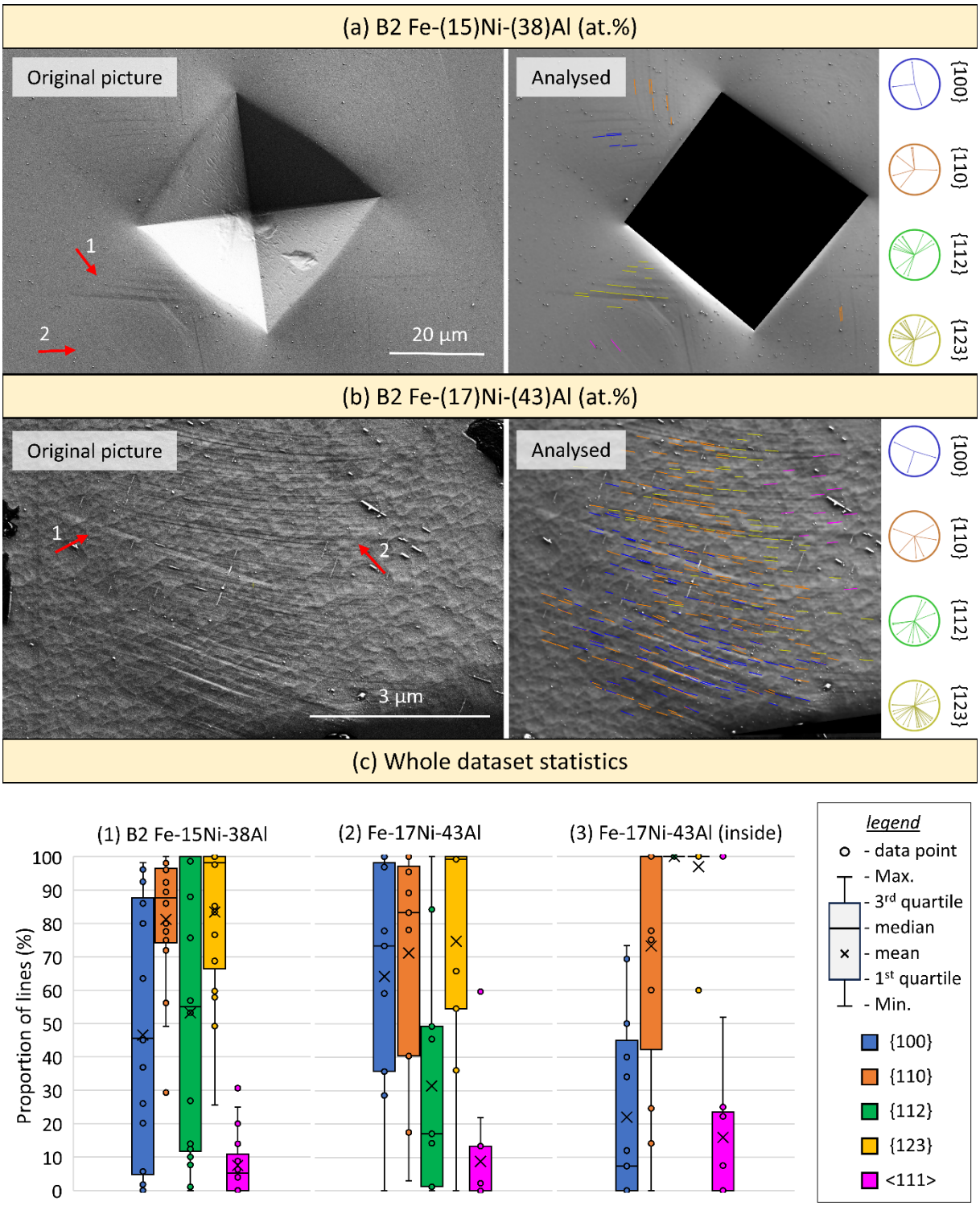


Figure 34: Analysis of B2 NiAlFe samples of intermediate compositions. (a) and (b) show typical slip traces observed outside the indents, and corresponding theoretical orientations. Red arrow points to "1" wavy slip traces or "2" straight slip traces. (c) gives the results from the slip trace analysis on all pictures for each sample, from respectively (1) 18 grains, (2) 11 grains and (3) 13 indents. (3) was performed inside small indents (which are not shown on the figure).

Looking at the SEM micrographs in Figure 34 (a) and (b), for the first time in our experiments, we seem to observe two distinct kinds of slip trace networks near the indents in these sample:

- Straight, well contrasted slip traces usually aligned with {110} or {100} planes, similar to B2 TiFe behaviour (Chapter 3), but also short and close to the indent corners (red arrows "1" on Figure 34).
- Wavy, sometimes diffuse, less contrasted slip traces, forming large intersecting networks, showing orientations that are frequently unambiguously of <111> type, similar to bcc Fe behaviour (Chapter 3) (red arrows "2" on Figure 34).

Looking at the results of the slip trace analysis on these samples (Figure 34 (c)), we see that {110} planes are likely dominantly activated, with average proportions of ≈80% and ≈70% when analysing outside the indents. In both samples a small portion of unambiguous <111> type slip traces are systematically observed over most grains tested, suggesting the activation of {112} and/or {123} type slip, as predicted by the gradient sample §4.4.3. Looking this time at the analysis inside small indents in the Fe-17Ni-43Al (at.%) sample, we get the same repeated observation of <111> type slip traces across many indents, and a significant portion of lines that do not match {110} orientations. The statistics from the inside analysis correspond very well to what was measured in the gradient sample at this Ni composition (§4.4.3.1, Figure 32), with ≈74% {110} and ≈16% <111> on average between all indents tested, compared to ≈86% {110} and ≈15% <111> at the Ni=16.25±+1.25 (at.%) bin in the gradient sample.

An unexpected observation from the statistics of these two samples (obtained via the outside analysis) is that their average {100} match fractions are very large, respectively ≈45% and ≈65%, and their {112} match fractions are relatively small, respectively ≈50% and ≈30% despite the much higher probability of matching the latter by cheer chance (assuming a random line orientation). If {112} match slip was predominant near those compositions, we would have expected a much higher proportion of {112} match. The large proportions of {100} and {110} match, combined with the small proportion of {112} match and the unambiguous observation of <111> type slip suggests that these bulk samples may slip on a mix of <100>{100} and <111>{112} slip systems, as well as {110} planes. If that is the case, it would mean that the transition in slip direction in the gradient, rather than a sharp transition from <100> to <111>, may be "smooth" involving a mix of <100> and <111> type slip for a range of compositions, with {112} planes only momentarily activated a portion of the time. This would mean that the FeAl-NiAl system, when deformed at room temperature, behaves similarly to when deformed at 600°C [108], where it was observed that both <111> and <100> slip coexist near the transition in slip direction. We can only suggest this hypothesis, as it is also possible that we simply "missed" the B2 NiAlFe composition showing predominant {112} type slip, as is expected from observations in the B2 CuZn-NiZn system [61]. A more thorough statistical analysis of the data is required to conclude on which hypothesis is most likely to be true, which will be the object of Chapter 5 (where it will be confirmed that a smooth transition involving the coexistence of <100> and <111> type slip is most likely).

4.4.4.3 Comparison to literature

Visual assessments and bulk samples of intermediate compositions both support that the data gathered during the experiment is representative of the evolution of the slip activity in the FeAl-NiAl composition range. Since NiAl and FeAl slip activities have been extensively studied, we can now compare our conclusions to literature. The next Figure 35 summarizes our main conclusions, and compares them to previous work in literature, notable to the active slip directions determined via TEM in [108] in this composition range, at room temperature.

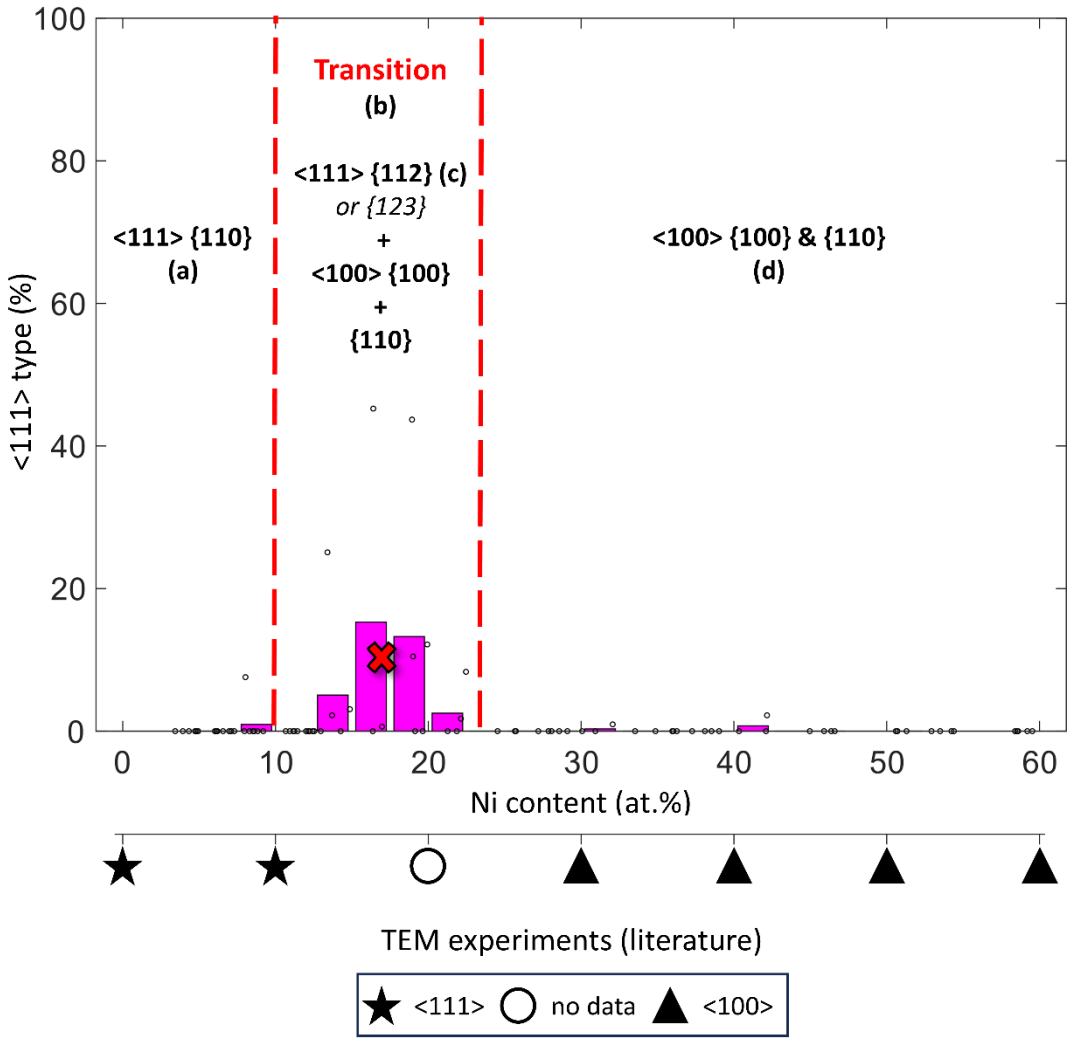


Figure 35: Validation of the experiment on the B2 FeAl-NiAl system. The graphic shows the data from Figure 32 (§4.4.3.1) (<111> type matches), the slip activity proposed for each part of the sample in §4.4.3.3, as compared to TEM work from literature [108]. The proportion of <111> type matches measured in the validation bulk-sample 17Ni-Al-Fe §4.4.4.2 is indicated with a red cross. In addition to these, multiple works from literature support the proposed slip activity:

- (a) dominant <111>{110} slip systems in B2 FeAl [69] [60] [57]
- (b) the transition <111> to <100> takes place between 10-30 Ni at.% [108]
- (c) the transition involves {112} planes [61] [37]
- (d) active <100>{100} & {110} slip systems in B2 NiAl [69] [64] [67]

Therefore, our experimental approach gave a reliable indication of the evolution of slip activity in this composition range, in agreement with visual inspections, previous work in literature, and allowed to predict the composition of two monolithic B2 samples presenting intermediate slip activities, likely to involve a mix of {110}, <111>{112} and <100>{100} type slip.

4.5 Summary

A diffusion gradient from B2 intermetallic Fe-35Al to Ni-40Al was prepared, and analysed using a recently developed automated indentation-based slip trace analysis technique to rapidly assess the slip behaviour <100> vs <111> on {100}, {110}, {112} and/or {123}. The key findings of our experiments are as follows:

- A new approach shows that slip traces from low load ≈0.02kg microhardness indentations can successfully be analysed inside-indents (rather than outside higher load indents as in previous work) enabling localised measurement of slip activity relative to the composition gradient. This inside-indent analysis was validated using fcc Ni and B2 Ti_2AlMo as reference samples.
- The inside-indent automated slip trace analysis was used to evaluate transitions in active slip systems across the Fe35Al-Ni40Al gradient: Fe rich <111>{110} → Fe-(10-25)Ni-40Al <111> {112} {123} + likely <100> {100} and {110} → Ni rich <100> {110} {100}, consistent with the reported slip activities for B2 FeAl, B2 NiAl, and for the pseudo-binary FeAl-NiAl composition range from TEM work in literature on bulk samples.
- Instructed by the gradient results, two bulk B2 Fe-15Ni-38Al and Fe-17Ni-43Al samples predicted to show intermediate sample slip behaviours were prepared. The samples' slip traces comprised a mix of straight and wavy slip traces, with distinct contrasts (suggesting different levels of pile-up), usually matching {110} or {100} planes when straight, or unambiguously {112} and/or {123} when wavy. The analysis outside-indent and inside-indent of the second sample gave consistent results.
- This experimental and automated analysis approach consists of, for an array of ≈30 small indents, <30 min of microhardness indentations, <15 min of a coarse EBSD mapping, <2.5h of high-resolution SEM imaging, <30min of EDX measurement of the indents and <30min for performing automated slip trace analysis. This experimental work is cheaper, easier, and considerably faster than conventional TEM and single crystal testing methods for slip system analysis.
- The ease & speed of the technique enables the collection of large datasets, offering increased statistical representation of slip behaviour (e.g. slip populations for varied compositions and crystal orientations). This information on slip behaviour (e.g. the proportions of slip on different slip systems) is beneficial for onward predictive modelling of deformation, such as in crystal plasticity models.
- Additional data can be easily acquired depending on the needs of the studies due to the localised, non-destructive aspect of the approach.
- The advantages of this new technique can specifically be readily used to accelerate the study of alloying additions and stoichiometry modifications on the slip activity of intermetallic compounds, the understanding of which is key for bulk intermetallics, and their use as reinforcing phases in advanced alloys, e.g. superalloys.

5 Solving the problem of ambiguity in bcc slip plane identification using indents and statistics

5.1 Abstract

Material science is a discipline with many variabilities, known and unforeseen, where predictive models are often held back by the availability & accuracy of experimental data. In micromechanics in particular, a challenge is to quantify deformation, i.e. dislocation activity on the different active slip systems. TEM and single crystal testing offer clean unambiguous information on active slip systems, but often lack representativity, with limited statistics. Automated indentation-based slip trace analysis could overcome these limitations, as the approach & easier experimental procedure can access much larger data sets, whilst indentation promotes a variety of stress components simultaneously giving more varied insights into the deformation behaviour of an alloy. The key problem with indentation-based slip trace analysis is that the slip system identification is often ambiguous, in particular when testing bcc or B2 alloys, e.g. {112} slip traces are usually closely oriented to {123} planes, complicating the distinction between the two slip activities. Therefore, despite observing a large variety of slip events, the number of unambiguous observations can be lower than competing techniques. In this work we introduce a statistical analysis approach to assist solving the problem of ambiguity in bcc plane type identification, as applied to recently developed automated indentation-based slip trace analysis. Using a basic sample response simulation, P-value calculations, and hypothesis testing, it is shown how we can estimate and compare the likelihood of competing possible hypotheses on the samples bulk slip activities, confirming, as well as gaining new insights on previously surveyed B2 and bcc samples slip activities. It will notably be shown how we were able to prove the existence of <100> type slip in B2 (17)Ni-(43)Al-Fe, at a 95% confidence level, without having observed a single unambiguous {100} slip trace orientation.

5.2 Introduction

In this chapter, we present a statistical analysis procedure to better evaluate the amount of evidence provided by automated indentation-based slip trace analysis. It will be shown how meta-analysis can be performed to combine efforts from different research groups, increasing the hypothesis rejection rate and building more precise conclusions on our possible sample slip activities. Applied to previously gathered data, all conclusions from the statistical analysis are consistent with previously hypothesised slip activities in the samples, including bcc Fe slipping on a mix of {110} {112} and {123} plane, B2 TiFe predominantly slipping on {110}, and B2 (17)Ni-(43)Al-Fe (at.%) showing an intermediate slip activity with a possible mix of {110} and {112} planes. This approach has the means to solve debates surrounding the relative contributions of {123} slip over {112} slip in bcc, usually subject to controversy due to ambiguity, and provide us with easy to interpret P-values for evaluating the likelihood of competing hypothesis, based on the amount of data gathered. We also gain new insights on the geometrical dependencies between the different family of bcc plane types regarding their corresponding slip trace orientations and tendencies to be ambiguous with each other.

This methodology promotes the interest of using P-value calculation and statistical tools to refine assessments of slip activities in general, which can apply to other crystal structures and slip trace analysis approaches.

5.2.1 Slip trace analysis and ambiguity in bcc

Common micromechanical testing approaches involve the empirical observation of specific unambiguous events, for example, observing a dislocation under a specific geometry via TEM or activating slip at a specific angle during a single crystal compression. Many of these approaches are heavily reliant on high experimenter skill, and can be subject to personal bias, assumptions on possible slip activities, may lack representativity, as well as their observations being numerically limited. A key question for building crystal plasticity models is to quantify dislocation activity on distinct slip systems. Whilst, the critical resolved shear stress of competing slip systems in a sample can be measured [45], knowing the CRSS will not necessarily inform on how each plane type contributes to large scale deformation, e.g. when differences in CRSS are measured. Such crucial questions can dictate mechanical behaviour, especially during slip transmission at grain boundaries or between different phases.

In our previous work was introduced a new approach for slip system identification and quantification (Chapter 3 and 4), using automated microhardness indentation-based slip trace analysis. This technique consists in performing microhardness indents on a flat polished sample, a coarse EBSD mapping of the area surrounding the indents, and imaging the slip traces visible at the surface near the indents using SEM. The pictures and EBSD data are then analysed using the newly developed code, which automatically segments the pictures in small ≈100*100 px areas, detects lines in each segment, and scores the lines based on a comparison of their orientations to identify which lines are more likely to be aligned with slip traces. Once compared to theoretical slip plane orientations calculated from the local crystal orientation, the likely slip activity of the material can be assessed. The technique was found able to unambiguously identify key slip activities, in agreement with literature, and especially

differentiate samples slipping on <111> {112} and/or {123} planes from samples slipping predominantly on {110} planes. However, it encountered a similar "blocking" problem of other mechanical testing technique: although it can be easily stated that there is unambiguous evidence of some specific active slip systems, the overall bulk slip activity of the samples (i.e. the contribution of each slip system to the deformation) cannot be determined without resorting to assumptions based on previous work in literature.

Statistical analysis and probabilistic inferences are common practice amongst multiple scientific disciplines such as genetics, physics, social sciences and participated to greatly enhance the speed of scientific discovery. Quantum physics in particular taught us that probabilistic interpretations of physical phenomenon can lead to appropriate predictive model building. In substance, a statistical analysis can be seen as a way of assessing the reliability of a conclusion, after considering the amount of data gathered and the context in which this data was gathered. More specifically, these tools allow to state and test hypotheses, and assess the reliability of the data gathered in their support, or against them.

Since automated indentation-based slip trace analysis is still in early-stage development, it is interesting to push the analysis of the data further, and see how strong and how reliably conclusions on the samples slip activities can be made when the data is taken independently from previous work in literature. In this work, we will go through generalities concerning statistical tools, hypothesis testing, and how they can be applied in the context of automated indentation-based slip trace analysis. In particular, it will be shown how to accurately estimate the experimental outcome under each slip activity hypothesis tested, via a simple simulation work, and how to evaluate the strength of the evidence gathered during the experiments, for, or against such hypothesis. We will go through each of the statistical tools used and state what assumptions are made, with a main objective to reduce the assumptions on the physicality of the measurement to a minimum whilst guaranteeing control over the hypotheses' false rejection rate. Finally, we will apply this statistical analysis to previously gathered data from B2 TiFe, bcc Fe and B2 (17)Ni-(43)Al-Fe (at.%), identifying there distinct slip activities and gaining new insights on them.

5.2.2 Hypothesis testing applied to indentation-based slip trace analysis

Hypothesis testing and P-value calculations are generally absent from micromechanical studies. Therefore, in this section we propose a brief overview, generalities about this approach to data analysis, accompanied with how it translates to the specific context of automated indentation-based slip trace analysis. The subject of hypothesis testing is highly documented as it concerns multiple research fields, and many independent resources are available online. We recommend the article by S. Schmit [117] which lays out many of these basic principles, in particular concerning multiple hypothesis testing. Through this section, we will alternate between basic statistical definitions and examples to show how they can apply to the context of bcc slip trace analysis.

5.2.2.1 P-value

A P-value can be defined as an evaluation of the likelihood of obtaining an experimental outcome given the amount and nature of the data gathered under a specific hypothesis.

Let us take as an example an indentation-based slip trace analysis. Say that over a random set of grain orientations indented, we have observed 10 unique independent slip trace orientations, 90% of which are unambiguously attributed to {110} planes, and 10% are clearly not {110} planes. We want to test the hypothesis that, under a random applied stress, our sample slips 50% of the time on {110} planes. We will consider that indenting a random grain orientation is equivalent to applying a random stress to our materials, although we note that an indenter may apply a slightly biased stress (e.g. mostly compressive and/or shearing). Since the data gathered suggests that the sample slips more than 50% of the time on {110} planes, we will define a null hypothesis H0 that we seek to disprove in favour of an alternative hypothesis H1 as:

H0: the sample slips 50% of the time on {110} planes

H1: the sample slips more than 50% of the time on {110} planes

The P-value under H0, in this context, would basically be the answer to the question: "how frequently do we expect to find the experimental result, 90% of {110} slip, or a more extreme outcome (>90%) after 10 observations, given that H0 is true".

Observing a {110} slip plane can be conceptualised as random binomial variable: sometimes they will be observed, sometimes they will not (binary yes/no), and the outcome cannot be predicted before indenting because different slip systems may activate depending on the random stress conditions and the unknown mechanical properties of the metal. In statistics, it is common to talk about a "success", here a "success" associated with our random binomial variable would be "observing an unambiguous {110} type slip". In this example, the P-value calculation is rather simple, it is the sum of the probability of observing 9 independent {110} slip and 10 independent {110} slip (≥90% of success) after 10 trials. To calculate these probabilities, we use the binomial probability formula:

$$(1)\ P(X = k) = \binom{n}{k} p^k (1-p)^{n-k}$$

With:

- n the total number of trials, here 10
- k the number of successes, here 9 and 10
- p the probability of success, here 0.5 (50%)
- $\binom{n}{k}$ the binomial coefficient, defined as $\binom{n}{k} = \frac{n!}{k!(n-k)!}$

Replacing the values in (1) we get:

$$(2)\ P(X = 9) = 10 * 0.5^9 * 0.5^1 \approx 0.0098$$
$$(3)\ P(X = 10) = 1 * 0.5^{10} * 1 \approx 0.0010$$

And now summing (2) and (3) to get the P-value:

$$\text{P-value} = P(X \geq 9) = P(X = 9) + P(X = 10) = 0.0108$$

We find a P-value of ≈ 0.01, it can be interpreted directly stating that if H0 is true, there would be 1% chance to obtain an experimental result as extreme or more extreme than what was observed. This statement gives an unbiased perspective on the strength of the evidence provided by the experiment against H0: the lower the P-value, the stronger the evidence against H0. Here we could qualitatively say that the evidence against H0 is strong, and the alternative H1 is likely to be true. It is often useful to have an objective criterion to know if H0 can be formally discarded as being false in favour of H1, which leads us to the concept of hypothesis testing.

5.2.2.2 Hypothesis testing, Type 1 and Type 2 error

Once we have a P-value, which evaluates the likelihood of obtaining the experimental result under a specific hypothesis, the validity of the hypothesis can be tested. Conventionally, a 95% confidence level is commonly used for hypothesis testing, which is arbitrarily decided (any level can be used). At this confidence level, if the experimental result has less than 5% chance of being obtained under H0 (P-value < 0.05), it will be considered that the evidence gathered is strong enough to formally reject H0. In the previous example, we have P-value = 0.01 < 0.05, therefore the outcome of the experiment is significant at a confidence level of 95%, and H0 can be reasonably discarded in favour of the alternative H1, that the sample slips more than 50% of the time on {110} planes. This hypothesis testing process has a few consequences, involving what are called type 1 and type 2 errors.

Type 1 error:

If we were to repeat the experiment on multiple independent samples, calculating the corresponding P-values and performing the hypothesis testing at a confidence level of 95%, it is expected that we will wrongly reject H0 5% of the time, even if H0 is true in the sample tested. This is called a type 1 error: to wrongly state that a hypothesis is false when the hypothesis is, in fact, true. We often talk of type 1 error rate, the frequency of false rejections, which at this confidence level is 5%.

Type 2 error:

A Type 2 error is usually considered less problematic, it consists in failing to reject a hypothesis even though the hypothesis is false. Scientifically speaking, it is often better to state “we failed to disprove H0” when H0 is false (=type 2 error), than to wrongly state “H0 is false” if H0 is true (=type 1 error).

5.2.2.3 The multiple hypothesis testing problem

In the case of indentation-based slip trace analysis applied to bcc and B2, the slip traces orientations are compared to 4 plane types simultaneously, and the observed slip traces are almost never unambiguous, meaning that they usually can be associated to more than one plane type. If we lay the hypothesis H1: “the sample slips 100% of the time on {110} planes”, we are expecting other plane types orientations rather than {110} to be matched due to random chance, even though they are not physically activated during sample deformation. Therefore, the measurement obtained is expected to consist of a certain amount of match for each plane type considered, in proportions affected by geometrical dependencies between

the families of planes, the context of the grain orientation tested, the experimental uncertainties and, of course, the sample's slip activity. Following the latest example, H1 which will be called the global hypothesis, is equivalent to a set of sub-hypotheses on each plane types which must be simultaneously true for H1 to be true:

Global Hypothesis on the sample slip activity:

H1: the sample slips 100% of the time on {110} planes

Is equivalent to a set of sub-hypotheses on an expected measurement:

- H1A: it should be measured a% {100} match
- H1B: it should be measured b% {110} match
- H1C: it should be measured c% {112} match
- H1D: it should be measured d% {123} match

With here b≈100% assuming the slip trace analysis correctly attributes slip traces to their originating plane type.

By testing H1, we are testing a single hypothesis on the sample slip activity, that the sample slips 100% of the time on {110} planes. However, any hypothesis on the sample slip activity could be tested, involving any mix of active slip planes.

e.g.:

H1: 100% {100}, 0% {110}, 0% {112}, 0% {123}

H2: 70% {100}, 10% {110}, 5% {112}, 15% {123}

…

Hi: $\{100\}_p$, $\{110\}_p$, $\{112\}_p$, $\{123\}_p$ with $\{100\}_p + \{110\}_p + \{112\}_p + \{123\}_p = 100\%$

Each of these global hypotheses will have specific expected measurements associated to them, and therefore sets of sub-hypotheses (a, b, c, d % of match expected for each plane type), which need to be considered simultaneously to perform the hypothesis testing. If we set as an objective to prove that H1 is true, we will necessarily have to disprove all alternative hypotheses Hi, hence why all plane types, which are believed to be activable, must be considered. A note that it cannot be formally proven that something happens 100% of the time (this would require an infinitely large dataset), but it could be proven that it happens, for example, >99% of the time (see later discussion in §5.4.4).

Multiple hypothesis testing problem and Family wise error rate (FWER)

In principle, to disprove H1 (or any Hi), all we must do is disprove any of the sub-hypothesis constituting H1. For example, if it can be disproved that there is 100% chance of matching {110} planes, e.g. by showing a slip trace in the sample that is clearly not a {110} plane, the global hypothesis H1 will be disproven regardless of how frequently the other plane types are matched. However, this raises a problem called "the multiple hypothesis testing problem".

Imagine that we calculate the P-value of the experimental results for each sub-hypothesis, comparing how frequently each plane type was matched by the slip trace orientations to their expected proportion of match, and proceed to do hypothesis testing at a 95% confidence level for each of them. Since we are now considering multiple hypotheses simultaneously, the probability to have at least one sub-hypothesis wrongly rejected is higher than the probability to wrongly reject the sub-hypotheses individually. This phenomenon is associated to a value called the "Family-Wise Error Rate" or FWER: the probability of randomly obtaining at least one significant result amongst a set of hypotheses tested simultaneously.

To illustrate that with the situation in bcc, if 4 plane types are considered, and a confidence level of 95% is used on each individual sub-hypothesis test, the probability to have at least one false rejection is equivalent to the probability of not having 4 "successful" hypothesis tests in a row, and therefore can be calculated as:

FWER = 1 – (0.95)^4 = 0.185

By testing four sub-hypotheses simultaneously instead of one, and looking for at least one rejection, the risk of falsely rejecting the global hypothesis is increased from 5% to 18.5%. Therefore, the confidence level in the conclusion is no longer 95%. This FWER increases the more hypotheses are simultaneous tested, and tends to reach 100%. This means that ignoring some plane types when we do not think they can get activated may be of interest in certain situations for strengthening the hypothesis rejection, which will be discussed in section §5.4.1.6.

Statistical procedures are available to control this FWER, guarantee that it remains below 5%, and maintain a 95% confidence level on the global hypothesis test. These procedures involve either adjustment of the individual sub-hypotheses P-values, or adjustment of the P-value threshold beyond which each sub-hypothesis tested is rejected. An example of a well-known procedure for FWER control is the Bonferroni correction [118] which, for a desired confidence level of "1-α" (here α=0.05) and "m" simultaneous tests, consists in testing if each sub-hypothesis P-value is $< \frac{\alpha}{m}$ instead of < α. These procedures usually result in an increase of the type 2 error rate (fewer global hypotheses are rejected), but they are required so to control the type 1 error rate.

Note that this FWER does not apply to the fact that we are testing multiple global hypotheses: we can lay out 10s of Hi, or 1000s of Hi, the P-values under each Hi will not be affected as they are being tested independently (e.g. the outcome of the hypothesis test on H1 is independent from the fact that we also test the hypothesis H2).

In summary, to apply hypothesis testing to the indentation-based slip trace analysis experimental outcome, and hopefully obtain clear unbiased information on the amount of evidence provided by the experiments, we need to:

- Lay out all the slip activity hypotheses of interest Hi
- Estimate the expected measurement for each plane type under each Hi
- Calculate the P-value under each Hi, by comparing the experimental results to each sub-hypothesis of Hi

- Perform hypothesis testing for each Hi whilst controlling the FWER

The target of this work is to accomplish each of these steps, considering the full scope of possible slip activities, using all the information gathered regarding the different plane types matched and see how efficiently we can reasonably narrow down the possible bulk slip activities of the samples. In particular, it will be highlighted which slip activities are clearly disproven, and slip activities that are best supported by the data. An objective during this process will be to use as minimum assumptions on the data (and the physics associated) as possible to guarantee that the type 1 error rate is ≤5%, and maintain a confidence level of 95% on the conclusions.

5.3 Methodology

Up until now when using the automated indentation-based slip trace analysis, mechanistic conclusions have been limited to broad statements, such as “there is unambiguous evidence of <111> type slip”, or “it was observed 100% of {110} match, therefore these observations are consistent with a sample slipping exclusively on {110} planes”. These kinds of statements are the only “safe” statements that can be made without solving the problem of ambiguity in plane type identification posed by the complexities of the bcc lattice. In this work, we aim to go beyond that, and better evaluate the amount of evidence gathered by the approach, while the logic presented also extends to different crystal structures or slip trace analysis methodologies.

To this end, a better understanding of the measurement is required: evaluating how many observations are made, identifying any dependency links between observations, seeing what can be said about the probability distribution of the experimental results, and finally deciding based on these which statistical analysis procedures are best adapted for evaluating the level of evidence gathered. After this discussion, a small algorithm will be presented which is designed to automatically perform hypothesis testing from newly gathered automated indentation-based based slip trace analysis experimental measurement, with the objective to identify the likely bulk slip activity of the sample.

5.3.1 Data characteristics, assumptions, and solutions

5.3.1.1 The data

First, let us clearly state what we are trying to quantify: we want to know the sample’s bulk slip activity, which will be defined as a “Proportion of independently activated types of slip systems under a random applied stress”, or a “Likelihood of activating a type of slip system under a random applied stress”. One could also argue that the observations in these experiments are made at the “meso-scale”, which can matter as to the interpretation of wavy slip traces (discussed in Chapter 1, §1.3.3). Therefore, to be more precise, the objective will be to measure the “meso-scale bulk slip activity” of a bcc or B2 sample.

The mechanical test consists of microhardness-indenting a sample, where it can be considered that an unknown stress state is applied to a random grain orientation. The resulting slip traces are imaged using Scanning Electron Microscopy (SEM), and grain orientation(s) measured by

Electron Backscatter Diffraction (EBSD). Then, the pictures are analysed by the newly developed code (Chapter 3), by detecting and quantifying line segments aligned with the slip traces, and then comparing their orientations to the theoretical orientations of each plane type, based on the local EBSD determined crystal orientation. The measurement, the proportions of lines matching each plane type, is subject to random chance for several reasons: depending on what grain orientation was tested, and what (complex) stress conditions the indenter applied on the grain, different slip systems may be activated, and they will be subject to a specific ambiguity due to the geometrical conditions and experimental uncertainties. Some theoretical plane type orientations will be matched by the lines because they correspond to the slip planes physically activated, some others due to the ambiguity in plane type identification.

Let us now consider how many of these observations, subject to random chance, can be described as “independent tests”, and if any assumptions can be made on the probability distribution of the experimental outcome.

5.3.1.1.1 independence of observations within a grain tested

Figure 36 displays different scenarios that are expected to be encountered when doing indentation-based slip trace analysing using the automated code for slip trace orientation detection, within the same grain (typically next to a single indent).

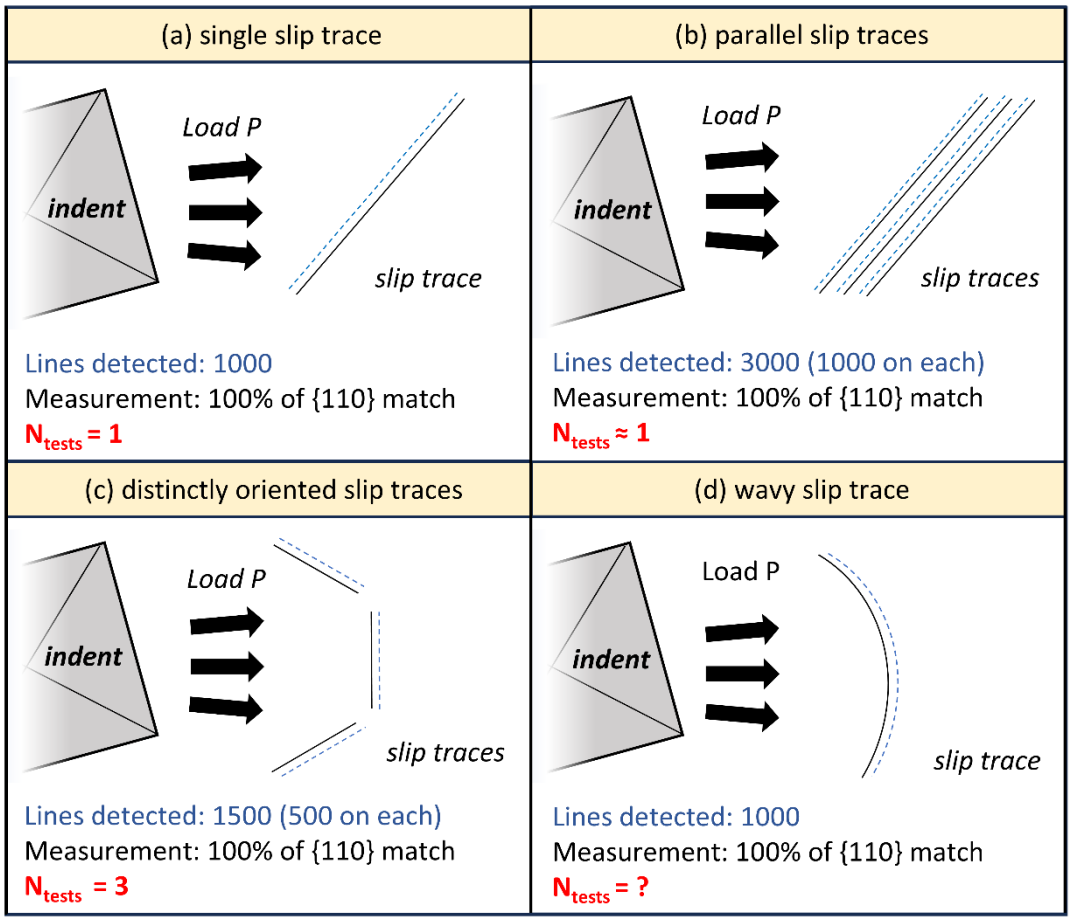


Figure 36: Different scenarios of a slip trace analysis within a grain leading to the same outcome « 100% of {110} match ». A detected line is « a new independent observation » only if it is detected on a distinctly oriented slip trace, or if the stress state can be considered different. Locally, along a slip trace, the unkown stress state (« load P ») may be considered approximatively uniaxial.

Let us say that we are imaging a single slip trace in a grain, as represented in Figure 36 (a). Depending on the imaging conditions, and the settings of the code, any number of lines might get detected aligned with this slip, anywhere from a single line to hundreds. None of these lines are independent observations, they are, in substance, the same observation of the same slip system, as they will match the exact same plane type orientations, leading to the same proportions of plane type orientations matched independently of the total amount of lines detected (for this picture). Also, locally, the stress state may be considered approximatively homogeneous along the slip. The reasoning is similar when considering networks of parallel slip traces, as illustrated on Figure 36 (b). Lines detected on one slip trace or the other will have the same orientation, matches, and are in a sense the same observation. Indeed, parallel adjacent slip traces are likely subjected to very similar stress components. Therefore, considering each individual parallel slip trace as a new test is equivalent to, e.g., performing the same single crystal compression test repeatedly and systematically activating and observing the same slip system. In such case, although the confidence that this particular slip system activates under this particular stress state increases, no new information on the sample bulk slip activity is gained by the repetition.

Let us now imagine that a few slip trace networks are visible in the grain, with distinct orientations, as in Figure 36 (c). A certain proportion of the lines detected will be aligned with each network, which will have distinct orientations and therefore will likely match different plane types. Those may be considered as distinct observations, and the proportion of lines detected on each slip system will be indicative of their relative contribution to the deformation. This however raises multiple problems:

- It is unclear if we can consider 2 distinct slip networks in the same grain as being "independent observations", as locally the stress state is "fixed" and the geometry of the indenter and crystal lattice could create dependencies between the different slip planes that may activate.
- The technique currently quantifies the proportions of lines matching each plane types within a picture, but does not quantify the relative proportions of lines detected on separate differently oriented slip trace networks.
- Furthermore, as seen on Figure 36 (d), how do we include in this reasoning wavy slip traces? Should we consider that a curved slip trace is, in a sense, and infinite amount of unique slip trace orientations but in infinitely small proportions?

This reasoning applies to single pictures, but it also applies if several indents are made within the same grain. Indeed, in our previous work, we noted that large indents made within the same grains usually display almost identical slip trace networks, leading to basically identical statistics when comparing indents within the same grains, even when rotating the indenter between indentations. If 100s of indents were made within the same grain, it is likely that no substantial information will be gained in the process. Similarly to parallel slip traces, the only information gained by making more indents and pictures in the same grain is an increase in the confidence that the statistics obtained for said grain are representative of this specific grain response to a micro-indentation.

In summary, the measurement, the overall proportion of lines detected in a picture matching a plane type, includes contributions from all slip trace networks and therefore contains some information on the dislocation density on each of them, e.g. if one of them is longer than the other, if they show different levels of pile-up (step height), or if more unique parallel slip traces are visible for one of them, more lines will be detected with the corresponding orientation, changing their relative contribution to the overall statistics. However, the exact number of observations made, i.e. of independent random tests within a grain, is difficult to quantify and even conceptualize.

5.3.1.1.2 Independence of observations across different grains

Let us now consider observations made in differently oriented grains. Since the grain orientations tested can be considered random, these should be considered independent tests. Indeed, due to the change in crystal orientation, the stress state should now differ significantly, and the geometry will likely lead to different ambiguities when observing the slip trace orientations (different plane type match proportions). Add to these the experimental variabilities and it becomes fair to assume an observed slip trace orientation in a grain is independent from an observed slip trace orientation in another grain, both in terms of stress

state and ambiguity. There may be issues if some grain orientations tested are close in orientations (e.g. the sample has a specific grain texture), as these could lead to similar observations. However, considering that grain orientations in a sample are usually significantly different, this is not likely to cause issue (at least when testing a small number of grains). It should therefore be reasonable to assume that slip traces detected in different grains are independent observations, with more information gathered about the sample bulk slip activity every time a new grain orientation is tested.

5.3.1.1.3 Addressing dependencies

Assuming that each new grain orientation tested leads to at least one new independent observation, we propose to "ignore" the fact that multiple unique slip orientations may be detected within the same grain, and assume that only one observation is made per grain orientation tested. From there, we will use as data (measurement) the proportion of lines matching each plane type averaged between each grain orientation tested. To get these values, if several pictures (and/or indents) are analysed within the same grains, the lines detected in each picture are summed to get the statistics for the grain considered, and then this value is averaged between all grains tested.

Indeed, if there is one thing to be certain of, it is that at least one independent slip system activation occurred and was observed per grain orientation tested (which is true as long as one line is detected in the grain, assuming the line detection works). This approximation allows us to by-pass the questioning about dependencies between activated slip systems within the same grain, wavy slip traces, and how to quantify their relative contribution to the statistics. Let us illustrate this with an example:

e.g: after testing 10 grains, it is measured that on average 80% of the lines detected in a grain match {110} planes, and 20% do not. Considering that exactly 1 observation was made in each grain, we observed 10 uniquely oriented slip traces, amongst which 8 unique independent slip traces match {110} planes (80%) and 2 unique independent slip do not match {110} planes (20%)

By doing that, an equivalence is made between the probability of matching a plane type in 10 separate grains and the actual proportion of plane type orientations matched by the lines within the grains. This equivalence is not strictly true since the probability of matching varies from grain to grain, which may lead to some level of approximation when calculating corresponding P-value. However, we believe that assuming only 1 unique slip orientation to be observed per grain is a large underestimation of the evidence gathered, as after indentation grains usually displayed 2 to 3 clearly identifiable unique slip trace orientations, proportionally equivalent in terms of contributions to the statistics (i.e. similar length and contrast).

e.g.: In the previously analysed B2 TiFe sample (Chapter 3), it was measured 100% of lines matching {110} plane orientations in 9 grains tested. These lines were detected on 2 to 3 distinct slip systems per grain tested, making it a total of 18 to 27 distinctly oriented slip trace networks which systematically matched {110} plane orientations, giving a qualitatively strong indication of predominant {110} slip behaviour. In the statistical analysis in this work, using

the same data, it will be considered that exactly 9 unique slip trace networks were observed to match {110} plane orientations, leading to an underestimation of the amount of evidence gathered during that experiment.

As we can see from this example, the underestimation of the amount of data gathered likely compensates for the approximation made by this equivalence, and should lead to an overestimation of the P-values. Therefore, the type 1 error rate should be controlled (maintained ≤5%), but at the cost of an increase in the type 2 error rate (less hypotheses will be rejected).

5.3.1.1.4 Assumptions of normality & variation of probability between tests

After addressing the question of dependencies between observations, more aspects of the data must be considered for the choice of the statistical procedures. Taking examples from previous work (Chapters 3 and 4), three samples, bcc Fe, B2 TiFe, B2 (17)Ni-(43)Al-Fe (at.%), will be analysed here, as these three should display distinct slip activities on which greater insights may be gained. The samples tested in these experiments contained: 17 grains in bcc Fe, 9 grains in TiFe and 11 grains in B2 (17)Ni-(43)Al-Fe (at.%). Considering that 1 grain orientation tested is equivalent to 1 independent observation, it can be seen that the amount of data gathered is small, in the sense that we cannot work under assumptions of normality (for that, more than 30 observations are usually recommended, which also depends on the probability of the events). Also, and even more critically, the probability of matching a plane type orientation varies between the grain orientations tested due to the change in geometry, because of that we know little about the probability distribution of the experimental outcome (the distribution will likely not follow a bell curve). This adds yet another layer of constraint as to how to calculate the P-values, for example we cannot use the t-distributions [119], appropriate for small sample sizes, as these work under the assumption of identical probabilities between the tests.

5.3.1.1.5 Assumptions of dependencies during multiple hypothesis testing

Finally, as discussed in previous sections, the global hypotheses on the samples bulk slip activities involve sets of sub-hypotheses on each plane type {100}, {110}, {112} and {123}, with specific expected measurements for each (expected proportions of lines matching each plane type). These sub-hypotheses are not independent tests within a global hypothesis, for example, {112} planes and {123} planes can have similar geometries within the bcc lattice, and so, under most circumstances, it is expected that these planes will result in closely oriented slip traces. As a result, the probability for a slip trace to match a {112} plane orientation knowing that it matches a {123} plane orientation is likely to be higher than the probability to match a {112} plane orientation if the slip trace orientation was completely random. This problem extends to all plane types (there will be some level of dependency between their orientations), but also to any additional sub-hypotheses, for example if we want to quantify the proportions of lines unambiguously <111> type (lines that match exclusively {112} and/or {123} plane type orientations). These dependencies, plane type related and grain orientation related, are difficult to solve analytically but can be estimated and accounted for through a simple simulation work, which will be described §5.3.2.2. However, such dependencies add a final layer of constraints as to what procedure can be used to control the FWER.

5.3.1.2 Choice of statistical procedures

As we have just seen, the data is rather constraining in its nature: absence of normality, variation of the probability of success between tests, and dependencies between the multiple hypotheses tested. These limit the choice of appropriate statistical procedures to perform hypothesis testing whilst controlling the type 1 error rate. In this section, we propose to calculate the P-values of the sub-hypotheses using the Poisson binomial distribution, and then address the multiple testing problem under dependency by controlling the FWER with the harmonic mean P-value.

5.3.1.2.1 P-value calculation: Poisson binomial distribution

For calculating the P-values associated to the individual plane match fractions measured, we need to account for the variation of matching probability between the grain orientation tested, the absence of normality and as a result the unknown probability distribution under the hypotheses.

The experimental result is a proportion of success with regards to each plane type, after testing a specific number of grain orientations, each with their own specific probabilities of matching the plane types depending on the hypotheses tested. Assuming a unique slip trace orientation is detected in each grain orientation tested, we propose to conceptualise each grain tested as an independent binomial variable of probability of success Pi, with Pi depending on the Euler angle of the grain, experimental variabilities, and the hypothesis tested. This idea is illustrated on Figure 37.

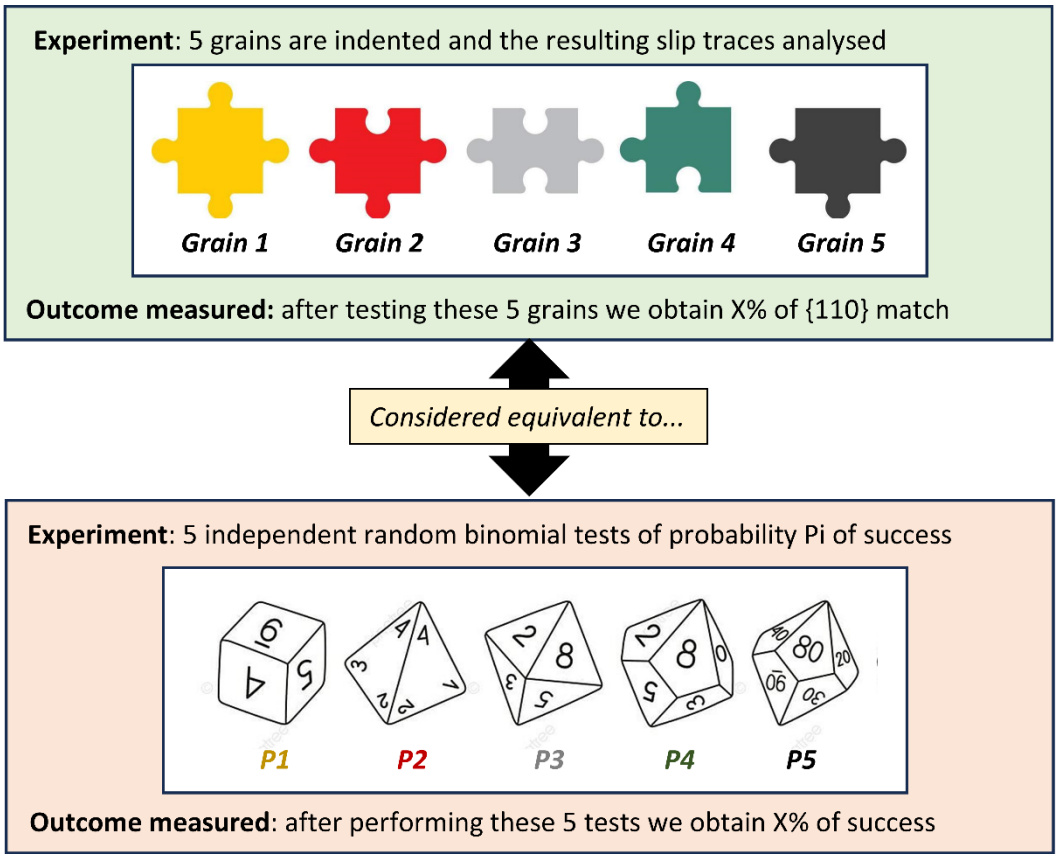


Figure 37: Illustration of the equivalence proposed, here considering {110} matches. A grain tested is conceptualised as a single independent random binomial test of known probability of success Pi, which is the likelihood for a detected line to match a {110} plane orientation in this grain assuming the hypothesis tested is true (which will be estimated via a simulation in §5.3.2.2).

To calculate the P-value in this context, we will use the small amount of data gathered at our advantage, using the Poisson binomial distribution, which allows the calculation of the exact P-value under any dependency assumptions, and any variation of probability between the tests, as long as the Pi of each test is known [120]. Multiple mathematical approaches can be used to calculate the P-value using the Poisson Binomial distribution, and since all the calculations are made automatically within the code, the discrete Fourier transform approach was chosen [121] as it was found easiest to code. In this context, to calculate the probability of obtaining "k" success after "n" tests of known probability $\{p_1,p_2,p_3\ldots p_n\}$ of success we use the following equation:

$$P(X=k)=\frac{1}{n+1}\sum_{l=0}^{n}C^{-lk}\prod_{m=1}^{n}(1+(C^{l}-1)p_m$$

With $C=\exp\left(\frac{2i\pi}{n+1}\right)$ and $i=\sqrt{-1}$,

From there the P-value of obtaining k or more successes can be calculated as:

$$P(X \geq k) = \sum_{m=k}^{n} P(X = m)$$

And the P-value of obtaining k or less successes as:

$$P(X \leq k) = \sum_{m=0}^{k} P(X = m)$$

This raises a new problem; in order to use the Poisson binomial distribution and to calculate a P-value, an integer number of trials "n" is required (which here is the number of grains tested) but also an integer number of successes "k". Or, although we are working under the assumption that exactly one unique slip trace is observed in each grain orientation tested, the data obtained, i.e. the average proportion of lines matching the different plane types in each grain, may be measured across more than one unique slip orientation per grain if more than one unique slip orientation is detected in a grain, in infinite possible proportions. The measurement is continuous, whilst the Poisson binomial distribution expects a discontinuous number of events.

e.g.: Say we have tested 10 grains in a sample, and measured that on average 82% of detected lines in each grain match {110} planes. We are working under the assumption that exactly 1 unique slip is observed in each grain. Therefore, we performed 10 unique independent trials and have observed 10*0.82 = 8.2 successes in terms of "unique" slip traces matching {110} planes. The value of "8.2" has some physical meaning attached to it, as it accounts for all observed slip traces and their relative contribution to the statistics, but it is not an integer and therefore cannot be used for calculating the P-values.

The "rounding approximation":

A simple way to by-pass this issue is to round up or down the proportion of match observed depending on the hypothesis tested, picking the situation leading to the highest P-value.

e.g.: We obtain 82% of {110} matches after 10 grains tested, leading to "8.2" successes measured.

If testing H1: 100% of {110} match expected,

➔ round up assuming 9 successes, and calculate P(X≤9).

if testing H2: 80% of {110} match expected,

➔ round down, assuming 8 successes, and calculate P(X≥8)

This rounding controls the type 1 error rate. Indeed, under the hypothesis H1 expecting 100% of {110} match, *we know* there are less than 9 successes out of ten trials (we have observed "8.2" successes), therefore by calculating the P-value of having 9 or less successes under H1, we are necessarily overestimating the P-value. Similarly, under the hypothesis H2 expecting 80% of {110} match, *we know* there are more than 8 successes out of ten trials, and therefore calculating the P-value of having 8 or more successes overestimates this P-value.

This choice of rounding is conservative, meaning that it controls the type 1 error rate at the cost of an increase of type 2 error rate, and will get increasingly more conservative as the amount of grain orientations tested decreases:

e.g.: if we test 2 grains, and observe 82% of {110} match (1.64 successes) we will have to round up to 2 successes, or down to 1 success assuming respectively 100% or 50% of match observed depending on the hypothesis tested, which is very different from the 82% measured and will heavily reduce the power of our analysis (the evidence against the hypotheses is largely underestimated).

However, **it tends to become approximatively exact** as the number of grains tested increases:

e.g.: if we test 20 grains, and observe 82% of {110} match (16.4 successes) we will have to round up to 17 successes, or down to 16 successes assuming respectively 85% of match or 80% of match, depending on the hypothesis tested. We are here working under the assumption of a % of success very close to what was observed (the evidence against the hypotheses is only slightly underestimated).

This overestimation of the P-value increases, by definition, the type 2 error rate. The strength of the evidence gathered against the hypotheses is underestimated, which makes it harder to find significant results and reject the hypotheses. It, however, does not involve any assumption on dependency or on the probability distribution of the data, and should therefore be a safe choice for controlling the type 1 error rate, which is the main objective. One could also consider that it further compensates for the approximation made previously §5.3.1.1.3 where it was assumed that the average measurement between the grains is the result of exactly 1 observation per grain despite the varying probabilities of match between the grains. The discontinuity and asymmetry of the probability distribution as well as the "rounding approximation" will be visible and accounted for when interpreting the P-values in the results section (§5.4.1.5).

5.3.1.2.2 FWER control: Harmonic mean P-value approach to multi testing

The dependencies between the different sub-hypotheses tested simultaneously add constraints as to what approach can be used to control the FWER. Few approaches are available to account for dependencies between hypotheses, and are usually highly conservative, such as the Holm-Bonferroni method [122]. Such approach will lead to a large increase of type 2 errors and very little hypothesis rejections. A more recent alternative is the Harmonic mean P-value (HMP) which grounds itself in Bayesian statistics [123] [124]. It consists in calculating the harmonic mean of the P-values of the sub-hypotheses. When simultaneously testing "N" sub-hypotheses with P-values $\{p_1,p_2,p_3,\ldots,p_N\}$ the HMP can be calculated as follows:

$$HMP = \frac{1}{\sum_{i=1}^{N} \frac{1}{N * p_i}}$$

The idea from there is to interpret the HMP directly as a P-value, and proceed, for example, to test if the HMP is below 0.05 to do a significance test at a 95% confidence level. On top of

having stronger power than alternative statistical procedures, a key advantage of the HMP is that it provides a P-value associated to the global hypothesis. This will allow not only to perform hypothesis testing, but also to identify which groups of hypotheses are best supported by the data (highest P-values), and potential dependency links between them, which is particularly useful in the context of slip trace analysis.

This HMP has limitations as it is expected to introduce some level of inaccuracy to the P-value calculation. However, it should be approximatively exact for low HMP ≤ 0.05 under unknown dependency structure, meaning that it can be used for performing 95% confidence level hypothesis testing and conserve a type 1 error rate (or FWER) ≈ 5%. Since we made a few conservative assumptions when calculating each sub-hypothesis P-values (previous paragraph), basically underestimating the amount of data gathered (assuming 1 observation per grain, and rounding up or down so to overinflate the P-values), we judge the small inaccuracy introduced by the HMP to be reasonable, i.e. that the type 1 error rate will likely be <5%. However, caution is needed when interpreting high HMPs (>0.05) as they become increasingly more inaccurate. So, to put is simply, the global P-values calculated from these HMPs should not be interpreted literally when they get higher than 0.05, but they can still be interpreted comparatively, giving us insights on which families of slip activity hypotheses are best supported by the data.

Now that we have decided which statistical procedure to use to calculate the P-values and control the FWER, we can translate it into an algorithm, which will then be applied to previously gathered data on several samples.

5.3.2 Step by step analysis process

The following sections will describe the step-by-step statistical analysis process, as was coded in a MATLAB^{TM} algorithm, including: which hypotheses are tested §5.3.2.1, how is estimated the expected proportion of match for each plane type in each grain tested for these hypotheses (the model) §5.3.2.2, how are calculated the sub-hypotheses P-values §5.3.2.3, the global hypotheses HMPs, as well as how is performed hypothesis testing §5.3.2.4.

5.3.2.1 Laying out the hypotheses of interest

When studying bcc and B2 metals, one might want to test specific hypotheses, for example from literature it is expected that some B2 compounds slip exclusively on {110} planes, i.e. the hypothesis: “100% of slip occurs on {110} planes” is of interest. It is also thought that in bcc Fe the CRSS of plane types {110}, {112} and {123} are similar [45], therefore under a random stress state one could assume the activation of a mix of all plane types in the following proportions: 12/48 {110}, 12/48 {112}, 24/48 {123} based on their respective number of independent slip systems, making such hypothesis of interest. The problem with testing only such hypotheses is that we are already starting to draw a conclusion based on what we think should happen, and discarding many possible slip activities. Since we are using automation tools, it is very easy to test any hypothesis, the only limiting part being the computation time required. In this work, will be tested all hypothesis Hi defined as:

$$\text{Hi: } \{100\}_p \text{ , } \{110\}_p \text{ , } \{112\}_p \text{ , } \{123\}_p$$

such that $\{100\}_p + \{110\}_p + \{112\}_p + \{123\}_p = 1$

With $\{xyz\}_p$ the proportion of {xyz} slip systems activated under a random applied stress state. A 5% step in proportions of active planes between each hypothesis will be used, ranging from 0 to 100% for each plane type.

e.g.:

H1: 100% $\{100\}_p$, 0% $\{110\}_p$, 0% $\{112\}_p$, 0% $\{123\}_p$

H2: 95% $\{100\}_p$, 5% $\{110\}_p$, 0% $\{112\}_p$, 0% $\{123\}_p$

H3: 90% $\{100\}_p$, 5% $\{110\}_p$, 5% $\{112\}_p$, 0% $\{123\}_p$

Etc.

This leads to a total of 1772 hypotheses tested. Notice that these hypotheses include the hypotheses evoked above such as 100% of {110} slip, and 12/48 {110}, 12/48 {112}, 24/48 {123} slip.

5.3.2.2 Calculating expected measurement

Now that the hypotheses have been defined, we need to estimate what measurement is expected under each hypothesis, given the hypothesis to be true. This estimation can be made via the simulation of randomly oriented lines, in a similar way to what was done in previous works ([95] and Chapters 3 and 4). Here there will be a major difference in that the line orientations will not be generated completely randomly, but will be biased in their orientations along specific plane type orientations based on the specific hypothesis considered. For example, if testing the hypothesis “100% of slip occurs on {110} planes”, the simulation will randomly generate 100% of lines closely oriented to random {110} plane orientations, and measure what plane orientations they match. This simulation will be made for each grain orientation tested in the sample, as each grain orientation is expected to show distinct probabilities of matching the plane types, and for each hypothesis tested. This simulation process is presented in Figure 38.

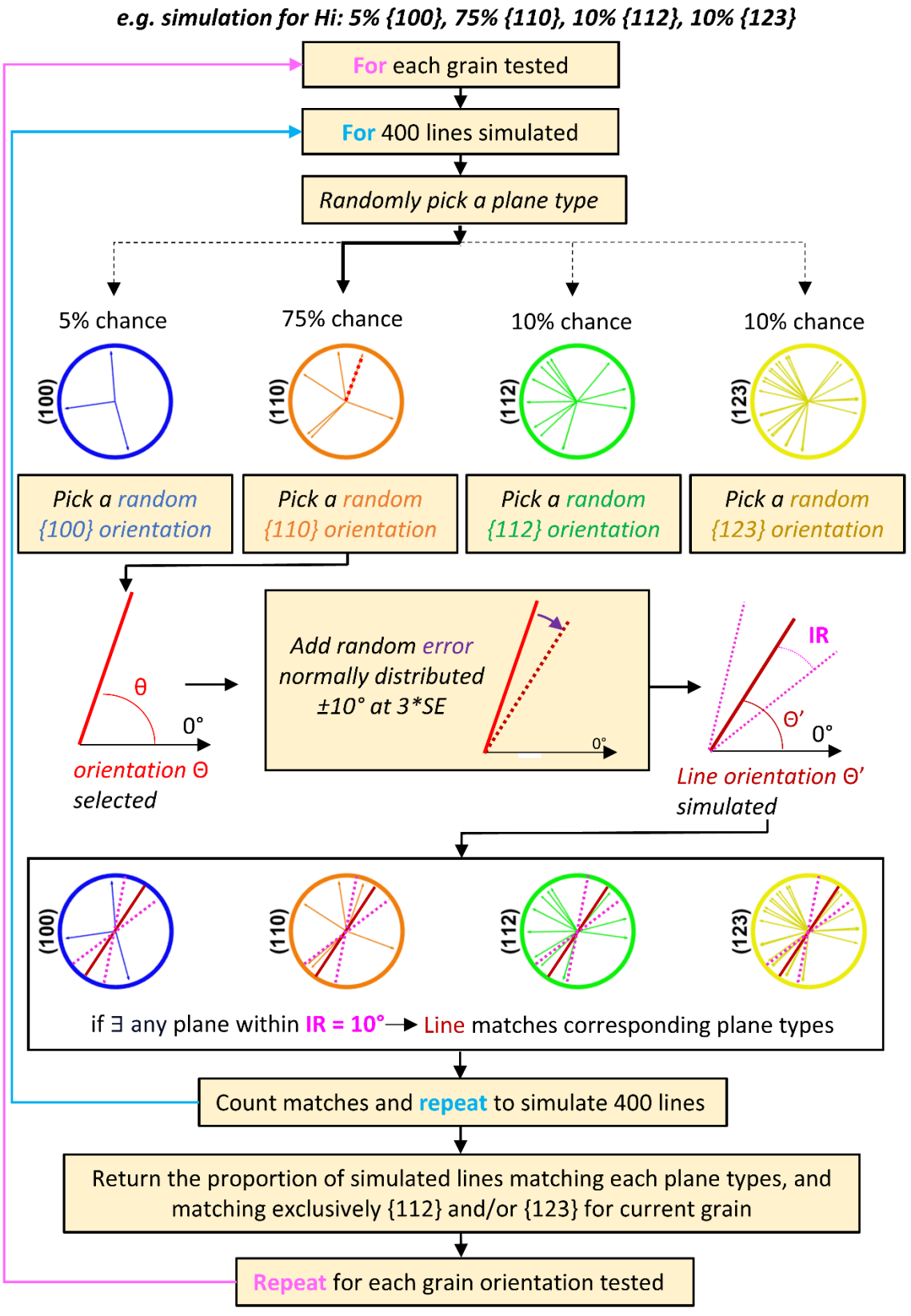


Figure 38: Expected measurement simulation process for each Hi. In this example, Hi presumes a slip activity in proportions $\{100\}_p$=5%, $\{110\}_p$=75%, $\{112\}_p$=10%, and $\{123\}_p$=5%. Theoretical plane orientations are calculated based on the average crystal orientation in the grain tested. Each proportion of match obtained gives the corresponding probability of matching estimated for each grain under Hi.

In the example in the Figure 38, is calculated the expected proportion of slip traces that will be observed as matching each plane type (for each grain tested), in a specific sample with a specific set of grain orientations tested, based on the hypothesis Hi which here supposes a bulk sample slip activity of 5% {100}, 75% {110}, 10% {112} and 10% {123}. First, each simulated line orientation is randomly selected from the theoretical slip trace orientations calculated based on the EBSD determined grain orientation considered, amongst each plane type with a certain probability based on the hypothesis tested. Then, after a line orientation is randomly selected, a random angular error is added to it, normally distributed so that the lines have <99.7% chance (3*SE) to be within 10° of the original orientation. This error simulates the experimental variability of the slip trace orientation detection based on estimations made in our previous work (Chapter 3). Indeed, it is not expected that the slip traces detected will be perfectly aligned to the theoretical slip planes, they should have a variable angular error compared to these, due to inaccuracies in the EBSB determined Euler angle, imaging conditions, local crystal rotations, and line orientation detection inaccuracies (code related). Finally, the simulated line orientation is compared to each plane type theoretical slip trace orientations, using an identification range IR of 10° to consider orientations as matching, so to be in the same conditions as during experiments. The code also tests if the line orientation is unambiguously <111>, i.e. if it matches exclusively {112} and/or {123}.

Due to this random normally distributed angular error, it is possible for simulated lines to have more than 10° of difference with their original plane orientation, which means that the simulation anticipates a small proportion (0.03%) of misattributed lines within the data sets. The choice of 10° at 3*SE is arbitrary (although, based on previous experimental work, see Chapter 3), but note that attempts at running the analysis using 10° at 2*SE (95.3% of simulated lines are within 10°) lead to overall similar calculated probabilities and P-values. However, this choice can have some importance for extreme case scenarios, for example if it is expected exactly 0% of match or 100% of match, as the variability of the sample response in such contexts is expected to be exactly null (the P-values calculations can behave asymptotically in these contexts). These small changes in expected proportions of misattributed lines can make a difference on whether these “extreme” hypotheses are considered reasonably likely or not. This will be taken in consideration during our analysis of the samples §5.4, however, note that it only concerns a few boundary case scenario hypotheses and this choice should have a neglectable impact on most hypotheses tested.

These probabilities (or expected proportions of match) are estimated from a population of 400 randomly oriented lines, and are therefore given with a certain standard error. The standard error is maximal if an event has 50% chance of success, and decreases if the probability of success is closer to 0 or 100%. Based on binomial statistics, this maximal standard error can be calculated using the following formula:

$$(1)\ SE = \frac{1}{\sqrt{n}} * \sqrt{p(1-p)}$$

Injecting p=0.5 and n=400 in (1):

$$(2)\ SE = \frac{1}{\sqrt{400}} * \sqrt{0.5(1-0.5)} = 0.025$$

These estimations of probabilities of success should therefore be given with a standard error of at worse 2.5% when the estimated probability of success (of matching) is 50%. We limit ourselves to 400 lines since we will be testing 1772 hypothesis, and the computation time increases dramatically as the number of lines simulated increases (currently close to 15 min per grain tested). We choose to test more hypothesis, with a slightly lower accuracy, than to test less hypothesis with a higher accuracy, as in a sense the high number of similar hypotheses tested compensates for their individual P-value imprecisions, we are doing statistics within statistics. This uncertainty on the probabilities estimated in each grain accumulates the more grain orientations are tested, which will affect the accuracy of the P-values calculated from them, which also cascades down to the HMP calculation. Such variability is difficult to solve analytically, but will be visible and accounted for in the result section §5.4.1.5 when comparing the HMPs of different hypotheses.

5.3.2.3 P-Value calculation

The P-value calculation is performed using the Poisson binomial Distribution. The Fourier transform approach is used to do these calculations, and the number of observed successes is rounded up (ceil) or down (floor) so to pick the scenario of highest P-value, as was described in §5.3.1.2.1, using as inputs:

- The experimentally measured proportion of lines matching each plane types in a grain, or unambiguously <111> (i.e. that match exclusively {112} and/or {123}), averaged between all grains tested
- The probability of matching each plane types, or unambiguous <111> orientations, in each grain, based on the simulation (previous §5.3.2.2) for the hypothesis tested.

The following Figure 39 summarises the calculation process, in terms of inputs and outputs, for each Hi tested.

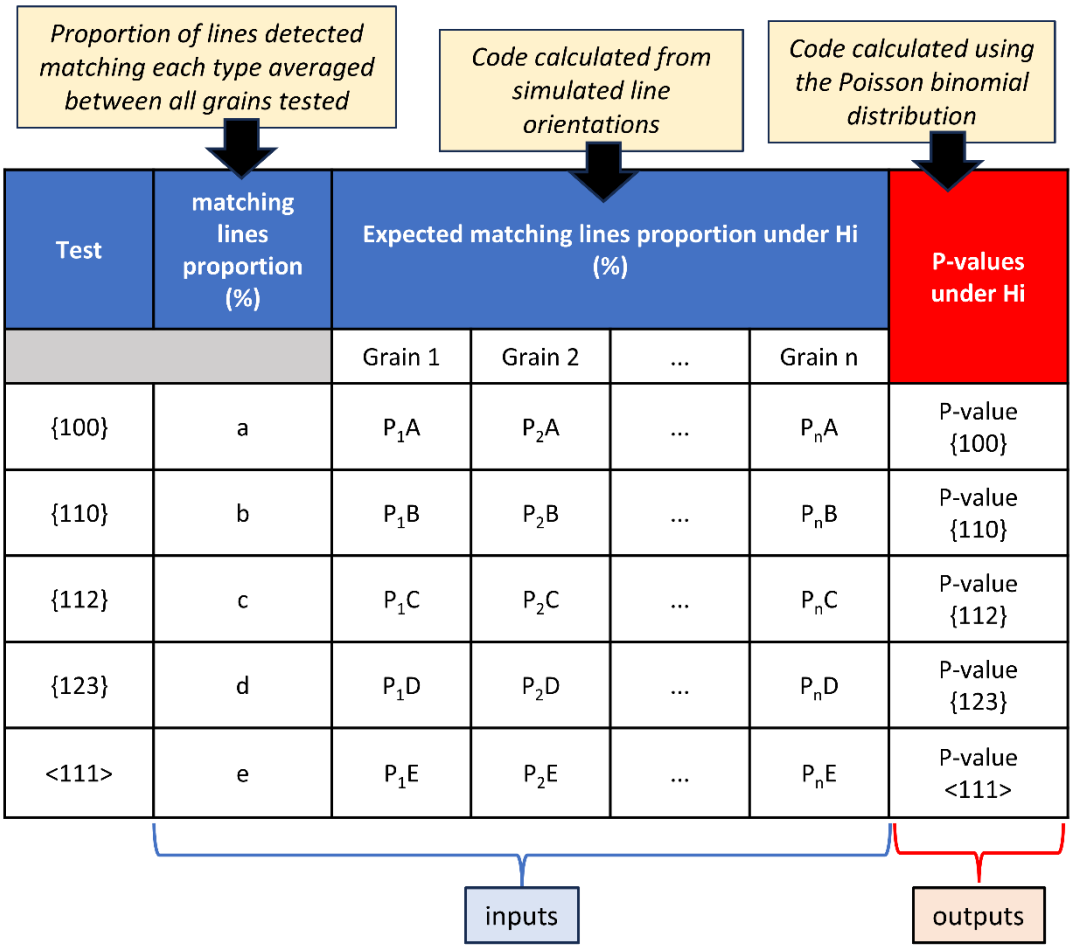


Figure 39: Illustration of the P-value calculations in terms of inputs and outputs, for n grains analysed in the sample and for each Hi tested. All five P-values will be used to calculate the harmonic mean P-value of each Hi (next section).

5.3.2.4 HMP and hypothesis testing

Finally, a harmonic mean P-value associated to the global hypothesis Hi is calculated from the individual P-values associated to each test calculated as in previous section §5.3.2.3 under Hi, which we will note $\{p_{1i}, p_{2i}, p_{3i}, p_{4i}, p_{5i}\}$ following the row order of the table in Figure 39. Taking back the equation of the HMP, the HMPi of hypothesis Hi is therefore calculated as:

$$HMPi = \frac{1}{\sum_{n=1}^{5} \frac{1}{5 * p_{ni}}}$$

Hypothesis testing is then performed as follow:

For each Hi: if HMPi <0.05, reject hypothesis

The evidence gathered is considered strong enough to reject the corresponding Hi if the HMPi calculated is <0.05, which should allow to draw conclusions on the samples bulk slip activities at a 95% confidence level, based on our discussion §5.3.1. The hypothesis rejection rate "r" is then calculated, defined as:

$$r = \frac{n(Hi\ rejected)}{n(total\ number\ of\ Hi)}$$

This rejection rate will be compared between the samples to see how efficient the statistical analysis is at narrowing down the possible slip activity hypotheses depending on the experimental measurement and the number of grains tested.

5.4 Results

The data sets of different samples previously analysed using automated indentation-based slip trace analysis, including bcc Fe, B2 TiFe, and B2 (17)Ni-(43)Fe-Al (at.%) were processed for hypothesis testing using the methodology proposed in §5.3.2. The data used as an input for each sample is the proportion of lines matching each plane type or unambiguously <111>, averaged between all grains, from an analysis using 10° IR, a score threshold of 10 and a segmentation size of 100px (identical to previous Chapter 3 and 4 when analysing slip traces outside large indents), and the list of grain orientations (Eulers angle) tested in each sample. The P-Value calculations and hypothesis testing are based on the following assumptions:

- It was assumed that during indentation, the slip traces would be generated on random active slip planes in proportions corresponding to what we call the "meso-scale bulk slip activity" of the sample
- It was assumed that lines detected on slip traces have a random orientation normally distributed within 10° of the originating slip plane theoretical orientation (at 3*SE, i.e. 99.7% chance to be within 10°).
- It was assumed that at least one new randomly stressed slip is observed per grain orientation tested.

All the assumptions, and associated statistical procedures, were made to guarantee control over the type 1 error rate, so to draw conclusions at a 95% confidence level, but note that multiple approximations made to allow these calculations are likely to reduce the power of the analysis and may lead to fewer rejections than what could be achievable.

In this section, we will first go in details on the analysis of B2 TiFe §5.4.1, to check the validity of this statistical analysis, observing whether the estimated probabilities and P-values are a priori consistent with expectations. At the same time, we will see dependency links between the different plane types probability of matching (geometry related) §5.4.1.2 as well as the influence of including or ignoring additional tests when the corresponding slip planes are not expected to be active §5.4.1.6. After that in §5.4.2, we will see the influence of gathering additional data by repeating the experiment on a second B2 TiFe sample of similar composition, and seeing how the hypothesis rejection rate evolves when performing the meta-analysis of both datasets. Then §5.4.3 we will compare the results of the statistical analysis between different samples displaying different slip activities, gaining new insights on there likely bulk slip activities. Finally, in §5.4.4, we propose to estimate the amount of data that would be needed to come to specific conclusions using this indentation-based slip trace analysis methodology, gaining insights on their experimental feasibility.

5.4.1 Demonstration - Analysis on TiFe

5.4.1.1 Decomposition of the analysis

During the estimation of the P-values and calculations of the probabilities, we had to make a few assumptions and approximations on the nature of the data measured, which may lead to errors in the calculations and the hypothesis testing. We propose a few checks to see if the results are a priori consistent with expectations. The data set of B2 TiFe gathered in Chapter 3 will be used, comprising 9 grain orientations tested. During this experiment, it was found the following proportion of lines matching each condition (averaged between the grains):

56.5% {100}, 100% {110}, 39.1% {112}, 53.2% {123}, 0% <111>

With "<111>" being lines matching exclusively {112} and/or {123} orientations, therefore providing unambiguous evidence of active <111> type slip direction (here, none were observed). These results were considered consistent with common reported B2 slip activities involving predominant slip on {110} planes (all slip traces observed match {110} orientations), which was therefore attributed to this sample. This statement is also in agreement with previous reports of <100>{110} slip in B2 TiFe [125]. From there, the objective of the statistical analysis would be to measure how strongly the data gathered in B2 TiFe is in support of this hypothesis, and whether other slip activity hypotheses could reasonably lead to the same experimental outcome.

In a first time, only hypotheses involving a mix of {100}, {110} and {112} active slip planes will be considered since those are the most reported B2 slip planes, and allow easier visualisation than in the quaternary situation (which will be represented §5.4.2 and §5.4.3). The average probabilities of matching in each grain, estimated via simulation, and the calculated P-values are shown on Figure 40, for each plane type or unambiguous <111> type slip. On the ternary plots (Figure 40), all Hi presuming slip plane activation in proportions such as $\{100\}_p+\{110\}_p+\{112\}_p=1$, and $\{123\}_p=0$ are represented.

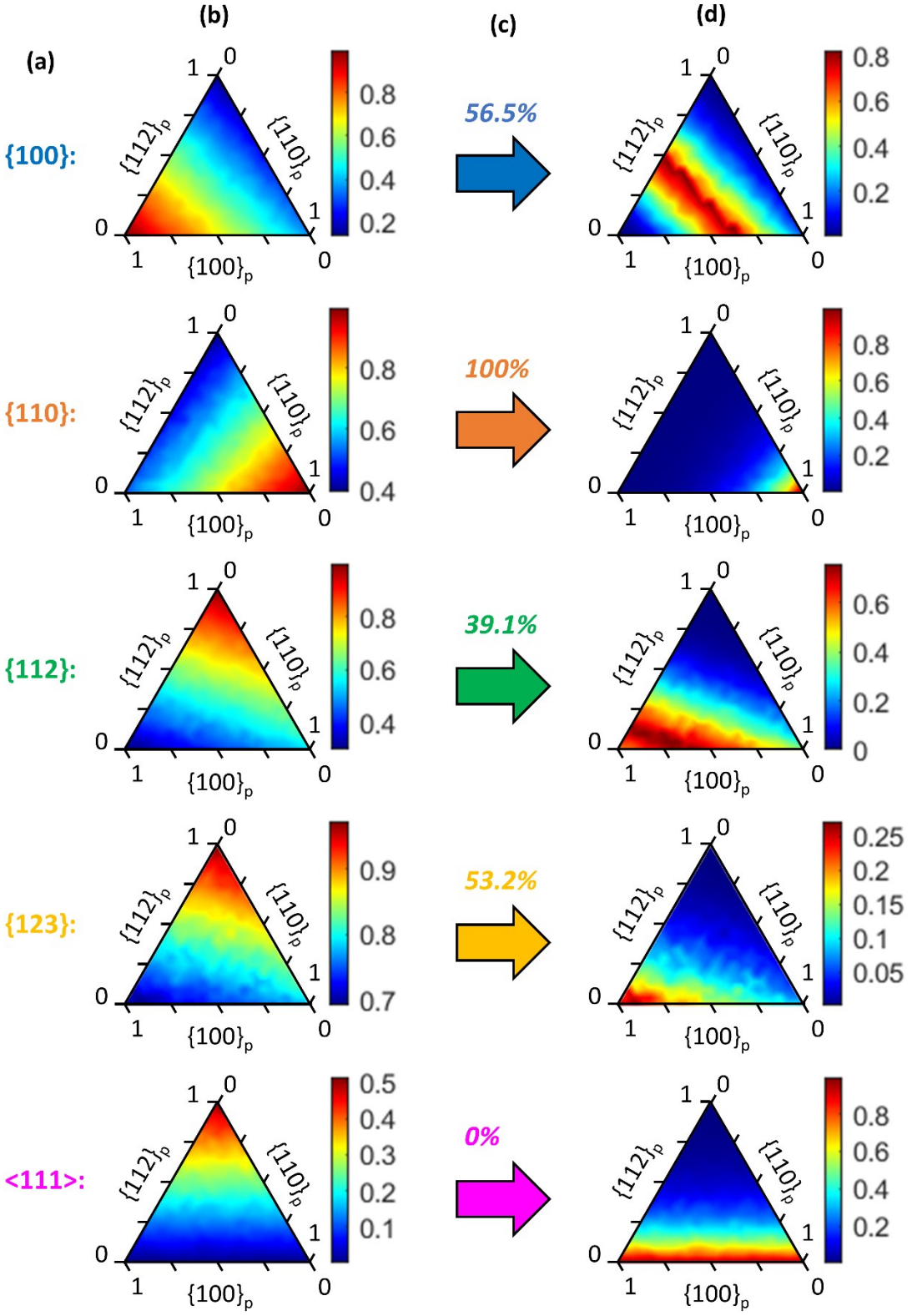


Figure 40: Statistical analysis of the B2 TiFe dataset (9 grains). (a) the event (or test) considered, i.e. observing a line matching a plane type orientation or matching exclusively {112} and/or {123} (« <111> »). (b) The estimated probability of success of the event, averaged between the grains, (c) the experimentally measured proportion of success and (d) the P-value of obtaining said experimental measurement. The ternary diagrams are plotted as a function of the presumed proportions of active slip planes under each Hi, such that $\{100\}_p+\{110\}_p+\{112\}_p=1$

5.4.1.2 Estimated probabilities & geometrical dependencies between planes

Let us start by looking at Figure 40 (b). The average probability of matching each plane type in the 9 grains tested is represented for each Hi. Note that the probability of matching can vary significantly from grain to grain (not represented), which was taken in consideration for the calculation of the P-values (§5.3.1.2.1 & §5.3.2.3). Looking at the estimated probability of matching {110} planes under each hypothesis considered, we see that those are highest under hypotheses involving large proportions of active {110} planes, which is consistent with expectations. Similarly, the estimated probability to match {112} planes is highest under hypotheses of high $\{112\}_p$.

Beyond these simple checks, we gain insights as to the geometrical dependencies between the different plane types. Indeed, we see that the probability of matching {110} planes is higher under hypotheses of high $\{100\}_p$ (≈50%) than under hypothesis of high $\{112\}_p$ (≈40%). This means that lines detected on a sample of slip activity involving dominant {100} type slip are more likely to frequently match {110} orientations than if the slip activity involved dominant {112} slip. As for {112} and {123} planes, we find that the probability to match {123} is highest assuming $\{112\}_p$ is very large, reaching close to ≈97% if $\{112\}_p=1$. The reciprocal was also calculated (not represented here), and it is found that on this dataset, the probability to match {112} assuming $\{123\}_p=1$ is ≈82%.

We see again links between the probabilities of matching the different plane types. Those confirm our suspicions of geometrical dependencies between the plane types, with respectively {100}-{110} and {112}-{123} theoretical orientations likely to be closely oriented, i.e. to be ambiguously oriented with each other. Hypotheses involving these pairs of slip activities will therefore be more challenging to tell apart as they expect similar experimental measurements (also discussed later in §5.4.4).

An unexpected dependency between the plane types is that the probability to match {112} planes is especially low when supposing slip predominantly on {100} planes, ≈30% if $\{100\}_p=1$ compared to ≈54% assuming $\{110\}_p=1$, which means that a low measured proportion of {112} match can be a strong indication of active {100} planes.

Let us look now at the probability of being unambiguously <111>, i.e. to match exclusively {112} and/or {123} planes, since these observations were crucial in our previous works (Chapters 3 and 4). This test is uniquely different to the others in that it does not correspond to any specific plane type, it is an additional measurement, an additional test, which was designed specifically for identifying unambiguous evidence of <111> type slip. We see on Figure 40 (b) that the probability of observing such slip traces is high for slip activities involving active {112} planes, reaching at maximum ≈50%, and tends to be 0% for slip activities involving exclusively {100} and {110}. This is of course, exactly what is expected, since unambiguously <111> type slip traces are defined as slip traces not matching {100} and {110} planes, making them unlikely to be observed if {100} and {110} planes are frequently activated. These large differences in probabilities, 0 versus 45%, mean that considering this <111> test will be very efficient for distinguishing slip activities involving {112} & {123} planes from slip activities involving {100} & {110} planes. However, this test is basically powerless for differentiating

{110} from {100} dominated slip activities, as the same 0% of success is expected for all these hypotheses.

A last observation is that, apart from the <111> test, these probabilities are never constant nor symmetrical in these ternary plots, this means that all hypotheses should have a different set of expected match proportions for each plane type, and may therefore be statistically disproven if sufficient data is gathered (see §5.4.4).

5.4.1.3 P-value calculations on TiFe

From here on, when referring to "the {110}-{100} axis", we will refer to the range of hypotheses presuming $\{110\}_p+\{100\}_p = 1$. On Figure 40 (d) are represented the calculated P-values using the data gathered in B2 TiFe, obtained from comparing the amount of match experimentally observed (Figure 40 (c)), to the estimated probability of matching in each grain, under each hypothesis (the calculations are described in §5.3.2.2 & 5.3.2.3). By definition, the P-value of a hypothesis should be high if the experimental outcome is close to the expected measurement, as opposed to lower the further apart the experimental measurement is to the expected value.

Let us start by looking at the {110} plane match test. It was experimentally measured that 100% of detected lines match {110} planes, therefore hypotheses involving predominant slip on {110} planes should be well supported by the data with regards to this particular test. Indeed, looking at the P-value corresponding (Figure 40 (d)), the highest P-values are found for hypotheses assuming predominant slip on {110}. Now looking at the {100} plane match test, which was experimentally measured to be 56.5%, we see that a large range of hypotheses expect close to 56.5% of {100} match (Figure 40 (b)). Looking now at the P-value calculation for this test (Figure 40 (d)), we see that a large range of hypotheses are considered "similarly supported", with the highest P-values correlating with the hypotheses expecting a probability of matching {100} planes close to 56.5%. One last obvious example is the <111> test P-values. As we can see, the experimental outcome, 0% of <111> type match, best supports any hypothesis involving a mix of exclusively active {100} and {110} planes with high P-values, close to 1, along the {100}-{110} axis.

These observations extend to all P-values calculated, showing that the calculations behave as expected and demonstrating that, a priori, the probability estimations and P-value calculations give results consistent with expectations.

5.4.1.4 Harmonic P-value and hypothesis testing

From the P-values associated with each test, a harmonic mean P-value (HMP) is calculated for the global hypotheses, taking in consideration all tests P-values simultaneously. These HMPs can be interpreted directly as the P-values corresponding to the global hypotheses on slip activity, which is an accurate statement when the HMPs are small (e.g. <0.05) but gets increasingly inaccurate as the HMPs get higher than 0.05. High HMPs can still be interpreted comparatively.

The HMP accounts for the increase in FWER associated with the multiple hypothesis testing problem, and evaluates the information brought by each test P-values simultaneously. From Figure 40 (d), those can be qualitatively assessed:

- The {110} P-values best support slip activities involving dominant slip on {110}
- The <111> P-values best support hypotheses along the {110}-{100} axis, and show strong evidence against hypotheses involving a large $\{112\}_p$
- The {112} and {123} P-values best support hypotheses on the {110}-{100} axis, with a slight preference for hypotheses presuming dominant slip on {100}
- The {100} P-values support a large range of hypotheses, but present evidence against hypotheses involving predominant slip on {100} or {112}

The HMPs calculated from these P-values are represented in Figure 41, next to the hypothesis testing plot where it is shown which hypothesis are rejected at a 95% confidence level (i.e. when HMPi < 0.05).

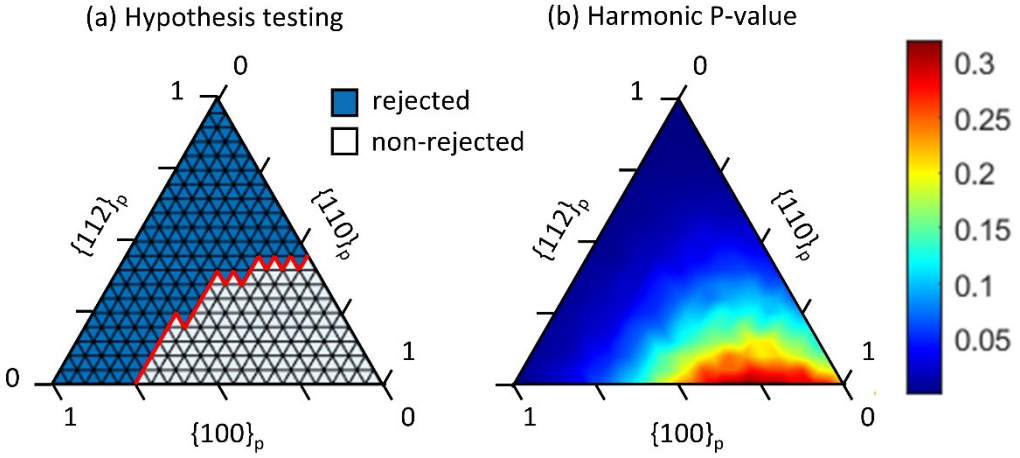


Figure 41: Statistical analysis on B2 TiFe (9 grains indented) with (a) the hypothesis testing at a 95% confidence level, from the calculated Harmonic P-value (HMP) represented in (b), for each hypothesis Hi, as a function of the presumed proportion of active {100}, {110} and {112} planes. A Hi is rejected if HMPi<0.05. In (a) a Hi on the red line is rejected by the statistical analysis.

As can be seen on Figure 41 (b), the HMPs calculated appear to best support hypotheses along the {110}-{100} axis, in particular the {110} dominated hypotheses, which is consistent with the information brought by each test P-values. On Figure 41 (a) the hypothesis test is performed on these HMPs. It can be seen that unrejected hypotheses are concentrated along the {110} – {100} axis, and the hypotheses of smallest $\{110\}_p$ rejected expect 25% {110}.

Therefore, a formal conclusion based on this statistical analysis can be drawn as follows: the analysis, after indenting 9 grains, estimates at a confidence level of 95% that the B2 TiFe sample, when subjected to a random applied stress, must be slipping on {110} planes >25% of the time. The results of the analysis support notably a range of hypotheses involving a mix of {110} and {100} slip planes, including the hypothesis of slip exclusively on {110} slip planes, which is consistent with previously reported B2 slip activities, and TEM reports of B2 TiFe slipping on <100>{110} slip systems.

5.4.1.5 Inaccuracies in the estimations

As those calculations are based on the probability of success of each test, which was estimated via simulation, these P-values are given with some inaccuracies. To gain clearer insights on these variabilities, Figure 42 represents the P-values calculations for each test (Figure 42 (a)) and the resulting HMP (Figure 42 (b)) for hypotheses on the {100}-{110} axis.

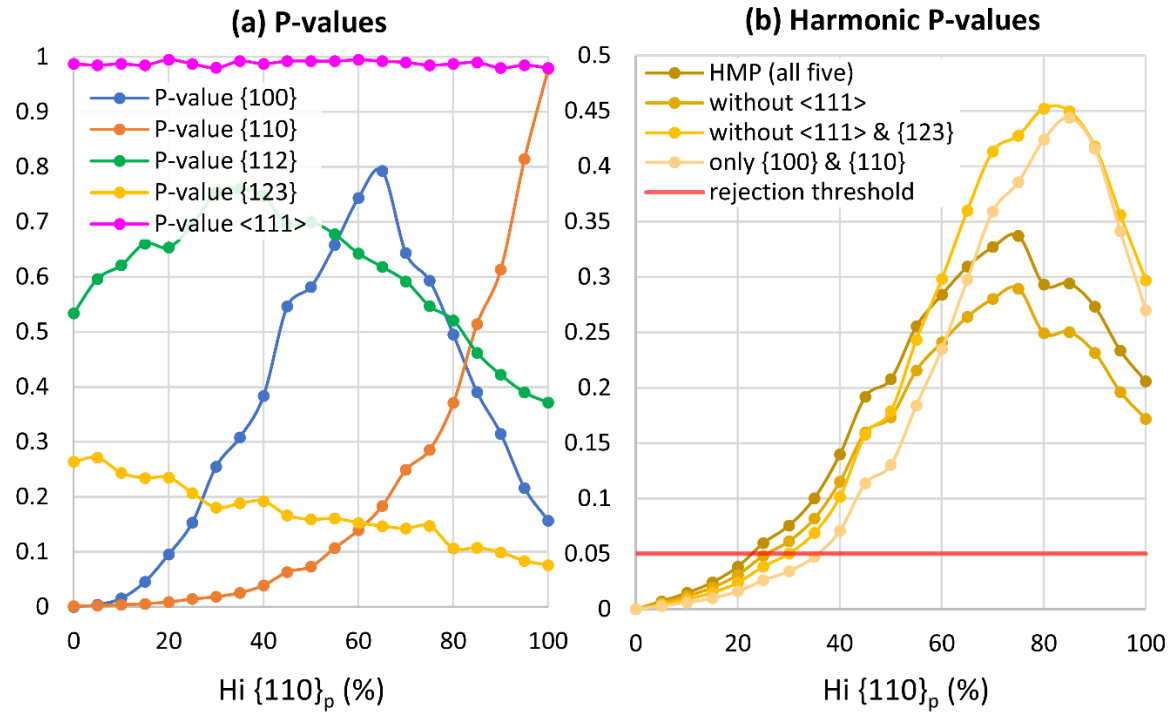


Figure 42: Statistical analysis on B2 TiFe, for each hypothesis Hi tested which presumes $\{100\}_p+\{110\}_p=1$. (a) Shows the P-values calculated for each measured plane type and exclusive {112} and/or {123} (« <111> ») line matching proportions. (b) Shows the Harmonic mean P-values (HMPs) calculated from these five tests P-values, and the HMPs when ignoring one or more test, which reduces the FWER.

Looking Figure 42 (a) it can be noticed that the P-values do not form bell-shaped curves, with notably a "peak" of high P-value for the {100} test near $\{110\}_p=65\%$. This is due in part to the discontinuity introduced by the "rounding approximation" (see §5.3.1.2.1) abruptly changing the P-values when the expected and measured proportions are close, but also to the variation of probability of success between the grains tested, resulting in a likely asymmetrical probability distribution of the experimental outcomes.

Another observation is that both the P-values on Figure 42 (a), and the resulting HMPs on Figure 42 (b) show visible variability, i.e. their curves are not smooth. This is a direct consequence of the standard error on the probability estimations (SE≤2.5%, see §5.3.2.2). We note, however, that these variabilities appear to be very small for the hypotheses considered here, and the HMPs curve calculated from the five tests P-values is reasonably steady. Therefore, this lack of smoothness should only marginally affect the hypothesis testing close the 0.05 threshold, and mostly for hypotheses where the probability of success of their tests (sub-hypotheses expected match proportions) are estimated close to 50%.

These observations highlight that we need to take the P-value calculations with a grain of salt. Although they appear to behave as expected, they are given with a set of assumptions and experimental variabilities which may have an impact on boundary case scenarios, e.g. when considering extreme experimental results (100% or 0% of match), and when many HMPs are close to the 0.05 threshold for hypothesis rejection (the variability may lead to a portion of these HMPs getting wrongly rejected). However, the overall trend of the HMPs should give a reasonably good approximation of the statistical behaviour. In order to take into account the variability in these estimations we propose to add a 5% uncertainty to our formal conclusion (since 5% is the step between hypotheses tested), and state for example that the B2 TiFe sample slips >20% of the time on {110} planes, instead of >25%, with a confidence level of 95%.

5.4.1.6 On the inclusion of additional tests

Since the more sub-hypotheses are tested simultaneously, the more the FWER should increase, we might be tempted to ignore additional tests which do not bring any useful information to the analysis, in order to increase the hypothesis rejection rate. For example, if we start considering literature, we know that TiFe most likely slips in the <100> direction, and therefore hypotheses involving {112} and/or {123} slip could be ignored. On Figure 42 (b) are represented the HMP calculations for hypotheses involving exclusively a mix of {110} and/or {100}. Those HMPs are calculated (a) considering all 5 tests (b) ignoring the <111> test (c) ignoring both the <111> and {123} tests and (d) considering exclusively {110} and {100} tests.

We can see that the more tests are ignored, the more hypotheses are rejected by the statistical analysis. Indeed, this is expected when ignoring the <111> test, as it shows almost identical P-values assuming predominant {100} or {110} slip. This test does not bring any information to differentiate between hypotheses on the {100}-{110} axis, and therefore, taking it in consideration only results in an increase in the FWER, and therefore in less hypotheses rejected. For the other {112} and {123} tests, we notice that their P-values are not constant on the {100}-{110} axis (Figure 42 (a)), therefore, they may bring some information to the analysis to distinguish between these hypotheses. However, as we can see on Figure 42 (b), the HMPs decrease near the 0.05 threshold resulting in more hypotheses rejections if ignoring the {112} and {123} tests. Therefore, in this context, the {112} and {123} tests do not seem to bring enough information to compensate for the increase in FWER due to their inclusion in the analysis. A note that these observations were made using the B2 TiFe dataset, and some of the tests discussed could have more influence under different experimental conditions (typically if the IR decreases, which will affect the probabilities of matching each plane type) or if more data is gathered. When ignoring <111>, {112} and {123} measurements, the smallest $\{110\}_p$ Hi rejected increases from 20% to 30%.

In conclusion, the impact of the inclusion of additional tests in the analysis is situational, all plane types and <111> type match proportions can bring useful information to the hypothesis testing depending on what hypotheses we seek to investigate and/or differentiate. Other tests could also be included, for example testing if the lines match exclusively {100} planes. Based on the present analysis, we find no real benefit in making generic assumptions on the sample slip activities, and ignoring some of the tests. Therefore, to maintain consistency with our

previous works (Chapters 3 and 4), and to easily compare between samples, all five tests will be considered when assessing the samples slip activities in the following sections.

5.4.2 TiFe and meta-analysis

The statistical analysis on B2 TiFe showed the expected statistical behaviour from the estimations of probabilities, P-value calculations for each measurement, and HMP calculations. However, the outcome ">20% of active {110} planes" may be disappointing, since this leaves a wide range of plausible B2 slip activities involving a mix of {110} and {100} planes. In practice we expect from literature [125], and our own appreciation of the experiment (Chapter 3), that TiFe most likely slips predominantly on {110} planes, which cannot be concluded with certainty based on this statistical analysis.

For the specific case of B2 TiFe, which is of particular interest to the development of titanium-based bcc+B2 alloys [3] [36], another experiment was performed to gather more data. A new B2 TiFe sample (sample 2) was prepared following the same methodology as the B2 TiFe sample described in Chapter 3 (sample 1) . One difference is that sample 2 was heat treated longer (100h instead of 24h) which lead to larger grains. The sample's composition was measured using Scanning Electron Microscopy Energy Dispersive X-ray spectrometry (SEM/EDX), from three ≈500mm scans of 30s each at 20kV, and found to be 50.9±0.1Ti & 49.1±0.1Fe at.%, which is considered close enough to the composition of sample 1, i.e. 51.6±0.2 Ti & 48.4±0.2 Fe at.% (determined in Chapter 3). Sample 2 notably displayed similar microstructural features as sample 1, including visible hydrides, and a small volume fraction of titanium rich precipitates. The sample was microhardness indented using a ≈0.5kg load, similarly to sample 1, and slip traces imaged in the same Apreo HiVac SEM, using the same imaging conditions (see Chapter 3). The hydrides were a bit larger in this sample, which affected the visibility of some slip traces. In total, 7 imaged grains, which gave satisfactory slip trace detection when processed using the automated slip trace analysis code, were analysed in the new sample (using the same code parameters as sample 1).

This new sample gives the opportunity to compare the results of the statistical analysis of two, reasonably similar samples, performed on separate dates but using the same equipment and methodology. Furthermore, a meta-analysis can be performed by combining the data gathered in the two experiments, seeing the direct influence of gathering more data on the hypothesis rejection rate. Note that different statistical approaches can be used to perform meta-analysis, e.g. using the P-values calculated in each experiment [126], but we will here use the easier and more appropriate option of simply combining the datasets as those should be compatible.

A single line detected in sample 2 was identified as being unambiguously <111> (amongst hundreds). After visually inspection of the code output, this line is most likely an error in the detection. Rather than eliminating the corresponding grain (which otherwise presents very good slip trace visibility) from the analysis, it was decided to keep the data from this grain, but round the measured {110} and <111> type matches (respectively to 100 and 0%), so to avoid having to perform the "rounding approximation" when calculating the corresponding P-values (see §5.3.1.2.1). This leads to a few more hypotheses being rejected by the statistical analysis,

since these two tests P-values no longer need to be overinflated, and is unlikely to increase the type 1 error rate.

The next Table 7 shows the average proportions of lines matching the different conditions between the grains tested in each experiment, 9 grains in sample 1, and 7 grains in sample 2. The meta-analysis values are obtained by averaging between the respective measurements of all 16 grains.

Table 7: Proportion of detected lines matching each condition, averaged between the grains tested, for each experiment and the meta-analysis on B2 TiFe

Test	{100} (%)	{110} (%)	{112} (%)	{123} (%)	<111> (%)
Sample 1	56.5	100	39.1	53.2	0
Sample 2	57.2	100	29.0	59.1	0
Meta-analysis	56.8	100	34.7	55.8	0

As can be seen in Table 7, the measured match proportions on sample 2 are very similar to sample 1, suggesting a good repeatability of the experimental approach, and likely similar slip activities. The hypotheses HMPs are calculated for all slip activity hypotheses considered, involving any mix of {100}, {110}, {112} and {123} planes, with a step of 5% in proportion of planes activated between hypotheses. These are represented as tetrahedrons on Figure 43, and the corresponding hypothesis testing are shown on Figure 44. The representation as tetrahedrons, inspired from [127], allow to visualise most hypotheses simultaneously and give an easy to interpret, straight forward insight on the behaviour of the HMPs, highlighting which families of hypotheses are best supported by the measurement, and which hypotheses are clearly rejected. On these tetrahedrons, the vertices represent hypotheses presuming one exclusively active slip plane type, the edges a mix of 2 active plane types, the faces a mix of 3 active plane types, and finally the volume a mix of four active plane types.

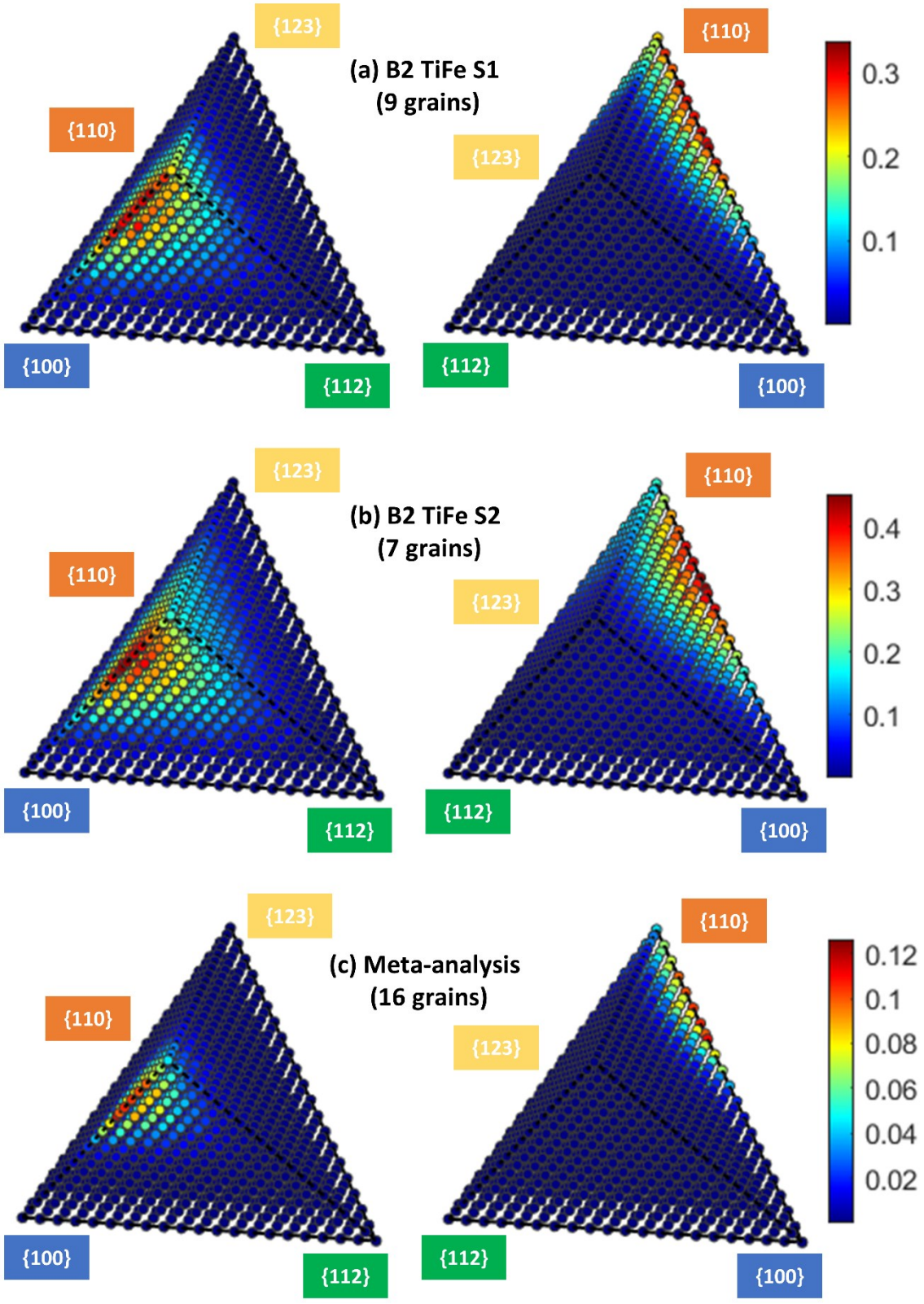


Figure 43: Harmonic mean P-values calculated for each hypothesis Hi, as a function of the presumed proportion of active {100}, {110}, {112} and {123} planes. The tetrahedrons are shown from two perspectives, where the vertices labels show which plane type is assumed predominant, e.g. at the vertex « {110} » the Hi presumes $\{100\}_p+\{112\}_p+\{123\}_p=0$ and $\{110\}_p=1$. (a) analysis of the first B2 TiFe sample « S1 » (b) analysis of the second B2 TiFe sample « S2 » and (c) meta-analysis combining both datasets.

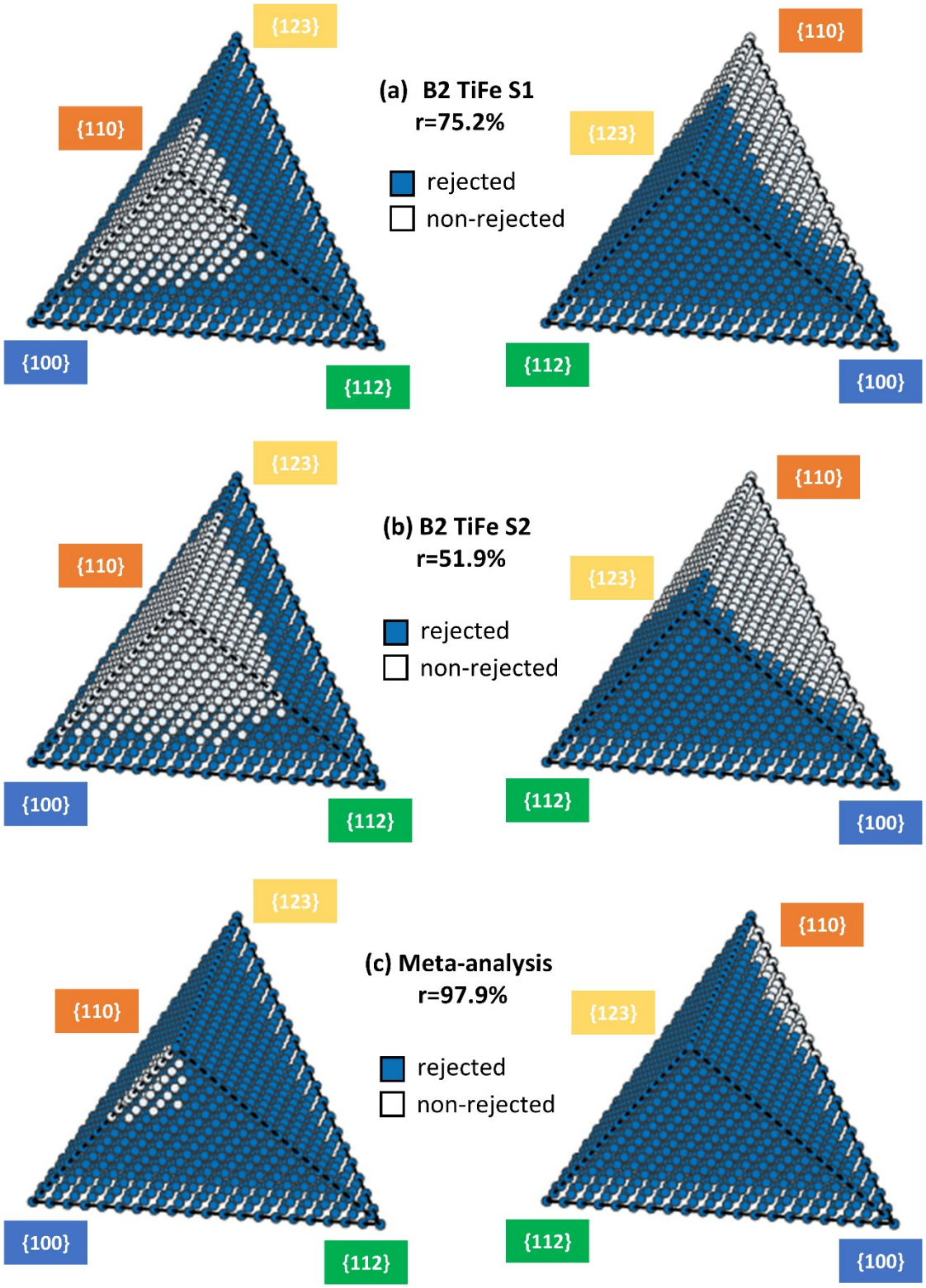


Figure 44: Hypothesis testing for each hypothesis Hi, as a function of the presumed proportion of active {100}, {110}, {112} and {123} planes. The tetrahedrons are shown from two perspectives, where the vertices labels show which plane type is assumed predominant, e.g. at the vertex « {110} » the Hi presumes $\{100\}_p+\{112\}_p+\{123\}_p=0$ and $\{110\}_p=1$. (a) Analysis of the first B2 TiFe sample « S1 » (b) Analysis of the second B2 TiFe sample « S2 » and (c) Meta-analysis combining both datasets. A hypothesis Hi is rejected if its HMPi < 0.05. The hypothesis rejection rate r = n(rejections)/n(hypotheses) is indicated for each sample.

Let us look first at the Figure 43 (a), where HMPs calculated from the dataset of sample 1 are represented for each Hi. We see that high HMPs are concentrated along the {100}-{110} axis, suggesting that hypothesis involving a mix of {110} and {100} planes are best supported by the data. When looking at the formal hypothesis test on this dataset, Figure 44 (a), a large range of hypotheses are considered possible, with a rejection rate of 75.2%.

Looking this time at Figure 43 (b) where the HMPs of sample 2 are represented, we find a very similar repartition of HMPs to sample 1, in support of the {100}-{110} axis. However, the range of hypotheses covered by high HMPs is larger than in sample 1. As a result, the hypothesis testing, shown on Figure 44 (b), results in a smaller hypothesis rejection rate of 51.9%. Less grain orientations were tested in sample 2, it is therefore expected that the smaller data set leads to fewer hypotheses rejection. When considering both statistical analysis outcome, we see that both data sets are compatible, as in they have common, non-rejected hypotheses which can explain B2 TiFe slip activity.

Let us now look at the meta-analysis, which is the combination of both datasets analysed as if they were the result of the same experiment. As we can see on Figure 43 (b), the meta-analysis displays a much narrower range of hypothesis as “high P-values”, and the hypothesis rejection rate is much higher, reaching 97.9% (Figure 44 (c)). This is a direct consequence of having more grain orientations tested: more data was gathered, and therefore more evidence is available to reject false hypotheses. A clear preference for predominant {110} slip is emerging on the {110}-{100} axis, where all hypotheses involving < 55% active {110} slip now formally rejected at a confidence level of 95%. An unexpected observation is that the hypothesis assuming 100% $\{110\}_p$ is rejected. This means that the statistical analysis judges more likely that at least some portion of {100} planes are active. Indeed, this would explain the large proportion of observed {100} match during both experiments (≈56%).

The formal conclusion (after correction to account for inaccuracies in the probability estimations, see §5.4.1.5), from the statistical analysis of the indentation-based slip trace analysis on a total of 16 grains, is that B2 TiFe slips >45% of the time on {110} planes at a confidence level of 95%. All hypotheses involving no active {100} slip planes were rejected, to the exception of the exclusive slip on {110} planes hypothesis. From there, considering that the hypothesis of exclusive slip on {110} plane is at the edge of being rejected, it would be reasonable to assume that at least some amount of {100} planes are active in B2 TiFe, which is physically possible since for example B2 NiAl, which slips on the <100> slip direction, was reported to slip on {100} planes under specific stress conditions [69]. As can be seen, the statistical analysis reaches similar conclusion on this sample than we did in Chapter 3, but also pushes the analysis further by considering all measurements simultaneously.

5.4.3 Comparison between samples of different slip activities

In this section are compared the outcome of the statistical analysis on three datasets of previously presented samples: B2 TiFe using the meta-analysis including 16 grains (from this work), bcc Fe including 17 grains tested (Chapter 3), and B2 (17)Ni-(43)Al-Fe including 11 grains tested (Chapter 4). These samples are expected to display distinct slip activities, respectively <100> {110} dominant slip, a mix of <111> {110} {112} {123} slip, and a possible

mix of <100> {100} {110} & <111> {110} {112}. The proportions of match used for the analysis are shown in the Table 8, and result from the automated indentation-based slip trace analysis, performed using the same indentation load of 0.5kg on each sample, and analysed using an identification range IR of 10°, a score threshold of 10 and a segmentation size of 100px.

Table 8: Proportion of lines matching each condition, averaged between the grains tested for each sample compared.

Test	{100} (%)	{110} (%)	{112} (%)	{123} (%)	<111> (%)
B2 TiFe (meta)	56.8	100	34.7	55.8	0
Bcc Fe	35.5	48.4	87.9	97.9	29.8
(17)Ni-(43)Al-Fe	64.2	71.1	31.4	74.7	8.9

The HMPs resulting from the statistical analysis of each dataset are represented on Figure 45, and the hypothesis testing outcome on Figure 46.

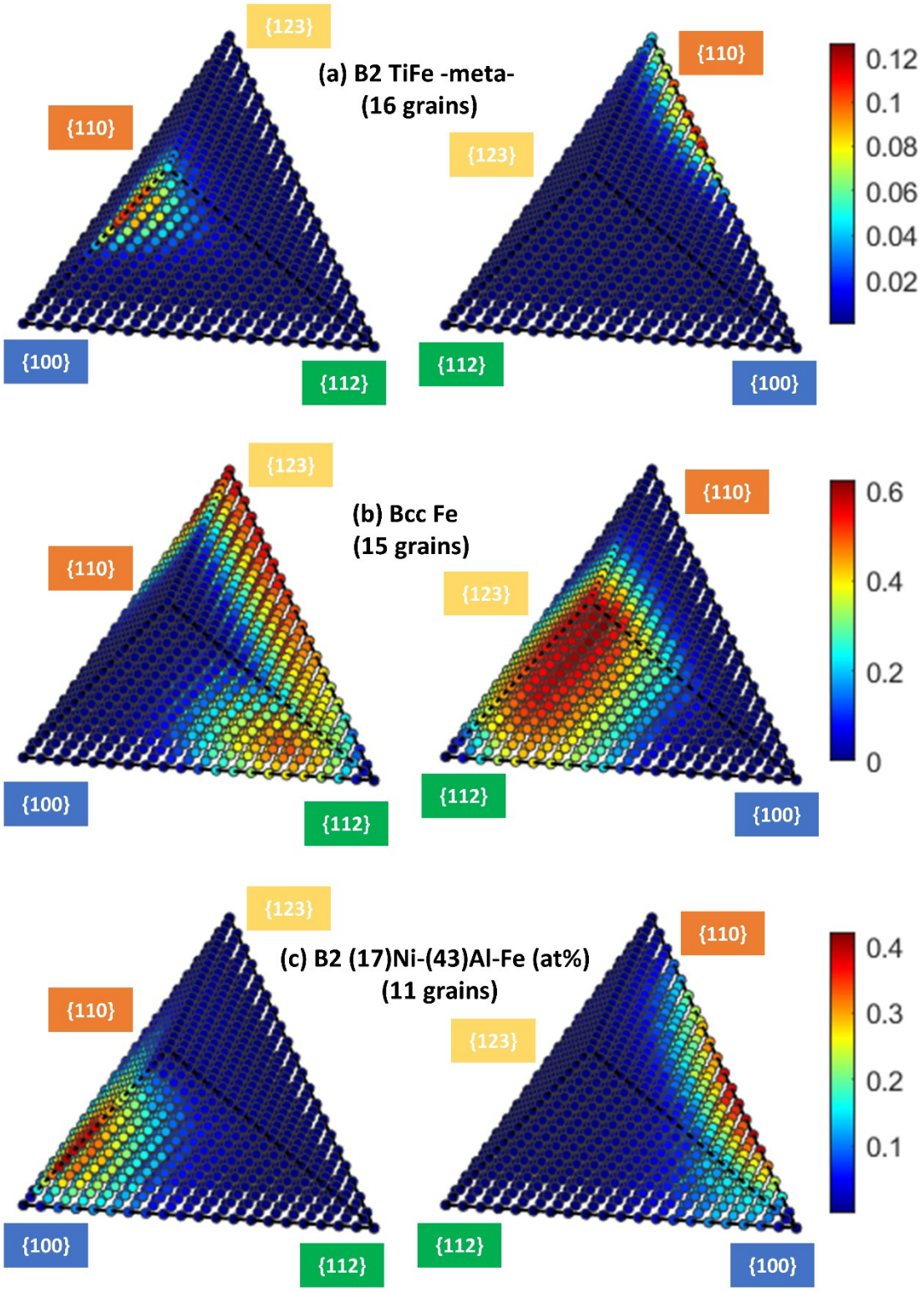


Figure 45: Harmonic mean P-values calculated for each hypothesis Hi, as a function of the presumed proportion of active {100}, {110}, {112} and {123} planes. The quaternary plots are shown from two perspectives, the vertices labels showing which plane type is assumed predominant, e.g. at the vertex « {110} » the Hi presumes $\{100\}_p+\{112\}_p+\{123\}_p=0$. (a) analysis of the meta-analysis dataset of B2 TiFe (b) analysis of the bcc Fe dataset and (c) analysis of the B2 (17)Ni-(43)Al-Fe sample.

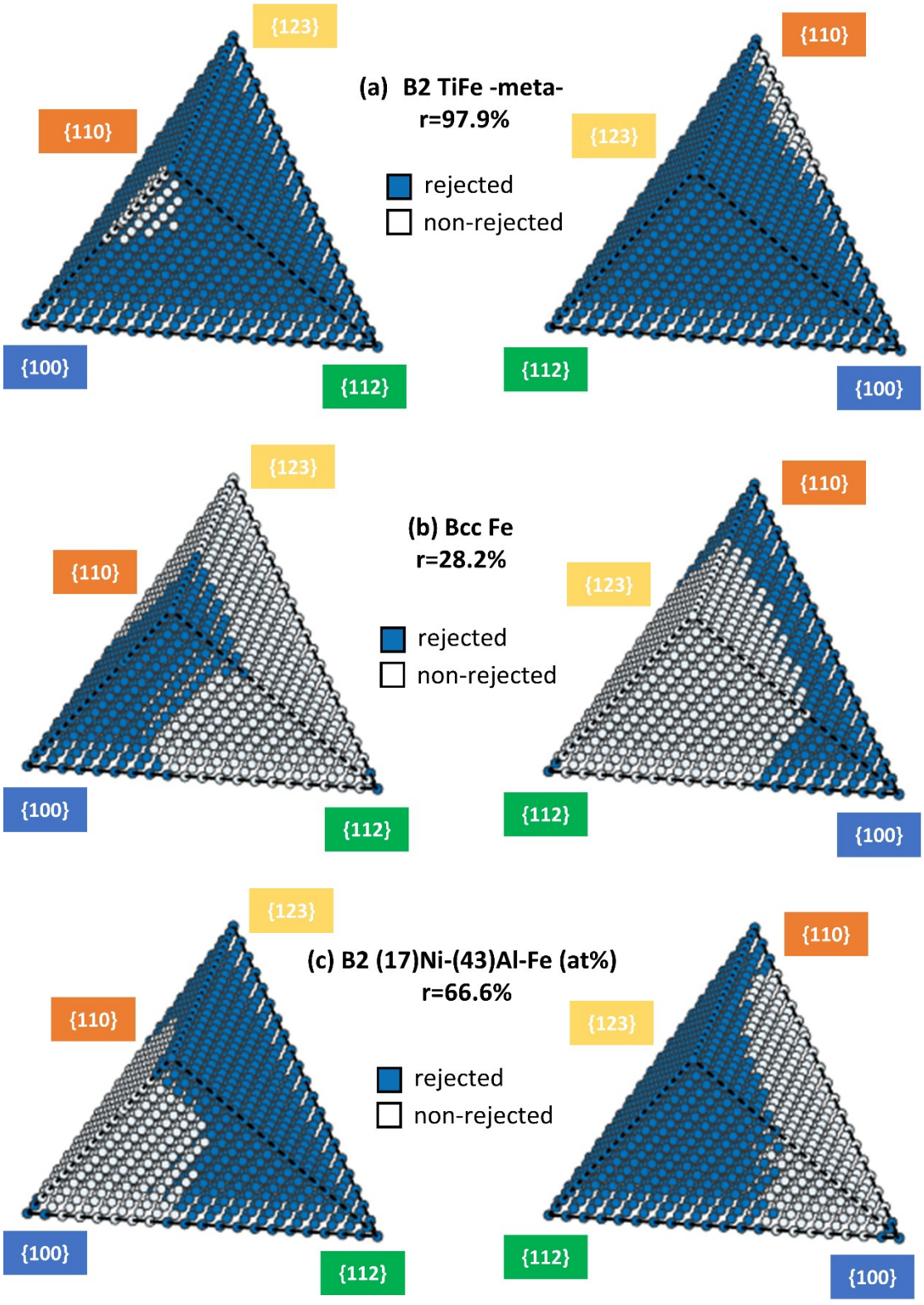


Figure 46: Hypothesis testing for each Hi, as a function of the presumed proportion of active {100}, {110}, {112} and {123} planes. The tetrahedrons are shown from two perspectives, where the vertices labels show which plane type is assumed predominant, e.g. at the vertex « {110} » the Hi presumes $\{100\}_p+\{112\}_p+\{123\}_p=0$ and $\{110\}_p=1$. (a) analysis of the meta-analysis dataset from B2 TiFe (b) analysis of the bcc Fe dataset and (c) analysis of the B2 (17)Ni-(43)Al-Fe dataset. The hypothesis rejection rate r = n(rejections)/n(hypotheses) is indicated for each sample.

As we can see on these figures, the statistical analysis results in significantly different HMPs distributions and hypothesis tests for each sample. Let us first look at the analysis on bcc Fe, shown on Figure 45 (b) and Figure 46 (b). In our previous work (Chapter 3) we inferred from the unambiguous evidence of <111> type slip that the sample must slip on <111>{112} and/or {123} slip planes, we also expect from literature that Fe bcc slips on {110}, {112}, and {123} planes in proportions equivalent to the number of active slip systems (12/48, 12/48, 24/48 respectively), since all three slip systems are thought to have similar critical resolved shear stress [45]. Looking at Figure 46 (b), it can be seen that hypotheses along the {110}-{100} axis are rejected during hypothesis testing, which is clearly different from the behaviour of B2 TiFe (Figure 46 (a)). This demonstrates that the two samples have likely "incompatible slip activities". The rejection rate is small, and much lower in this sample than the others (28.2%). This is likely due to the intermediate nature of the slip activity in the sample and the associated measurements, but also to the difficulty at differentiating {112} from {123} type slip which are expected to be active in this sample (see later discussion in §5.4.4). In a sense, the large amount of non-rejected hypothesis in this sample, centred around intermediate slip activities involving {110}, {112} and {123}, is exactly what we would expect. A new information given by the statistical analysis is that bcc Fe must slip less than 65% of the time on {110} plane (after correction), which is consistent with an expected $\{110\}_p$ of 25%.

Figure 45 (c) and Figure 46 (c) show the statistical analysis outcome on the dataset of B2 (17)Ni-(43)Al-Fe. In our previous work (Chapter 4), this composition was selected because it should be close to the transition regime between dominant <100> and dominant <111> type slip in the B2 NiAl-FeAl composition range. It was notably found evidence of unambiguous <111> type slip in multiple grain orientations tested, both when performing the slip trace analysis inside and outside the indents. As a result, this sample is expected to slip at least a portion of the time on {112} planes, which is thought to get energetically favoured close to the transition between <100> and <111> type slip activities [37]. Also, the very small portion of {112} match, combined with the large portion of {100} match left us wondering if <100>{100} type slip could be coexisting with <111>{112} slip, however, no unambiguous evidence of the former was found to confirm this hypothesis. Looking at the statistical analysis on Figure 45 (a), we see that the high HMPs are concentrated along the {110}-{100} axis, in a similar fashion to B2 TiFe, except this time hypotheses of exclusive slip on {110} planes are clearly rejected, and hypotheses involving large proportions of active {100} planes are well supported by the data. The hypothesis testing, shown on Figure 46 (c), with a rejection rate of 66.6%, clearly rejects all hypotheses which presume $\{100\}_p \leq 10\%$, demonstrating that {100} type slip must be activated at least 5% of the time in this sample, at a 95% confidence level. This hypothesis testing seemingly comes to a contradiction, as hypotheses presuming exclusive slip on {110} and/or {100} planes are considered very likely, despite the observation of 8.9% of unambiguous <111> type slip in this sample, which should present strong evidence against them. This is simply the result of the "rounding approximation" (see §5.3.1.2.1): due to the small amount of grains tested and the small proportion of <111> match observed in this sample, when calculating the P-values of hypotheses expecting less than the observed 8.9% <111> match, the observed proportion of match is rounded to 0, and the P-values of obtaining 0 or more <111> match are calculated to guarantee control over the type 1 error rate. This

means that the information brought by the <111> test is nullified for these hypotheses. Since we are aware of this approximation, and know from the detailed analysis of this sample in Chapter 4 that <111> type slip is very likely to be active in this sample, we now know thanks to the added information of the statistical analysis that this B2 (17)Ni-AlFe sample must be slipping on a mix of <100> and <111> type slip.

Another interesting observation is that the non-rejected hypothesis of highest {112} content presume $\{112\}_p$=40% , which means that the sample must slip <45% of the time on {112} planes, and therefore, we can confidently say that B2 17Ni-AlFe doesn't slip dominantly on {112} (contrarily to was observed in B2 Cu(Ni)Zn [61]), and is likely dominated by a mix of {100} & {110} planes.

In summary, combining this statistical analysis with the experimental results of Chapter 4, the transition in slip direction in the B2 NiAl-FeAl composition range must involve a "smooth" transition where both <100> and <111> slip directions coexist, within a likely large range of compositions between ≈10 and 25 Ni at.%, most likely dominated by a mix of {100} and {110} type slip with only momentarily a small proportion of active {112} planes.

5.4.4 Exploring the limits of the technique

Due to the ambiguity in slip plane identification, almost no unambiguous observation can be made when using indentation-based slip trace analysis in bcc, which means that if we were to look at an individual slip trace, we likely will not know which slip plane generated it. Yet, as seen through these experimental results, the statistical tendency for observed slip traces to match some plane type orientations more frequently than others bring small amounts of information after each measurement, which given enough independent slip traces are observed, informs on the bulk slip activity of the material.

Theoretically, any slip activity, involving any mix of active {100}, {110}, {112}, or {123} slip plane could be proven (or rather disproven), if each hypothesis on the sample slip activity expects a specific, unique set of measurement for each plane type. This should be true as long as a pair of two distinct plane types are not both expected to be matched as frequently as the other under distinct hypotheses. For example, taking the same order of magnitude as evaluated in the experiments, if {123} planes have ≈100% of being matched under any hypothesis, and {112} planes have ≈82% chance of being matched if {123} planes are exclusively active, then slip activities involving a mix of {112} and {123} planes can be distinguished:

Under H1: "100% of active {123}", we expect 100% of {123} match and 82% of {112} match

Under H2: "100% of active {112}", we expect 100% of {123} match and 100% of {112} match

Since H1 and H2 expect different sets of measurements, any hypothesis involving a mix of {123} and {112} will be different with regards to their expected {112} proportion of match, and can be statistically proven/disproven via the measured {112} match proportion. This reasoning extends to each "binary" combination of plane types (e.g. {100}-{110}, {100}-{123} etc.), as the simulation (§5.4.1.2) expects different proportions of match under each active plane types hypothesis, and therefore, each hypothesis is likely to involve a unique set of expected

measurements. However, this will no longer be true if e.g. both {123} and {112} planes are expected to be matched 100% of the time, all the time:

Under H1: “100% of active {123}”, we expect 100% of {123} match and 100% of {112} match

Under H2: “100% of active {112}”, we expect 100% of {123} match and 100% of {112} match

Therefore, we should guarantee that no more than one plane type (e.g. {123} planes) is expected to be matched 100% of the time under different hypotheses. This can be controlled via the identification range IR, itself ruled by experimental uncertainties surrounding plane type identification (see Chapter 3). With the 10° IR used in this work, all plane types are expected to be matched at distinct rates, and never exactly 100% of the time. As long as this is true, using indentation-based slip trace analysis, it should be possible to disprove any slip activity hypothesis provided that sufficient data is gathered.

Now, one might wonder, how much data **is** sufficient data? What is theoretically true may not be experimentally feasible. For example, it is impossible to infer an exact bulk slip activity since this would require an infinitely large number of observations. However, we could come to a conclusion within a certain standard error. The amount of data needed to reach a certain standard error is difficult to evaluate in the case of this statistical analysis, since we must consider the increase in FWER due to the multiple hypothesis testing problem, the influence of the HMP calculations, and the unknown dependencies between the different plane types geometries, which may contribute differently to the hypothesis testing depending on the hypothesis. We propose here to qualitatively evaluate the order of magnitude of data needed to prove different case scenarios of specific interests.

To get a decent estimation of the amount of data required, let us step back to the fundamentals of binomial statistics. After “n” random independent binomial tests of presumed probability of success “p”, the measurement is expected to be found within 2*SE ≈95% of the time, with SE defined as:

$$SE = \frac{1}{\sqrt{n}} * \sqrt{p(1-p)}$$

The standard error SE therefore depends on p and n. If the experimental measurement is found beyond the ±2*SE confidence interval, we can therefore consider that the probability of success was not p, disproving the associated hypothesis on the sample at a ≈95% confidence level. Note that this is a large simplification of the statistical analysis developed in this chapter (e.g. it supposes identical p between the tests), and risks underestimating the amount of data needed to reach a conclusion. However, it can still give us insights on the order of magnitude of the data required under different scenarios. Let us define “P_{exp}” as the experimentally measured proportion of success. In order to disprove Hi under which “p” success is expected at a 95% confidence level, the following inequality must be true:

$$(1)\ 2 * SE = 2 * \frac{1}{\sqrt{n}} * \sqrt{p(1-p)} < |P_{exp} - p|$$

Expressing this inequality as a function of n, we obtain:

$$(2)\ n > 4 * \frac{p(1-p)}{|P_{exp}-p|^2}$$

Based on equation (2), the following Figure 47 represents log(n) = f(|P_{exp}-p|) for different values of p.

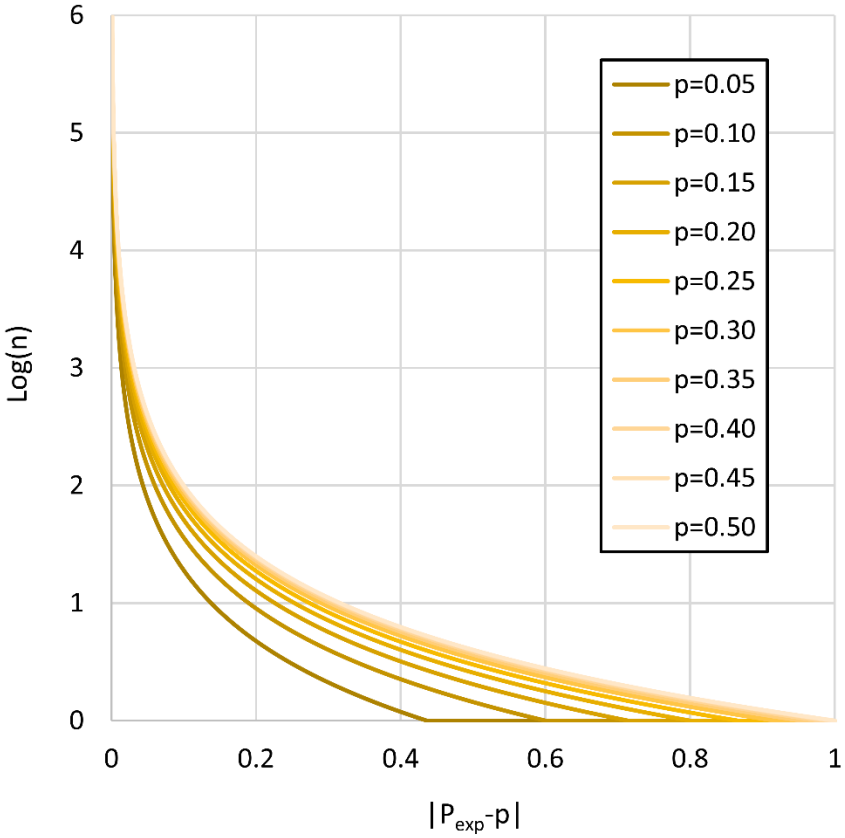


Figure 47: Estimation of the quantity of grains "n" that must be tested to disprove a hypothesis Hi at a ≈95% confidence level, as a function of the difference between P_{exp} the experimentally measured proportion of lines matching a plane type (the sample response), and p the expected proportion under Hi.

Figure 47 gives us a basic appreciation of the order of magnitude of grains that is needed to reject hypotheses in different situations. These statistics behave asymptotically as a function of |P_{exp}-p|, and vary significantly depending on p. The smaller the difference between the measurement and the hypothesis Hi tested, and the closer p is to 0.5, the more tests are need to disprove Hi. We will now check if those estimations are consistent with the statistical analysis of this paper, and then use them to estimate the quantity of data required to reach certain levels of precision on the samples' likely slip activities.

5.4.4.1 Proof checking, comparison to previous analysis outcome

First, let us check if those estimations, based solely on binomial laws, approximatively agree with the outcome of the more complete statistical analysis. Say that we seek to disprove the hypothesis Hi: "the B2 TiFe sample slips 50% of the time on {110} planes", which is the hypothesis of lowest {110} content that was rejected during the meta-analysis (§5.4.2 & §5.4.3). Under this Hi, the hypothesis expects a mix of {110} and {100} planes. Assuming that

{100} slip traces have about 50% chance of matching {110} orientations (based on estimations made in §5.4.1.2), it is expected under Hi p≈75% of {110} match. The experimental measurement was P_{exp}=100% of {110} match. Injecting these values in equation (2) we get:

$$n > 4 * \frac{0.75(1-0.75)}{|1-0.75|^2} = 12$$

We obtain that n > 12 grains is needed to reject Hi, which is of the same order of magnitude as the 16 grains tested during the analysis of this sample, which led to the same rejection. Therefore, these estimations should be qualitatively representative of the order of magnitude of grains we need to test to come to the targeted conclusions.

5.4.4.2 Demonstrating that a sample slips ≈100% of the time on {110} planes

B2 compounds, as well as bcc compounds at low temperature, are often found to slip predominantly on {110} planes [37] [38]. Assuming all slip traces observed consistently match {110} plane orientations, let us estimate how much data would be needed to disprove the hypothesis Hi: "the sample slips 95% of the time (or less) on {110} planes", i.e. proving that the sample slips on {110} > 95% of the time. The active plane type most likely to match {110} orientations by accident is {100}, therefore the hypothesis which we need to disprove is the hypothesis "the sample slips 95% of the time on {110}, and 5% of the time on {100}", expecting p≈97.5% of {110} match. We are assuming {110} planes are consistently matched, i.e. P_{exp}=100%, therefore taking back equation (2):

$$n > 4 * \frac{0.975(1-0.975)}{|1-0.975|^2} = 156$$

We get that n > 156 grains are needed, which is an order of magnitude higher than the previous example.

5.4.4.3 Demonstrating that a sample slips ≈100% of the time on {112} planes

Let us now evaluate the amount of data needed to identify a slip activity involving predominant slip on {112}, since this is a reported B2 slip activity of particular interest [37]. This is more challenging than previous example since {123} planes are expected to match {112} orientations very frequently, more frequently than {100} planes were expected to match {110} orientations. As a result, the $|P_{exp}-p|$ will be smaller (see Figure 47). Assuming slip exclusively on {123} planes, we expect to observe ≈82% {112} match (based on §5.4.1.2). Let us follow the same reasoning as in previous example. Imagine a "fictive" experimental outcome where {112} planes are matched 100% of the time after n grains are tested, i.e. P_{exp}=100% of {112} match. We want to prove that the sample slips >95% of the time on {112} planes. The plane type most likely to match {112} orientations by accident is {123}, therefore, we need to test the hypothesis Hi: "the sample slips 95% of the time on {112}, and 5% of the time on {123} planes". Under Hi, we expect p≈99.1% of {112} match, now injecting the values in (2):

$$n > 4 * \frac{0.991(1-0.991)}{|1-0.991|^2} = 440$$

We get that n > 440 grains are needed, which is superior by a factor 3 to the previous example, which comes directly from the fact that {112} planes and {123} planes are more difficult to tell apart experimentally than {110} and {100}.

5.4.4.4 Demonstrating that a sample slips ≈25% of the time on {112} planes

An even more challenging scenario would be to try to prove the supposed slip activity of bcc Fe, which involves notably proving that it slips 25% of the time on {112} planes (12/48 active slip systems involve {112} planes). This is more challenging than previous example because the value p (Figure 47) will be less extreme, and therefore more experimental variability is expected in this context. Proving Hi: "bcc Fe slips 25±5% of the time on {112}" would consist in disproving both H1: "bcc Fe slips 20% on {112} and 80% on {123} planes" and H2: "bcc Fe slips 30% {112} and 70% {123}". Is expected under H1 and H2 respectively p_1≈85.6% or p_2≈87.4% {112} match. Assuming now that the expected {112} match proportion if Hi is true was experimentally measured, i.e. P_{exp}≈86.5% of {112} match, we can inject these values back in equation (2):

For H1, with p=85.6%

$$n > 4 * \frac{0.856(1-0.856)}{|0.865-0.856|^2} = 6087$$

For H2, with p=87.4%:

$$n > 4 * \frac{0.874(1-0.874)}{|0.865-0.874|^2} = 5438$$

Calculating each we get that n>6087 grains tested would be need, which is superior by an order of magnitude to the estimations of previous example, and represents a huge amount of data.

5.4.4.5 Experimental feasibility and possible improvements

In conclusion, yes, it is theoretically possible to prove any slip activity hypothesis using indentation-based slip trace analysis, without even knowing what plane activation resulted in each individually observed slip trace. However, using the current methodology, not all conclusions of interest on the sample bulk slip activity are achievable experimentally.

Testing ≈100s of grains is possible, as we previously analysed 99 indents (Chapter 4) without difficulties. To deform this many grains, testing samples with small grains sizes, or indenting them with higher loads (or spherical indenters) could help deforming and imaging large amounts of grains rapidly. Beyond a few hundreds of indents, the current methodology risks quickly becoming unmanageable. However, future improvements on the methodology could enable them.

For example, if experimental variabilities surrounding slip plane attribution were reduced, it would allow to decrease the identification range IR used for theoretical plane type orientation attribution (IR=10° was used during this statistical analysis), and consequently, the probability p of matching plane types unrelated to the deformation "by accident". As a result, for

example, the probability to match {112} assuming {123} planes are active will be lower, further distinguishing the expected {112} match measurement under hypotheses involving {112} and/or {123} slip (increasing $|P_{exp}-p|$ on Figure 47). Such reduction in IR will likely improve the power of all plane type match measurement at distinguishing between hypotheses. An easy way to reduce experimental variabilities surrounding slip plane identification would be to improve the accuracy of the automated line orientation detection. To do that, we can simply opt for larger segmentation sizes, using higher resolution pictures. Another leverage would be to perform more accurate EBSD mappings, which were made relatively coarsely throughout the presented experiments, this could improve in the process the accuracy of plane type orientations predictions.

A more radical approach can be to adapt the sub-hypotheses tested to the context, using literature to discard some options, e.g. ignore {123} planes if deemed reasonable. This could unlock the possibility to observe more unambiguous situations (e.g. unambiguous {100} slip), which once considered can help distinguishing between hypotheses, in the same way the unambiguous <111> type slip allows for a strong distinction between slip activities hypotheses along the {100}-{110} axis from those along the {112}-{123} axis.

Another limiting factor to consider is the amount of time needed to perform the simulation §5.3.2.2, which is currently of ≈15min per grain tested, although note that the code is not fully optimised yet. The P-values calculations may simplify when “n” gets very large, as it is possible that the probability of matching averaged between the grains will eventually stabilise, meaning that beyond a certain amount of grains tested, the average probabilities of matching in every sample may be close to identical (whilst keeping in mind that the sample grain texture risks biasing these probabilities). If this can be proven to be true, we may be able to perform a shorter simulation, and the same reference probabilities may be used for all samples when the number of grains tested is sufficiently large.

Finally, if collecting large amount of data is unavoidable to reach certain conclusions, we could rely on a collective effort, standardising the procedure and combining the data obtained by different experiments, from different research groups. As the experimental work is trivial, short-term projects could collect small amounts of data on different materials, to identify their “main families” of bulk slip activities. As per §5.4.3 and Chapters 3 & 4, such insights can already be very useful, especially for B2 compounds. Then, performing meta-analysis, similarly to what was done in §5.4.2, on these small independent projects could at term allow to obtain precise data for crystal plasticity models.

5.5 Summary

In this chapter, we have introduced statistical tools as a way to infer meso-scale bulk slip activity from automated indentation-based slip trace analysis. With minimal assumptions, using notably a large plane type identification range of 10° leading to mostly ambiguous plane type identifications, testing 1772 distinct hypotheses involving the possibility of slip on {100}, {110}, {112}, and {123} plane types simultaneously, and from the analysis of small datasets of 11 to 17 grains tested (<1 day of experimental work each), it is demonstrated at a 95% confidence level that:

- B2 TiFe slips on {110} planes >45% of the time, the analysis also suggesting a small proportion of active {100} planes. The statistical analysis is consistent with our previous works suggesting predominant slip on {110} slip systems and TEM experiments from literature identifying <100>{110} type slip.
- Bcc Fe slips <65% of the time on {110} plane, whilst {112} and/or {123} planes must be active (in proportions anywhere between 0 to 100%). This is consistent with a slip activity in proportions 12/48 {110}, 12/48 {112} and 24/48 {123} expected due to the similar reported CRSS of these plane types.
- B2 (17)Ni-(43)Al-Fe (at.%) slips >5% of the time on {100} planes, thus proving the existence of <100> type slip in this sample. This adds to the repeated observations of unambiguous <111> type slip in this sample, therefore confirming the intermediate nature of its slip activity, involving a mix of <100> and <111> type slip.

As was shown in this work, the samples' possible bulk slip activities can be further narrowed down via gathering more data, i.e. testing more unique grain orientations, and performing a meta-analysis using previously and newly gathered data. Future improvements on current methodology can involve the reduction of the slip plane orientation identification experimental uncertainties (targeting IR<10°), which should allow to reach more precise conclusions from significantly smaller datasets. Also, the statistical analysis proposed may be adjusted in the future if more efficient hypothesis testing procedures are found to be applicable, especially when testing larger sample sizes as those may allow simplifications as per the central limit theorem.

6 Conclusion

In this PhD Thesis, we have investigated the possibility of using automated indentation-based slip trace analysis as an efficient screening tool to accelerate the ongoing development of bcc+B2 bcc-superalloys.

A key step in this research was the development of an automation code for slip trace identification, presented in Chapter 3. Not only does the automation increase the speed and repeatability of the technique, it also gives access to significantly higher statistics that alternative manual approaches. As a result, indentation-based micromechanical characterisation, which prior to our work was rarely used, is now an exploitable methodology over popular alternative micromechanical testing approaches (such as TEM, micropillar compressions and/or single crystal testing). In Chapter 3, we notably showed how from only a few (≈10) indents we can already access reliable statistics on the sample's slip activity, being able to differentiate between the {110} dominated B2 TiFe and B2 Ti_2AlMo, from the frequent <111>{112} and/or {123} slip in B2 Ti_2AlNb and bcc Fe, in agreement with previous literature reports. All these assessments can be made despite the highly ambiguous bcc slip plane characterisation, i.e. the possible overlap of plane types orientations for a given crystal orientation (e.g. a {110} slip trace may be closely oriented to a {123} orientation).

Once the technique's basic principles were established & validated, we applied it to a series of "real life" scenarios to seek B2 intermetallic compositions that are most likely to favour ductile bcc+B2 behaviours. This was done in Chapter 4, where a compositionally graded sample between B2 FeAl-NiAl was tested using the newly developed technique. It was shown how, in a single experiment, and from a single sample (≈a few mm^2) we were able to accurately assess the evolution of slip activity as a function of composition, notably spotting a composition range between 10-25 Ni at.% where slip transition from <100> to <111> should occur, in agreement with previous TEM work in literature. Our technique offers a quicker, more continuous, quantitative information on slip activity as a function of composition than alternative approaches, in a highly simplified and lower cost experimental approach.

Finally, to fully exploit the potential of this approach for collecting large statistics, we developed a statistical analysis tool to better evaluate the evidence gathered via this approach. This was done through a simple sample slip activity simulation, P-value calculations and hypothesis testing. It was shown how the statistical analysis reaches conclusions similar to the statements we made throughout Chapter 3 and 4, but also how it was also able to push the analysis further, gaining new information on the likely samples' slip activities, as well as giving more objective assessments on the confidence level we can have on these conclusions. This statistical analysis notably allowed to confirm that a portion of {100} planes are likely active in B2 TiFe, whilst B2 (17)Ni-(43)Al-Fe (at.%) must display a mix of <100> and <111> type slip, both of which without having to observe a single unambiguous {100} type slip trace. The latter sample analysis confirms that the transition in slip direction in the B2 FeAl-NiAl composition range happens "smoothly", as in <100> and <111> coexist for a range of compositions, and unlike previous reports made in the B2 CuZn-NiZn system, {112} type slip planes are unlikely to become predominantly activated during this transition.

Building from this work, many applications and adaptations of the technique may be further investigated, as the simplicity of the experimental approach could make it accessible to most researchers, making us excited for the various possible continuations of this research.

7 Future work

Automated indentation-based slip trace analysis is a promising technique offering the means to solve many debates surrounding bcc and B2 slip activities. Beyond optimisation of the code and/or the statistical analysis process to access even larger statistics, a number of other concepts were considered alongside the thesis work presented, which did not reach completion but could warrant further investigation.

The B2 TiFe intermetallic is a key component of titanium based superalloys [2] [3] [103], a problem being that it is thought to favour <100> type slip (see Chapter 3, 5, and [125]), which participates in the lack of ductility in these alloys. To see if aluminium addition may unlock other slip systems in the B2 phase (e.g. possibly favour <111> slip), an investigation of the B2 TiFe-Ti_2FeAl composition range was performed via the diffusion gradient approach detailed in Chapter 4. The resulting slip trace analysis, presented in Figure 48, suggests an increased tendency for <100>{100} type slip as the aluminium content of the B2 TiFe precipitates increases. However, no unambiguously <111> type slip traces were observed across the 92 analysed indents. The size of the indents across the gradient was also measured, and is displayed in Figure 49, giving an indication of the evolution of hardness across the sample. No clear correlation between hardness and slip activity was found in either of the B2 FeAl-NiAl (Chapter 4) nor the B2 TiFe-Ti_2FeAl diffusion gradients, however, the more independent slip systems were thought to be active, the wavier the observed slip traces were, which is often considered to indicate increased ductility in bcc.

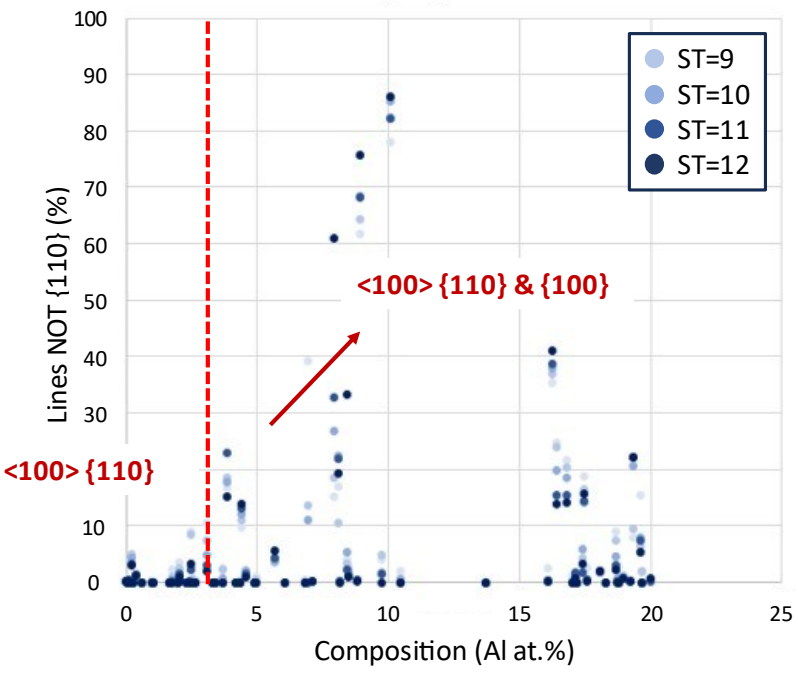


Figure 48: Analysis of the B2 TiFe-Ti_2FeAl system via the gradient approach detailed in Chapter 4. The graphic shows the proportions of lines that do not match {110} planes, for each indent, as a function of the average EDX measured indent Al at.% composition (for ST=9,10,11,12, IR=16°, and averaged between analysis using N=100, 120 and 140px, as per Chapter 4), as well as the suggested evolution of slip activity.

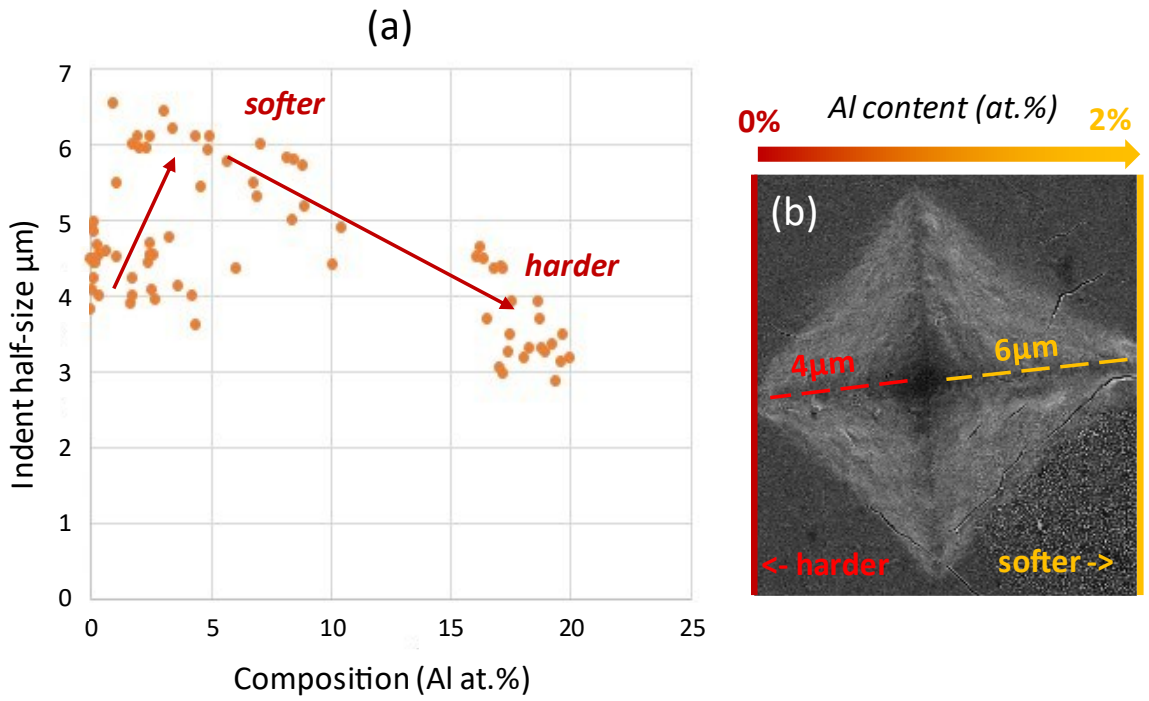


Figure 49: Evolution of the size of the indents across the B2 TiFe-Ti_2FeAl composition range. (a) Shows the manually measured size of the indents (mean between the two halves of the diagonals of the indent) as a function of the composition, with (b) showing a highly asymmetric indent due to the sharp changes in hardness across the gradient.

The slip trace analysis technique was also applied to several dual phase titanium-based bcc+B2 alloys reinforced with B2 TiFe precipitates. We were able to see the behaviour of slip traces at the interface between the bcc matrix and B2 precipitates, gaining insights on the slip transfer mechanism. Different bcc+B2 TiAlFe alloys, kindly provided to us by R Mellor et al. [2], were indented and analysed. In those alloys, due to the large precipitate sizes, it was possible to easily observe the slip transfer as well as the change in slip system between the <111> slipping bcc Ti matrix and the <100>{110} dominated TiFe precipitates, with many unambiguous observations of wavy <111> type slip traces transferring to likely {110} planes, as illustrated on Figure 50 (a). In contrast, in bcc+B2 TiFeNb alloys, no such slip transfer was observed, and slip bands appeared to bend around the precipitates, pilling-up and forming voids, as shown on Figure 50 (b). Finally, the TiFeAlNb bcc+B2 system was investigated, with this time systematic observations of slip transfer at all precipitate sizes, as can be seen on Figure 50 (c), with also a tendency to match {110} orientations when in the precipitates.

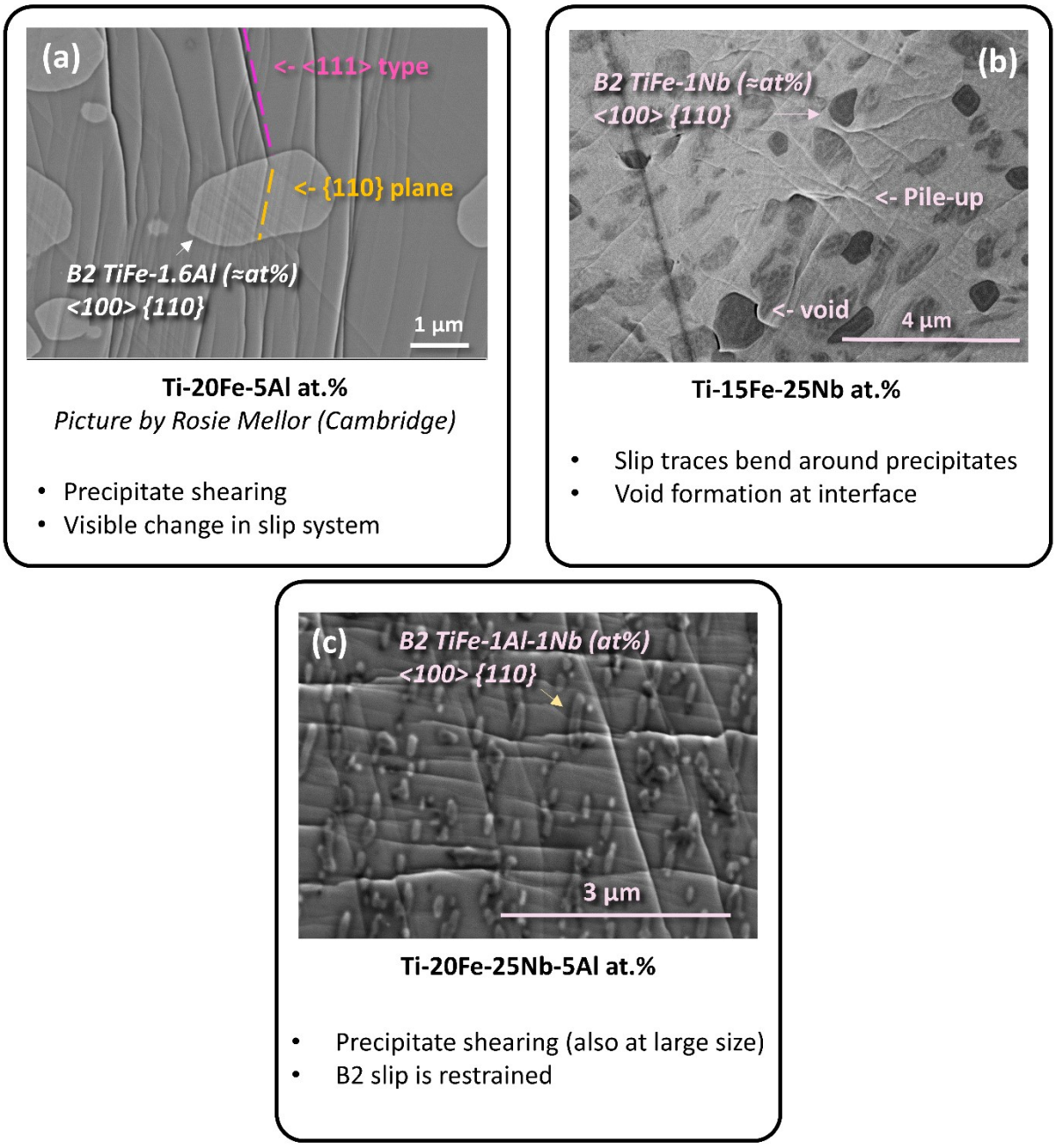


Figure 50: Investigation of slip transfer at the bcc/B2 interface in several two-phase bcc+B2 titanium-based alloys. Noticeable features are identified on the figures with arrows. Dominant slip systems expected in the B2 phase are indicated. In (a) is illustrated the typical change in slip system observed in the TiFeAl alloys via automated indentation-based slip trace analysis.

Considering the differences in compositions, precipitate sizes, misfits, and possible slip activities in each sample, it is still unclear why these bcc+B2 alloys behave so differently, making a compelling case for more thorough investigations. However, it was postulated that the significant drop in hardness of the B2 TiFe phase following small aluminium addition (as shown in Figure 49) may be a key factor to unlock the possibility of slip transfer in the TiFeAl and TiFeAlNb alloys.

When slip transfer is present in a bcc+B2 alloy, we noted that the meso-scale slip activities tend to be similar to the slip activity of the limiting phase. In the TiFeAl alloys investigated, the

proportion of {110} match increases in the presence of B2 TiFe precipitates cutting, the higher the volume fraction of precipitates there is, but also as a function of the size of the indents. Therefore, we postulate the following (likely far from complete) relationship, which we will call "the slip filter theory":

$$S_{meso} \propto V_p * P_t * L$$

With:

- S_{meso} the meso-scale measured slip activity (e.g. proportion of {110} match)
- V_p the volume fraction of precipitates
- P_t the likelihood of slip transfer
- L the average distance travelled by dislocations before reaching the surface (which depends notably on indentation size)

This relationship is built from the simple idea that the more likely dislocations are to interact with the precipitates before forming the slip traces at the sample surface, the more likely they are to transfer on the limited precipitate slip systems. As a result, by measuring S_{meso} using our slip trace analysis approach for different indentation sizes (varying L), we may be able to infer either V_p or P_t, or even the precipitates slip activity, which are all key material parameters controlling dual-phase alloys' mechanical properties. We can also postulate that there will be a critical volume fraction V_c of precipitates such that any V_p beyond V_c will lead to the same measured S_{meso}, as the probability of interaction between dislocations and precipitates should eventually reach close to 100%.

A further idea would be to use the automated line detection approach to measure and quantify the "waviness" of slip traces in a sample, which could potentially be used to assess alloys' ductility. Depending on the waviness of the slip traces, the detected lines orientations distribution will form either sharp peaks when slip traces are straight (all lines are nicely aligned with their specific slip orientation), or wider peaks when slip traces are wavy (lines detected on wavy slip traces will show variability in their orientations). Therefore, by quantifying the average width of these line orientations distribution peaks across a sample, we could evaluate the tendency for wavy slip in a material, and eventually link it to the materials' properties (e.g. tendency for cross-slip, SFE, and/or ductility).

Many opportunities arise from the automated indentation-based slip trace analysis technique developed during this project, making us hopeful for continuations of this research approach.

References

[1] R. C. Reed, 'The Superalloys: Fundamentals and Applications', *Cambridge University Press*, 2006.

[2] R. Mellor, 'The potential for superlattice precipitate reinforcement in titanium-iron alloys', *Apollo - University of Cambridge Repository*, Mar. 2024, doi: 10.17863/CAM.106827.

[3] A. J. Knowles *et al.*, 'A new beta titanium alloy system reinforced with superlattice intermetallic precipitates', *Scripta Materialia*, vol. 140, pp. 71–75, Nov. 2017, doi: 10.1016/j.scriptamat.2017.06.038.

[4] B. Douat, C. Coupeau, J. Bonneville, M. Drouet, L. Vernisse, and L. Kubin, 'Atomic-scale insight into non-crystallographic slip traces in body-centred cubic crystals', *Scripta Materialia*, vol. 162, pp. 292–295, Mar. 2019, doi: 10.1016/j.scriptamat.2018.10.032.

[5] D. Caillard, B. Bienvenu, and E. Clouet, 'Anomalous slip in body-centred cubic metals', *Nature*, vol. 609, pp. 936–941, Sep. 2022, doi: 10.1038/s41586-022-05087-0.

[6] B. W. Lagow, 'Materials Selection in Gas Turbine Engine Design and the Role of Low Thermal Expansion Materials', *JOM*, vol. 68, no. 11, pp. 2770–2775, Nov. 2016, doi: 10.1007/s11837-016-2071-2.

[7] M.-T. Perez-Prado and M. E. Kassner, 'Creep of Intermetallics', in *Fundamentals of Creep in Metals and Alloys*, Elsevier, 2015, pp. 189–232. doi: 10.1016/B978-0-08-099427-7.00009-8.

[8] S. Vogel, D. Bhattacharyya, G. B. Viswanathan, D. Williams, and H. L. Fraser, 'Phase Transformation Textures in Ti6Al4V Alloy', *Materials Science Forum - MATER SCI FORUM*, vol. 495–497, pp. 681–686, Sep. 2005, doi: 10.4028/www.scientific.net/MSF.495-497.681.

[9] J. Xu, J. Zhu, J. Fan, Q. Zhou, Y. Peng, and S. Guo, 'Microstructure and mechanical properties of Ti–6Al–4V alloy fabricated using electron beam freeform fabrication', *Vacuum*, vol. 167, pp. 364–373, Sep. 2019, doi: 10.1016/j.vacuum.2019.06.030.

[10] F. Appel, J. D. H. Paul, M. Oehring, U. Fröbel, and U. Lorenz, 'Creep behavior of TiAl alloys with enhanced high-temperature capability', *Metall and Mat Trans A*, vol. 34, no. 10, pp. 2149–2164, Oct. 2003, doi: 10.1007/s11661-003-0279-6.

[11] Z. Zhu, F. L. Ng, H. L. Seet, and S. M. L. Nai, 'Tailoring the microstructure and mechanical property of laser powder bed fusion fabricated Ti–6Al–2Sn–4Zr–2Mo via heat treatment', *Journal of Alloys and Compounds*, vol. 895, p. 162648, Feb. 2022, doi: 10.1016/j.jallcom.2021.162648.

[12] G. Fargas, J. Roa, B. Sefer, R. Pederson, M.-L. Antti, and A. Mateo, 'Influence of cyclic thermal treatments on the oxidation behavior of Ti-6Al-2Sn-4Zr-2Mo alloy', *Materials Characterization*, vol. 145, Aug. 2018, doi: 10.1016/j.matchar.2018.08.049.

[13] F. Appel *et al.*, 'Recent Progress in the Development of Gamma Titanium Aluminide Alloys', *Advanced Engineering Materials*, vol. 2, no. 11, pp. 699–720, 2000, doi: 10.1002/1527-2648(200011)2:11<699::AID-ADEM699>3.0.CO;2-J.

[14] O. Genc and R. Unal, 'Development of gamma titanium aluminide (γ-TiAl) alloys: A review', *Journal of Alloys and Compounds*, vol. 929, p. 167262, Dec. 2022, doi: 10.1016/j.jallcom.2022.167262.

[15] V. Recina, J. Ahlström, and B. Karlsson, 'Sample preparation and microstructural characterization of the gamma titanium aluminide Ti-48Al-2W-0.5Si', *Materials*

Characterization, vol. 38, no. 4, pp. 287–300, Apr. 1997, doi: 10.1016/S1044-5803(97)00033-8.

[16] K. Maruyama, R. Yamamoto, H. Nakakuki, and N. Fujitsuna, 'Effects of lamellar spacing, volume fraction and grain size on creep strength of fully lamellar TiAl alloys', *Materials Science and Engineering: A*, vol. 239–240, pp. 419–428, Dec. 1997, doi: 10.1016/S0921-5093(97)00612-6.

[17] S. F. Franzén and J. Karlsson, 'γ-Titanium Aluminide Manufactured by Electron Beam Melting, an Investigation of Microstructural Behavior and Related Mechanical Properties for Aerospace Applications', *Chalmers Publication Library, diploma work no 37/2010*, 2010.

[18] T. M. Pollock and S. Tin, 'Nickel-Based Superalloys for Advanced Turbine Engines: Chemistry, Microstructure and Properties', *Journal of Propulsion and Power*, vol. 22, no. 2, pp. 361–374, 2006, doi: 10.2514/1.18239.

[19] S. Zhao, X. Xie, G. D. Smith, and S. J. Patel, 'Microstructural stability and mechanical properties of a new nickel-based superalloy', *Materials Science and Engineering: A*, vol. 355, no. 1, pp. 96–105, Aug. 2003, doi: 10.1016/S0921-5093(03)00051-0.

[20] Md. Shahwaz, P. Nath, and I. Sen, 'A critical review on the microstructure and mechanical properties correlation of additively manufactured nickel-based superalloys', *Journal of Alloys and Compounds*, vol. 907, p. 164530, Jun. 2022, doi: 10.1016/j.jallcom.2022.164530.

[21] Q. Zhang, Y. Chang, L. Gu, Y. Luo, and B. Ge, 'Study of microstructure of nickel-based superalloys at high temperatures', *Scripta Materialia*, vol. 126, pp. 55–57, Jan. 2017, doi: 10.1016/j.scriptamat.2016.08.013.

[22] R. C. Reed, 'The Superalloys: Fundamentals and Applications'

[23] Y. Ma *et al.*, 'The BCC/B2 Morphologies in AlxNiCoFeCr High-Entropy Alloys', *Metals*, vol. 7, no. 2, Art. no. 2, Feb. 2017, doi: 10.3390/met7020057.

[24] D. G. Shaysultanov, G. A. Salishchev, Yu. V. Ivanisenko, S. V. Zherebtsov, M. A. Tikhonovsky, and N. D. Stepanov, 'Novel Fe36Mn21Cr18Ni15Al10 high entropy alloy with bcc/B2 dual-phase structure', *Journal of Alloys and Compounds*, vol. 705, pp. 756–763, May 2017, doi: 10.1016/j.jallcom.2017.02.211.

[25] T. Xu, Q. Chen, Li. Ji, Z. Zheng, K. Wang, and H. Liu, 'BCC/B2 structure and dislocation strengthening behavior in high Ti content TiAlVCrNb high-entropy alloys', *Journal of Alloys and Compounds*, vol. 956, p. 170179, Sep. 2023, doi: 10.1016/j.jallcom.2023.170179.

[26] K. Ma *et al.*, 'Chromium-based bcc-superalloys strengthened by iron supplements', *Acta Materialia*, vol. 257, p. 119183, Sep. 2023, doi: 10.1016/j.actamat.2023.119183.

[27] S. A. Kube, C. Frey, C. McMullin, B. Neuman, K. M. Mullin, and T. M. Pollock, 'Navigating the BCC-B2 refractory alloy space: Stability and thermal processing with Ru-B2 precipitates', *Acta Materialia*, vol. 265, p. 119628, Feb. 2024, doi: 10.1016/j.actamat.2023.119628.

[28] T. E. Whitfield *et al.*, 'An assessment of the thermal stability of refractory high entropy superalloys', *Journal of Alloys and Compounds*, vol. 857, p. 157583, Mar. 2021, doi: 10.1016/j.jallcom.2020.157583.

[29] R. D. Jones, 'Deformation in A2/B2 Alloys', *PhD thesis, University of Cambridge*, Aug. 2016.

[30] H. Bei and E. P. George, 'Microstructures and mechanical properties of a directionally solidified NiAl–Mo eutectic alloy', *Acta Materialia*, vol. 53, no. 1, pp. 69–77, Jan. 2005, doi: 10.1016/j.actamat.2004.09.003.
[31] L. Hu, W. Hu, G. Gottstein, S. Bogner, S. Hollad, and A. Bührig-Polaczek, 'Investigation into microstructure and mechanical properties of NiAl-Mo composites produced by directional solidification', *Materials Science and Engineering: A*, vol. 539, pp. 211–222, Mar. 2012, doi: 10.1016/j.msea.2012.01.083.
[32] G. Ghosh and G. B. Olson, 'Integrated design of Nb-based superalloys: Ab initio calculations, computational thermodynamics and kinetics, and experimental results', *Acta Materialia*, vol. 55, no. 10, pp. 3281–3303, Jun. 2007, doi: 10.1016/j.actamat.2007.01.036.
[33] D. Locq, P. Caron, C. Ramusat, and R. Mévrel, 'Quaternary chromium-based alloys strengthened by Heusler phase precipitation', *Materials Science and Engineering: A*, vol. 647, pp. 322–332, Oct. 2015, doi: 10.1016/j.msea.2015.09.033.
[34] Ö. N. Doğan, X. Song, D. Palacio, and M. C. Gao, 'Coherent precipitation in a high-temperature Cr–Ni–Al–Ti Alloy', *J Mater Sci*, vol. 49, no. 2, pp. 805–810, Jan. 2014, doi: 10.1007/s10853-013-7763-1.
[35] E. L. Calvert, A. J. Knowles, J. J. Pope, D. Dye, and M. Jackson, 'Novel high strength titanium-titanium composites produced using field-assisted sintering technology (FAST)', *Scripta Materialia*, vol. 159, pp. 51–57, Jan. 2019, doi: 10.1016/j.scriptamat.2018.08.036.
[36] R. Mellor, P. Vacek, N. Jones, P. Midgley, and H. Stone, 'Research data supporting "Precipitate nanostructuring that enhances lattice compatibility in a Ti-Fe-Al alloy"', Apr. 2023, doi: 10.17863/CAM.92062.
[37] M. Yamaguchi and Y. Umakoshi, 'The deformation behaviour of intermetallic superlattice compounds', *Progress in Materials Science*, vol. 34, no. 1, pp. 1–148, Jan. 1990, doi: 10.1016/0079-6425(90)90002-Q.
[38] C. R. Weinberger, B. L. Boyce, and C. C. Battaile, 'Slip planes in bcc transition metals', *International Materials Reviews*, vol. 58, no. 5, pp. 296–314, Jun. 2013, doi: 10.1179/1743280412Y.0000000015.
[39] L. Kaun, A. Luft, J. Richter, and D. Schulze, 'Slip Line Pattern and Active Slip Systems of Tungsten and Molybdenum Single Crystals Weakly Deformed in Tension at Room Temperature', *physica status solidi (b)*, vol. 26, no. 2, pp. 485–499, 1968, doi: 10.1002/pssb.19680260212.
[40] J. Richter, 'The Influence of Temperature on Slip Behaviour of Molybdenum Single Crystals Deformed in Tension in the Range from 293 to 573 °K .II. Slip Geometry and Structure of Slip Bands', *physica status solidi (b)*, vol. 46, no. 1, pp. 203–215, 1971, doi: 10.1002/pssb.2220460118.
[41] D. Veselý, 'The Study of Slip Bands on the Surface of Mo Single Crystals', *physica status solidi (b)*, vol. 29, no. 2, pp. 685–696, 1968, doi: 10.1002/pssb.19680290218.
[42] G. Zhou *et al.*, 'Mesoscale slip behavior in single crystal and bicrystal tantalum', *Materialia*, vol. 28, p. 101730, May 2023, doi: 10.1016/j.mtla.2023.101730.
[43] T. Yalcinkaya, W. A. M. Brekelmans, and M. G. D. Geers, 'BCC single crystal plasticity modeling and its experimental identification', *Modelling Simul. Mater. Sci. Eng.*, vol. 16, no. 8, p. 085007, Dec. 2008, doi: 10.1088/0965-0393/16/8/085007.

[44] Y. Liu *et al.*, 'Quasi in-situ study on the slip activation mechanism of high purity tantalum during compress deformation', *Journal of Materials Research and Technology*, vol. 20, pp. 4008–4017, Sep. 2022, doi: 10.1016/j.jmrt.2022.08.078.
[45] C. Tian, D. Ponge, L. Christiansen, and C. Kirchlechner, 'On the mechanical heterogeneity in dual phase steel grades: Activation of slip systems and deformation of martensite in DP800', *Acta Materialia*, vol. 183, pp. 274–284, Jan. 2020, doi: 10.1016/j.actamat.2019.11.002.
[46] C. Du, F. Maresca, M. G. D. Geers, and J. P. M. Hoefnagels, 'Ferrite slip system activation investigated by uniaxial micro-tensile tests and simulations', *Acta Materialia*, vol. 146, pp. 314–327, Mar. 2018, doi: 10.1016/j.actamat.2017.12.054.
[47] L. Dezerald, D. Rodney, E. Clouet, L. Ventelon, and F. Willaime, 'Plastic anisotropy and dislocation trajectory in BCC metals', *Nat Commun*, vol. 7, no. 1, Art. no. 1, May 2016, doi: 10.1038/ncomms11695.
[48] G. Po *et al.*, 'A phenomenological dislocation mobility law for bcc metals', *Acta Materialia*, vol. 119, pp. 123–135, Oct. 2016, doi: 10.1016/j.actamat.2016.08.016.
[49] A. Patra, T. Zhu, and D. L. McDowell, 'Constitutive equations for modeling non-Schmid effects in single crystal bcc-Fe at low and ambient temperatures', *International Journal of Plasticity*, vol. 59, pp. 1–14, Aug. 2014, doi: 10.1016/j.ijplas.2014.03.016.
[50] D. Caillard, 'Geometry and kinetics of glide of screw dislocations in tungsten between 95K and 573K', *Acta Materialia*, vol. 161, pp. 21–34, Dec. 2018, doi: 10.1016/j.actamat.2018.09.009.
[51] Z. Li and Y. Cui, 'Non-Schmid Effect on the Fracture Behavior of Tungsten', *Crystals*, vol. 13, no. 3, Art. no. 3, Mar. 2023, doi: 10.3390/cryst13030417.
[52] P. R. Thornton, T. E. Mitchell, and P. B. Hirsch, 'The dependence of cross-slip on stacking-fault energy in face-centred cubic metals and alloys', *Philosophical Magazine*, vol. 7, no. 80, pp. 1349–1369, Aug. 1962, doi: 10.1080/14786436208213168.
[53] J.-P. Couzinié *et al.*, 'High-temperature deformation mechanisms in a BCC+B2 refractory complex concentrated alloy', *Acta Materialia*, vol. 233, p. 117995, Jul. 2022, doi: 10.1016/j.actamat.2022.117995.
[54] P. Castany, M. Besse, and T. Gloriant, 'In situ TEM study of dislocation slip in a metastable β titanium alloy', *Scripta Materialia*, vol. 66, no. 6, pp. 371–373, Mar. 2012, doi: 10.1016/j.scriptamat.2011.11.036.
[55] I. Baker, 'A review of the mechanical properties of B2 compounds', *Materials Science and Engineering: A*, vol. 192–193, pp. 1–13, Feb. 1995, doi: 10.1016/0921-5093(94)03200-9.
[56] Y.-S. Lin, M. Cak, V. Paidar, and V. Vitek, 'Why is the slip direction different in different B2 alloys?', *Acta Materialia*, vol. 60, no. 3, pp. 881–888, Feb. 2012, doi: 10.1016/j.actamat.2011.10.055.
[57] V. Paidar, Y.-S. Lin, M. Cak, and V. Vitek, 'Why is the slip direction in CuZn and FeAl different than in CoTi?', *Intermetallics*, vol. 18, no. 7, pp. 1285–1287, Jul. 2010, doi: 10.1016/j.intermet.2009.11.015.
[58] E. Hwang *et al.*, 'Predicting ductility in quaternary B 2 -like alloys', *Phys. Rev. Materials*, vol. 5, no. 3, p. 033604, Mar. 2021, doi: 10.1103/PhysRevMaterials.5.033604.
[59] N. I. Medvedeva, O. N. Mryasov, Yu. N. Gornostyrev, D. L. Novikov, and A. J. Freeman, 'First-principles total-energy calculations for planar shear and cleavage decohesion processes in *B* 2-ordered NiAl and FeAl', *Phys. Rev. B*, vol. 54, no. 19, pp. 13506–13514, Nov. 1996, doi: 10.1103/PhysRevB.54.13506.

[60] I. Baker, 'An Overview of the Mechanical Properties of FeAl', *MRS Proc.*, vol. 1128, pp. 1128-U02-01, 2008, doi: 10.1557/PROC-1128-U02-01.
[61] M. Yamaguchi and Y. Umakoshi, 'The operative slip systems and slip line morphology in βCuZn and β(CuNi)Zn alloys', *Acta Metallurgica*, vol. 24, no. 11, pp. 1061–1067, Nov. 1976, doi: 10.1016/0001-6160(76)90137-1.
[62] T. Takasugi and M. Yoshida, 'Transmission electron microscopy observation for activated slip systems of B2 FeTi', *Philosophical Magazine Letters*, vol. 72, no. 5, pp. 303–310, Nov. 1995, doi: 10.1080/09500839508242468.
[63] K. H. Hahn and K. Vedula, 'Room temperature tensile ductility in polycrystalline B2 NiAl', *Scripta Metallurgica*, vol. 23, no. 1, pp. 7–12, Jan. 1989, doi: 10.1016/0036-9748(89)90083-5.
[64] R. T. Pascoe and C. W. A. Newey, 'The Mechanical Behaviour of the Intermediate Phase NiAl', *Metal Science Journal*, vol. 2, no. 1, pp. 138–143, Jan. 1968, doi: 10.1179/030634568790443477.
[65] N. J. Zaluzec and H. L. Fraser, 'The origin of dislocations with b = <110> in single crystals of β-nial compressed along <001> at elevated temperatures', *Scripta Metallurgica*, vol. 8, no. 9, pp. 1049–1054, Sep. 1974, doi: 10.1016/S0036-9748(74)80002-5.
[66] B. Shao, D. Shan, B. Guo, and Y. Zong, 'Plastic deformation mechanism and interaction of B2, α2, and O phases in Ti22Al25Nb alloy at room temperature', *International Journal of Plasticity*, vol. 113, pp. 18–34, Feb. 2019, doi: 10.1016/j.ijplas.2018.09.004.
[67] R. Srinivasan, M. F. Savage, R. D. Noebe, and M. J. Mills, 'Effects of Deviation from Stoichiometry on Deformation Behavior of Hard-Oriented NiAl Single Crystals', *MRS Online Proceedings Library (OPL)*, vol. 552, p. KK9.10.1, Jan. 1998, doi: 10.1557/PROC-552-KK9.10.1.
[68] D. K. Patrick, K.-M. Chang, D. B. Miracle, and H. A. Lipsitt, 'Burgers Vector Transition in Fe-Ai-Ni Alloys', *MRS Online Proceedings Library (OPL)*, vol. 213, p. 267, Jan. 1990, doi: 10.1557/PROC-213-267.
[69] C. L. Fu and M. H. Yoo, 'Deformation behavior of B2 type aluminides: FeAl and NiAl', *Acta Metallurgica et Materialia*, vol. 40, no. 4, pp. 703–711, Apr. 1992, doi: 10.1016/0956-7151(92)90012-4.
[70] C. Li *et al.*, 'Microstructures and mechanical properties of body-centered-cubic (Al,Ti)0.7(Ni,Co,Fe,Cr)5 high entropy alloys with coherent B2/L21 nanoprecipitation', *Materials Science and Engineering: A*, vol. 737, pp. 286–296, Nov. 2018, doi: 10.1016/j.msea.2018.09.060.
[71] X. Yan, J. Ju, L. Zuo, D. Ma, J. Hu, and T. Zhang, 'Variation of BCC/B2 coherent microstructure and resultant improvement in strength of Al0.7CrxFe3−xCoNi high-entropy alloys', *Materials Characterization*, vol. 203, p. 113129, Sep. 2023, doi: 10.1016/j.matchar.2023.113129.
[72] J. Luster and M. A. Morris, 'Compatibility of deformation in two-phase Ti-Al alloys: Dependence on microstructure and orientation relationships', *Metall Mater Trans A*, vol. 26, no. 7, pp. 1745–1756, Jul. 1995, doi: 10.1007/BF02670762.
[73] S. Suri, G. B. Viswanathan, T. Neeraj, D.-H. Hou, and M. J. Mills, 'Room temperature deformation and mechanisms of slip transmission in oriented single-colony crystals of an α/β titanium alloy', *Acta Materialia*, vol. 47, no. 3, pp. 1019–1034, Feb. 1999, doi: 10.1016/S1359-6454(98)00364-4.
[74] Z. Zheng, S. Waheed, D. S. Balint, and F. P. E. Dunne, 'Slip transfer across phase boundaries in dual phase titanium alloys and the effect on strain rate sensitivity',

International Journal of Plasticity, vol. 104, pp. 23–38, May 2018, doi: 10.1016/j.ijplas.2018.01.011.

[75] E. Werner and W. Prantl, 'Slip transfer across grain and phase boundaries', *Acta Metallurgica et Materialia*, vol. 38, no. 3, pp. 533–537, Mar. 1990, doi: 10.1016/0956-7151(90)90159-E.

[76] E. Nieto-Valeiras, S. Haouala, and J. LLorca, 'On the effect of slip transfer at grain boundaries on the strength of FCC polycrystals', *European Journal of Mechanics - A/Solids*, vol. 91, p. 104427, Jan. 2022, doi: 10.1016/j.euromechsol.2021.104427.

[77] C. Zhang, H. Song, D. Oliveros, A. Fraczkiewicz, M. Legros, and S. Sandfeld, 'Data-mining of in-situ TEM experiments: On the dynamics of dislocations in CoCrFeMnNi alloys', *Acta Materialia*, vol. 241, p. 118394, Dec. 2022, doi: 10.1016/j.actamat.2022.118394.

[78] K. Tougou, A. Shikata, U. Kawase, T. Onitsuka, and K. Fukumoto, '*In-situ* TEM observation of dynamic interaction between dislocation and cavity in BCC metals in tensile deformation', *Journal of Nuclear Materials*, vol. 465, pp. 843–848, Oct. 2015, doi: 10.1016/j.jnucmat.2015.05.046.

[79] W. Zhang *et al.*, 'Micro/nano-mechanical behaviors of individual FCC, BCC and FCC/BCC interphase in a high-entropy alloy', *Journal of Materials Science & Technology*, vol. 114, pp. 102–110, Jul. 2022, doi: 10.1016/j.jmst.2021.11.017.

[80] A. B. Hagen and C. Thaulow, 'Low temperature in-situ micro-compression testing of iron pillars', *Materials Science and Engineering: A*, vol. 678, pp. 355–364, Dec. 2016, doi: 10.1016/j.msea.2016.09.110.

[81] N. Kheradmand, B. R. Rogne, S. Dumoulin, Y. Deng, R. Johnsen, and A. Barnoush, 'Small scale testing approach to reveal specific features of slip behavior in BCC metals', *Acta Materialia*, vol. 174, pp. 142–152, Aug. 2019, doi: 10.1016/j.actamat.2019.05.031.

[82] M. Ben Haj Slama *et al.*, 'Electron channeling contrast imaging characterization and crystal plasticity modelling of dislocation activity in Ti21S BCC material', *Materialia*, vol. 15, p. 100996, Mar. 2021, doi: 10.1016/j.mtla.2020.100996.

[83] L. Patriarca, W. Abuzaid, H. Sehitoglu, and H. J. Maier, 'Slip transmission in bcc FeCr polycrystal', *Materials Science and Engineering: A*, vol. 588, pp. 308–317, Dec. 2013, doi: 10.1016/j.msea.2013.08.050.

[84] J. D. Carroll, B. G. Clark, T. E. Buchheit, B. L. Boyce, and C. R. Weinberger, 'An experimental statistical analysis of stress projection factors in BCC tantalum', *Materials Science and Engineering: A*, vol. 581, pp. 108–118, Oct. 2013, doi: 10.1016/j.msea.2013.05.085.

[85] D. Lunt *et al.*, 'Understanding the role of local texture variation on slip activity in a two-phase titanium alloy', *Acta Materialia*, vol. 216, p. 117111, Jun. 2021, doi: 10.1016/j.actamat.2021.117111.

[86] R. Sperry, A. Harte, J. Quinta da Fonseca, E. R. Homer, R. H. Wagoner, and D. T. Fullwood, 'Slip band characteristics in the presence of grain boundaries in nickel-based superalloy', *Acta Materialia*, vol. 193, pp. 229–238, Jul. 2020, doi: 10.1016/j.actamat.2020.04.037.

[87] A. Harte *et al.*, 'The effect of solid solution and gamma prime on the deformation modes in Ni-based superalloys', *Acta Materialia*, vol. 194, pp. 257–275, Aug. 2020, doi: 10.1016/j.actamat.2020.04.004.

[88] H. Yu, S. Das, H. Yu, P. Karamched, E. Tarleton, and F. Hofmann, 'Orientation dependence of the nano-indentation behaviour of pure Tungsten', *Scripta Materialia*, vol. 189, pp. 135–139, Dec. 2020, doi: 10.1016/j.scriptamat.2020.08.014.

[89] T. Vermeij, R. Peerlings, M. Geers, and J. Hoefnagels, 'Automated Identification of Slip System Activity Fields from Digital Image Correlation Data', *Acta Materialia*, vol. 243, p. 118502, Jan. 2023, doi: 10.1016/j.actamat.2022.118502.
[90] J. S. K.-L. Gibson, R. Pei, M. Heller, S. Medghalchi, W. Luo, and S. Korte-Kerzel, 'Finding and Characterising Active Slip Systems: A Short Review and Tutorial with Automation Tools', *Materials*, vol. 14, no. 2, p. 407, Jan. 2021, doi: 10.3390/ma14020407.
[91] K. A. Nibur and D. F. Bahr, 'Identifying slip systems around indentations in FCC metals', *Scripta Materialia*, vol. 49, no. 11, pp. 1055–1060, Dec. 2003, doi: 10.1016/j.scriptamat.2003.08.021.
[92] P. A. Sabnis, S. Forest, N. K. Arakere, and V. A. Yastrebov, 'Crystal plasticity analysis of cylindrical indentation on a Ni-base single crystal superalloy', *International Journal of Plasticity*, vol. 51, pp. 200–217, Dec. 2013, doi: 10.1016/j.ijplas.2013.05.004.
[93] A. E. Giannakopoulos, P.-L. Larsson, and R. Vestergaard, 'Analysis of Vickers indentation', *International Journal of Solids and Structures*, vol. 31, no. 19, pp. 2679–2708, Oct. 1994, doi: 10.1016/0020-7683(94)90225-9.
[94] A. J. Knowles, D. Dye, R. J. Dodds, A. Watson, C. D. Hardie, and S. A. Humphry-Baker, 'Tungsten-based bcc-superalloys', *Applied Materials Today*, vol. 23, p. 101014, Jun. 2021, doi: 10.1016/j.apmt.2021.101014.
[95] K. Venkatraman, M. Ben Haj Slama, V. Taupin, N. Maloufi, and A. Guitton, 'Tuning critical resolved shear stress ratios for bcc-titanium Ti21S via an automated data analysis approach', *Modelling Simul. Mater. Sci. Eng.*, vol. 29, no. 5, p. 055014, Jul. 2021, doi: 10.1088/1361-651X/abfeb0.
[96] G. Nolze, M. Jürgens, J. Olbricht, and A. Winkelmann, 'Improving the precision of orientation measurements from technical materials via EBSD pattern matching', *Acta Materialia*, vol. 159, pp. 408–415, Oct. 2018, doi: 10.1016/j.actamat.2018.08.028.
[97] R. G. Brown and P. Y. C. Hwang, *Introduction to Random Signals and Applied Kalman Filtering*, (3 ed.). New York: John Wiley & Sons, 1996.
[98] D. Boulfelfel, R. M. Rangayyan, L. J. Hahn, and R. Kloiber, 'Three-dimensional restoration of single photon emission computed tomography images', *IEEE Transactions on Nuclear Science*, vol. 41, no. 5, pp. 1746–1754, Oct. 1994, doi: 10.1109/23.317385.
[99] V. T. Witusiewicz *et al.*, 'Thermodynamic re-modelling of the ternary Al–Mo–Ti system based on novel experimental data', *Journal of Alloys and Compounds*, vol. 749, pp. 1071–1091, Jun. 2018, doi: 10.1016/j.jallcom.2018.03.283.
[100] V. Raghavan, 'Al-Nb-Ti (Aluminum-Niobium-Titanium)', *J. Phase Equilib. Diffus.*, vol. 31, no. 1, pp. 47–52, Feb. 2010, doi: 10.1007/s11669-009-9623-x.
[101] G. Cacciamani, J. De Keyzer, R. Ferro, U. E. Klotz, J. Lacaze, and P. Wollants, 'Critical evaluation of the Fe–Ni, Fe–Ti and Fe–Ni–Ti alloy systems', *Intermetallics*, vol. 14, no. 10, pp. 1312–1325, Oct. 2006, doi: 10.1016/j.intermet.2005.11.028.
[102] 'BMW AG Group Standard, Cold-rolled DP steels (GS 93005–11). Technical Report, 2009'.
[103] P. O'Kelly, A. Watson, G. Schmidt, M. Galetz, and A. J. Knowles, 'Ti-Fe Phase Evolution and Equilibria Toward β-Ti Superalloys', *J. Phase Equilib. Diffus.*, vol. 44, no. 6, pp. 738–750, Dec. 2023, doi: 10.1007/s11669-023-01066-8.
[104] E. M. Dematteis, N. Berti, F. Cuevas, M. Latroche, and M. Baricco, 'Substitutional effects in TiFe for hydrogen storage: a comprehensive review', *Mater. Adv.*, vol. 2, no. 8, pp. 2524–2560, 2021, doi: 10.1039/D1MA00101A.

[105] L. Barrow, A. T. W. Barrow, J. Almer, and M. R. Daymond, 'The Zr20Nb–H phase diagram and the characterisation of hydrides in β-Zr', *Journal of Nuclear Materials*, vol. 442, no. 1–3, pp. 292–297, Nov. 2013, doi: 10.1016/j.jnucmat.2013.08.031.
[106] A. J. Knowles *et al.*, 'Laves phase intermetallic matrix composite in situ toughened by ductile precipitates', *Scripta Materialia*, vol. 140, pp. 59–62, Nov. 2017, doi: 10.1016/j.scriptamat.2017.06.043.
[107] B. Poole and F. P. E. Dunne, 'Slip band interactions and GND latent hardening in a galling resistant stainless steel', *Materials Science and Engineering: A*, vol. 813, p. 141176, May 2021, doi: 10.1016/j.msea.2021.141176.
[108] D. K. Patrick, K.-M. Chang, D. B. Miracle, and H. A. Lipsitt, 'Burgers Vector Transition in Fe-Ai-Ni Alloys', *MRS Proc.*, vol. 213, p. 267, 1990, doi: 10.1557/PROC-213-267.
[109] A. Misra, G. Ghosh, G. Olson, and R. Bishop, 'Phase equilibria in prototype Nb-Pd-Hf-Al alloys', *Metallurgical and Materials Transactions A*, vol. 34, pp. 1771–1782, Sep. 2003, doi: 10.1007/s11661-003-0143-8.
[110] N. Yurchenko, E. Panina, D. Shaysultanov, S. Zherebtsov, and N. Stepanov, 'Refractory high entropy alloy with ductile intermetallic B2 matrix / hard bcc particles and exceptional strain hardening capacity', *Materialia*, vol. 20, p. 101225, Dec. 2021, doi: 10.1016/j.mtla.2021.101225.
[111] L. Zhichao, M. Dong, L. Xiongjun, and Z. Lu, 'High-throughput and data-driven machine learning techniques for discovering high-entropy alloys', *Commun Mater*, vol. 5, no. 1, pp. 1–19, May 2024, doi: 10.1038/s43246-024-00487-3.
[112] E. L. Calvert, A. J. Knowles, J. J. Pope, D. Dye, and M. Jackson, 'Novel high strength titanium-titanium composites produced using field-assisted sintering technology (FAST)', *Scripta Materialia*, vol. 159, pp. 51–57, Jan. 2019, doi: 10.1016/j.scriptamat.2018.08.036.
[113] K. Goto, A. Ikeda, T. Osada, I. Watanabe, K. Kawagishi, and T. Ohmura, 'High-throughput evaluation of stress–strain relationships in Ni–Co–Cr ternary systems via indentation testing of diffusion couples', *Journal of Alloys and Compounds*, vol. 910, p. 164868, Jul. 2022, doi: 10.1016/j.jallcom.2022.164868.
[114] O. Franke, K. Durst, and M. Göken, 'Nanoindentation investigations to study solid solution hardening in Ni-based diffusion couples', *Journal of Materials Research*, vol. 24, no. 3, pp. 1127–1134, Mar. 2009, doi: 10.1557/jmr.2009.0135.
[115] V. V. Shastry, V. D. Divya, M. A. Azeem, A. Paul, D. Dye, and U. Ramamurty, 'Combining indentation and diffusion couple techniques for combinatorial discovery of high temperature shape memory alloys', *Acta Materialia*, vol. 61, no. 15, pp. 5735–5742, Sep. 2013, doi: 10.1016/j.actamat.2013.06.017.
[116] L. Borasi, A. Slagter, A. Mortensen, and C. Kirchlechner, 'On the preparation and mechanical testing of nano to micron-scale specimens', *Acta Materialia*, p. 120394, Sep. 2024, doi: 10.1016/j.actamat.2024.120394.
[117] S. Schmit, 'Multiple Hypothesis testing', MultiThreaded (accessed Dec. 2024). [Online]. Available: https://multithreaded.stitchfix.com/blog/2015/10/15/multiple-hypothesis-testing/
[118] R. A. Armstrong, 'When to use the Bonferroni correction', *Ophthalmic Physiol Opt*, vol. 34, no. 5, pp. 502–508, Sep. 2014, doi: 10.1111/opo.12131.
[119] S. Senn and W. Richardson, 'The first t-test', *Statistics in Medicine*, vol. 13, no. 8, pp. 785–803, 1994, doi: 10.1002/sim.4780130802.

[120] Y. H. Wang, ‘On the Number of Successes in Independent Trials’, *Statistica Sinica*, vol. 3, no. 2, pp. 295–312, 1993.
[121] M. Fernandez and S. Williams, ‘Closed-Form Expression for the Poisson-Binomial Probability Density Function’, *IEEE Transactions on Aerospace and Electronic Systems*, vol. 46, no. 2, pp. 803–817, Apr. 2010, doi: 10.1109/TAES.2010.5461658.
[122] S. Holm, ‘A Simple Sequentially Rejective Multiple Test Procedure’, *Scandinavian Journal of Statistics*, vol. 6, no. 2, pp. 65–70, 1979.
[123] I. J. Good, ‘Significance Tests in Parallel and in Series’, *Journal of the American Statistical Association*, vol. 53, no. 284, pp. 799–813, Dec. 1958, doi: 10.1080/01621459.1958.10501480.
[124] D. J. Wilson, ‘The harmonic mean p-value for combining dependent tests’, *Proceedings of the National Academy of Sciences*, vol. 116, no. 4, pp. 1195–1200, Jan. 2019, doi: 10.1073/pnas.1814092116.
[125] T. Takasugi and M. Yoshida, ‘Transmission electron microscopy observation for activated slip systems of B2 FeTi’, *Philosophical Magazine Letters*, vol. 72, no. 5, pp. 303–310, Nov. 1995, doi: 10.1080/09500839508242468.
[126] R. Guerra, C. J. Etzel, D. R. Goldstein, and S. R. Sain, ‘Meta-analysis by combining p-values: Simulated linkage studies’, *Genetic Epidemiology*, vol. 17, no. S1, pp. S605–S609, 1999, doi: 10.1002/gepi.1370170798.
[127] R. Susmaga and I. Szczęch, ‘Visualization support for the analysis of properties of interestingness measures’, *Bulletin of the Polish Academy of Sciences Technical Sciences*, vol. 63, no. 1, pp. 315–327, Mar. 2015, doi: 10.1515/bpasts-2015-0036.

Appendix 1

Extra information on the algorithm

Matlab™ Hough transform functions used, as lines of code:

```
% input:

Ji = ("segment analysed") % Ji is a 2D N*N matrix of a binary picture, a segment from the picture analysed on which edge detection was performed

angleList = -90:0.1:89;

% angleList defines the orientations that the Hough transform can find. Defined as such, a step of 0.1° is used by the Hough transform to find the line orientations. Note that this is much smaller than the identification range used and therefore should not affect the precision of the results.

% Now detecting lines in the segment using Hough transform functions:

[H,theta,rho] = hough(Ji, 'Theta', angleList);

P = houghpeaks(H,3,'threshold',0.3*max(H(:))); % the input "3" here decides the number of lines that will be detected.

lines = houghlines(Ji,theta,rho,P,'FillGap',100,'MinLength',4);

% "Fillgap" is the maximum amount of space in pixel between two identified lines of the same orientation that will be "filled" to draw a unique line. "Minlength" defines the minimum amount of consecutively aligned white pixels that will be considered as being a line. Defined as such, in a segment, the three longest alignments of white pixel, regardless of how discontinuous they are, should be identified and associated to three unique lines.
```

The output "lines", containing the orientations and positions of the three lines detected is then stored, for each segment, and will be analysed by the rest of the code.

Miscellaneous functions:

'…' being the matrix of pixel corresponding to the pictures/segments:

wiener2(… ,[5 5]) is used for smoothing the pictures, which is common practice prior to edge detection algorithms. Quoting open access MathWorks documentation: "The Wiener filter tailors itself to the local image variance. Where the variance is large, `wiener2` performs little smoothing. Where the variance is small, `wiener2` performs more smoothing. […] The adaptive filter is more selective than a comparable linear filter, preserving edges and other high-frequency parts of an image". This smoothing is reapplied 10 times to the pictures, which helps erasing miscellaneous features, image scanning related noise, and highlighting slip traces.

imadjust(…) is used to adjust the contrast of the segments before edge detection, using default settings.

edge(… , 'Canny') is used to perform edge detection on the contrast adjusted segments, using a Canny algorithm.

Appendix 2

Additional data on the B2 FeAl-NiAl diffusion gradient

This appendix supplements Chapter 4, showing in Figure A2.1 the uncertainties on the measured average composition of each indent made on the B2 FeAl-NiAl gradient, and in Figures A2.2-A2.3 additional outcomes from their automated slip trace analysis for various analysis parameters, a small interpretation of the latter two figures is given at the end of this appendix.

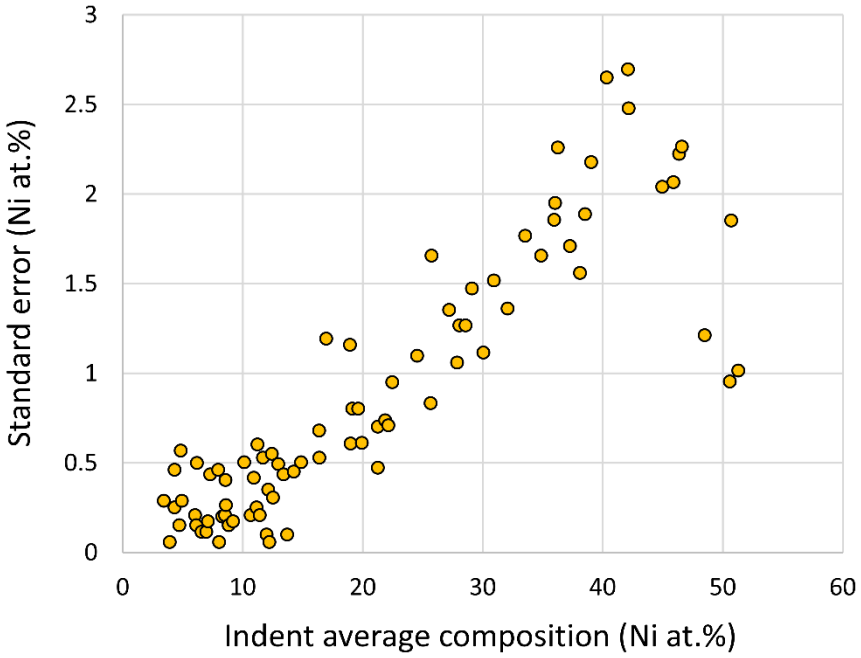


Figure A2.1: Variability of the EDX measured Ni (at.%) composition of each indent in the B2 FeAl–NiAl gradient. The indent average composition (x-axis) is determined from 3 EDX point scans performed as described in §4.3 of Chapter 4, and is therefore given with a standard error (y-axis) due to changes in composition depending on the position of the point scans. Note that this variability is highest in areas of the gradient where the slip activity was not measured to evolve significantly, and therefore the uncertainty on Ni composition should affect only marginally the interpretation of the slip activity evolution.

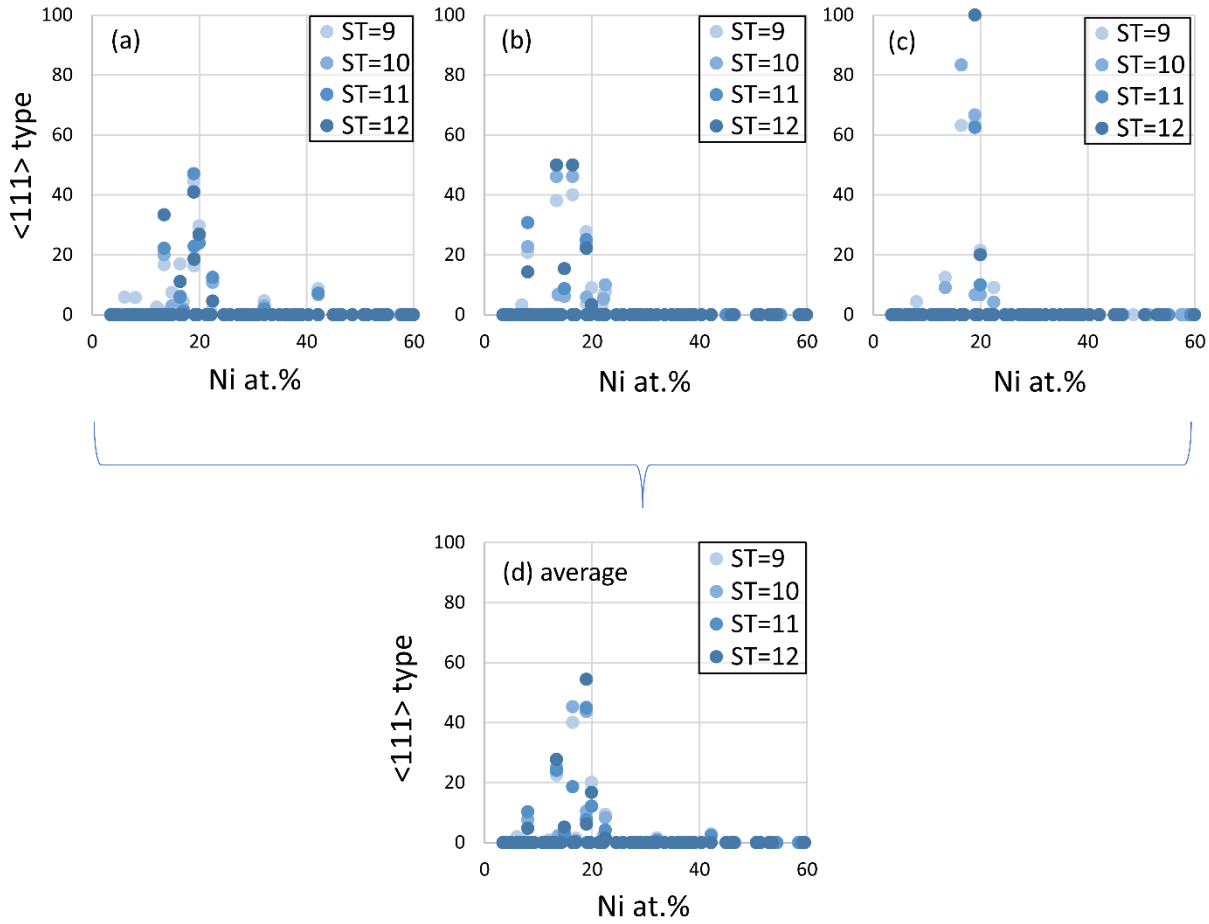


Figure A2.2: Automated slip trace analysis output, per indent, on the NiAl-FeAl diffusion gradient for different segmentation size N, (a) N=100px, (b) N=120px, (c) N=140px, (d) averaged between the three, and for different score threshold ST (9 to 12). The y-axis shows the proportion of lines matching exclusively {112} and/or {123} orientations, and therefore unambiguously aligned with a <111> type slip, detected on the picture associated with each indent. The x-axis is the average EDX measured composition of the indent. Results are shown for various score threshold ST, which is the minimum score (§3.3.1.4) a line must have to be included in the statistics.

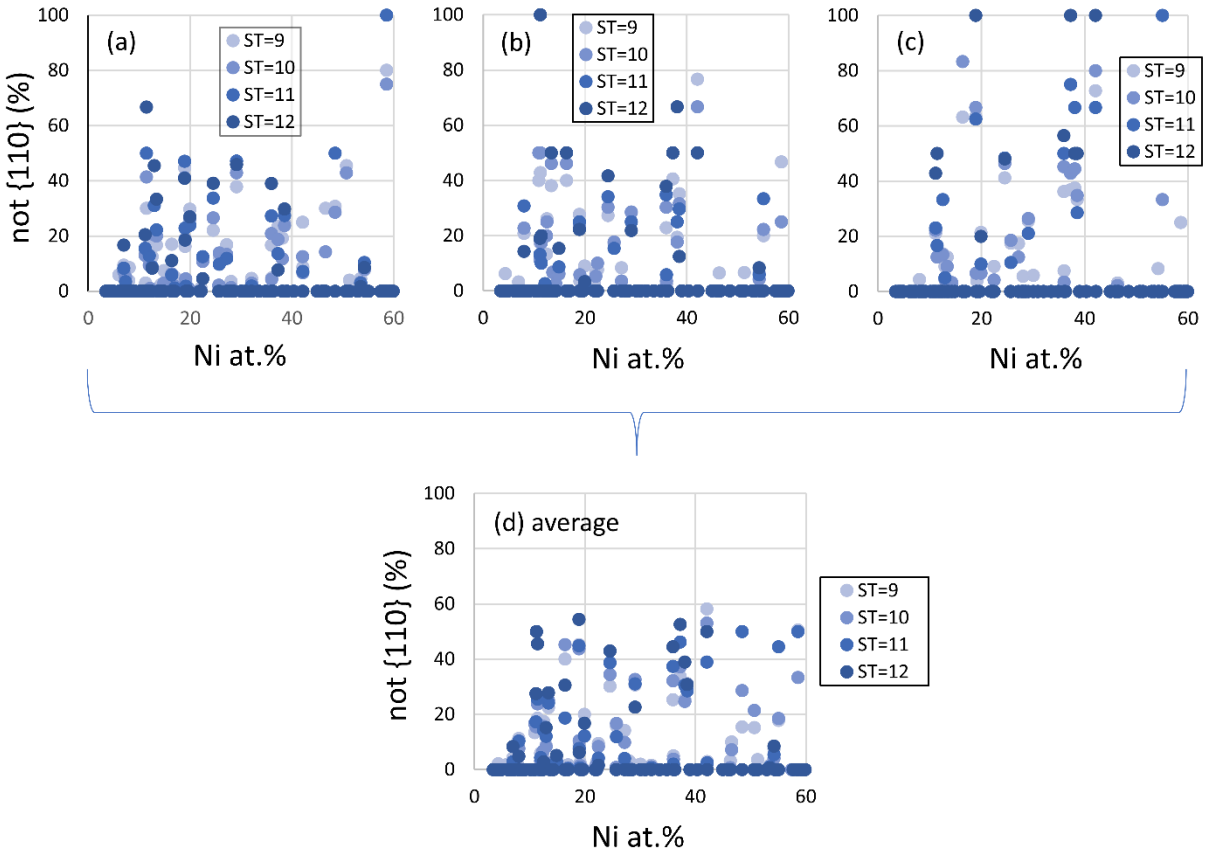


Figure A2.3: Analysis of the gradient using different code parameters (lines not matching {110} orientations). Automated slip trace analysis output, per indent, on the FeAl-NiAl diffusion gradient for different segmentation size N, (a) N=100px, (b) N=120px, (c) N=140px, (d) averaged between the three, and for different score threshold ST (9 to 12). The y-axis shows the proportion of lines that do not match {110} planes, and therefore unambiguously aligned with a slip from another plane type, detected on the picture of the indent. The x-axis is the average EDS measured composition of the indent. Results are shown for various score threshold ST, which is the minimum score a line must have to be included in the statistics.

Explanation & interpretation:

In theory, higher segmentation sizes N and higher score threshold ST are less likely to include portions of misattributed lines in the analysis (i.e. lines that do not match their originating slip plane type). A consequence however is that they lead to a lower variety of slip traces detected, disadvantaging in particular the detection of wavy slip traces. As a result, the measurements per indents are more extreme using such parameters (proportions of match are closer to either 100% or 0% in (c)). Note that any of these analysis parameter combinations are, in principle, equally valid, but they perform slightly differently for detecting different kind of slip traces. Indents which showed no lines detected at a set of score + segmentation size were ignored, which concerns mostly high Ni content indents, since the slip trace visibility is lower in this part of the sample.